Characterizing Agricultural N_2O Emissions in the U.S. Midwest Using a Novel Top-Down Approach Based on Airborne In Situ Measurements

Maximilian Eckl

SIGILL. UNIVERSITAT. LUDOVIC. MAXIM.

München 2021

Characterizing Agricultural N_2O Emissions in the U.S. Midwest Using a Novel Top-Down Approach Based on Airborne In Situ Measurements

Maximilian Eckl

Dissertation
an der Fakultät für Physik
der Ludwig–Maximilians–Universität
München

vorgelegt von
Maximilian Eckl
aus Niedermünchsdorf

München, den 26. August 2021

Erstgutachter: Prof. Dr. Markus Rapp
Zweitgutachter: Prof. Dr. Christoph Knote
Tag der mündlichen Prüfung: 16. November 2021

Zusammenfassung

Distickstoffmonoxid (N_2O) ist nach Kohlenstoffdioxid und Methan das drittwichtigste langlebige, anthropogene Treibhausgas und heutzutage die dominante ozonabbauende Substanz in der Stratosphäre. Anthropogene Emissionen, vor allem auf Grund von Düngung landwirtschaftlicher Regionen, haben dazu geführt, dass die atmosphärischen Konzentrationen seit dem Start der Industrialisierung um über 20 % auf etwa 334 ppb angestiegen sind. Trotz seiner wichtigen Rolle, wird N_2O kaum in den Plänen zur Emissionsreduktion innerhalb des Pariser Abkommens berücksichtigt. Ein Grund dafür ist die unzureichende Charakterisierung regionaler N_2O Quellen auf Grund fehlender Messungen und Methodiken, welche für eine gründliche Analyse komplexer N_2O Flächenquellen nötig sind.

In dieser Arbeit wird die Hypothese untersucht, ob regionale flugzeuggetragene in situ Messungen von N_2O geeignet sind, um N_2O Emissionen aus landwirtschaftlich intensiv genutzten Regionen zu bestimmen und um neueste Bottom-up-Emissionsinventare zu evaluieren. Hierfür wird ein außergewöhnlicher in situ N_2O Datensatz verwendet, welcher im Zuge des Atmospheric Carbon and Transport-America (ACT-America) Projekts bei fünf Flugzeugmesskampagnen in allen vier Jahreszeiten von 2016 bis 2019 über dem östlichen Teil der USA zusammengetragen wurde. Der Datensatz besteht aus hochpräzisen Luftproben und einzigartigen, kontinuierlichen Messungen mit einem Absorptionsspektrometer (Quantum Cascade Laser Spectrometer (QCLS)), welches im Zuge dieser Arbeit für N_2O optimiert und bei zwei der fünf Flugzeugmesskampagnen erfolgreich eingesetzt wurde. In Kombination mit WRF (Weather Research and Forecasting model) Simulationen und vorhandenen atmosphärischen Dispersionsrechnungen, werden N_2O Emissionen im Bottom-up-Inventar EDGAR (Emissions Database for Global Atmospheric Research) skaliert, um so die Emissionen aus dem mittleren Westen der USA (MW) – einer Region mit einer der intensivsten Landwirtschaften weltweit – zu quantifizieren.

Mit den QCLS Messungen und WRF Simulationen sind die N_2O Emissionen im MW im Oktober 2017 ($0.42 \pm 0.28\,\mathrm{nmol\,m^{-2}\,s^{-1}}$) und im Juni/Juli 2019 ($1.06 \pm 0.57\,\mathrm{nmol\,m^{-2}\,s^{-1}}$) quantifiziert worden. Die Luftproben, die für alle fünf ACT-America Kampagnen verfügbar sind, wurden verwendet, um die Saisonalität der Emissionen zu untersuchen. Hauptsächlich auf Grund von Düngung, hat diese Studie für den Frühling 75 % und für den Herbst 13 % höhere Emissionen ergeben als für den Sommer. Emissionsabschätzungen für den Winter waren höchstwahrscheinlich auf Grund von Frost/Tau Zyklen des Bodens sogar 230 % höher als für den Sommer. Die Ergebnisse sind konsistent mit anderen bodengebundenen Top-down-Studien, jedoch sind weitere Studien nötig um die Komplexität von N_2O Emissionen komplett abbilden zu können. Vergleiche mit dem Bottom-up-Inventar EDGAR haben gezeigt, dass EDGAR N_2O Emissionen im MW deutlich (Faktoren zwischen zwei und zehn) und in extremen Fällen sogar um Faktoren bis zu 20 unterschätzt. Monatliche Emissionsabschätzungen für 2011–2015 mit dem prozessbasierten Modell DayCent (daily time-step version of the CENTURY model) sind signifikant besser als EDGAR (Faktoren zwischen zwei und fünf), da DayCent regionale Besonderheiten, wie Bodenbedingungen und Wetter, berücksichtigt. Eine Sensitivitätsanalyse basierend auf den Luftproben und Dispersionsrechnungen deutet daraufhin, dass die Heterogenität von N_2O Bodenemissionen im MW im Sommer vorwiegend mit der Bodentemperatur und im Frühling und Herbst vorwiegend mit der Bodenfeuchte korreliert. Im Winter wird das Bodenemissionsgeschehen durch Frost/Tau Zyklen bestimmt. Für eine umfassende quantitative Analyse sind zusätzlich Simulationen mit einem prozessbasierten Modell nötig.

Diese Arbeit zeigt, dass flugzeuggetragene in situ N_2O Messungen gut geeignet sind, um regionale N_2O Emissionen zu charakterisieren. Dies ist ein wertvoller Beitrag zum Bestreben ein nationales N_2O Monitoring System zu entwickeln, die Grundlage für Emissionsreduktionsstrategien, welche dringend benötigt werden um die Ziele des Pariser Abkommens zu erreichen.

Abstract

Nitrous oxide (N_2O) is, after carbon dioxide and methane, the third most important long-lived anthropogenic greenhouse gas and nowadays the dominant ozone-depleting substance in the stratosphere. Anthropogenic emissions, mainly released due to fertilization practices in agricultural regions, have increased atmospheric concentrations by more than 20 % since the start of the industrialization to about 334 ppb. Despite its important role, N_2O is almost ignored in emission reduction plans submitted to the Paris Agreement. One of the reasons for this is the insufficient characterization of regional N_2O sources due to the lack of measurements and methodologies required for thorough analyses of complex N_2O area sources.

This thesis investigates the hypothesis that regional-scale airborne in situ measurements of N_2O are well-suited to characterize N_2O emissions from intensively cultivated agricultural regions and to evaluate state-of-the-art bottom-up emission inventories. To this end, an exceptional in situ N_2O dataset is used, which has been collected in the course of the Atmospheric Carbon and Transport-America (ACT-America) project (2016–2019) during five aircraft campaigns covering all four seasons over the eastern part of the U.S. It consists of high-precision flask measurements and unique continuous measurements with an absorption spectrometer (Quantum Cascade Laser Spectrometer (QCLS)), which, in the course of this work, was optimized for N_2O and successfully deployed during two of the five aircraft campaigns. In combination with WRF (Weather Research and Forecasting model) simulations and available atmospheric dispersion calculations, N_2O emissions in the bottom-up inventory EDGAR (Emissions Database for Global Atmospheric Research) are scaled to quantify emissions from the U.S. Midwest – a region with one of the most intensive agriculture in the world.

Using a combination of QCLS measurements and WRF simulations, N_2O emissions in the Midwest in October 2017 ($0.42 \pm 0.28\,\mathrm{nmol\,m^{-2}\,s^{-1}}$) and June/July 2019 ($1.06 \pm 0.57\,\mathrm{nmol\,m^{-2}\,s^{-1}}$) have been quantified. Flask measurements, available for all five ACT-America deployments, were further used to study the seasonality of emissions. Primarily due to fertilization, emissions in spring were found to be 75 % higher than in summer, while in fall, they were observed to be 13 % higher than in summer. In winter, estimated emissions even exceeded the summer estimates by 230 %, most likely due to freezing/thawing processes of the soils. The results of this study are consistent with other ground-based top-down studies. However, further studies are needed to be able to fully capture the complexity of N_2O emissions. Comparisons with the bottom-up inventory EDGAR show that EDGAR underestimates Midwest N_2O emissions significantly (factors between two and ten), for exceptional cases even by factors up to 20. Monthly Midwest emission estimates for 2011–2015 calculated with the process-based model DayCent (daily time-step version of the CENTURY model) are significantly closer to the results of this thesis than EDGAR (factors between two and five), since DayCent considers regional characteristics like soil conditions and weather. A sensitivity analysis using the flask measurements and dispersion calculations indicates that the heterogeneity of N_2O soil emissions in the Midwest mainly correlates with soil temperature in summer and soil moisture in spring and fall. In winter, soil emissions are dominated by freezing/thawing processes. For a thorough quantitative analysis, additional simulations with a process-based model are required.

This work shows that airborne in situ N_2O measurements are suitable for characterizing regional N_2O emissions. This is a valuable contribution to the effort to establish a national N_2O emission monitoring system, the basis for emission reduction strategies, which are urgently needed to meet the targets of the Paris Agreement.

Parts of the methods and results presented in this thesis have been published in the following article:

Eckl, M., Roiger, A., Kostinek, J., Fiehn, A., Huntrieser, H., Knote, C., Barkley, Z. R., Ogle, S. M., Baier, B. C., Sweeney, C., & Davis, K. J. (2021). Quantifying Nitrous Oxide Emissions in the U.S. Midwest: A Top-Down Study Using High Resolution Airborne In-Situ Observations. *Geophysical Research Letters*, *48*(5), e2020GL091266. https://doi.org/10.1029/2020gl091266

M. Eckl conducted the measurements, processed the data, performed the WRF-Chem simulations, analyzed all data, and wrote the manuscript. A. Roiger developed the research idea and supported together with A. Fiehn, H. Huntrieser, and Z. R. Barkley the interpretation of the analyses. J. Kostinek characterized the QCLS instrument, developed the basis for the data processing, was available for any questions regarding the instrument, and together with A. Fiehn supported the measurements. C. Knote and Z. R. Barkley supported the development of the simulation setup and strategy. S. M. Ogle provided the DayCent simulations and supported their interpretation. B. C. Baier and C. Sweeney conducted the PFP measurements. K. J. Davis was the PI of the ACT-America project and supported the study in all aspects.

Parts of this thesis are literal excerpts of the paper including paragraphs from the Sections 3.2, 3.3.1, 3.4, 5, 9, A.7, and A.8.

Contents

List of Figures and Tables

Figures

Tables

1 Introduction

Climate is changing. From preindustrial times (1850–1900) to 2020, the Global Mean Surface Temperature (GMST) has risen by 1.2 ± 0.1 °C, with 2011–2020 being the warmest recorded decade ever (WMO, 2021). The latest report of the World Meteorological Organization (WMO) about the state of the climate in 2020 summarizes the implications of the prevailing global warming (WMO, 2021): Melting of sea ice, shelf ice, and glaciers, thawing of permafrost, rising of the sea level, and an enhanced frequency and severity of extreme weather events are only some of the consequences mankind is facing. Consequences are severe and concern nature, society, as well as economy around the world. They range from rising poverty and damaged infrastructure to the collapse of entire ecosystems. For example, already from the 1980s to the 2010s the increased frequency and severity of weather extremes multiplied the yearly number of billion dollar weather and climate disaster in the U.S. by four (NOAA, 2021). An ongoing global warming is expected to dramatically exacerbate the consequences of climate change (IPCC, 2013).

There is a consensus among the scientific community, that the man-made accumulation of long-lived Greenhouse Gases (GHGs) in the atmosphere in the last two centuries is a main driver of climate change (IPCC, 2013). Since the start of the industrialization, the world population and economy have experienced an enormous growth going hand in hand with a significant demand for food, energy, and other resources. The fulfillment of these needs comes along with an ongoing increase of anthropogenic GHG emissions, mostly carbon dioxide (CO_2), methane (CH_4), and nitrous oxide (N_2O) (e.g., Friedlingstein et al., 2020; Saunois et al., 2020; Tian et al., 2020). The resulting rise in the atmospheric abundances of CO_2, CH_4, and N_2O have altered the Earth's radiation budget which has been identified as one of the main drivers of climate change (Myhre et al., 2013). To limit the impacts and risks of climate change, 196 nations have signed the Paris Agreement in 2016 within the United Nations Framework Convention on Climate Change (UNFCCC, 2015). The overarching goal is to keep the rise of the GMST well below 2 °C with respect to the preindustrial reference and to undertake serious efforts to limit the global warming to 1.5 °C as this would significantly reduce the consequences of climate change. The key step to achieve this goal is the substantial reduction of anthropogenic GHG emissions. However, a special report by the Intergovernmental Panel on Climate Change (IPCC, 2018) predicts that already between 2030 and 2052 the GMST will be 1.5 °C higher than preindustrial levels if the current trend of GHG emission strengths persists, highlighting the need of an instantaneous reduction of anthropogenic emissions.

N_2O is one of the three main anthropogenically emitted GHGs contributing significantly to global warming (Myhre et al., 2013) and is nowadays additionally recognized as the dominant ozone depleting substance in the stratosphere (Ravishankara et al., 2009). Table 1.1 compares key characteristics of the three dominant anthropogenic GHGs. The global atmospheric N_2O abundance in February 2021 reached 334 ppb representing an increase of over 20 % since the industrialization. Considering that N_2O is a 298-times more effective GHG than CO_2 and that its atmospheric lifetime is 116 yr, this increase has altered the Earth's radiation budget significantly and persistently. Anthropogenic activities, and in particular agriculture with the application of synthetic fertilizers, are predominantly responsible for rising atmospheric N_2O mole fractions (Ciais et al., 2013; Tian et al., 2018; Tian et al., 2020). Despite the crucial role of nitrous oxide in the atmosphere, only one country, namely Uruguay, formulates clear targets for N_2O in its emission reduction plan submitted to the Paris Agreement. Recently, however, there is rising effort initiated to change this to meet the 2 °C target (Kanter et al., 2020). Especially since newest studies revealed that the recent increase of N_2O emissions is larger than the least optimistic emission projections of the IPCC (Thompson et al., 2019; Tian et al., 2020), the urgent need to reduce N_2O emissions becomes undeniable. Detailed knowledge about N_2O sources and sinks is a fundamental prerequisite for an effective emission reduction policy. In this context, atmospheric measurements of N_2O and accurate model simulations are the key to validate national inventory systems which report and monitor N_2O emissions and to evaluate the impact of emission reduction efforts (Ogle et al., 2020).

	N_2O	**CO_2**	**CH_4**
Global atmospheric mole fraction in February 2021:	334 ppb [1]	416 ppm [2]	1889 ppb [3]
Atmospheric abundance compared to 1750 [4]:	123 %	148 %	260 %
Atmospheric lifetime:	116 yr [5]	centuries to thousands of years [6]	9 yr [7]
GWP_{100} (global warming potential) [8,9]:	298	1	34
Contribution to anthropogenic radiative forcing of well-mixed GHGs [8,10]:	~6 %	~64 %	~17 %

[1] Dlugokencky (2021b) | [2] Dlugokencky and Tans (2021) | [3] Dlugokencky (2021a) | [4] WMO (2021) | [5] Prather et al. (2015) | [6] Archer et al. (2009) | [7] Prather et al. (2012) | [8] Myhre et al. (2013) | [9] with inclusion of climate-carbon feedbacks | [10] global mean between 1750 and 2011

Table 1.1: Overview of the three main anthropogenically emitted GHGs. The global warming potential on a 100 year horizon (GWP_{100}) describes the amount of heat that is absorbed by a GHG compared to the heat that is absorbed by the same mass of CO_2. The radiative forcing describes the change of the Earth's radiation budget due to natural or anthropogenic influences, like the increasing atmospheric concentrations of GHGs since 1750. Values for CO_2 and CH_4 are for comparison only and are not discussed in this thesis.

Although being desperately needed, accurate N_2O emission estimates are rare. A few bottom-up inventories exist which use emission factors to translate activity data to emission estimates.

However, the underlying data often rely on basic assumptions and are not well evaluated using independent measurements. Hence, uncertainties in such inventories are often large (Nisbet & Weiss, 2010), especially regarding N_2O. For example, in the widely used gridded Emissions Database for Global Atmospheric Research (EDGAR, 2020) the uncertainty of N_2O emission estimates from agriculture, the main anthropogenic source, is higher than 300 % on a global average (Solazzo et al., 2021). This is one to two orders of magnitude larger than the uncertainties of emission estimates of the other two main anthropogenic GHGs, CO_2 and CH_4. On a regional scale, N_2O emission estimates are likely worse (e.g., Janssens-Maenhout et al., 2019; Solazzo et al., 2021). The large uncertainties are caused by the nature of N_2O emissions from soils. Because different agricultural practices, weather, and soil conditions affect soil N_2O emissions directly, they are spatially and temporally highly heterogeneous (Stehfest & Bouwman, 2006) and are therefore difficult to capture with a simple emission factor approach. More sophisticated regional bottom-up estimates of N_2O emissions are provided by biogeochemical models like the daily time-step version of the CENTURY model (DayCent; Parton et al., 1998; Del Grosso et al., 2001; Del Grosso et al., 2011). Such models simulate soil processes and thereof resulting N_2O emissions and, thus, are capable of capturing the large heterogeneity of soil N_2O emissions to a certain extent. However, such estimates are only available for a few regions and times, because underlying processes are complex and simulating them requires a large set of detailed spatio-temporal input data like soil conditions and agricultural activity. Overall, uncertainties of N_2O bottom-up estimates are large, making an explicit and independent validation mandatory.

The method of choice to validate bottom-up emission estimates are top-down approaches (Nisbet & Weiss, 2010). They use independent atmospheric measurements of GHGs in combination with inverse modeling approaches to quantify emissions from local to global scales. In recent years, top-down approaches based on ground-based, airborne and even satellite observations were increasingly used and continuously improved, especially to study CH_4 emissions from point sources (e.g., Karion et al., 2013; Jacob et al., 2016; Luther et al., 2019). However, for that accurate sensing of small GHG enhancements above large atmospheric background mole fractions is required, making measurements challenging. This is particularly true for N_2O, whose typical enhancements in the atmosphere – even close to sources – are well below 1 % of the atmospheric background. Compared to CO_2 and CH_4, whose anthropogenic sources are typically point sources (power plants, oil & gas production, landfills), the dominating anthropogenic source of N_2O is agriculture. Hence, emissions are released over large areas leading to smaller enhancements much more difficult to detect above the atmospheric background, even for state-of-the-art measurement instruments. Despite the need of atmospheric N_2O measurements and top-down studies, they are rare and, thus, regional N_2O emissions are still highly uncertain (Reay et al., 2012). The German initiative to establish a national Integrated Greenhouse Gas Monitoring System (ITMS) even lists agricultural N_2O emissions as the first of the major sources of uncertainty in German GHG emission reports emphasizing the urgent need for N_2O top-down studies, especially in intensively cultivated agricultural regions.

The U.S. Midwest illustrates the high uncertainty of regional N_2O emission estimates. This region is a global hotspot of anthropogenic N_2O emissions (see Figure 1.1 and Miller et al., 2012). It is one of the most intensively cultivated agricultural regions worldwide accounting for around 25 % of world corn and soybean production in 2018 (FAO, 2020; USDA-NASS, 2020). Exceptionally large N_2O emissions spread over a large area are the consequence. A few top-down studies exist that quantify N_2O emissions in this important source region based on tall-tower measurements (Miller et al., 2012; Griffis et al., 2013; Chen et al., 2016; Fu et al., 2017) and airborne flask measurements (Kort et al., 2008). They agree, that common bottom-up estimates like EDGAR significantly underestimate anthropogenic emissions by factors between roughly two and 30, but they strongly disagree in the magnitude of underestimation. Hence, true emission amounts remain highly uncertain.

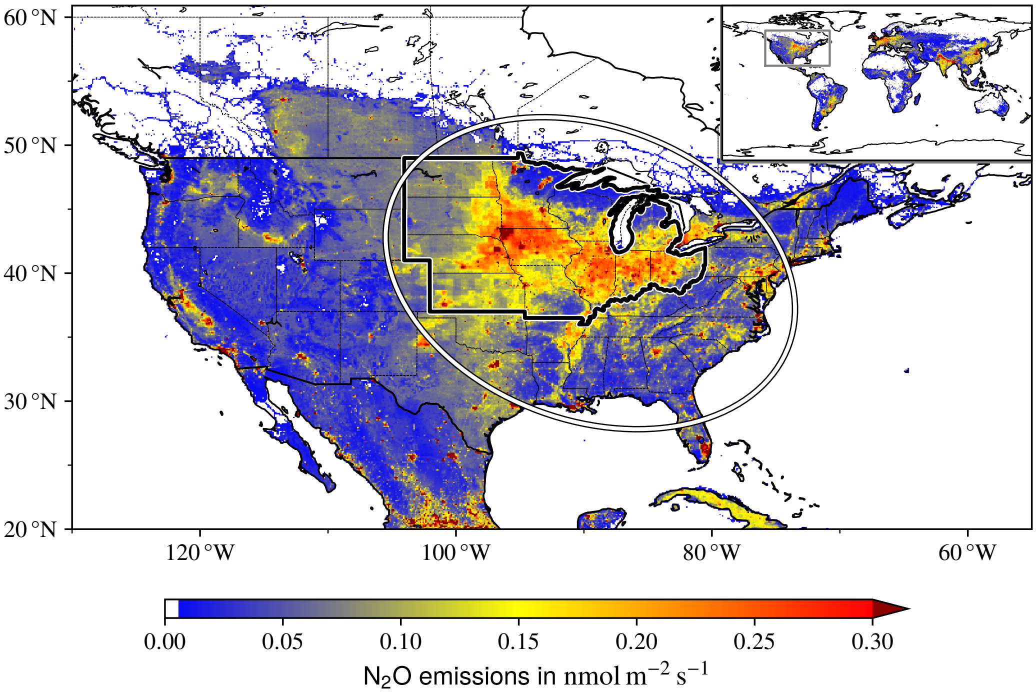

Figure 1.1: Anthropogenic N_2O emissions worldwide and in the U.S. in 2015 following EDGAR version 5.0 (Crippa et al., 2019; EDGAR5.0, 2019). The U.S. Midwest is encircled by a thick black line. The ACT-America study region is encircled in white.

Motivated by the urgent need for accurate N_2O emission estimates and the recent success in studying CH_4 point sources using airborne measurements, the present thesis investigates the potential of a top-down approach based on airborne in situ measurements and atmospheric transport model simulations to study regional N_2O emissions. Since agriculture is the dominant anthropogenic source of N_2O and emissions thereof are expected to be highly uncertain, the focus is on intensively cultivated agricultural regions. The following is hypothesized:

> **“Regional-scale airborne in situ measurements are well-suited to characterize N_2O emissions from area sources such as intensively cultivated agricultural regions and to evaluate related bottom-up emission estimates.”**

To test this hypothesis, the U.S. Midwest is investigated. This region is well-suited as it is a paramount example for a globally relevant but insufficiently characterized agricultural N_2O source region. The following three research questions are formulated:

RQ1: Can N_2O emissions in the U.S. Midwest be quantified by using regional-scale airborne in situ measurements in combination with atmospheric transport model simulations?

RQ2: How do state-of-the-art bottom-up estimates of N_2O emissions in the U.S. Midwest compare to the airborne top-down emission estimates derived herein?

RQ3: Can dominant drivers of N_2O emissions in the U.S. Midwest be identified using regional-scale airborne in situ measurements and atmospheric transport model simulations?

To answer these questions, a unique airborne in situ dataset of N_2O mole fractions is investigated, which was gathered during the Atmospheric Carbon and Transport-America (ACT-America) project. This project covers five field campaigns in four seasons from 2016 to 2019 focusing on the eastern half of the U.S. including the Midwest (see Figure 1.1). Within this thesis, a Quantum Cascade Laser Spectrometer (QCLS) was optimized and successfully deployed during two of the five field campaigns collecting continuous, high-resolution measurements of N_2O dry air mole fractions above the Midwest. To support this dataset, high-accuracy flask measurements conducted during all five field campaigns were additionally used. Together with model simulations, which were partly performed within this thesis and partly provided by the ACT-America team, these measurements are used to quantify N_2O emissions in the Midwest and to constrain their seasonality (**RQ1**). Results are compared against two state-of-the-art bottom-up estimates, EDGAR and DayCent (**RQ2**), and are used to investigate the dominant emission drivers (**RQ3**). This work is an important contribution to the proposal to establish a N_2O inventory system for the U.S. which is essential for the development of an effective N_2O emission reduction strategy (Ogle et al., 2020). The findings additionally serve as a guideline for the characterization of other N_2O source regions around the world, thus paving the way for national inventory systems like the German ITMS.

This thesis is structured as follows: Chapter 2 summarizes relevant background information for the present thesis. This covers a description of the Earth's atmosphere focusing on the role, distribution, and transport of GHGs. Furthermore, atmospheric N_2O and its sources and sinks are presented in detail as well as possible methods to investigate GHGs in the atmosphere. Chapter 3 describes the employed measurement instrument QCLS, models, and datasets. The setup of the QCLS during the ACT-America deployment is presented in Chapter 4 together with the processing of the measurement data, conducted laboratory experiments, and the assessment of the instrument performance. Chapter 5, 6, and 7 contain the studies which answer the research questions. In Chapter 5, the continuous N_2O measurements conducted within this thesis are used to quantify emissions for a total of ten case studies. In Chapter 6, flask measurements available for five ACT-America campaigns are used to study the seasonality of N_2O emissions. Chapter 7 discusses the sensitivity of N_2O emissions to driving parameters such as soil moisture and soil temperature. Finally, the main findings of this thesis are summarized and concluded in Chapter 8 followed by an outlook for future studies in Chapter 9.

2 Theoretical Background

Within this study N_2O emissions in the U.S. Midwest region are characterized to reduce uncertainties present in current emission estimates. Therefore, airborne in situ observations have been conducted within the ACT-America project. This chapter summarizes the theoretical and conceptual fundamentals of this thesis. Section 2.1 addresses the Earth's atmosphere, including its radiation budget and the role of GHGs like N_2O. Further, the vertical structure of the atmosphere is depicted with special focus on the lowermost part, the Planetary Boundary Layer (PBL), as it is directly influenced by surface emissions and, hence, of special interest for this study. N_2O, its sources and sinks, and drivers that control emissions are summarized in Section 2.2. Section 2.3 concludes this chapter and describes methods to study atmospheric GHGs. These encompass approaches to quantify emissions and the functionality of absorption spectroscopy, a common principle to measure in situ atmospheric concentrations of chemical compounds exploited for the observations conducted within this study.

2.1 The Earth's Atmosphere

This section is based on Wallace and Hobbs (2006) and Seinfeld and Pandis (2016) if not otherwise specified.

Up to an approximate altitude of 105 km the Earth's atmosphere is a uniform mixture of gases consisting of molecular nitrogen N_2 (~78 %), molecular oxygen O_2 (~21 %), and the noble gas Argon (<1 %). The next most abundant component is water vapor (H_2O) with highly variable volume fractions ranging from ~0.001 % up to ~5 %, depending on altitude, season, temperature, and other parameters. A vast zoo of trace gases, for example carbon dioxide (CO_2), methane (CH_4), and nitrous oxide (N_2O), are the last component. Although their share is small, they play a crucial role in the atmosphere as they alter the radiation budget (see Section 2.1.1) and chemical properties of the atmosphere. It is common to report concentrations of single components as mole fractions relative to dry air. Typical units are percent ($1\,\% = 1 \times 10^{-2}$), parts per million ($1\,\text{ppm} = 1 \times 10^{-6}$), parts per billion ($1\,\text{ppb} = 1 \times 10^{-9}$), and parts per trillion ($1\,\text{ppt} = 1 \times 10^{-12}$). Overall, ambient air can be approximated as an ideal gas. An ideal gas is defined as a mixture of gas particles that have no spatial extent and interact only through elastic collisions among each other. Its properties are related by the ideal gas law:

$$p \cdot V = n \cdot R_u \cdot T \tag{2.1}$$

Where p is the pressure, V the volume, n the amount of substance (in mol), and T the temperature of an air parcel. R_u denotes the universal gas constant ($R_u \approx 8.314\,\text{J}\,\text{K}^{-1}\,\text{mol}^{-1}$).

In the following, Section 2.1.1 summarizes the radiation budget of the atmosphere and the role of GHGs like N_2O. The vertical structure of the atmosphere is addressed in Section 2.1.2. The focus is on the lowest part of the atmosphere, the PBL, because in this layer the signature of chemical compounds emitted at the surface, which is of interest for this study, is most prominent.

2.1.1 The Radiation Budget and Greenhouse Gases

Solar radiation enters the Earth system and is partly reflected and partly absorbed. The Earth system itself emits thermal radiation. The spectra of the solar and thermal radiation (see Figure 2.1) are defined by the temperature of their emitting bodies. The sun emits radiation at a wavelength λ mainly between 200 nm and 4 µm, covering the ultraviolet (UV: $\lambda \lesssim 380\,\mathrm{nm}$), visible (VIS: $380\,\mathrm{nm} \lesssim \lambda \lesssim 780\,\mathrm{nm}$), and near-infrared (NIR: $780\,\mathrm{nm} \lesssim \lambda \lesssim 4\,\mu\mathrm{m}$) wavelength regions. Thermal radiation is characterized by infrared wavelengths longer than roughly 4 µm

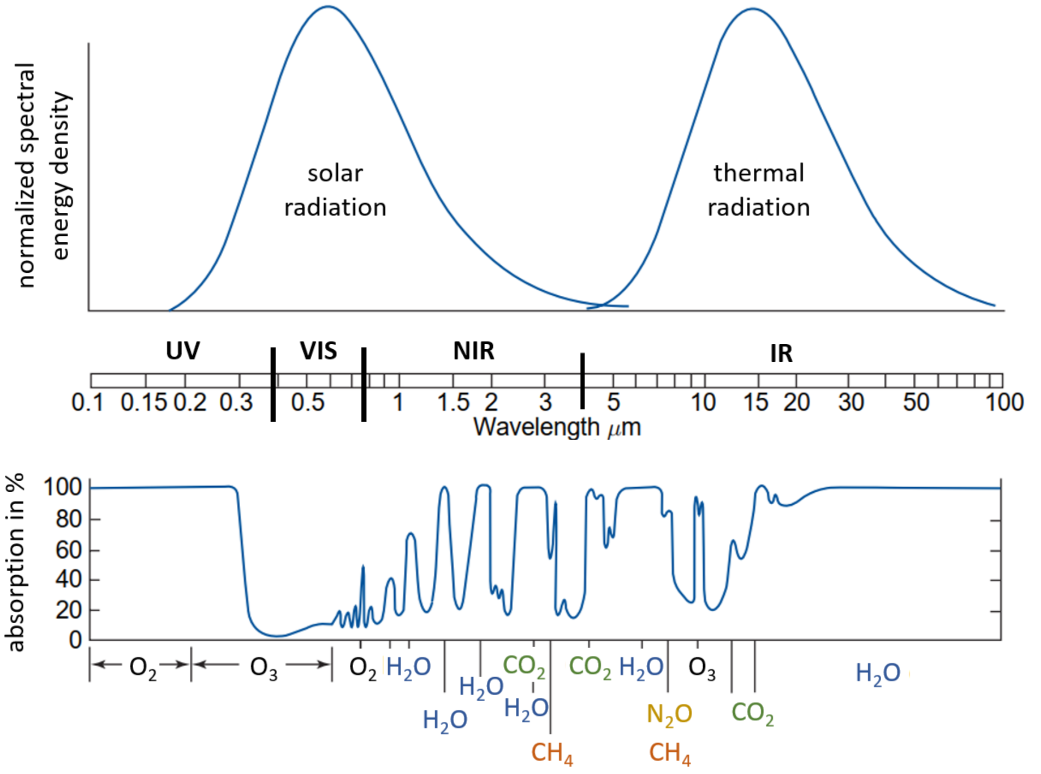

Figure 2.1: (Upper panel) Qualitative solar and thermal spectrum. The two curves have been scaled, so that their areas match. The wavelength scale is logarithmic. Ultraviolet (UV: $\lambda \lesssim 380\,\mathrm{nm}$), visible (VIS: $380\,\mathrm{nm} \lesssim \lambda \lesssim 780\,\mathrm{nm}$), and infrared ($\lambda \gtrsim 780\,\mathrm{nm}$) wavelength ranges are indicated. The infrared region is divided into the near-infrared (NIR: $780\,\mathrm{nm} \lesssim \lambda \lesssim 4\,\mu\mathrm{m}$) region, which is dominated by solar radiation, and longer infrared wavelengths (IR: $\lambda \gtrsim 4\,\mu\mathrm{m}$), which are dominated by terrestrial radiation. (Lower panel) Spectrum of monochromatic absorptivity of the entire atmosphere. (Figure adapted from Fu, 2006, p. 118)

(IR). Hence, solar and thermal radiation can be clearly distinguished. Overall, at an effective radiation temperature of the Earth system of 255 K there is a balance between incoming and outgoing radiation. If the budget is positive (less outgoing than incoming radiation), the Earth system warms, which increases the emitted thermal energy, until the equilibrium is restored. A negative budget has the opposite effect and leads to a cooling of the Earth system. Radiative forcing is a measure for the deviation from the radiation equilibrium.

Absorption and reflection of radiation occurs at the surface and in the atmosphere. In the atmosphere, cloud droplets, solid particles, and molecules absorb and scatter radiation and hence influence the Earth's radiation budget. The lower panel in Figure 2.1 shows the absorptivity of the entire atmosphere. Most of the UV radiation is absorbed by O_2 and ozone (O_3) in the higher atmosphere (above the troposphere; see Section 2.1.2). In the VIS wavelength range, where the energy density of the solar radiation is largest, just a small portion is absorbed. The NIR and IR (i.e., thermal radiation) regions are characterized by strong absorption bands, which are caused by GHGs. The most important are H_2O, CO_2, CH_4, and N_2O. This high transparency of the atmosphere regarding solar radiation together with the strong absorption of thermal radiation causes the greenhouse effect. Sunlight travels largely without interactions through the atmosphere and heats the Earth's surface which radiates thermally. GHGs absorb characteristic parts of the radiation from the surface and heat the atmosphere inducing emission of thermal radiation in all directions. The downward portion reduces the effective cooling efficiency of the surface resulting in a higher equilibrium temperature. There is a consensus among the scientific community that the significant accumulation of GHGs in the atmosphere due to anthropogenic activity especially since the industrialization, has enhanced and is still enhancing the greenhouse effect primarily causing the prevailing global warming (IPCC, 2013).

2.1.2 The Vertical Structure and the Planetary Boundary Layer

The atmosphere is assumed to be in a hydrostatic equilibrium denoting that an air parcel is vertically balanced by the downward gravity force and the upward pressure gradient force (pressure decreases with increasing altitude). This is described by the following hydrostatic equation:

$$\frac{\mathrm{d}p}{\mathrm{d}h} = -\rho g \tag{2.2}$$

The change of pressure p with altitude h (pressure profile) is defined by the air density ρ and gravitational acceleration g. Solving this equation reveals an exponential decay of p and ρ with altitude. At sea level p is on average 1013.25 hPa. At an altitude of approximately 5.5 km p is around 500 hPa. Hence, half of the mass of the Earth's atmosphere is located below this altitude.

A typical temperature profile for the midlatitudes is displayed in Figure 2.2. In the troposphere, spanning from the surface up to the tropopause at roughly 12 km, the temperature decreases linearly with altitude. The troposphere is the relevant layer for this thesis. Nevertheless, for the sake of completeness, the remaining layers are shortly presented in the following. The stratosphere extends from the tropopause to the stratopause at roughly 45 km and is characterized by an increase in temperature with altitude. This layer contains most of the atmospheric O_3 (~90 ‰; Dameris, 2010) which absorbs solar UV radiation leading to the photodissociation of O_3, thus protecting the troposphere from shortwave radiation (see Section 2.1.1). This process heats the stratosphere and explains the increase in temperature with altitude. Above the stratosphere, in the mesosphere, which spans up to approximately 90–100 km, the temperature decreases with altitude again. In the thermosphere, solar radiation can lead to ionization of air particles and also to the photodissociation of N_2 and O_2. Both processes heat the ambient air, resulting in a positive upward temperature gradient.

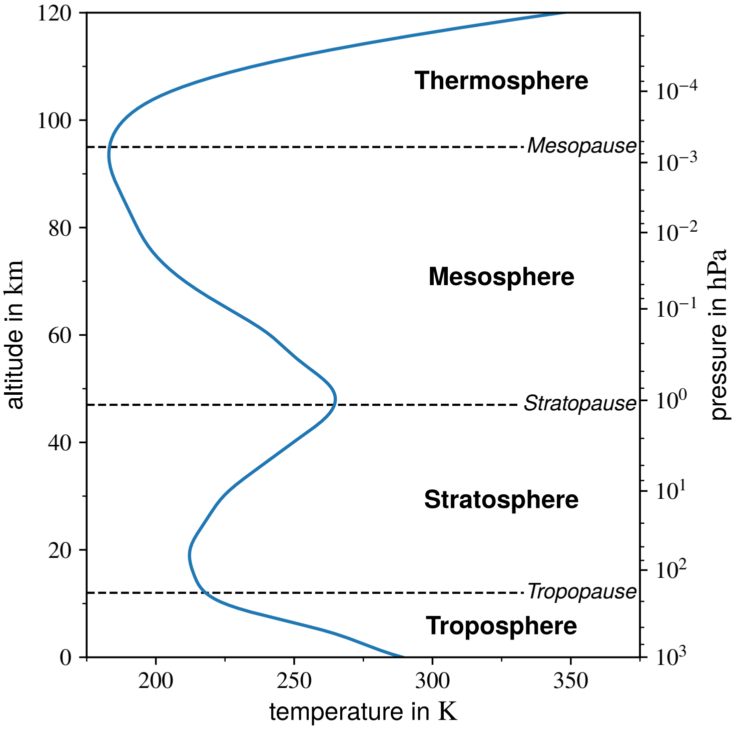

Figure 2.2: Yearly average temperature profile at 45°N, 0°E and at 12:00 UTC estimated with the whole-atmosphere empirical model NRLMSIS 2.0 (Emmert et al., 2021, NRL stands for the U.S. Naval Research Laboratory and MSIS stands for Mass Spectrometer Incoherent Scatter radar).

The PBL is the lowest part of the troposphere and is most affected by the surface. Figure 2.3 shows typical vertical profiles of temperature T, specific humidity q, and horizontal wind speed U in a daytime PBL over land. The height of the PBL z_{PBL} can range from tens of meters to 4 km and more and is highly variable in space and time. The lowermost, roughly 5 ‰ of the PBL is the surface layer (SL) which is directly influenced by the surface. Above the SL, friction and heating at the surface induces turbulence and vertical movement creating a well-mixed layer (ML). At this, thermal convection is a central process. The surface heats adjacent air parcels (large vertical T gradient in the SL) which lowers their density (see Equation 2.1) compared to the surroundings and thus creates buoyancy. The warm air parcels ascend and cool because of expansion (constant vertical T gradient in ML) until their temperature equals the surroundings again. This leads to an inversion at z_{PBL} that caps the PBL from the free atmosphere (FA). In the transition or entrainment zone (EZ) some exchange between the PBL and FA occurs only due to turbulence and inertia of rising air parcels. The horizontal wind profile is dominated by surface friction. It decelerates U in the SL while generating turbulence which in turn propagates upwards up to z_{PBL} causing a relatively constant U throughout the ML. The dominant source of atmospheric water vapor is near-ground evaporation, explaining the q profile. The SL is fed with H_2O which propagates upwards and is uniformly mixed up to z_{PBL} through convection and turbulence. Since the inversion caps the water vapor source (surface) from the FA, the FA is dryer compared to the PBL.

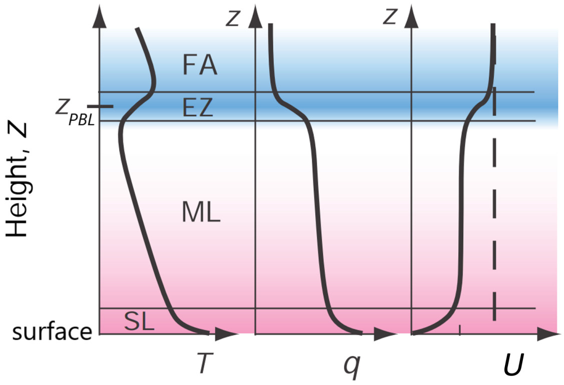

Figure 2.3: Vertical profiles of temperature T, specific humidity q, and wind speed U in a typical daytime PBL. The PBL spans from the surface to height z_{PBL}. The layers are divided into surface layer (SL; roughly 5 % of z_{PBL}), well-mixed layer (ML), entrainment zone (EZ), and free atmosphere (FA). (Figure adapted from Stull, 2006, p. 392)

Typical profiles of N_2O and other anthropogenic GHGs are analogue to the q profile, because most of their emission sources are located at the surface (see Section 2.2.1). GHGs emitted from such sources are distributed in the vertical and advected within the PBL. Thus, to sample them with in situ airborne observations, measurements in a well-mixed PBL are required, and should be conducted far enough downwind of the sources, so that their signature is uniformly mixed up to z_{PBL}. However, because the lowest possible flight altitude is limited, such airborne measurements require a well-established/high enough PBL to be adequately sampled by aircraft. The explanations in the previous paragraph imply that the dominant driver of the PBL is surface heating due to radiation. Radiation is highest in the summer, while the surface temperature typically peaks in the afternoon. During night the surface cools and the PBL collapses. Furthermore, a solid surface exhibits a significantly lower heat capacity than water and hence heats quicker, favoring the development of the PBL. However, weather patterns like low pressure systems are able to suppress the development due to, for example, large-scale subsidence. Overall, highest z_{PBL} occurs during summer, in the afternoon, over land surface, and during fair weather conditions constraining the optimal time for airborne in situ measurements to study trace gas emissions. Therefore, measurement flights during ACT-America were mostly performed in the afternoon to ensure an optimally developed PBL.

2.2 The Greenhouse Gas Nitrous Oxide

N_2O plays a crucial role in the atmosphere. Since the Montreal Protocol (1987) successfully led to a reduction of chlorofluorocarbons, N_2O is nowadays the dominant ozone-depleting substance in the stratosphere (Ravishankara et al., 2009). Furthermore, it is a potent GHG with a 265 times higher global warming potential on a 100-year horizon than CO_2 (Myhre et al., 2013). Accounting for around 6 % of the total anthropogenic radiative forcing of well-mixed GHGs in 2011, N_2O is, after CO_2 and CH_4, the third most important long-lived anthropogenic GHG (Myhre et al., 2013) and exhibits an atmospheric lifetime of 116 ± 9 yr (Prather et al., 2015). Figure 2.4 shows global atmospheric N_2O dry air mole fractions since year 1 AD. In the preindustrial era concentrations stayed relatively constant between 260 ppb and 280 ppb. Since the 19th century the atmospheric N_2O abundance has been rising due to anthropogenic activity (Kroeze et al., 1999). Especially since the beginning of the 20th century a dramatic, ongoing increase has been observed. The starting signal coincides with the development of the Haber-Bosch process which enabled the industrial synthesis of reactive nitrogen (N) and thus the production of affordable, synthetic N-fertilizer (Battye et al., 2017), the main anthropogenic source of N_2O (see Section 2.2.1). In January 2021, the average global N_2O abundance was 334 ppb denoting a 20–30 % increase since the start of the industrialization.

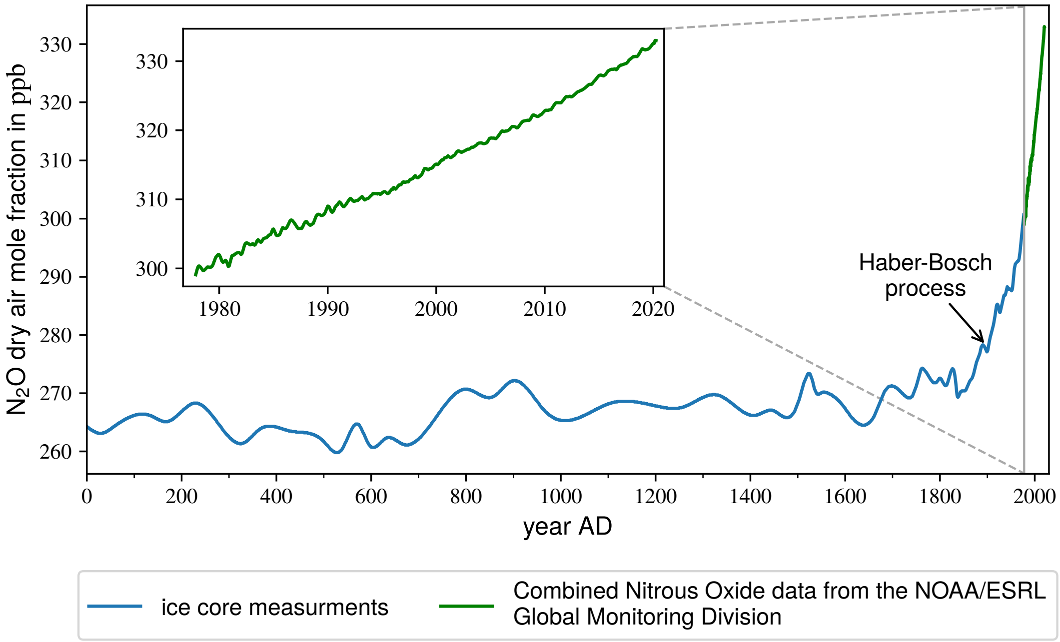

Figure 2.4: Global atmospheric N_2O concentrations since year 1 AD, derived from ice core measurements (1 AD–1977 AD: MacFarling Meure, 2004; MacFarling Meure et al., 2006) and from the NOAA/ESRL Global Monitoring Division (1978–2021: NOAA/ESRL, 2021a).

In the following, Section 2.2.1 summarizes sources and sinks of N_2O and Section 2.2.2 introduces the drivers that control N_2O emissions from the dominant source, i.e. soils.

2.2.1 The Global N_2O Budget

This section is based on the study of Tian et al. (2020) if not otherwise specified.

A large variety of natural and anthropogenic sources exist. Figure 2.5 summarizes global N_2O sources in 2007–2016. Table A.1 in the appendix provides a more detailed itemization. Overall, global N_2O emissions in this decade were 17.0 (12.2–23.5) $\mathrm{Tg\,N\,yr^{-1}}$, consisting of 57 % natural and 43 % anthropogenic emissions. Natural sources are dominated by emissions from soils under natural vegetation and oceans (see Section 2.2.2 for a description of the underlying processes). Just a small portion emerges from inland waters, estuaries, and coastal zones or is chemically produced in the atmosphere, typically initiated by lightning. Anthropogenic sources can be divided in four main categories:

1. Direct emissions from N additions to soils and water (agriculture)
2. Non-agricultural direct sources
3. Indirect emissions from anthropogenic N additions
4. Perturbed fluxes from climate/CO_2/land cover change

Direct emissions from agriculture are the dominating anthropogenic source, accounting for over 22 % of global total N_2O emissions. The application of N-fertilizers enhances fluxes from soils into the atmosphere and contributes most to agricultural emissions, followed by manure left on pasture, manure management, and aquaculture. Eleven percent of global N_2O emissions originate from other (non-agricultural) direct emissions, i.e. fossil fuel combustion and industry, waste and waste water, and biomass burning. A special category are indirect emissions that account for nearly 8 % of total emissions. Drainage and runoff transports N-compounds, added to soils and water by human activity, to remote regions where they are transformed to N_2O and emitted to the atmosphere. Since agriculture is mainly responsible for anthropogenic N additions (Battye et al., 2017), this category is assigned to agricultural emissions as well. However, distinguishing indirect emissions from natural emissions is challenging and transitions are fluent as it is difficult to constrain the runoff of N-compounds. Furthermore, because N_2O emissions from soils are highly sensitive to changes in numerous environmental conditions, like temperature, soil moisture and vegetation (see Section 2.2.2), climate change as well as changes in the land cover and atmospheric CO_2 abundance perturb N_2O fluxes. This effect is responsible for roughly 1 % of global emissions in 2007–2016 and is expected to increase in the future (Griffis et al., 2017).

The global N_2O sink for the decade 2007–2016 is estimated to be 13.5 (12.4–14.6) $\mathrm{Tg\,N\,yr^{-1}}$. At the surface, only a negligible amount of N_2O is removed (0.01 (0.0–0.3) $\mathrm{Tg\,N\,yr^{-1}}$). In the troposphere, N_2O is chemically inert. The almost exclusive sink is stratospheric loss due to the following reactions (Seinfeld & Pandis, 2016):

$$\begin{aligned} \mathrm{N_2O} + h\nu &\longrightarrow \mathrm{N_2} + \mathrm{O(^1D)} \\ \mathrm{N_2O} + \mathrm{O(^1D)} &\longrightarrow 2\,\mathrm{NO} \\ \mathrm{N_2O} + \mathrm{O(^1D)} &\longrightarrow \mathrm{N_2} + \mathrm{O_2} \end{aligned} \tag{2.3}$$

In the stratosphere UV radiation photodissociates N_2O to N_2 and excited oxygen $O(^1D)$. The excited oxygen can react with N_2O to produce nitric oxide NO, O_2, and N_2.

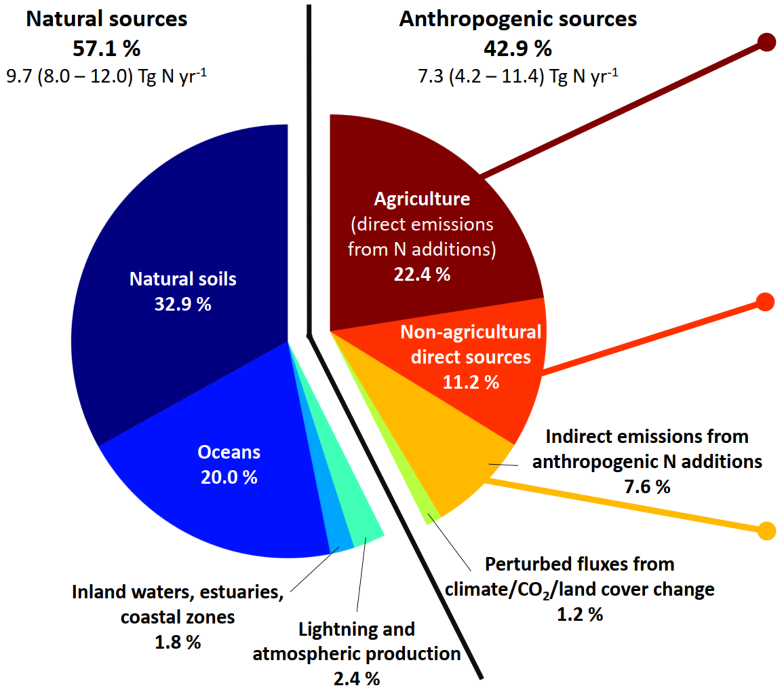

Agriculture	Emissions in % of total
Direct soil emissions:	13.5
Manure left on pasture:	7.1
Manure management:	1.8
Aquaculture:	0.6
Subtotal:	*22.4*

Non-agricultural direct sources	Emissions in % of total
Fossil fuels and industry:	5.9
Waste and waste water:	1.8
Biomass burning:	3.5
Subtotal:	*11.2*

Indirect emissions from N additions	Emissions in % of total
Inland waters, estuaries, coastal zones:	2.9
Atmospheric N deposition:	5.3
Subtotal:	*7.6*

Figure 2.5: Global N_2O sources in 2007–2016 following Tian et al. (2020). Due to rounding subtotals can be different to the sum of individual contributions. Sources are given in Tg N yr^{-1} or percent of total sources, i.e. 17.0 (12.2–23.5) Tg N yr^{-1}. The ranges are minimum-maximum estimates.

The total global N_2O sink is significantly smaller than the source. This imbalance is consistent with the observed growth in global atmospheric N_2O concentrations. Since the 1980s natural N_2O emissions have not changed, whereas anthropogenic emissions increased by 30 %, mainly because of increased direct agricultural emissions. Hence, the observed growth in the atmospheric abundance of N_2O is largely assigned to agriculture. Analyses of interannual variations and long-term trends in the isotopic composition of N_2O confirm this (Park et al., 2012). In recent years, global N_2O emissions have grown at a faster rate than expected (Thompson et al., 2019) and exceeded highest emission scenarios (Gidden et al., 2019; Tian et al., 2020), indicating that the growth rate of atmospheric N_2O concentrations is increasing more than expected.

An important source region of anthropogenic N_2O emissions is the U.S. From 1970 to 2015, yearly emissions stayed relatively constant at 1 Tg (see Figure 2.6a). This is mainly because cropland emissions leveled in the second half of the 20th century (Tian et al., 2018), which is in turn caused by a leveling of the fertilizer consumption (Battye et al., 2017). In contrast, global anthropogenic N_2O emissions increased from roughly 5.5 Tg in 1970 to 8.5 Tg in 2015. Rapidly rising cropland emissions in China, South Asia, and Southeast Asia (Tian et al., 2018) contribute largely to this trend. Nevertheless, in 2015 the U.S. is still responsible for over 10 % of global anthropogenic N_2O emissions and, hence, is an important source region. Over 80 % of anthropogenic U.S. emissions are attributed to agriculture (see Figure 2.6b), implying that the densely farmed Midwest is an emission hotspot. This region is one of the most intensively cultivated agricultural regions worldwide accounting for ~25 % of world corn and soybean production in 2018 (FAO, 2020; USDA-NASS, 2020). As a result, the Midwest contributes significantly to global anthropogenic N_2O emissions (Miller et al., 2012) underlining the importance of the research objectives pursued herein.

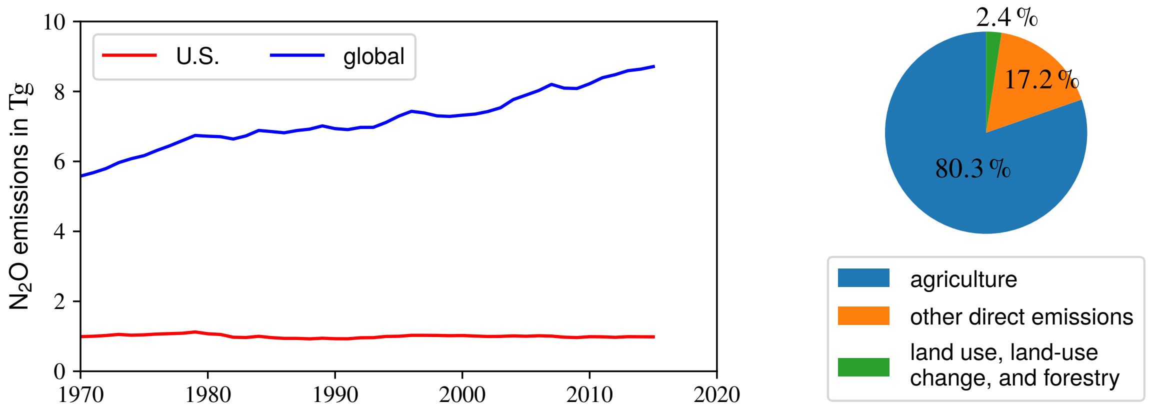

(a) Yearly anthropogenic emissions

(b) U.S. emissions in 2018

Figure 2.6: Global and U.S. anthropogenic N_2O emissions. (a) Yearly emissions from 1970 to 2015 in the bottom-up inventory EDGAR version 5.0 (see Section 2.3.1; Crippa et al., 2019; EDGAR5.0, 2019). (b) Sector-wise U.S. emissions in 2018 (EPA, 2020).

2.2.2 The Drivers of N_2O Soil Emissions

Approximately ⅔ of global N_2O emissions originate from soils (see Section 2.2.1). The "hole-in-the-pipe" model introduced by Firestone and Davidson (1989) conceptually describes N_2O emissions from soils and is shown in Figure 2.7. Basically, two microbial processes control soil emissions, nitrification and denitrification. These cover numerous, complex transformations of reactive N-compounds (e.g., ammonium NH_4^+ and nitrate NO_3^-) by bacteria and fungi. Nitrification describes the oxidation of NH_4^+ to NO_3^- and denitrification the transformation of NO_3^- to N_2. During both, N_2O and NO can be produced as a byproduct and released. Overall, the formation of N_2O is controlled by two factors. The first factor is the availability of reactive N-compounds. Natural processes, like the consumption of atmospheric N_2 by plants, add reactive nitrogen to soils. However, also anthropogenic activity adds N-compounds (mainly in the form of synthetic fertilizer and manure) boosting the formation of N_2O. The second factor controlling the formation of N_2O is the soil condition. Environmental drivers like soil temperature, soil moisture, and soil texture, influence nitrification and denitrification. Thus, soil N_2O emissions are characterized by a high spatio-temporal variability (Butterbach-Bahl et al., 2013). In the following the main environmental drivers are outlined. For a detailed description of the underlying physical, chemical, and biological mechanisms the interested reader is referred to Ussiri and Lal (2013).

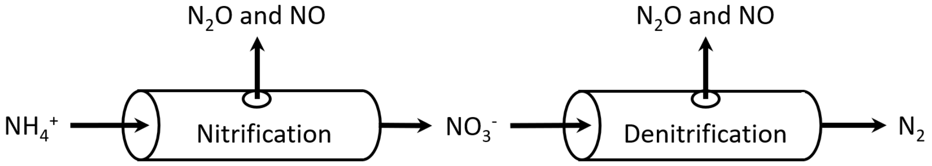

Figure 2.7: "Hole-in-the-pipe" model describing soil N_2O emissions following Firestone and Davidson (1989). Nitrification transforms ammonium NH_4^+ to nitrate NO_3^- while N_2O and nitric oxide NO is released. Denitrification transforms NO_3^- to N_2 while N_2O and NO is released.

Frequent changes in soil moisture (e.g., due to precipitation) and soil temperature are the dominant drivers of soil N_2O emissions. They are responsible for up to 95 % of the temporal variations (Kitzler et al., 2006). Soil moisture controls the production of N_2O by regulating the oxygen supply of the microbes. Based on the "hole-in-the-pipe" model, Davidson (1991) provides a model of the relationship between soil N_2O fluxes and soil moisture (see Figure 2.8). Maximum emissions of N_2O occur in soils with a water-filled pore space (WFPS) of 70–80 % depending on the soil type. In drier soils mainly NO is produced, whereas in wetter soils N_2 emissions dominate. Davidson et al. (2000) evaluated this model against field measurements and have found good agreement on the regional and global scale but less accuracy on finer scales. Other measurements however indicate that most soils exhibit the maximum of N_2O emissions at higher WFPS than 80 % (e.g., Schindlbacher et al., 2004; Schaufler et al., 2010). The same studies also show that higher soil temperatures favor the microbial production of N_2O resulting in a nonlinear increase of emissions with increasing temperature. Soil temperatures around 0 °C play a special role, since freezing/thawing occurs while many microbes are still active inducing strong N_2O emission events (Butterbach-Bahl et al., 2013). Such events potentially account for more than half of the annual N_2O fluxes of croplands (Wagner-Riddle et al., 2007) and for 17–28 % of global agricultural N_2O emissions (Wagner-Riddle et al., 2017).

Vegetation has been identified as another control mechanism of soil N_2O emissions. Niklaus et al. (2016) concluded, that unless fertilizer is applied, a greater plant diversity is capable of reducing emissions. However, there is also evidence that the plant types/composition is more important than the species richness itself (Niklaus et al., 2006; Abalos et al., 2013). So-called N-fixing plants like legumes (e.g., soybeans, alfalfa, or lentils) are of special interest. They transform atmospheric N_2 to reactive N-compounds which are made available to the soil enhancing the N cycling processes and hence N_2O emissions (Niklaus et al., 2006; Niklaus et al., 2016). Since the second half of the 20th century, the cultivation of N-fixing plants, mainly soybeans, has increased enormously accounting for roughly 20 % of anthropogenic reactive N sources nowadays (Battye et al., 2017). Beside the drivers discussed above, the soil organic carbon content, pH-value, bulk density, and drainage affect N_2O emissions from soils under natural vegetation (Stehfest & Bouwman, 2006), however less significant. As such, they are less relevant for this study and, hence, are not further examined here. Detailed explications can be found in, for example, Ussiri and Lal (2013).

Altogether, N_2O emissions from soils are highly complex. Predicting their response to environmental changes like global warming is hence challenging. While the influence of single drivers

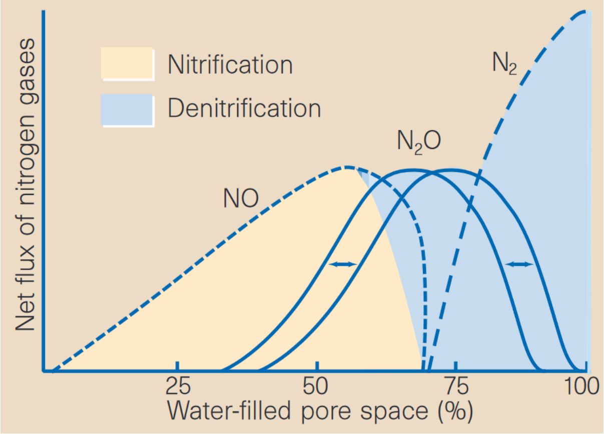

Figure 2.8: Model of N_2O, NO, and N_2 soil emissions dependence on soil moisture (i.e., WFPS) following Davidson (1991). Nitrification and denitrification regimes are indicated. Highest N_2O fluxes are between 70–80 % WFPS depending on soil properties. (Reprinted by permission from Springer Nature Customer Service Centre GmbH: Springer Nature, Nature, *“Nitrogen oxides and tropical agriculture”*, Bouwman, ©1998)

is well known (Leuzinger et al., 2011), the impact of multiple drivers is much more difficult to estimate as processes are typically nonlinear and interact synergistically or antagonistically among each other (Larsen et al., 2010). However, there are indications that aspects of climate change (e.g., higher soil temperature or increased CO_2 availability for plants) will increase future soil N_2O emissions (positive feedback) (Del Grosso & Parton, 2012). For example, Griffis et al. (2017) projects a strong positive feedback of agricultural soils to warmer and wetter conditions under current trends in climate and anthropogenic N use. A recent modeling study by Xu et al. (2020) concluded that already from 1961–2014 warming and an increased CO_2 abundance continuously accelerated N_2O emissions from cropland underlining the future importance of climate change feedbacks. Within this work, in Chapter 7, the effect of soil moisture and temperature as well as precipitation on Midwest N_2O emissions is analyzed explicitly.

2.3 Studying Greenhouse Gas Emissions

To fully understand GHG emissions, to make reliable future projections, and to develop efficient mitigation procedures, sources and sinks must be quantified. Two basic approaches exist, bottom-up and top-down. Bottom-up approaches use statistical activity data, whereas top-down approaches are based on independent GHG measurements in the atmosphere. Section 2.3.1 presents both approaches and summarizes their advantages and disadvantages.

Atmospheric measurements of GHGs, the basis of top-down emission estimates, are challenging since enhancements are typically small relative to the background concentrations. For example, N_2O enhancements are mostly less than 1 % of the background abundance highlighting the need of precise and accurate instruments. For this study, aircraft-based in situ measurements have been conducted sampling the U.S. Midwest. However, such measurements are especially challenging. They require a fast response time, a high precision, and must be stable against rapid and intense environmental changes to ensure measurements with high spatial resolution (Fried et al., 2008). Several successful field deployments prove that absorption spectroscopy instruments are capable of fulfilling these requirements (e.g., Santoni et al., 2014; Kooijmans et al., 2016; Pitt et al., 2016; Catoire et al., 2017; Gvakharia et al., 2018; Kostinek et al., 2019). Section 2.3.2 describes the concept of such instruments.

2.3.1 Top-Down vs. Bottom-Up Emission Estimates

Most bottom-up estimates use statistical activity data (e.g., maps of N-fertilizer application rates) multiplied with emission factors (e.g., N_2O emissions per amount of applied N-fertilizer) to estimate emissions. The big advantage of this approach is that it allows for compiling global gridded inventories divided into different emission sectors. However, the quality of such estimates depends on the quality of the input data. In reality, the drivers of emissions are often spatially and temporally highly variable. This heterogeneity is rarely or never caught by the available statistical activity data which are often based on strong simplifications introducing uncertainties (e.g., Griffis et al., 2013). For example, it is common to use proxy data like maps of cropland combined with a constant emission factor to distribute country emission totals in a gridded emission map (e.g., Janssens-Maenhout et al., 2013). Regional characteristics such as soil type or vegetation are not considered leading to large local uncertainties. Additionally, the emission factors are often more complex than presumed. For example, Thompson et al. (2019) found indications that in regions with high N-input the response of N_2O emissions to an increasing N-fertilizer application is probably nonlinear. Furthermore, the quality of the provided activity data may also depend on the reporting country/organization leading to nationwide inconsistencies.

Following IPCC (2006), bottom-up approaches are classified in three so-called *Tiers* which differ in the quantity of the underlying information and the complexity of the underlying analysis. *Tier 1* and *Tier 2* estimates are both based on the emission factor approach described above. While *Tier 1* uses default emission factors defined by the IPCC (available from the emission factor database: https://www.ipcc-nggip.iges.or.jp/EFDB/main.php), *Tier 2* employs country-specific emission factors and other parameters. *Tier 3* provides the most sophisticated bottom-up emission estimates, derived with higher-order methods. Typically, models are used to simulate physical processes that provoke emissions. Driven by spatially and temporally resolved data, like soil characteristics or weather data, such models estimate sources and sinks tailored to a specific region and time. The downside of such process-based models is that their application is complex and requires a large amount of input data.

Contrary to the bottom-up approach, the top-down approach is based on independent measurements of trace gas concentrations in the atmosphere. Typically, inverse modeling is used to constrain sources and sinks with the observations (e.g., Hirsch et al., 2006; Corazza et al., 2011; Thompson et al., 2019), providing estimates of emission fluxes that do not (exclusively) rely on activity data. However, there are three limitations. First, attributing such estimates to emission sectors is challenging since sources are often collocated. Second, the transport of emitted GHGs through the atmosphere must be known to be able to relate the measurements to the source region. Atmospheric transport models are capable of simulating the transport but they are not perfect introducing uncertainties to top-down estimates. Third, atmospheric observations of GHGs are limited in their spatial and temporal coverage. Ground-based observation networks like the National Oceanic and Atmospheric Administration (NOAA)/Earth System Research Laboratories (ESRL)/Global Monitoring Laboratory (GML) Cooperative Air Sampling Network (https://www.esrl.noaa.gov/gmd/ccgg/flask.html) collect long-term time series around the world, but measurement sites are sparse hindering to study specific point or regional sources which are far off the measurements sites. Airborne measurements are suitable to sample such sources but provide only snapshots. Satellite measurements exhibit a great temporal and spatial coverage but are more complex in their interpretation and suffer from higher measurement uncertainties and lower spatial resolution. Nevertheless, studies have shown that the top-down method is a valuable tool to evaluate bottom-up estimates (Nisbet & Weiss, 2010).

Overall, for N_2O the data situation is especially poor compared to CO_2 and CH_4. To my best knowledge, the Emissions Database for Global Atmospheric Research (EDGAR) is the only gridded bottom-up inventory with a global coverage, providing emission estimates (*Tier 1–2*) for all relevant N_2O emission sectors after 2010. Section 3.4.1 presents the two most recent EDGAR versions, namely version 4.3.2 and 5.0, since both are further examined within this study. Beside EDGAR, some biogeochemical models exist allowing for *Tier 3* soil emission estimates. Such models are typically used on a regional or national scale. The daily time-step version of the CENTURY model (DayCent) is a prevalent example for this and its product is discussed within this thesis (see Section 3.4.2).
Atmospheric N_2O measurements or top-down emission estimates are rare as well. Some studies exist which quantify N_2O emissions in the U.S. Midwest based on ground-based measurements (e.g., Miller et al., 2012; Griffis et al., 2013; Chen et al., 2016; Fu et al., 2017). Only very few analyses have been found that use airborne N_2O measurements benefiting from the high spatial resolution of such observations (Kort et al., 2008; Xiang et al., 2013; Gvakharia et al., 2020). However, none of them quantifies the U.S. Midwest but other regions in the U.S., except Kort et al. (2008), who have estimated N_2O emissions in central North America covering the Midwest using airborne flask measurements. Overall, all studies agree that common bottom-up inventories underestimate Midwest N_2O emissions to a large degree, but they significantly differ in the amount ranging from factors between approximately two and 30, highlighting the need of further studies to constrain Midwest emissions.

2.3.2 In Situ Observations With Absorption Spectroscopy

GHGs exhibit strong molecular absorption features in the IR. Using laser absorption spectroscopy enables to exploit these features to assess the concentration of the absorbing GHGs. This technique greatly benefits from the latest advancements in interband cascade lasers (ICLs) and quantum cascade lasers (QCLs) operating in the mid-IR wavelength region under ambient temperature (e.g., Beck et al., 2002; Capasso, 2010; Vurgaftman et al., 2011; Kim et al., 2015). As a result, in the last two decades numerous absorption spectrometers measuring atmospheric GHG abundances have been developed and deployed (e.g., Tittel et al., 2006; Dyroff et al., 2010; McManus et al., 2011; McManus et al., 2015).

The basic concept of such instruments is depicted in Figure 2.9. A QCL/ICL scans over a certain wavelength range $\Delta\lambda$. The emitted radiation is directed through a sample cell containing a gas mixture including the species of interest. $\Delta\lambda$ is chosen so that absorption lines of the species of interest are covered. A detector collects the outgoing radiation or absorption spectrum of the sample air which can be used to derive the concentrations of the absorbing constituents. The absorption occurring in the sample cell at wavelength λ is described by Bouguer-Lambert-Beer's law (Wallace & Hobbs, 2006):

$$I_\lambda = I_{0,\lambda} \cdot e^{-\tau_\lambda} \tag{2.4}$$

Where I_λ is the intensity of the outgoing radiation (laser beam after the sample cell; absorption spectrum) and $I_{0,\lambda}$ is the intensity of the incoming light (emitted by the laser; spectral baseline). τ_λ is the absorption optical depth of the sample air. It describes the absorption and is defined by:

$$\tau_\lambda = \int_0^d k_\lambda(p_{cell}, T_{cell})\, \eta \,\mathrm{d}z \tag{2.5}$$

Here, k_λ is the absorption cross section of the sample air describing the wavelength specific absorption of the medium. k_λ also includes the information about the absorption behavior of the species of interest and depends on the pressure (p_{cell}) and temperature (T_{cell}) in the sample cell. η is the number density of the sample air and d the length of the sample cell. Thus, the

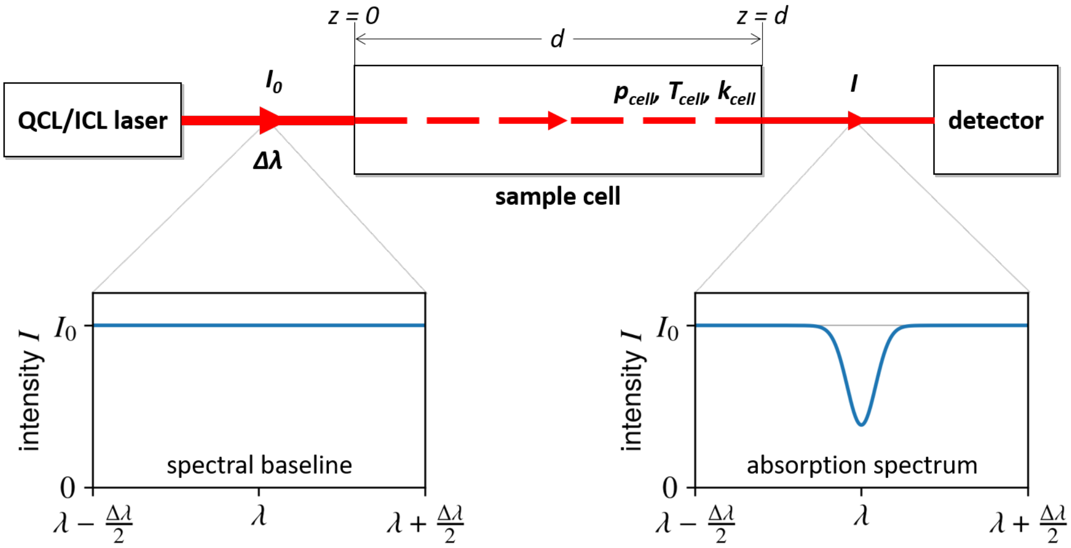

Figure 2.9: Schematics of an absorption spectroscopy instrument. A QCL/ICL scans over the wavelength range $\Delta\lambda$ around the center wavelength λ. The emitted radiation is directed into a sample cell of length d containing an absorbing medium. The outgoing absorption spectrum is collected by a detector. I_0 and I are the intensity of the incoming (emitted by the laser) and outgoing radiation, respectively. The absorbing medium or sample air has the temperature T_{cell}, pressure p_{cell}, and medium-specific absorption cross section k_{cell}. The two plots qualitatively show the incoming (left) and outgoing (right) spectrum.

absorption in the sample cell depends on the concentrations of absorbing constituents enabling their quantification. An example absorption spectrum is shown in Figure 2.9 in the lower right corner.

To derive mole fractions from absorption spectra, databases are needed containing the spectroscopic parameters of the absorbers, like the commonly used high-resolution transmission molecular absorption database (HITRAN; https://hitran.org/). They provide absorption cross sections (k_λ) for various molecules enabling to fit the absorption spectrum. By calculating the difference between spectral baseline/incoming radiation and absorption spectrum/outgoing radiation (area of absorption line) the abundance of the absorber can be retrieved (see Equation 2.4 and 2.5). As already mentioned, k_λ or the shape of the absorption line depends, not exclusively but mainly, on the temperature and pressure of the absorbing medium. Higher temperatures lead to broader absorption lines as each emitted photon is shifted to shorter or longer wavelengths by the Doppler effect depending on the velocity of the molecule relative to the detector. Furthermore, higher pressure also leads to broader absorption lines due to collisions of the molecules. Thus, for the operational use of absorption spectrometers, stable p_{cell} and T_{cell} are desired to diminish potential error sources.

3 Instrument, Models and Datasets

To answer the research questions, airborne in situ N_2O measurements over the U.S. Midwest have been conducted enabling the execution of top-down studies with atmospheric transport models. For the measurements, the Quantum Cascade Laser Spectrometer (QCLS) of the Deutsches Zentrum für Luft- und Raumfahrt (DLR) has been selected. This instrument allows for precise, high frequency measurements of GHGs including N_2O and was recently successfully deployed on different research aircraft (e.g., Kostinek et al., 2019; Kostinek, 2019; Fiehn et al., 2020; Klausner et al., 2020). During the fall 2017 and summer 2019 field campaigns of the Atmospheric Carbon and Transport-America (ACT-America) project, a unique airborne N_2O dataset over the eastern half of the U.S. has been gathered with the QCLS, enabling the studies presented herein. To assign observed N_2O enhancements to different source regions and to calculate respective emission rates, two state-of-the-art atmospheric transport models are used, the Weather Research and Forecasting model (WRF; Skamarock et al., 2019) and the Hybrid Single Particle Lagrangian Integrated Trajectory model (HYSPLIT; Draxler & Hess, 1997). Thereof resulting top-down emission estimates are compared to two recent bottom-up N_2O emission inventories, the *Tier 1–2* inventory EDGAR and *Tier 3* estimates produced with DayCent (see Section 2.3.1).

In this chapter, Section 3.1 provides a detailed description of the QCLS, followed by a presentation of the ACT-America project in Section 3.2. Next, the two well established atmospheric transport models, WRF and HYSPLIT, are described in Section 3.3. Finally, Section 3.4 depicts the two considered emission inventories, EDGAR and DayCent.

3.1 Quantum Cascade Laser Spectrometer

The spectrometer used in this study is based on the commercial Dual Laser Trace Gas Monitor available from Aerodyne Research Inc. (Billerica, USA). It is a tunable IR laser direct absorption spectrometer (see Section 2.3.2) and fully described in McManus et al. (2011). This commercial instrument has been modified and is optimized for airborne measurements (Kostinek et al., 2019; Kostinek, 2019). A general description of the instrument is given in Section 3.1.1, followed by a description of the sample flow in Section 3.1.2 and of the calibration system in Section 3.1.3. Finally, in Section 3.1.4 the data retrieval is addressed. The following is based on Kostinek et al. (2019) and Kostinek (2019) if not otherwise specified.

3.1.1 Instrument Description

The QCLS consists of six components: The optics compartment, the electronics compartment, the monitor module, the cooling/heating module, the scroll pump, and the power supply (see Figure 3.1a).

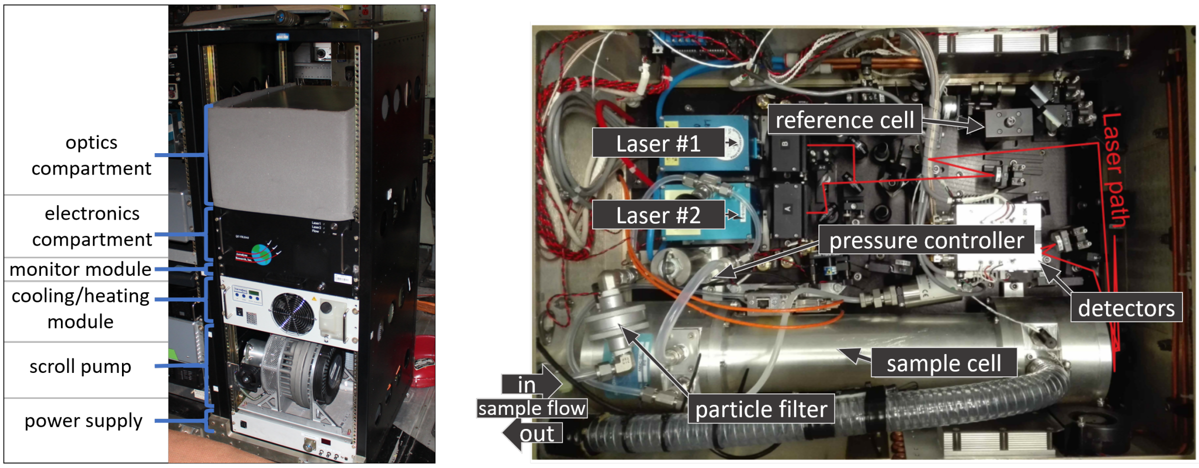

(a) Front view of the QCLS (b) Top view of the optics compartment

Figure 3.1: (a) Front view of the rack-mounted QCLS aboard NASA's C-130 during the ACT-America fall 2017 field deployment (see Section 3.2). (b) Top view of the optics compartment (Figure adapted from Kostinek et al., 2019). The main components are labeled. The laser path through the guiding optics is indicated as well as the entrance and exit of the sample flow.

The electronics and optics compartment are the core elements of the QCLS. The electronics compartment contains an embedded computing system which is responsible for data acquisition and the regulation of, for example, pressure and temperature controllers. The optics compartment primarily includes lasers, guiding optics, the sample cell and detectors (see Figure 3.1b). Two lasers are implemented, a continuous wave ICL (Laser #1; nanoplus GmbH, Gerbrunn, Germany) and a QCL (Laser #2; Alpes Lasers SA, St-Blaise, Switzerland). Their emitting center wavelength can be set by adjusting their operating temperature with Peltier elements. To both lasers a linear current ramp is applied to modulate their wavelength between a certain range around the configured center wavelength. At an operating temperature of 4.7 °C and 1.5 °C, Laser #1 and Laser #2 are modulated sequentially between 2988.520–2990.625 $\mathrm{cm^{-1}}$ and 2227.550–2228.000 $\mathrm{cm^{-1}}$, respectively. Located in the scanned range of Laser #1 there are absorption lines of CH_4, ethane C_2H_6, and H_2O. Laser #2 sees distinct absorption lines of N_2O, CO_2, and carbon monoxide CO (see Figure 3.4). From these absorption lines, mole fractions of the respective trace gas can be retrieved (see Section 3.1.4).

The guiding optics directs the laser beams into the sample cell. Since this approximately 1.6 m long path is not sealed (hereafter referred to as "open path"), the laser beams are influenced by the cabin pressure, temperature, and humidity before entering the sample cell. This is considered during the data retrieval by employing measurements of the cabin environment recorded by sensors within the optics compartment (see Section 3.1.4). The sample cell is an astigmatic

Herriott cell with an effective path length of 204 m and a net volume of approximately 2.1 l. Sample air constantly flows through the cell and is analyzed. An upstream pressure controller (P-502C-350A-AGD-39-V from Bronkhorst High-Tech B.V., Ruurlo, Netherlands) keeps the cell pressure constant. The cell is ideally operated at a cell pressure between 25 mbar and 80 mbar. The sample flow is further described in Section 3.1.2. After the sample cell, the laser beams are directed to one of two detectors. An auxiliary laser path is directed onto the second detector through a sealed reference cell containing pure CH_4 and N_2O. During startup this measurement is used for spectral referencing.
The spectrum of each laser is assigned to 450 spectral points. The frequency at which spectra are recorded can be adjusted while the wavelength modulation of the lasers occurs at a fixed frequency of 1.5 kHz. The acquired spectra are co-added until the desired output frequency is reached. During the ACT-America deployment, the output frequency was set to 2 Hz and, thus, each recorded spectrum consisted of 750 acquired spectra.

The liquid cooling/heating rack is used to keep the temperature in the optics compartment stable and to remove excess heat from the Peltier elements that control the temperatures of the lasers. For that the temperature of the cooling fluid (i.e., distilled water) is stabilized within ±0.05 K. The attached scroll pump pulls air from the inlet through chemically inert, flexible Polytetrafluoroethylene (PTFE) tubes into the sample cell and exhales into the aircraft cabin (see Section 3.1.2). The monitor module is used to control and supervise the instrument and data acquisition during research flights. Additionally, a module has been built that regulates the power supply of all QCLS components. It has been designed for an incoming voltage of 28 VDC which is typically required for aircraft deployment. After transforming to the required voltage, the power supply allots the power to the modules. Circuit breakers protect the aircraft and the QCLS from excess current. Model designation and manufacturer of the components are provided in Table 3.1.

Component:	**Model:**	**Manufacturer:**
Cooling/heating rack:	Thermorack 401	Solid State Cooling Systems, New York, U.S.A.
Scroll pump:	ISP 500C	Anest Iwata USA Inc., Cincinnati, U.S.A.
– motor:	DSE1-045-MB-161541	Baumüller Nürnberg GmbH, Nürnberg, Germany
– motor controller:	bmaXX2430	
Power inverter:	ACMaster 24/300	Mastervolt, Vierkirchen, Germany

Table 3.1: List of selected QCLS components with their model designation and manufacturer. More detailed information are provided in Kostinek et al. (2019).

3.1.2 Sample Flow

The sample flow is a crucial aspect of airborne in situ measurements because it determines the temporal and thus spatial resolution of observations. Figure 3.2 qualitatively depicts the sample flow through the QCLS including the calibration system (green-shaded part), which is described in Section 3.1.3. The scroll pump pulls sample air through the inlet, an industry-standard PTFE particle filter, the pressure controller, and the sample cell and exhausts into the aircraft. Components are connected via PTFE tubes with an inner diameter of $3/8''$.

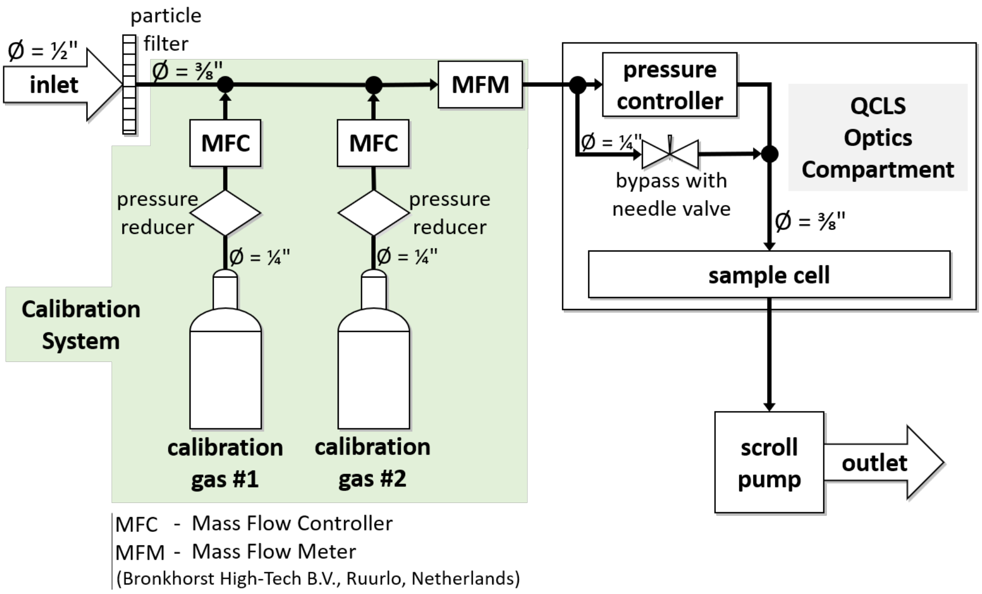

Figure 3.2: Schematic of the sample flow through the QCLS together with the integrated calibration system (green-shaded). All components between the calibration system and scroll pump (right top) are located inside the optics compartment (see Figure 3.1b). The scroll pump pulls the air from the inlet through PTFE tubes into the sample cell (see Section 3.1.2). The inner diameter of the PTFE tubes (Ø) is indicated. The calibration system is placed between the particle filter and optics compartment and enables the measurement of two different calibration gases (see Section 3.1.3).

High flow rates are desired to quickly exchange the air in the sample cell enabling a high temporal and thus spatial resolution. The scroll pump translates air with a nominal value of $500\,\mathrm{l\,min^{-1}}$ at standard conditions (i.e., standard pressure $p_0 = 1\,\mathrm{bar}$ and temperature $T_0 = 273.15\,\mathrm{K}$). Setting the cell pressure with the upstream pressure controller to 50 mbar, which is well within the optimal cell pressure range (25–80 mbar; see Section 3.1.1), results in a net flow rate of approximately $25\,\mathrm{l\,min^{-1}}$ at standard conditions. The time it takes to fully exchange the gas in the sample cell (hereafter referred to as "response time") limits the maximum achievable temporal resolution. Employing the ideal gas law (see Equation 2.1) allows for estimating the response time. Considering mass conservation and isothermal conditions, the volume of ambient air under standard conditions V_0 times the standard pressure p_0 equals the sample cell volume V_{cell} times the sample cell pressure p_{cell}. Dividing V_0 by the volumetric net flow rate of the QCLS Q delivers the theoretical system response time τ_r:

$$\tau_r = \underbrace{\frac{p_{cell} \cdot V_{cell}}{p_0}}_{=V_0} \cdot \frac{1}{Q} \tag{3.1}$$

With the given conditions ($p_0 = 1\,\mathrm{bar}$, $V_{cell} = 2.1\,\mathrm{l}$, $p_{cell} = 50\,\mathrm{mbar}$, and $Q = 25\,\mathrm{l\,min^{-1}}$ at standard conditions) the response time is $\tau_r = 0.25\,\mathrm{s}$. Hence, with this setup a temporal resolution of 2 Hz, like during the ACT-America deployment, is possible.

The inlet, the particle filter, and the PTFE tubing cause pressure drops, thus counteracting the scroll pump. These pressure drops should affect the flow rate as little as possible to sustain a maximal throughput and hence high temporal resolution. Increasing the pump power and thus the flow rate to compensate the pressure drops is not an option since then too much power would be consumed (for aircraft deployment the power consumption of the entire system is limited to 50 A at 28 VDC). The inlet is a PTFE tube in a stainless steel housing mounted at the hull of the aircraft. It is rear facing, thus preventing large particles, water droplets, and ice from entering the system. At aircraft cruise speeds (>70 $\mathrm{m\,s^{-1}}$), turbulence induced pressure drops at the inlet are likely. To minimize them, a PTFE tube with a relative large inner diameter of $1/2''$ is chosen. Downstream of the inlet, the particle filter is placed. It prevents the contamination of the system by aerosol particles which are larger than the pore size of the filter. However, the smaller the pore size the larger the pressure drop; 2 µm has been found to be a good compromise between protection and pressure drop.

During research flights the instrument faces quickly and strongly changing environmental conditions. Especially the ambient pressure influences the sample flow. For accurate absorption spectroscopy, the sample cell pressure and hence the net flow rate should be kept constant (see Section 2.3.2). The pressure controller is capable of compensating pressure variations of the sampled air. However, during airborne deployment the ambient pressure varies strongly between ~1000 hPa at mean sea level (MSL) and ~250 hPa at a flight altitude of 10 km or even less if flying higher. This enormous range cannot be fully handled by the employed pressure controller. At certain altitude/pressure level (~4 km above MSL) the pressure controller is fully open and not able to regulate anymore. Ascending further results in dropping cell pressure and flow rate (see Section 4.3). To elevate the altitude up to which the cell pressure can be regulated, a bypass of the pressure controller has been implemented. The bypass provides a basis sample flow into the cell, thus extending the dynamic range of the pressure controller. The flow through the bypass is adjustable by means of the needle valve, so that at the ground (highest ambient pressure) the pressure controller operates at the lower end of its dynamic range. This increases the altitude up to which the pressure controller is able to regulate to ~5 km above MSL (see Section 4.3).

3.1.3 Calibration System

Absorption spectrometers like the QCLS are highly sensitive to changes in environmental conditions (see Section 2.3.2), which can be extreme during airborne operation. Especially (but not exclusively) when the aircraft climbs or descends, the instrument faces rapid temperature and pressure changes which affect the measurement. Additionally, hardware effects, like often observed wavelength drifts of lasers over time, influence the measurements. Regular in-flight calibrations are necessary to correct for such effects. The calibration system is set up for two-point calibrations which turned out to be an effective approach for the QCLS and similar measurements systems (e.g., Gvakharia et al., 2018).

The calibration system of the QCLS is qualitatively depicted in the green-shaded part in Figure 3.2. It is based on two gas cylinders containing dry synthetic air which is mixed with a specific partitioning of the species measured by the QCLS. Both cylinders are attached to the sample line between the particle filter and the optics compartment via $1/4''$ PTFE tubes. Each calibration standard is regulated with a pressure reducer and a mass flow controller (MFC; F-201CV-20K-RGD-33-V from Bronkhorst High-Tech B.V., Ruurlo, Netherlands). The pressure reducer allows for monitoring the fill level of the gas cylinder and adjusts the upstream pressure of the MFC. The MFCs are controlled with the monitor module and regulate the injection of calibration gas into the sample cell. Attached to the inlet and upstream of the pressure controller valve, a mass flow meter (MFM; F-102E-RGD-33-V from Bronkhorst High-Tech B.V., Ruurlo, Netherlands) records the mass flow into the sample cell. When measuring air from a gas cylinder the respective MFC is regulated such that the mass flow from the gas cylinder is slightly higher than the sample flow recorded with the MFM measuring ambient air. Since the scroll pump preserves a constant mass flow through the system, this overflow leads to calibration gas being blown out of the inlet and blocks ambient air from entering the system, thus ensuring that only calibration gas is measured.

The two-point calibration is based on the assumption that the QCLS responds linearly to a linear increase of the abundance of an observed chemical compound. Figure 3.3 depicts the basic concept of a two-point calibration. The measured dry air mole fraction x_m can be calibrated x_c via the following calibration curve:

$$x_c = m \cdot x_m + b \tag{3.2}$$

The slope m and y-intercept b can be determined by measuring two calibration standards, a high H and a low L standard with given “true” mole fractions H_t and L_t, respectively:

$$\begin{aligned} m &= \frac{H_t - L_t}{H_m - L_m} \\ b &= H_t - m \cdot H_m = L_t - m \cdot L_m \end{aligned} \tag{3.3}$$

Where H_m/L_m is the measured mole fraction of the high/low standard.

3.1.4 Data Retrieval

To derive dry air mole fractions from raw absorption spectra recorded with the QCLS a retrieval software is necessary. Aerodyne provides TDLWintel. Additionally, for the QCLS a custom retrieval software, JFIT, has been developed (Kostinek et al., 2019; Kostinek, 2019), to double

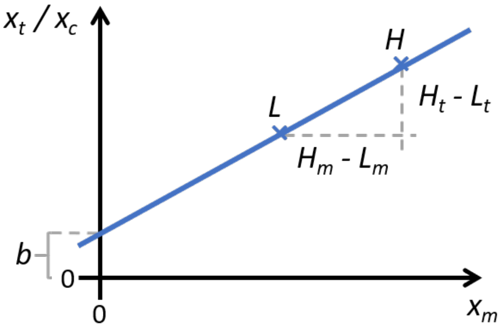

Figure 3.3: Schematics of a two-point calibration. The x-axis shows the measured mole fraction (x_m), the y-axis the "true" (x_t) or "calibrated" value (x_c), and the blue line the calibration curve. A high H and a low L calibration standard is used with given mole fractions H_t and L_t, respectively. By combining these "true" values with instrument measurements of the two standards (H_m and L_m) the slope and y-intercept of the calibration curve can be defined (see Equation 3.3).

check the TDLWintel output, to learn about possible error sources, and to allow for more flexibility. In the following, a short overview about both software is given. For a detailed description of JFIT and for a comparison of both software the reader is referred to Kostinek (2019).

Figure 3.4 shows a typical raw spectrum recorded by the QCLS measuring ambient air. Absorption lines of N_2O, H_2O, CH_4, and CO_2 are clearly visible. Between the lines no absorption occurs spanning the spectral baseline. TDLWintel and JFIT use the same approach to derive dry air mole fractions from such raw spectra. By fitting Voigt profiles to the absorption lines, a synthetic spectrum using tabulated absorption cross sections from the HITRAN database is created, whereby the abundance of the absorbing molecules is the unknown (see Equations 2.4 and 2.5). By minimizing the difference between the measured and synthetic spectrum the abundance is retrieved. Both software differ in how the absorption lines of the synthetic and measured spectrum are aligned and how the open path (see Section 3.1.1) is handled. In TDLWintel the user defines regions in the spectra of both lasers where no absorption occurs. According to these regions the spectral baseline is fitted. For the fit of the absorption lines, the user marks spectral regions where one or more species absorb. The influence of the open path is considered, but only for a static ambient/cabin pressure which is often not the case during flights. JFIT also splits the spectrum in smaller regions, but baseline and absorption lines are fitted simultaneously without needing user-defined markers. JFIT also uses measurements of the cabin pressure, temperature, and humidity measured by sensors inside of the optics compartment (see Section 3.1.1) to account for H_2O absorption along the open path.

In the setup presented herein, sample air is not dried before being measured in the sample cell. Hence, during the retrieval process the influence of water vapor, i.e. dilution and water broadening, has to be considered to derive dry air mole fractions. The water broadening describes the effect that spectral absorption lines are broadened due to collisions of water vapor and air molecules (see pressure broadening in Section 2.3.2). TDLWintel as well as JFIT

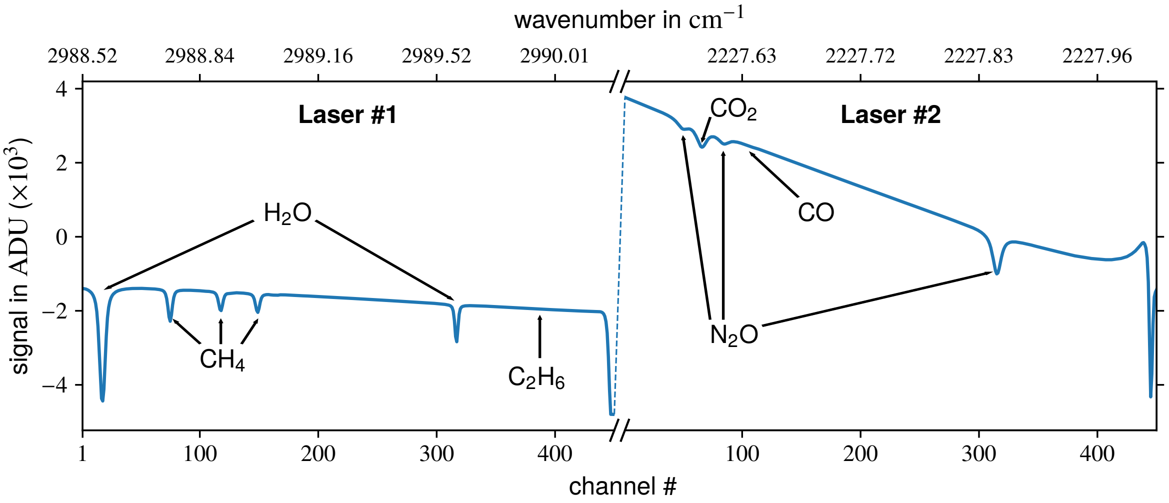

Figure 3.4: Typical raw spectrum of the QCLS measuring ambient air at a cell pressure of 46 mbar and a cell temperature of 298 K. The absorption lines of N_2O, H_2O, CH_4, C_2H_6, CO_2, and CO are marked with arrows. Zooming is required to properly see the absorption lines of C_2H_6 and CO. The signal strength is given in analog digital unit (ADU). It is a proxy for the detected light intensity.

account for this effect and correct it. Dilution describes the effect that the mole fraction of a constituent relative to moist air (i.e., dry air diluted with water vapor) is smaller than relative to dry air. Following Harazono et al. (2015), this effect can be corrected with the following equation:

$$c_x = \frac{c_x^m}{1 - c_{\mathrm{H_2O}}} \tag{3.4}$$

Where c_x is the desired dry air mole fraction and c_x^m the moist air mole fraction of species x. $c_{\mathrm{H_2O}}$ is the mole fraction of the water vapor. While TDLWintel already accounts for dilution and reports dry air mole fractions, JFIT does not and its output has to be manually corrected using Equation 3.4.

3.2 Atmospheric Carbon and Transport-America Project

ACT-America is a Earth Venture Suborbital-2 mission sponsored by the National Aeronautics and Space Administration (NASA) and led by the Pennsylvania State University (Davis et al., 2021). This project comprises five six-week airborne field campaigns between 2016 and 2019 which cover all four seasons (summer twice; 2016 and 2019). Two NASA aircraft were deployed, the C-130 (see Figure 3.5b) and B-200 (see Figure 3.5c), carrying state-of-the-art instruments, that measure GHGs and meteorological parameters such as temperature, wind, and humidity. During these deployments a rich dataset of in situ and remote sensing GHG measurements has been collected in the lower and middle troposphere over three regions, the East Coast, the Gulf Coast, and the Midwest of the U.S. (Wei et al., 2021). Figure 3.5a displays the flight tracks

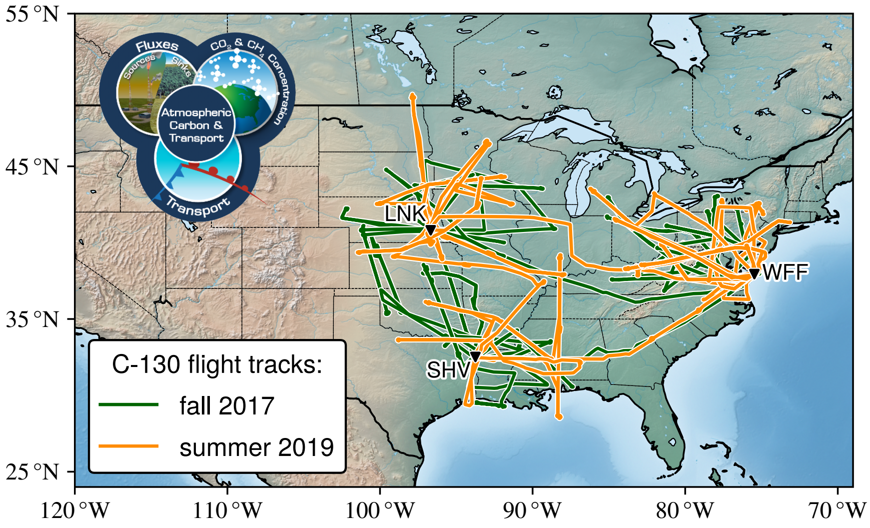

(a) ACT-America flight tracks

(b) NASA's C-130

(c) NASA's B-200

Figure 3.5: (a) Flight tracks of NASA's C-130 conducted during the fall 2017 and summer 2019 ACT-America field deployments. In the upper left corner there is the ACT-America logo obtained from https://airbornescience.nasa.gov/content/Atmospheric_Carbon_and_Transport_ACT-America. The three deployment sites are marked. These are the Wallops Flight Facility, Virginia (WFF), Shreveport, Louisiana (SHV), and Lincoln, Nebraska (LNK). (b) NASA's C-130 on the runway at WFF during the fall 2017 campaign. (c) NASA's B-200 at the airport in LNK during the summer 2019 campaign.

of NASA's C-130 during the fall 2017 and summer 2019 campaigns indicating the spatial coverage of the campaign. Each of the three regions was probed for two weeks during each field deployment. The marked deployment sites correspond to the three probed regions.

During the fall 2017 (10 Oct–13 Nov) and summer 2019 (17 Jun–27 Jul) field deployment the QCLS was mounted onboard the C-130 collecting, among others, continuous N_2O dry air mole fractions with a temporal resolution of 2 Hz and an uncertainty of ±0.8 ppb (Kostinek et al., 2019). Figure 3.5a displays the corresponding flight tracks. With over 200 flight hours of the C-130 an unprecedented dataset of continuous in situ N_2O measurements over large parts of the U.S. has been collected. As more direct observations of N_2O are urgently needed (Reay et al., 2012), these data are a valuable contribution to the effort of better understanding

N_2O sources. In addition to the continuous QCLS measurements of N_2O onboard the C-130, NOAA/GML collected whole-air flask samples (hereafter referred to as "Programmable Flask Package (PFP)") onboard of both aircraft which where measured for numerous trace gases including N_2O with an uncertainty of ±0.4 ppb (Sweeney et al., 2015; Sweeney et al., 2018; Baier et al., 2020). Taking 6–12 samples during each flight, onboard of each aircraft, and during each of the five field deployments, allowed for the compilation of an enormous, high-precision database of in situ N_2O point measurements in the troposphere. Together with the continuous QCLS measurements, these PFP samples are a valuable contribution to the community and enable extensive N_2O studies.

3.3 Atmospheric Transport Models

Atmospheric transport models are used to relate the aircraft-based in situ measurements conducted during ACT-America to surface N_2O sources. Two basic model concepts exist, the Eulerian and the Lagrangian approach. An Eulerian model describes the atmosphere on a discrete grid. At each grid point atmospheric properties like temperature, humidity, or N_2O mole fractions are simulated. In contrast, a Lagrangian model follows an air parcel backward or forward in time through the atmosphere enabling the determination of the origin of the respective air parcel. Both approaches are employed for this study to optimally answer the research questions. The Eulerian model WRF is presented in Section 3.3.1. Section 3.3.2 introduces the Lagrangian model HYSPLIT.

3.3.1 The Eulerian Model WRF

For this study a mesoscale model is needed that simulates the weather, the emission of N_2O from emission inventories, and the propagation of the emitted N_2O through the atmosphere by the simulated weather. Therefore, the state-of-the-art Numerical Weather Prediction (NWP) model Advanced Research WRF (ARW) version 4.0.2 (Skamarock et al., 2019) has been selected. This community model, which is officially supervised by the National Center for Atmospheric Research (NCAR), provides a fully-compressible, Eulerian non-hydrostatic equations solver and is steadily developed. Being thoroughly tested and highly accessible, and containing a large set of numerical and physical options and schemes, WRF is widely used for numerous applications in atmospheric research and forecasting (Powers et al., 2017). Using the WRF model coupled to Chemistry extension (WRF-Chem; Grell et al., 2005) enables to simulate the emission of N_2O from gridded inventories and the propagation of the emitted N_2O through the atmosphere. Since N_2O exhibits a long atmospheric lifetime of over 100 yr (see Section 2.2), it is assumed that chemically induced concentration changes can be neglected for model runs simulating only several days and, thus, N_2O is treated as a passive tracer. The detailed model setup is further elaborated in Section 5.2.

3.3.2 The Lagrangian Model HYSPLIT

HYSPLIT is one of the most widely used atmospheric transport and dispersion models (Stein et al., 2015). Originally developed to calculate air parcel trajectories, it has been extended to simulate complex dispersion with chemical interactions and deposition. HYSPLIT is mostly used to estimate the origin of air masses and to simulate the transport and dispersion of trace gases and particles like dust and allergens. A detailed description of the model can be found in Draxler and Hess (1997) and Stein et al. (2015). For this thesis, HYSPLIT's capability of calculating so-called footprints to estimate sources of N_2O is utilized. At a certain position and time in the atmosphere (receptor) a defined amount of particles is released and propagated backward in time. During the backward advection, dispersion occurs spreading the particles. By considering the spatial distribution of the particles, the contribution of surface emission areas to changes in the receptor concentration can be estimated. This contribution defines the footprint. A mathematical description is provided in Lin et al. (2003).

Bianca C. Baier (Cooperative Institute for Research in Environmental Sciences, University of Colorado-Boulder, Boulder, CO, USA and NOAA GML, Boulder, CO, USA) calculated HYSPLIT footprints for each PFP measurement conducted during all five ACT-America field deployments. 500 particles are released at the approximate position and time of each PFP sample. Every 15 min footprints are derived for ten days backward in time. High resolution WRF simulations, produced by the Pennsylvania State University for the ACT-America campaigns, serve as meteorological driver. Figure 3.6 shows an example footprint of a single PFP measurement.

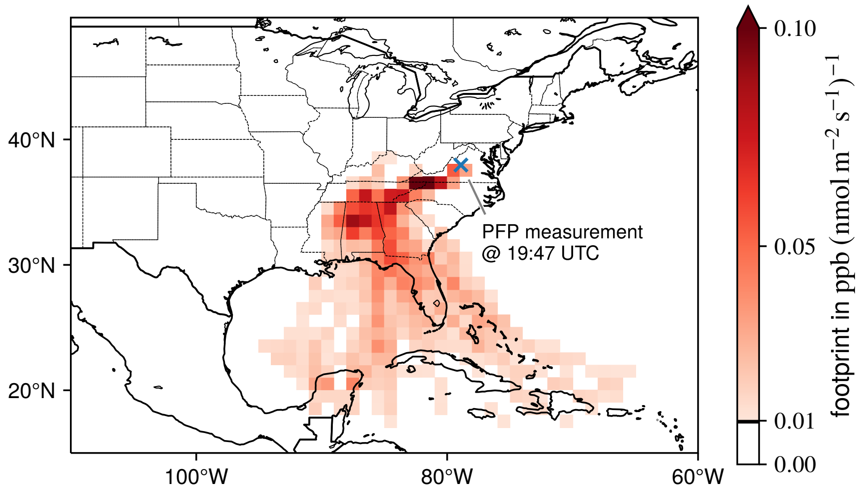

Figure 3.6: Example HYSPLIT footprint of a single PFP sample (blue cross) summed over ten days. The PFP has been collected onboard NASA's C-130 at 2237 m above MSL during the ACT-America campaign in fall 2017 on the Oct 10.

3.4 Emission Inventories

In this thesis two state-of-the-art N_2O bottom-up emission inventories are employed and evaluated against the top-down estimate of U.S. Midwest N_2O emissions. The first one is the widely used *Tier 1–2* inventory EDGAR (see Section 3.4.1). Here, the two most recent versions of EDGAR are used, version 4.3.2 (EDGAR4.3.2, 2017; Janssens-Maenhout et al., 2019) and version 5.0 (Crippa et al., 2019; EDGAR5.0, 2019). The second employed inventory is a *Tier 3* inventory, estimated with the biogeochemical model DayCent (Parton et al., 1998; Del Grosso et al., 2001; Del Grosso et al., 2011), provided by Stephen M. Ogle (Natural Resource Ecology Laboratory, Colorado State University, Fort Collins, CO, USA) (see Section 3.4.2). A description of the concepts of *Tier 1*, *2*, and *3* inventories and of their advantages and disadvantages is provided in Section 2.3.1 in the previous chapter.

3.4.1 Emissions Database for Global Atmospheric Research – EDGAR

EDGAR4.3.2 and EDGAR5.0 provides monthly resolved global N_2O fluxes from anthropogenic sources on a $0.1°\times0.1°$ grid for 2012 and 2015, respectively. Estimates for the different emission sectors are mostly based on *Tier 1* emission factors while some, which are less relevant for this work (e.g., the sectors "solvents and products use" or "chemical processes"), are based on *Tier 2* emission factors (see Janssens-Maenhout et al., 2019). For this thesis, the different sectors in EDGAR are merged into three main sectors: Agricultural emissions E_{AGR}, anthropogenic non-agricultural emissions E_{nonAGR}, and natural emissions E_N. Table 3.2 lists all the available EDGAR sectors with their corresponding IPCC (2006b) sector code and how they are assigned to the three main sectors. E_{AGR} covers N_2O fluxes from agricultural soils, manure management, agricultural waste burning, and indirect emissions from agriculture. E_{nonAGR} includes, among others, emissions from fossil fuel combustion, industry, and waste. Since EDGAR4.3.2 as well as EDGAR5.0 provide only anthropogenic emissions, i.e. E_{AGR} and E_{nonAGR}, both versions are supplemented with yearly natural N_2O emissions on a global $1° \times 1°$ grid from EDGAR version 2.0 (EDGAR2; Olivier et al., 1996; Olivier et al., 1999). This version contains N_2O fluxes from soils under natural vegetation and oceans forming E_N. All N_2O fluxes are assumed to emerge from the surface. This is valid except for aviation related emissions. Since those account for less than 0.3 % of yearly total Midwest N_2O emissions in EDGAR, they are omitted from E_{nonAGR} without affecting results significantly. Furthermore, it is assumed that the here presented main sectors E_{AGR}, E_{nonAGR}, and E_N cover all N_2O fluxes which are relevant in the Midwest.

3.4.2 Daily Time-Step Version of the CENTURY Model – DayCent

With the process-based, biogeochemical model DayCent direct soil N_2O emissions from crop- and grassland are estimated on a $0.5° \times 0.5°$ grid in the Midwest on a daily basis from 2011 to 2015, which were aggregated to a monthly time step (Section 5.5.3 discusses the applicability to the ACT-America period, i.e. 2016–2019). The model simulates fluxes of carbon and nitrogen

Custom merge:	**EDGAR sector:**	**IPCC (2006b) code:**
E_{AGR}	Manure management	3A2
	Agricultural waste burning	3C1b
	Agricultural soils	3C2+3C3+3C4+3C7
	Indirect N_2O emissions from agriculture	3C5+3C6
E_{nonAGR}	Power industry	1A1a
	Oil refineries and transformation industry	1A1b+1A1ci+1A1cii+1A5biii+ 1B1b+1B2aiii6+1B2biii3+1B1c
	Combustion for manufacturing	1A2
	Road transportation	1A3b
	Railways, pipelines, off-road transport	1A3c+1A3e
	Shipping	1A3d
	Energy for buildings	1A4+1A5
	Fuel exploitation	1B1a+1B2aiii2+1B2aiii3+1B2bi +1B2bii
	Chemical processes	2B
	Solvents and products use	2D3+2E+2F+2G
	Solid waste landfills	4A+4B
	Solid waste incineration	4C
	Waste water handling	4D
	Indirect emissions from NO_x and NH_3	5A
	Fossil fuel fires	5B
E_N	Natural soils (only EDGAR2)	–
	Oceans (only EDGAR2)	–
omitted	Aviation climbing and descent	1A3a_CDS
	Aviation cruise	1A3a_CRS
	Aviation landing and takeoff	1A3a_LTO
	Aviation supersonic	1A3a_SPS

Table 3.2: All emission sectors in EDGAR4.3.2, EDGAR5.0, and EDGAR2 (only natural) together with their IPCC (2006b) sector code (https://www.ipcc-nggip.iges.or.jp/EFDB/find_ef.php) and their assignment to the three main sectors E_{AGR}, E_{nonAGR}, and E_N (see Section 3.4.1). If not otherwise specified, sectors are included in EDGAR4.3.2 and EDGAR5.0. (Table adapted from Eckl et al., 2021)

between the atmosphere, vegetation, and soil thus deriving N_2O emissions (see Figure 3.7). Incorporating several environmental drivers, including weather patterns, agricultural practices like fertilization, soil characteristics, and crop features, this approach provides a more sophisticated estimate of soil emissions than the emission factor based EDGAR inventory. The GHG inventory of the United States Environmental Protection Agency (EPA, 2020) uses DayCent estimates of direct soil emissions for emissions reporting of agricultural soil N_2O to the UN Framework Convention on Climate Change. DayCent does not calculate emissions from manure management, agricultural waste burning, indirect soil emissions, and those associated with minor crops such as vegetables. The EPA inventory quantifies these sources and subsources with an emission factor approach. Here, their contribution is estimated by employing the yearly estimates from EPA, calculating their relative fraction of the EPA direct soil emissions, and adding them to our monthly estimates. As a result, the DayCent inventory properly accounts for the total agricultural emissions, but not the spatial distribution of agricultural sources which are not estimated by DayCent.

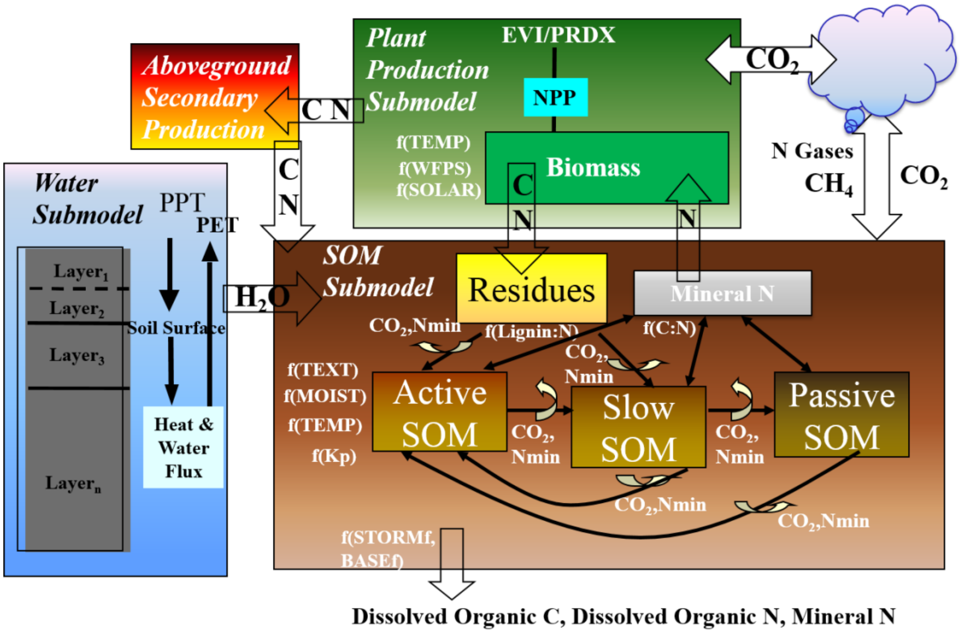

Figure 3.7: DayCent model flow diagram illustrating the simulated processes. (Figure adopted from EPA, 2021, p. A-390)

4 N_2O Measurements Using the Quantum Cascade Laser Spectrometer

Measuring atmospheric N_2O enhancements to study emissions is challenging. One reason is that the most important source types of N_2O, including agriculture, are area sources. Such sources can emit a large amount of GHGs in total, but emissions are distributed over a large area and, hence, related enhancements in the atmosphere are typically small. In the PBL, these enhancements are usually well below 1 % of the atmospheric background mole fraction of currently around 330 ppb. Thus, the accuracy and precision of in situ N_2O instruments are especially important to be able to distinguish such pollution signatures from the relatively high background. The DLR QCLS was already deployed for the measurement of N_2O (see Section 3.1; Kostinek et al., 2019; Kostinek, 2019). To enhance its detectable range of N_2O enhancements and, thus, its application range, within this study special effort has been put into further optimizing the QCLS N_2O product. The optimization includes laboratory work as well as the analysis of data collected during ACT-America onboard NASA's C-130 aircraft (see Section 3.2).

Frequent and regular in-flight calibrations are the basis for accurate measurements. These are described in Section 4.1. Furthermore, calibration standards have been obtained from NOAA. These standards are traceable to WMO calibration scales, enabling the comparison of QCLS data products with other instruments. Section 4.2 presents the calibrations with the NOAA standards. During the ACT-America 2019 field deployment it has been found that pressure variations in the sample cell and inconsistencies in the H_2O retrieval (needed to determine dry air mole fractions; see Section 3.1.4) introduce uncertainties to the N_2O datasets. Corrections therefore have been derived and are presented in Section 4.3 (cell pressure) and Section 4.4 (H_2O). To assess their benefit, the well-established, high-precision PFP samples (see Section 3.2), which have been collected onboard the C-130, are used as a reference. Finally, Section 4.5 discusses and summarizes the quality of the QCLS N_2O measurements gathered during the ACT-America deployment.

Although the QCLS is capable of additionally measuring CH_4, C_2H_6, CO_2, and CO, in the following only the calibration procedure for N_2O is described as it is the species of interest in the present thesis. However, the other chemical compounds were equally processed. Furthermore, in the following only Kostinek et al., 2019 is cited in place of additionally referring to Kostinek, 2019 since both publications contain the characterization of the DLR QCLS.

4.1 In-Flight Calibrations

During the campaigns so-called secondary calibration standards obtained from Air Liquide were used for in-flight calibrations. Such standards are relatively inexpensive and, hence, are attractive for the operational use, especially for the QCLS which consumes lots of calibration gas due to its high flow rate of ~25 l min^{-1} at standard conditions (see Section 3.1.2). However, the reported composition of these secondary standards exhibits high uncertainties. For N_2O the stated uncertainty is ±10 % or ±33 ppb (considering an ambient N_2O abundance of 330 ppb), which is much larger than expected atmospheric N_2O enhancements. Therefore, these standards are suited to correct for any instrument drifts and dependencies, but they are not suited to calibrate the retrieved absolute dry air mole fraction. For that, two so-called primary calibration standards from NOAA/GML were obtained and used to cross-calibrate the Air Liquide standards after the field campaigns in the laboratory, thus making the performed measurements comparable to other instruments (see Section 4.2).

To develop a workable calibration strategy for the airborne operation of the QCLS, three aspects must be considered. First, rapidly changing environmental conditions and potential instrument drifts during a flight make frequent and extensive in-flight calibrations necessary. Second, it is aimed to obtain the optimal spatial and temporal coverage with the measurements, but each calibration reduces the duty cycle and hence limits atmospheric data availability. Third, weight and space constraints onboard the aircraft limit the amount of available calibration gas. Together with the high flow rate of the QCLS and research flights that last several hours, the maximum possible number of calibrations is restricted. For the ACT-America field campaign, a calibration strategy was developed, comparable to the one proposed by Kostinek et al., 2019 for the DLR QCLS, and by Gvakharia et al., 2018 for a similar airborne in situ instrument. The strategy consists of regular two-point in-flight calibrations using the calibration system described in Section 3.1.3. Every 5 min a calibration is performed, where each calibration standard of two different N_2O mole fractions is measured for approximately 10 s. The T90 time, defined as the time period until 90 % of the signal is reached, was ~0.9 s during the summer 2019 research flights. Thus, measuring a calibration standard for 10 s is sufficient for an accurate calibration. With this calibration frequency environmental changes and instrument drifts can be caught decently while preserving a high duty cycle of over 90 % during a research flight.

For the two-point calibration a high and a low calibration standard is needed. Dry synthetic air (20.9 ± 0.2 % O_2 in N_2) (hereafter referred to as “zero air”) was used as the low calibration standard. Air Liquide provides no value for the potential N_2O contamination of the zero air. Since there is no significant absorption in the QCLS spectra when measuring zero air, the contamination with N_2O is assumed to be insignificant. Measuring zero air enables the determination of the spectral baseline which is mandatory for an accurate retrieval (see Section 2.3.2). For the high standard, calibration gas containing a target N_2O mole fraction of 328 ± 33 ppb in dry synthetic air was used. Figure 4.1 displays an example in-flight calibration cycle during ACT-America. Zero air is measured first, followed by calibration gas. For each of these calibration cycles the slope and y-intercept of the calibration curve is determined (see Equation 3.3). Between the cycles these coefficients are linearly interpolated and used to calibrate the measurements of ambient air.

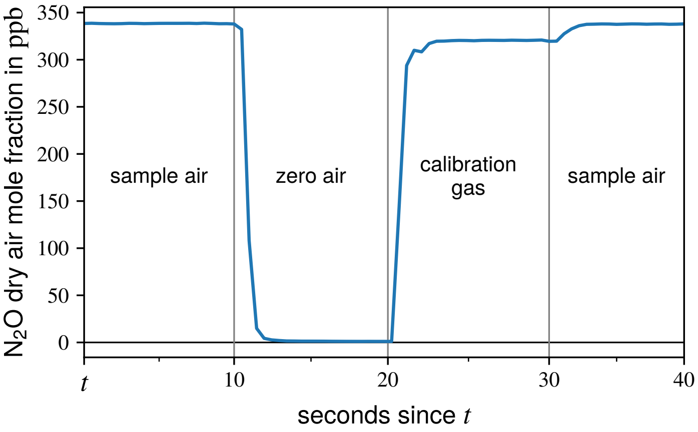

Figure 4.1: Example in-flight calibration cycle during ACT-America. The vertical lines indicate the switch-over from measuring ambient air to measuring zero air (t + 10 s), calibration gas (t + 20 s), and sample air again (t + 30 s).

The employed calibration cylinders have to supply enough calibration gas for the above described calibration strategy. Since NASA's C-130 is comparatively spacious, 10 l gas cylinders could be used for both standards containing 200 bar (zero air)/150 bar (calibration standard). Employing the ideal gas law (Equation 2.1), considering mass conservation, and assuming an isothermal expansion, the volume of zero air/calibration gas of a cylinder at normal pressure (p_0 = 1013.25 mbar) V_0 can be estimated via:

$$p_g \cdot V_g = p_0 \cdot V_0 \;\rightarrow\; V_0 = \frac{p_g \cdot V_g}{p_0} \tag{4.1}$$

p_g and V_g are the pressure and volume of a gas cylinder. Hence, for the low and high standards V_0 is approximately 1974 l and 1480 l, respectively. With a QCLS flow rate of 25 l min^{-1} at standard conditions (see Section 3.1.2) the endurance of a zero air/calibration standard gas cylinder is approximately 79 min/59 min. For longest ACT-America research flights (<10 h) a calibration standard has to provide calibration gas for 20 min to supply enough gas for the above described calibration strategy. Hence, the proposed calibration gas cylinders are suitable.

4.2 NOAA Calibration

After the field campaigns, the employed secondary standards obtained from Air Liquide are cross-calibrated against primary standards obtained from NOAA/GML. These standards contain compressed and dried air with ambient concentrations of N_2O, CH_4, C_2H_6, and CO_2. They are much pricier than the secondary standards, but NOAA assures a substantially higher accuracy for N_2O (±0.4 ppb) than Air Liquide (approx. ±33 ppb) and their standards are, related to N_2O, traceable to the WMO-N2O_X2006 calibration scale (Hall et al., 2007). Thus, the cross-calibration makes the QCLS N_2O measurements comparable to the measurements of other instruments which also use calibration standards that are traceable to the WMO scale.

Section 4.5 provides a comparison of the QCLS and PFP N_2O measurements conducted during ACT-America.

For the cross-calibration of a secondary standard in the laboratory, three calibration standards are attached to the in-flight calibration system described in Section 3.1.3. These three standards are two primary standards and the secondary standard to be calibrated. The remaining QCLS setup is the same as during airborne operation. The calibration sequence includes the measurement of the two primary standards, followed by the measurement of the secondary standard and a repeated measurement of the two primary standards. Each gas cylinder is thereby measured for 30 s. The respective calibration curves (see Equation 3.2) are determined for both primary standards measured at the beginning and at the end of each calibration sequence. In between, the calibration curve is linearly interpolated to enable the correction of any instrument drifts during the cross-calibration. Finally, the interpolation is applied to calibrate the secondary standard. In Figure 4.2, the calibrated values of the secondary standards is displayed. The shown calibration curve is the average over all calibration curves derived during the cross-calibration of the ten secondary standards. With a slope of $m = 1.002 \pm 0.002$ and a y-intercept of $b = 4.655 \pm 0.591$ variations among them are small. Table 4.1 summarizes the primary and secondary standards along with their reported and cross-calibrated N_2O abundances and uncertainties.

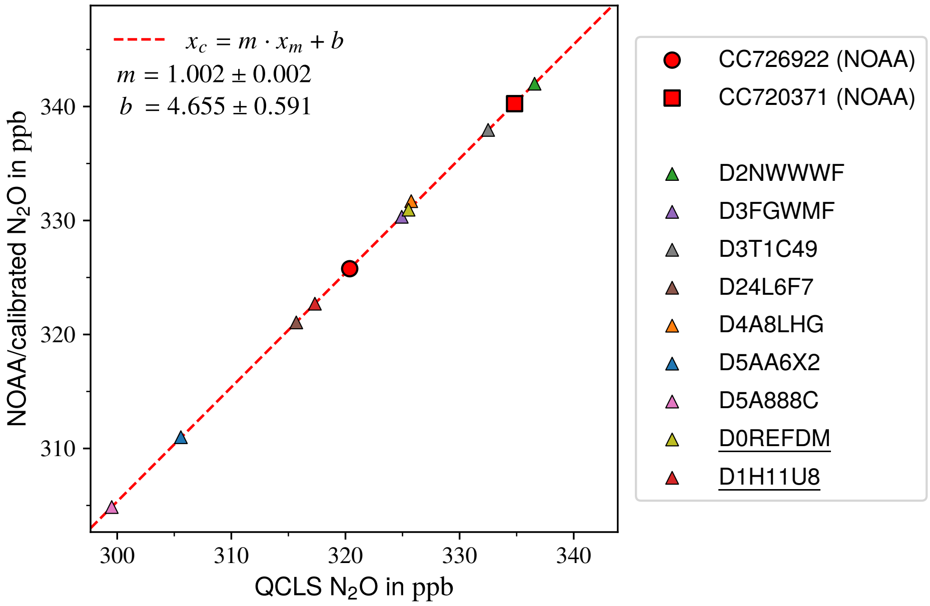

Figure 4.2: NOAA calibration of secondary calibration standards. Before and after each secondary standard (triangles), both primary (NOAA) standards are measured and a calibration curve is determined. Here, the average of all calibration curves is displayed (red dashed line; x_m and x_c is the measured and calibrated dry air mole fraction, respectively). Uncertainties are too small to be visible, but they are provided in Table 4.1. Cylinders which are only used in the laboratory and not for in-flight calibrations are underlined.

Calibration standard:	**Reported N_2O in ppb:**	**Calibrated N_2O in ppb:**
Primary (NOAA)		
CC726922	325.77 ± 0.40 *	–
CC720371	340.25 ± 0.40 *	–
Secondary (Air Liquide)		
D2NWWWF	270 ± 27	342.0 ± 0.9
D3FGWMF	330 ± 33	330.3 ± 0.9
D3T1C49	265 ± 27	338.0 ± 0.9
D24L6F7	312 ± 31	321.1 ± 0.9
D4A8LHG	335 ± 34	331.7 ± 0.9
D5AA6X2	373 ± 37	311.0 ± 0.9
D5A888C	307 ± 31	304.9 ± 0.9
<u>D0REFDM</u>	340 ± 34	331.0 ± 0.9
<u>D1H11U8</u>	329 ± 33	322.7 ± 0.9

* NOAA reports expanded or total uncertainties with a ~95 % confidence level

Table 4.1: Employed primary (NOAA) and secondary calibration standards (Air Liquide) with their N_2O abundance. The first column lists the gas cylinder number. Standards which are only used in the laboratory and not for in-flight calibrations are underlined. The second column lists the N_2O mole fractions with their 1σ uncertainties stated by Air Liquide and NOAA (calibration certificate numbers CC726922-A and CC720371-A; NOAA reports expanded uncertainties). All secondary standards were ordered with a target N_2O abundance of 328 ± 33 ppb. The third column lists the NOAA-calibrated N_2O abundance of the secondary standards after cross-calibration. The primary standards are assumed as the "truth".

4.3 Cell Pressure Correction

Above a certain altitude the QCLS cannot sustain the cell pressure (p_{cell}) since the ambient pressure at the inlet becomes too low. This is visualized in Figure 4.3, which shows the cell pressure of the QCLS during the ACT-America research flight on 27 Jul 2019. The cell pressure is regulated to p_{set} = 45 mbar. As long as the C-130 stays below approximately h_p = 4.8 km above MSL the cell pressure is maintained. If the aircraft climbs further, the cell pressure drops constantly, reaching values of 15 mbar at highest C-130 flight altitudes of approximately 9 km above MSL. During the regular in-flight calibrations, p_{set} sets up again since more sample or calibration air is in the system. Thus, in high altitudes calibration gas is measured at different conditions than ambient air, which introduces errors in the calibration procedure and in the final absolute mole fractions. With a laboratory experiment a correction for this error is derived.

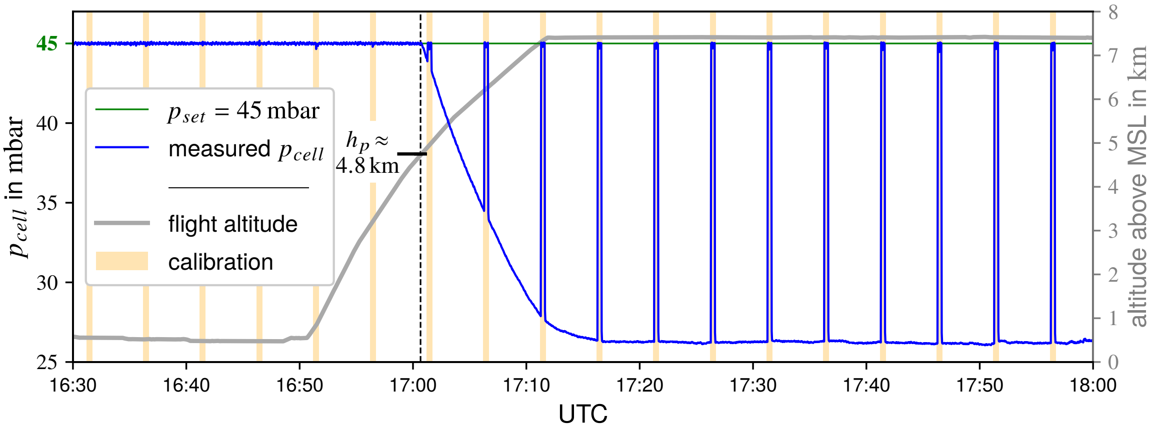

Figure 4.3: Part of the QCLS cell pressure p_{cell} time series of the research flight at 27 Jun 2019. The cell pressure is regulated to p_{set} = 45 mbar. Above an approximate altitude of h_p = 4.8 km above MSL the cell pressure drops when measuring ambient air while during calibration (orange-shaded) the cell pressure remains stable at 45 mbar.

In the laboratory experiment the influence of cell pressure variations between 50 mbar and 13 mbar on the retrieved N_2O dry air mole fraction is analyzed to derive a pressure correction. This cell pressure range covers the range experienced during ACT-America. The QCLS is set up as during field deployment (see Section 3.1), with one secondary standard and no zero air attached to the calibration system (see Section 3.1.3). The calibration gas is measured for approximately 20 s at a cell pressure of 50 mbar. Then, p_{cell} is subsequently reduced by 5 mbar until a cell pressure of 13 mbar is reached (the last step is only 2 mbar). At each interval the calibration gas is again measured for 20 s. This enables to quantify the response of the N_2O retrieval on a varying cell pressure. Afterwards, the calibration gas is measured again at p_{set} (i.e., 45 mbar) to correct the instrument drift during the experiment assuming a linear drift. However, the influence of the drift is one order of magnitude smaller than the effect due to cell pressure variations.

The above described experiment has been performed with eight different calibration standards (listed in Table 4.1). The results are displayed in Figure 4.4. The retrieved N_2O dry air mole fraction of all gas cylinders increases with a decreasing cell pressure (see Figure 4.4a). From highest to lowest p_{cell}, the difference in measured N_2O mole fractions is on average approximately 2 ppb, which is significant when it comes to typical ambient N_2O enhancements. By considering the deviation of the retrieved mole fraction relative to the retrieval at the setpoint cell pressure p_{set} = 45 mbar ($P(p_{cell}, p_{set})$), the different gas cylinders can be compared (see Figure 4.4b). In all eight experiments a similar, non-linear cell pressure dependency is observed. Two characteristics stand out: First, between a cell pressure of 40 mbar and 35 mbar there is a plateau. Second, there is a significant spread in the strength of deviation among the gas cylinders. At a cell pressure of 13 mbar the deviations range between 0.5 ‰ and 0.8 ‰. No reason for these two features could be found. All experiments were conducted with the same setup and under the same conditions. There is also neither a dependency on the order of the conducted experiments nor on the total N_2O abundance in the gas cylinders. For the correction of the field measurements, the discrete average curve $\overline{P}(p_{cell}, p_{set})$ is used. Intermediate cell pressures are interpolated linearly. Let $c(p_{cell})$ be the retrieved N_2O dry air mole fraction measured at p_{cell}, then the retrieval is corrected to p_{set} via:

$$c(p_{set}) = \frac{c(p_{cell})}{\overline{P}(p_{cell},\, p_{set}) + 100\,\%} \tag{4.2}$$

This correction is applied to the whole ACT-America 2019 dataset before calibration.

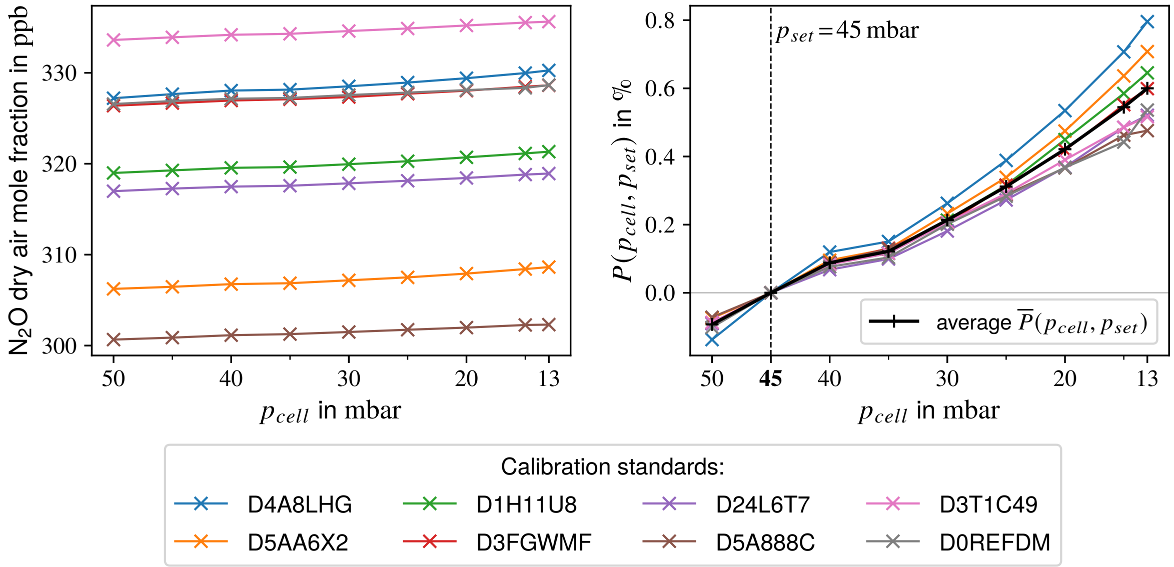

(a) Retrieved N_2O mole fraction

(b) Relative cell pressure dependence

Figure 4.4: Cell pressure dependence of retrieved N_2O dry air mole fraction. With the QCLS eight calibration standards have been measured at different cell pressures p_{cell}. (a) Retrieved N_2O dry air mole fraction vs. p_{cell}. (b) Deviation of the retrieved mole fraction relative to the retrieval at a cell pressure of p_{set} = 45 mbar ($P(p_{cell},\, p_{set})$). The average over the eight calibration standards $\overline{P}(p_{cell},\, p_{set})$ is used to correct the cell pressure dependency (see Equation 4.2).

To evaluate the quality of the presented correction, N_2O measurements of the QCLS are compared to 120 PFP samples which have been collected onboard the C-130 during the ACT-America field deployments. Although the PFP samples are not perfect (uncertainty of N_2O is ±0.4 ppb), they provide the best available measurements of trace gas mole fractions. The root-mean-square error (RMSE) is used as a measure for the discrepancy between both datasets. Let c^i_{PFP} be the i^{th} of N PFP N_2O measurements, and let c^i be the corresponding calibrated QCLS dry air mole fraction averaged over the sampling duration of the PFP sample, then the RMSE is defined as:

$$\mathrm{RMSE} = \sqrt{\frac{\sum_{i=1}^{N}(c^i - c^i_{\mathrm{PFP}})^2}{N}} \tag{4.3}$$

With the cell pressure correction, the RMSE is reduced from 2.1 ppb to 1.9 ppb (see Table 4.2 and Figure 4.6a for a scatter plot between c^i and c^i_{PFP}). The remaining RMSE is mostly caused by uncertainties in the QCLS H_2O retrieval, which is used to determine dry air mole fractions of N_2O. This is further examined in the next Section 4.4. However, the RMSE cannot become zero due to two reasons. First, PFP measurements are not perfect as mentioned above. Second, the comparison between both instruments is not perfect. A PFP collects sample air for several seconds or a minute and, hence, sees a N_2O abundance averaged over this timeframe. This average is compared to the corresponding average of the higher-frequent QCLS measurements. If the time axes of both datasets are not perfectly aligned due to, for example, different inlet line lengths, the QCLS and PFP measurements describe different air mixtures. The analyzed air mixture might also differ among both instruments if there are gaps in the averaged QCLS data due to, for example, calibration. Furthermore, if the PFP samples are stored over a long period before they are analyzed, the composition of the sampled air might change leading also to a discrepancy between QCLS and PFP measurements.

4.4 Water Vapor Correction

Since the QCLS does not dry the sample air, the water vapor abundance must be known, to confidently report N_2O dry air mole fractions (see Section 3.1.4). However, the QCLS water vapor measurement is not in-flight calibrated. Hence, calculating the water dilution (Equation 3.4) might introduce additional uncertainties to the final N_2O retrieval. By comparing QCLS water vapor measurements with other instruments the influence of this uncertainty source can be estimated. During ACT-America onboard NASA's C-130 two more instruments measuring H_2O were deployed; an in situ infrared cavity ring-down spectroscopy PICARRO G2301-m and an Edgetech Vigilant 137 hygrometer (Wei et al., 2021). Their inlets were next to the inlet of the QCLS and, thus, it can be assumed that all three H_2O analyzers saw the same air masses. Figure 4.5 shows their water vapor time series during the research flight on 04 Jul 2019. Overall, the measurements show the same signals. However, for H_2O mole fractions lower than roughly 1.5 % the QCLS and PICARRO are close to each other but both are significantly lower than the hygrometer. On the contrary, at higher water vapor abundances than 1.5 %, the QCLS is close to the hygrometer but both are significantly higher than the PICARRO. For example, at around 20:00 UTC the PICARRO states a H_2O mole fraction of around 2.4 %, whereas the QCLS and hygrometer report around 2.8 %. If the lower PICARRO value and not the QCLS value would be used to calculate the water dilution (Equation 3.4), the resulting N_2O dry air mole fraction would be lower. For a N_2O abundance of 330 ppb in moist air, the difference would be 1.4 ppb, which is significant when it comes to typical ambient N_2O enhancements. The QCLS as well as the PICARRO are not optimized for H_2O measurements, whereas the hygrometer is. However, the hygrometer experienced issues during its field deployment (as communicated at instrument status reports during the ACT-America field campaigns). For that reason, it is difficult to judge which H_2O time series is the most trustworthy one and, hence, whether or to what extent the QCLS H_2O mole fractions have to be corrected. Therefore, PFP N_2O measurements have been utilized to minimize errors in N_2O caused by uncertainties in H_2O. This is described in the following.

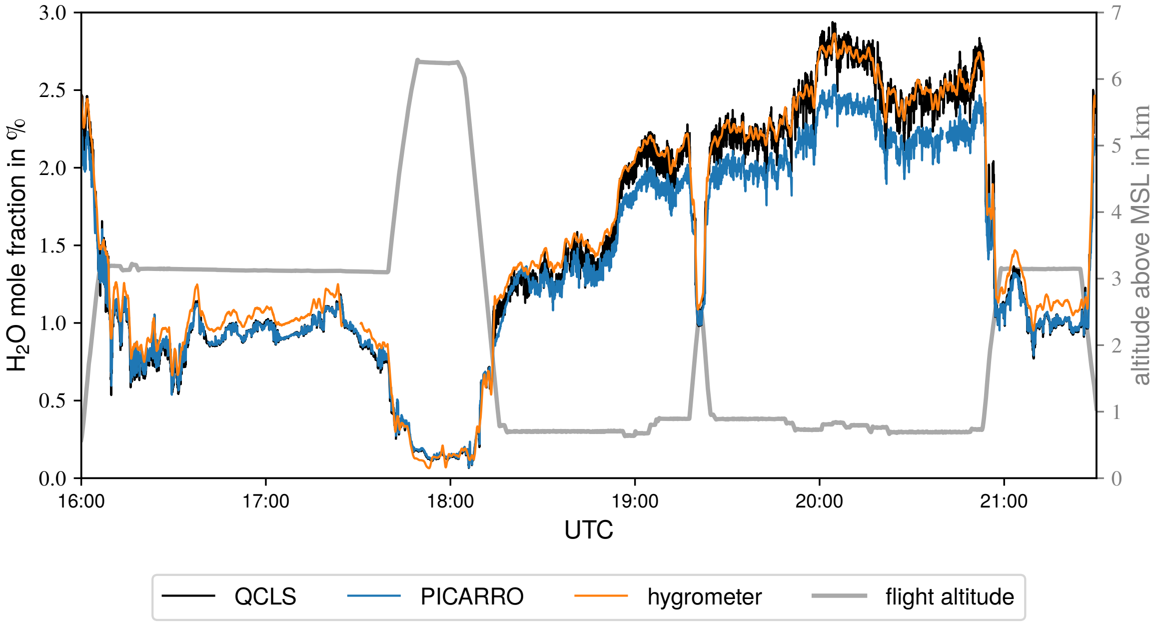

Figure 4.5: H_2O measurements of the QCLS, PICARRO, and hygrometer onboard NASA's C-130 during the research flight on 04 Jul 2019.

The approach is to multiply the calibrated N_2O dry air mole fraction retrieved with the QCLS c by a factor $W(c_{H_2O})$, which depends on the QCLS water vapor measurement c_{H_2O}, to get a corrected N_2O mole fraction c^*:

$$c^* = c \cdot W(c_{H_2O}) \tag{4.4}$$

By minimizing the RMSE between PFP and QCLS N_2O mole fractions (see Equation 4.3), $W(c_{H_2O})$ is determined. The minimization is performed with $W(c_{H_2O})$ being a first to third degree polynomial. Additionally, each minimization is executed with and without the cell pressure correction described in Section 4.3 to investigate whether there are synergies that worsen the results. The resulting RMSE are listed in Table 4.2. The cell pressure correction always reduces the RMSE in the order of 0.1 ppb. The water vapor correction leads to a further significant reduction. With the following linear $W(c_{H_2O})$ the lowest RMSE is achieved:

$$W(c_{H_2O}) = 1.0 - 0.3365 \cdot c_{H_2O} \tag{4.5}$$

Overall, by applying the cell pressure and water vapor correction, the RMSE is significantly lowered from 2.1 ppb to 0.7 ppb. It is important to note here that the water vapor correction relies on imperfect PFP measurements and also the comparison between QCLS and PFP datasets is not perfect limiting the gain of the correction (see Section 4.3). It is planned to examine the water vapor correction experimentally in the laboratory, independently of the PFP measurements. However, due to the tight schedule of the QCLS and changes in the hardware configuration, this has not been possible, yet.

RMSE in ppb		Cell pressure correction:	
		with	without
H_2O correction (polynomial degree of $W(c_{H_2O})$):	without	1.9	2.1
	linear	**0.7**	0.8
	quadratic	0.8	1.3
	cubic	1.0	1.4

Table 4.2: RMSE between PFP and QCLS N_2O measurements conducted onboard NASA's C-130 during the ACT-America 2019 campaign (Equation 4.3). The RMSE has been calculated for cell pressure (see Section 4.3) and H_2O corrected (see Section 4.4) QCLS data, as well as for unmodified data. In the course of the water vapor correction, for the underlying function of $W(c_{H_2O})$ (Equation 4.4) a linear, quadratic, and cubic polynomial is considered.

4.5 Data Quality

The quality of the QCLS N_2O data during ACT-America is assessed against PFP samples since those provide the best available in situ GHG measurements. In total, 120 PFP datapoints are used. Figure 4.6a displays PFP N_2O mole fractions against the corresponding QCLS mole fractions averaged over the PFP sampling times. The linear regression between QCLS and PFP datapoints yields a slope of 0.99 and y-intercept of 3.03, showing a strong agreement between both datasets. There is some discrepancy because the comparison between both datasets is not perfect since both instruments might describe slightly different air mixtures (see Section 4.3). A histogram of the residuals of both datasets is depicted in Figure 4.6b. The average residuum is $\mu = 0.1$ ppb with a standard deviation of $\sigma = 0.7$ ppb. The distribution appears to be Gaussian (orange curve) indicating that the residuals are driven by random processes or noise. The (near) zero μ is expected because in the course of the water vapor correction in Section 4.4, the distance between QCLS and PFP has been minimized. Kostinek et al., 2019 report a σ of 1.1 ppb for the residuals of five research flights conducted during the ACT-America field deployment in fall 2017. Reprocessing these five flights with the here presented approach results in a significantly lower σ of 0.5 ppb. It has to be noted here that for the fall 2017 campaign no primary/NOAA standards were available to cross-calibrate N_2O in the secondary standards, which were used for in-flight calibrations. Hence, the N_2O abundance in the secondary standards has been corrected so that after the calibration the offset between QCLS and PFP N_2O measurements becomes minimal. Overall, the proposed data processing approach significantly increases the compatibility of the N_2O products of both instruments.

As shown in the previous Sections 4.3 and 4.4, the QCLS N_2O retrieval is influenced by cell pressure variations during in-flight calibrations and uncertainties in the H_2O retrieval. Correcting these two error sources significantly improves the N_2O retrieval. However, there are further potential error sources. Pressure, temperature, and water vapor directly influence the

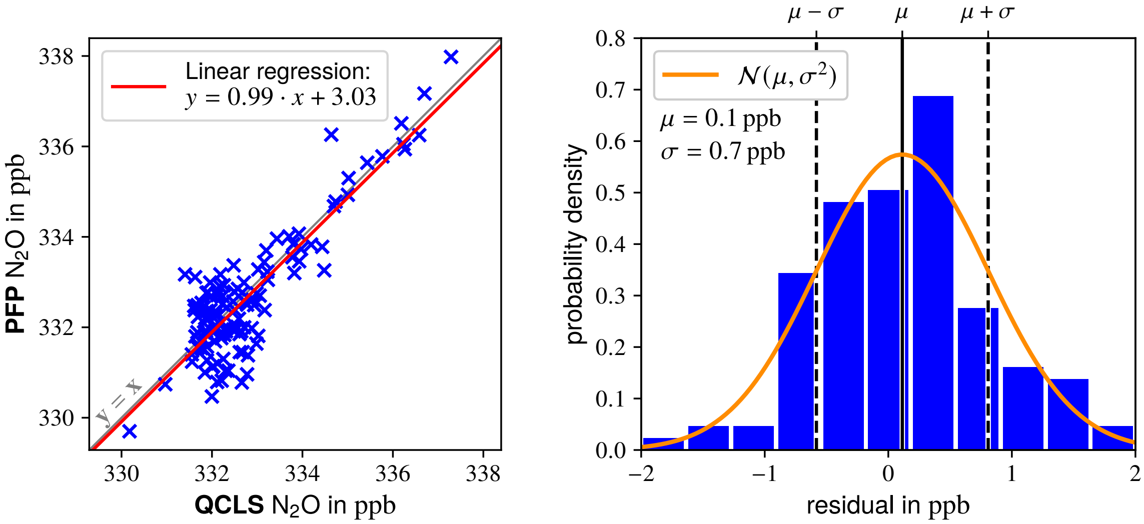

(a) QCLS vs. PFP

(b) Histogram of residuals

Figure 4.6: (a) QCLS vs. PFP N_2O dry air mole fraction measured during ACT-America 2019. (b) Histogram of the residuals between QCLS and PFP measurements. The displayed normal distribution (orange) is defined by the mean (μ = 0.1 ppb) and standard deviation (σ = 0.7 ppb) of the residuals. In total, 120 PFP N_2O samples are used.

line shapes in the absorption spectrum (see Section 2.3.2) and, thus, changes in these variables might affect the N_2O retrieval leading to uncertainties. To investigate these potential error sources, the water vapor correction approach (see Section 4.4) is employed to correct the QCLS N_2O retrieval for further variables than the H_2O retrieval. Temperature in the sample cell as well as temperature, pressure, and H_2O in the open path (see Section 3.1.1) are considered. With none of these variables a significant improvement of the N_2O retrieval could be achieved. Also linear combinations of these variables have been tested without a benefit. Thus, the QCLS N_2O retrieval is insensitive to changes of environmental conditions in the open path and to variations of temperature in the sample cell.

To sum up, a unique high resolution airborne in situ N_2O dataset over the U.S. has been produced suitable for extensive top-down studies. Frequent in-flight calibrations and calibration standards traceable to the WMO scale have enabled accurate measurements which are comparable to other instruments. By correcting the influence of cell pressure variations and uncertainties in the H_2O measurements on the N_2O retrieval, the robustness of the QCLS N_2O dataset could be increased significantly.

5 Quantifying U.S. Midwest N_2O Emissions

Parts of the text reproduced here has been published in Eckl et al. (2021) (see p. ix).

In this chapter, we quantify N_2O emissions for several flights conducted in parts of the U.S. Midwest in October 2017 and June/July 2019 with a top-down approach (**RQ1**). Unlike previous studies which have relied on observations with limited spatial coverage (e.g., Kort et al., 2008; Miller et al., 2012; Fu et al., 2017), this study uses continuous airborne in situ measurements of N_2O. By combining these observations with forward model simulations, we optimize agricultural fluxes from EDGAR4.3.2 and EDGAR5.0 (see Section 3.4.1) to quantify Midwest N_2O emissions. The employed method was already successfully applied in several CH_4 top-down studies (e.g., Barkley et al., 2017; Barkley et al., 2019a; Barkley et al., 2019b). The derived emission rates are finally compared to flux estimates of direct soil emissions produced with EDGAR and DayCent (see Section 3.4.2) (**RQ2**).

In the following, Section 5.1 describes the observations which are used for this study. The model setup and optimization strategy are depicted in Section 5.2 and 5.3, respectively. Section 5.4 provides a comparison of EDGAR and DayCent N_2O flux estimates. Next, in Section 5.5 the results of this study are presented and discussed. Finally, Section 5.6 summarizes this chapter.

5.1 Observations in Fall 2017 and Summer 2019

Continuous in situ N_2O measurements conducted with the QCLS onboard NASA's C-130 during the ACT-America fall 2017 and summer 2019 field campaigns are the data basis for this study (see Section 3.2). As the QCLS time series exhibit some data gaps due to calibration and minor instrument issues, PFP samples are merged into the continuous dataset to minimize them. N_2O plumes from surface sources are primarily found and transported in the PBL (see Section 2.1.2). Hence, to quantify U.S. Midwest emissions, N_2O measurements from transects within the PBL, above the study region are necessary. Additionally, these transects should last at least several minutes, so that a comparison between model output and observations is possible.

Ten flights have been selected that fulfill these requirements, four flights from 2017 (October) and six flights from 2019 (June/July). For each flight, the C-130 flew transects well within the PBL (at ~1000 ft above ground level (AGL)) for at least 45 min during which air above the Midwest was sampled. Figure 5.1a shows the selected transects, color-coded with the

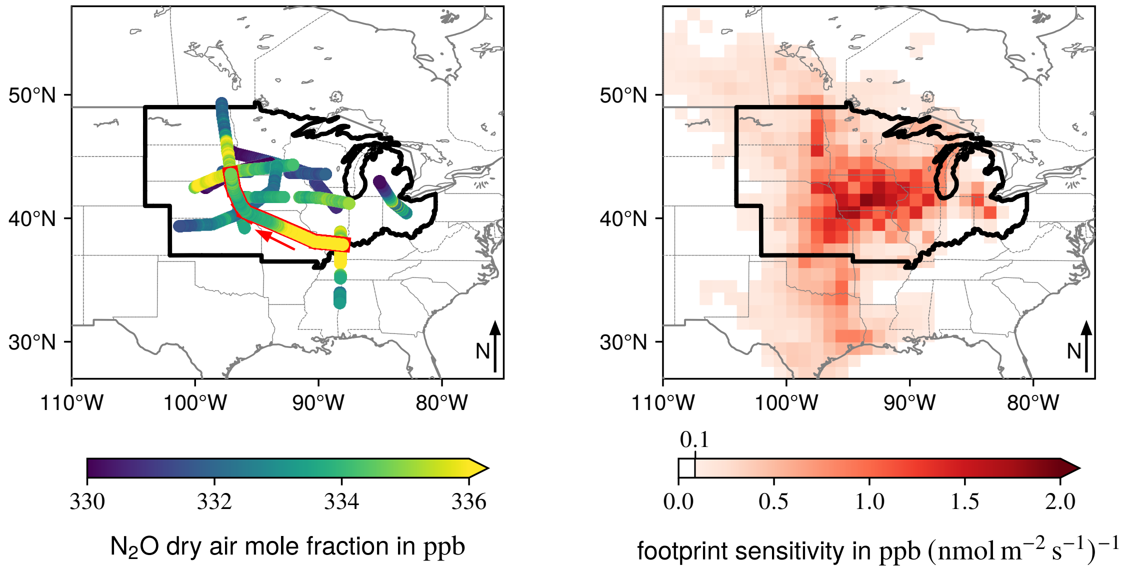

(a) Selected PBL transects

(b) PFP footprints of selected low level legs

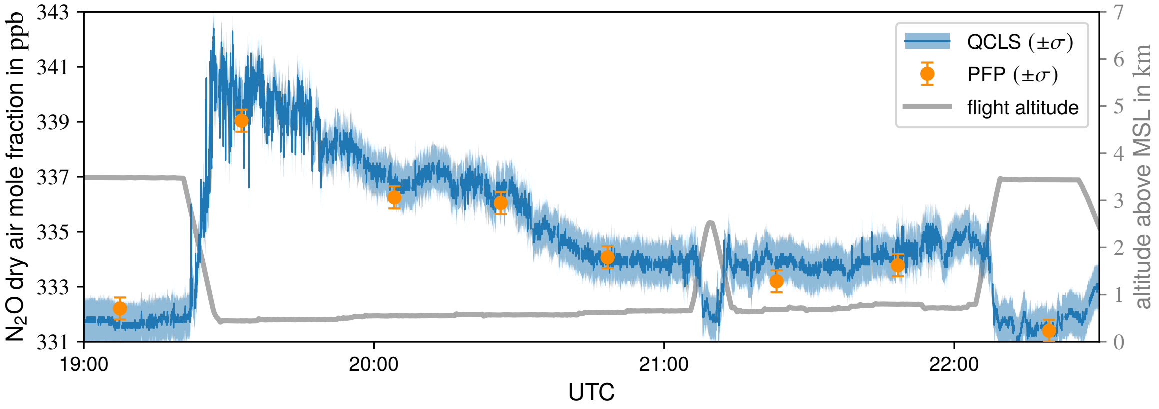

(c) Time series of 07 Jul 2019

Figure 5.1: Selected PBL transects (at ~1000 ft AGL) of the ACT-America campaigns in 2017 and 2019, color-coded with observed N$_2$O dry air mole fractions. The Midwest region used for emission estimation in the model is encircled by a thick black line. (b) Ten day HYSPLIT footprints of all PFP samples collected within the transects presented in (a). (c) Time series of N$_2$O dry air mole fraction of the flight on 07 Jul 2019 with error bars indicating ±0.8 ppb and coincident PFP measurements of N$_2$O (±0.4 ppb). The corresponding transect in (a) is encircled in red and was flown in direction of the red arrow. (Figure (a) and (c) are adapted from Eckl et al., 2021)

observed N_2O dry air mole fractions. Most of the Midwest is covered by these flights. Broad plumes spanning up to hundreds of kilometers have been caught. For example, during the transect on July 07, 2019 (see Figure 5.1c) extraordinary N_2O mole fractions up to 341 ppb have been measured while crossing Kentucky and nearly whole Missouri from east to west. HYSPLIT footprints quantitatively describe how surface emissions affect measurements (see Section 3.3.2) and help to constrain the region which is investigated within this study. The summed ten day footprints of all PFPs which were collected during the PBL transects are displayed in Figure 5.1b. While the origin of some measured air is south of the Midwest, the predominant portion originates from the study region, mainly from the center. Thus, this dataset is well qualified for the intended study. We are not aware of comparable continuous N_2O measurements spanning most of the Midwest across two seasons, highlighting the unique opportunity to quantify Midwest emissions with these data.

5.2 Model Data

The goal is to model the observed N_2O time series which were presented in Section 5.1. Therefore, WRF-Chem (see Section 3.3.1) is used to propagate N_2O enhancements emitted from emission inventories through the atmosphere. Each transect is simulated twice with different soil N_2O fluxes obtained from EDGAR4.3.2/EDGAR2 and EDGAR5.0/EDGAR2 (anthropogenic emissions, i.e. agricultural E_{AGR} and non-agricultural E_{nonAGR}, from v4.3.2/v5.0 and natural emissions E_N from v2; see Section 3.4.1). Initial N_2O concentrations and the inflow at the boundaries of the model domain are set to zero. Thus, we simulate only enhancements caused by emissions within the model domain during the time of the simulation. This additionally implies the assumption that all relevant N_2O sources are included in E_{AGR}, E_{nonAGR}, and E_N. Due to N_2O's long atmospheric lifetime of over 100 yr (see Section 2.2), we can neglect all chemically induced concentration changes in our simulations and, hence, treat N_2O as a passive tracer. Each simulation is performed with three different meteorological initial and boundary conditions: First, the 5th generation atmospheric reanalysis data (ERA5, 2017; Hersbach et al., 2020). It is a product of the European Centre for Medium-Range Weather Forecasts (ECMWF) and provides hourly global data on a 30 km horizontal grid. Second, the Global Data Assimilation System Final analysis (GDAS-FNL, 2015) of the National Centers for Environmental Prediction (NCEP). It also exhibits a global coverage with a horizontal resolution of 0.25° and is prepared every six hours. Third, NCEP's North American Regional Reanalysis (NARR, 2005). NARR covers North America with a horizontal resolution of 32 km and a temporal resolution of 3 h. As in Barkley et al. (2019a), we use these different simulations to estimate model transport errors (Díaz-Isaac et al., 2018) (see Section 5.3.2). The employed model physics configuration is summarized in Table 5.1.

The model domain consists of an outer (D01) and inner domain (D02) with a horizontal resolution of 15 km × 15 km and 3 km × 3 km, respectively. Figure 5.2 demonstrates the setup. The outer domain, centered over the Midwest, covers nearly the whole continental U.S., northern Mexico and southern Canada, whereas the extent and position of the inner domain is separately chosen for each flight so that the PBL transects are spaciously encapsulated. Figure 5.2 gives

Physical process:	**Used scheme:**	**Reference:**
Cloud microphysics	Thompson	Thompson et al. (2008)
Longwave radiation	RRTMG	Iacono et al. (2008)
Shortwave radiation	RRTMG	Iacono et al. (2008)
Cumulus parameterization	Kain-Fritsch (just D01)	Kain (2004)
PBL	MYNN 2.5 level TKE	Nakanishi and Niino (2006)
Land surface	Noah land-surface model	Chen and Dudhia (2001)
Surface layer	MYNN	Nakanishi and Niino (2006)

Table 5.1: Employed WRF physics configuration. For not listed physical processes, the WRF defaults were used. The cumulus parameterization was only applied in the outer domain (D01) and switched off in the inner domain. Detailed explanations of each scheme can be found in the given references and in the WRF user guide (https://www2.mmm.ucar.edu/wrf/users/).

an example for the setup of D02 for the flight conducted on Oct 10, 2017. Vertically, both domains consist of 50 terrain-following layers, extending up to a pressure level of 100 hPa (~16 km above MSL). From the surface up to roughly 800 hPa (~2 km above MSL) the vertical layers are denser to optimally resolve mainly the PBL (see Section 2.1.2), where the observed N_2O plumes are located. Two-way nesting enables the propagation of information between both domains. Output is generated every 5 min.

To ensure the optimal meteorological model solution and with it the optimal N_2O transport the WRF Four-Dimensional Data Assimilation (FDDA) (Deng et al., 2009) feature is applied. FDDA allows for observation and analysis nudging. In regular intervals temperature, horizontal wind, and water vapor fields in the model simulation are nudged towards the “truth” (observations) and the “best guess of the state of the atmosphere” (analysis fields) to reduce model errors. Here, the same nudging strategy as in Rogers et al. (2013) and Barkley et al. (2017) is used. While observation as well as analysis nudging is employed in the outer domain, in the inner domain only observations are nudged. Meteorological observations are obtained from global datasets provided by NCEP (NCEP, 2004a, 2004b). A detailed listing of the employed FDDA configuration and remaining WRF settings is provided in Section A.4 in the appendix.

5.3 Model Optimization Approach (Method 1)

The goal of the model optimization in this study is to minimize the difference between the observational and model data by modifying the N_2O surface fluxes which are employed in the course of the simulations, thus quantifying Midwest emissions. Therefore, we use an approach similar to the optimization described in Barkley et al. (2017). The underlying methodology is presented in Section 5.3.1, followed by a description of the uncertainty assessment in Section 5.3.2.

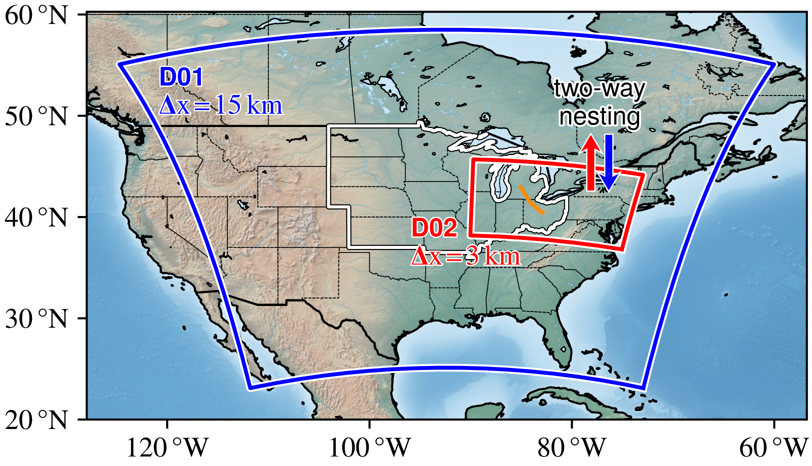

Figure 5.2: WRF domain setup. The outer domain (D01, blue) is the same for each simulation. The inner domain (D02, red) is separately chosen for each model run. The displayed D02 corresponds to the simulation performed for the flight on Oct 10, 2017. The low level leg of the flight is indicated in orange. The U.S. Midwest is encircled in white. Two-way nesting enables the propagation of information between both domains.

5.3.1 Methodology

The output of the model simulations is sampled along each research flight by extracting data at the grid points which are temporally and spatially closest to the measurements. This delivers modeled N_2O enhancements along the transects c_{mod}^{enh} which are caused be the incorporated emission inventories. To be able to directly compare them to the observed absolute N_2O dry air mole fractions c_{obs}, we first calculate the observed enhancements c_{obs}^{enh} by subtracting a background mole fraction c_{obs}^{bg} from c_{obs}:

$$c_{obs}^{enh} = c_{obs} - c_{obs}^{bg} \tag{5.1}$$

We derive one background for each campaign by taking the 2nd percentile of all PBL transects of the entire campaign (see Figure 5.3). This results in 329.9 ppb and 331.3 ppb for the fall 2017 and summer 2019 field deployment, respectively. The background is defined campaign-wise rather than transect-wise because during some transects we were not able to measure background mole fractions as we started a transect within a plume and did not exit the plume inside of the PBL (see Figure 5.1c).

We then compare modeled N_2O enhancements from our prior emissions ($E_{AGR}+E_{nonAGR}+E_N$) to the observed enhancements. Differences between both are minimized for each flight by scaling agricultural emissions E_{AGR} with a factor F_{AGR}, thus quantifying emissions. This process relies on the assumption that the discrepancy between model and observation is primarily driven by errors in E_{AGR}. Since agricultural emissions are the dominant N_2O source in our flights, we assume that errors in E_{nonAGR} and E_N are inconsequential to the overall solution. The complexity of soil N_2O emissions suggests that E_{AGR} exhibits a much higher uncertainty than

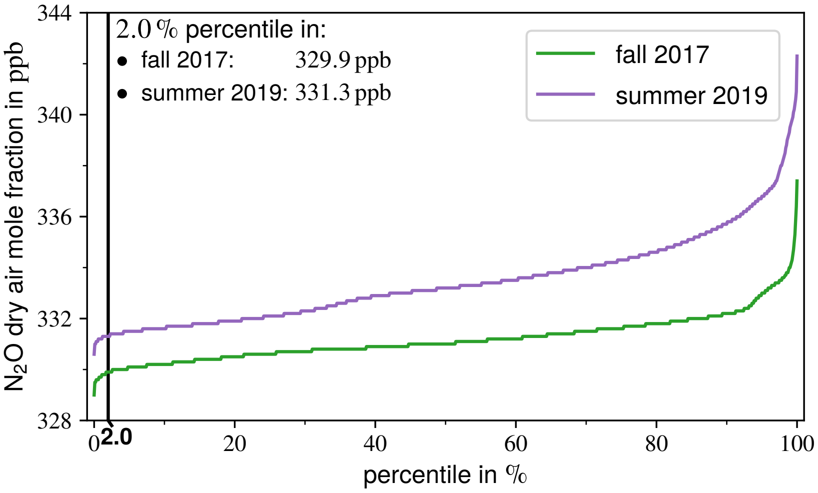

Figure 5.3: Percentiles of QCLS N_2O measurements conducted during the ACT-America fall 2017 and summer 2019 field campaigns. Low level leg data (at ~1000 ft AGL) of all conducted flights were merged and the corresponding percentiles were calculated. The 2^{nd} percentile defines the observed N_2O background mole fraction. (Figure adapted from Eckl et al., 2021)

other sources (see Section 2.2.2 and Butterbach-Bahl et al., 2013), supporting the presented approach.

As an equation, this optimization technique is described by calculating F_{AGR} through the minimization of the following cost function:

$$J(F_{AGR}) = |A_{obs} - \underbrace{(F_{AGR} \cdot A_{AGR} + A_{nonAGR} + A_N)}_{=A_{mod}(F_{AGR})}| \tag{5.2}$$

A_{obs} and A_{mod} is the time integral along a transect of observed and modeled enhancements, respectively, and are calculated via:

$$A_{mod/obs} = \int_{t_0}^{t_{end}} \mathrm{d}t \, c_{mod/obs}^{enh} \tag{5.3}$$

Here, t_0 denotes the start time and t_{end} the end time of the transect. A_{mod} consists of an agricultural portion A_{AGR} scaleable with F_{AGR}, a non-agricultural anthropogenic portion A_{nonAGR}, and a natural portion A_N. The integrals A_{AGR}, A_{nonAGR}, and A_N are calculated analogously to A_{obs} and A_{mod} following Equation 5.3. We compare integrals rather than enhancements because we are interested in the amount of N_2O emitted to the atmosphere. Neither the model transport nor the inventory is perfect and even small uncertainties in either of them could cause a shift or deformation in the alignment of the modeled plume relative to the observed plume. By minimizing the difference in the total N_2O enhancements rather than the point-by-point absolute error, we preserve the capability to solve for total N_2O emissions even when the modeled and observed plumes do not align. Overall, as all components of the cost function are scalars,

$J(F_{AGR})$ is minimal when equal to zero resulting in:

$$F_{AGR} = \frac{A_{obs} - A_{nonAGR} - A_N}{A_{AGR}} \tag{5.4}$$

However, a such derived agricultural scaling factor F_{AGR} is determined by enhancement integrals and, hence, might not be directly relatable to the gridded surface fluxes E_{AGR} if there is a nonlinear relationship between emissions and atmospheric N_2O enhancements. To derive the relationship between A_{AGR} and E_{AGR} we simulate each of the ten flights with a E_{AGR} multiplied by 10, 20, and 30 (F^E_{AGR}) and compare these factors with the resulting magnitude of enlargement in A_{AGR} (i.e., F_{AGR}). A linear regression between F^E_{AGR} and F_{AGR} exhibits negligible residuals and a slope and y-intercept which differs insignificantly from one and zero, respectively, proving the equivalence of F^E_{AGR} and F_{AGR} (see Table 5.2). Thus, due to the linearity between A_{AGR} and E_{AGR}, a F_{AGR} derived with Equation 5.4 denotes a F_{AGR}-folded E_{AGR}.

EDGAR version:	Slope – 1.0	y-intercept	Residual	$R - 1.0$
v4.3.2	-0.05×10^{-3}	-0.47×10^{-3}	0.02×10^{-3}	-0.02×10^{-7}
v5.0	1.28×10^{-3}	-1.26×10^{-3}	3.39×10^{-3}	-3.59×10^{-7}

Table 5.2: Results of a linear regression between F^E_{AGR} and F_{AGR} and their correlation R. Each of the ten flights is simulated with E_{AGR} multiplied by 10, 20, and 30 (F^E_{AGR}). F_{AGR} describes the corresponding magnitude of enlargement in A_{AGR}. The regression is performed via a least squares polynomial fit. The residual is the squared Euclidean 2-norm. (Table adapted from Eckl et al., 2021)

5.3.2 Uncertainty Assessment

We adopted the method of Barkley et al. (2019a) to assess uncertainties in our solutions. F_{AGR} is affected by uncertainties in the following variables:

1. Observed background mole fraction c^{bg}_{obs}
2. Integral of anthropogenic non-agricultural emissions A_{nonAGR}
3. Integral of natural emissions A_N
4. Model transport
5. Model wind speed and PBL height
6. Spatial distribution in EDGAR emissions

We quantify the influence of uncertainties 1 to 4 with a Monte Carlo approach. For each flight we repeat the optimization 10 000 times with a perturbed background mole fraction, A_{nonAGR}, and A_N. For the background we add a normal random number with $\mu = 0$ ppb and $\sigma = \pm 0.5$ ppb for 2017 and $\sigma = \pm 0.9$ ppb for 2019 to the observation derived value. These uncertainties are the standard deviation of the 2nd percentiles of all PBL transects of a whole campaign. Actually, the background uncertainties are dominated by large scale circulations and long term variability, such as seasons, and are probably not normally distributed. However, too few observations prevent the determination of the actual distribution. Here, we assume that a normal distribution is the best first order guess. A_{nonAGR} and A_N are independently multiplied by a factor drawn from a normal distribution with $\mu = 1.0$ and $\sigma = \pm 0.21$ and $\sigma = \pm 0.42$, respectively. Janssens-Maenhout et al. (2019) states the relative 1σ uncertainty of total EDGAR4.3.2 N_2O emissions in the U.S. to be 21 %. No sector-specific uncertainty is provided. Hence, we use this value as a rough estimate for the uncertainty of only non-agricultural emissions. As we could not find uncertainty estimates for EDGAR5.0 and EDGAR2 we assume them to be the same and twice as in EDGAR4.3.2, respectively. For days with large agricultural scaling factors, F_{AGR} the uncertainties of A_{nonAGR} and A_N affect the results only marginally. Hence, this uncertainty analysis is implicitly based on the assumption that E_{nonAGR} and E_N are well represented in the inventories compared to E_{AGR}. Following Butterbach-Bahl et al. (2013), mainly N_2O emissions from soils account for the uncertainty in N_2O budgets on regional and national scales, which supports our assumption. To account for the model transport error, we randomly select one of the three model runs with different meteorological initial and boundary conditions, creating variability in the plume shape. The resulting spread in F_{AGR} is used as its uncertainty.

The modeled wind speed and PBL height uncertainty (source 5) cannot be covered by the Monte Carlo simulation. The higher these variables, the more diluted the atmospheric N_2O enhancements. Thus, errors in the modeled wind speed and PBL height cause lower or higher simulated enhancements, thus producing biases. Following Barkley et al. (2017) we correct for those biases by applying a scaling factor based on the differences between the modeled and observed wind speed and PBL height:

$$c^{*}_{mod} = c^{enh}_{mod} \cdot \frac{U_{mod} \cdot Z_{mod}}{U_{obs} \cdot Z_{obs}} \tag{5.5}$$

Here, c^{enh}_{mod} is the modeled N_2O enhancement along a transect and c^{*}_{mod} the corresponding bias corrected one, which is further used for the model optimization. U_{mod}/U_{obs} is the modeled/observed wind speed averaged along the transect. For the observed PBL height Z_{obs} we use in situ soundings conducted with the C-130 at the beginning, the end, and during PBL transects. For each flown sounding the PBL height is determined as the lowest (regarding altitude) significant maximum of the observed virtual potential temperature (see Appendix A.2) lapse rate profile (Dai et al., 2014). The average of all determined PBL heights defines Z_{obs} of the transect. For the modeled PBL height Z_{mod} we use the modeled profiles at the grid point closest the the flown soundings and perform the same calculations as for Z_{obs}. However, there is a caveat here. We correct for model errors at the position of the aircraft at a certain time but we are simulating large areas for several days. The model error varies over space and time, thus, limiting the benefit of the posed bias correction. Table 5.3 summarizes the effect of the bias correction. On average, the modeled wind speed and PBL height is 8 % and 3 % higher than the observations, respectively. As shown in the following Section 5.5, the impact of this correction on our results is insignificant.

Our final source of uncertainty relates to errors in the spatial distribution of the N_2O fluxes in the prior inventory and is difficult to quantify. However, the mapping of emissions in EDGAR is based on several high-resolution proxy data sets (Janssens-Maenhout et al., 2019). For this

Day:	U_{obs} in m s^{-1}	U_{mod} in m s^{-1}	$\frac{U_{mod}}{U_{obs}}$	Z_{obs} in m	Z_{mod} in m	$\frac{Z_{obs}}{Z_{mod}}$	$\frac{U_{mod} \cdot Z_{mod}}{U_{obs} \cdot Z_{obs}}$
10 Oct 2017	3.5	5.2	1.5	1067	1134	1.1	1.6
		3.0	0.9		1319	1.2	1.1
		3.7	1.1		1325	1.2	1.3
18 Oct 2017	10.6	12.9	1.2	1417	1106	0.8	0.9
		12.9	1.2		1307	0.9	1.1
		12.8	1.2		1116	0.8	1.0
20 Oct 2017	13.1	17.9	1.4	1273	963	0.8	1.0
		17.3	1.3		1013	0.8	1.1
		17.2	1.3		1084	0.9	1.1
24 Oct 2017	15.7	15.9	1.0	1603	1565	1.0	1.0
		15.9	1.0		1716	1.1	1.1
		15.5	1.0		1668	1.0	1.0
20 Jun 2019	7.1	9.1	1.3	1480	1024	0.7	0.9
		9.0	1.3		1188	0.8	1.0
		8.4	1.2		1094	0.7	0.9
04 Jul 2019	4.9	5.1	1.0	1684	1784	1.1	1.1
		4.3	0.9		1944	1.2	1.0
		3.5	0.7		2080	1.2	0.9
07 Jul 2019	4.3	4.6	1.1	1889	2417	1.3	1.4
		3.7	0.9		2420	1.3	1.1
		3.5	0.8		2246	1.2	1.0
08 Jul 2019	9.0	10.2	1.1	1718	1955	1.1	1.3
		10.1	1.1		2055	1.2	1.3
		9.3	1.0		1994	1.2	1.2
10 Jul 2019	10.4	10.2	1.0	1767	1956	1.1	1.1
		10.9	1.0		1893	1.1	1.1
		10.2	1.0		2014	1.1	1.1
11 Jul 2019	6.7	7.3	1.1	1659	1861	1.1	1.2
		5.8	0.9		1638	1.0	0.9
		6.6	1.0		1608	1.0	1.0

Table 5.3: Modeled vs. observed average wind speed (U_{mod}/U_{obs}) and PBL height (Z_{mod}/Z_{obs}) during PBL transects. More detailed descriptions of U and Z are provided in Section 5.3.2. The listed factors describe the bias correction due to discrepancies between modeled and observed values (see Equation 5.5). In the model columns the first value belongs to the ERA5, the second to the GDAS-FNL, and the third to the NARR simulation. (Table adopted from Eckl et al., 2021)

reason, we assume its spatial errors to be small. Given the insignificant difference between modeled and observed wind speeds and PBL heights, the good agreement between modeled and measured plume structures support this assumption. Furthermore, since we quantify large areas and not point sources, slight misplacement in the inventory would only marginally affect our results. At the same time, missing or strongly misplaced fluxes would produce errors that are not considered in this study.

5.4 Emission Inventory Comparison

The simulations in this study incorporate EDGAR N_2O fluxes (see Section 5.2). EDGAR is a *Tier 1–2* inventory providing sector-specific fluxes with a global coverage (see Section 3.4.1). However, the available DayCent products provide *Tier 3* estimates of Midwest soil N_2O emissions and are supposed to be a more sophisticated than EDGAR (see Section 3.4.2). The reason for using EDGAR rather than DayCent in our simulations is that our DayCent products cover only the Midwest. This would introduce underestimations since we have sampled mainly but no exclusively Midwest air during the research flights (see Section 5.1). Additionally, DayCent estimates are only available for 2011–2015. Thus, by using them for the simulations we would give up the advantage of DayCent providing time- and location-specific estimates. EDGAR uses a more climatological average emissions dataset, which is better suited for the intended study.

The spatial distribution of agricultural Midwest N_2O emissions in EDGAR and DayCent is similar. Figure 5.4 shows prior July N_2O emissions in the outermost model domain from (a) agricultural (E_{AGR}) and (b) non-agricultural EDGAR5.0 sources (E_{nonAGR}). Compared to EDGAR4.3.2 no significant differences in the spatial distribution of emissions is seen, both versions just differ in the strength of the surface fluxes. Agricultural emissions are concentrated in the Midwest, coinciding with the densely farmed Corn Belt. Non-agricultural emissions emerge mainly from urban areas while emissions from rural areas are low. Figure 5.4c shows natural EDGAR2 emissions (E_N) which are used to supplement the anthropogenic EDGAR4.3.2 and EDGAR5.0 emissions. E_N is uniformly distributed within the model domain and slightly increases towards the Gulf Coast. Overall, the Midwest is a hotspot of N_2O emissions because of its intensive agriculture.
DayCent estimates of direct soil N_2O emissions in July 2015 are displayed in Figure 5.4d. Similar to EDGAR, the Midwest is a prominent source of N_2O. We are not able to perform a detailed comparison of the spatial distributions in EDGAR and DayCent since both do not cover the same set of sources. However, in terms of the overall magnitude, DayCent estimates much higher surface fluxes compared to EDGAR, despite containing fewer sources (gridded total agricultural DayCent emissions are not available; see Section 3.4.2).

Monthly Midwest N_2O emissions in EDGAR are lower than DayCent estimates. Figure 5.5 displays the monthly evolution of E_{AGR}, E_{nonAGR}, and E_N averaged over the Midwest. Both EDGAR versions have an annual average E_{AGR} of approximately $0.10\,\mathrm{nmol\,m^{-2}\,s^{-1}}$. However, unlike EDGAR5.0, EDGAR4.3.2 exhibits a seasonal cycle ranging from $0.05\,\mathrm{nmol\,m^{-2}\,s^{-1}}$ in winter up to $0.24\,\mathrm{nmol\,m^{-2}\,s^{-1}}$ in spring. In spring, when most N-fertilizer is applied, the

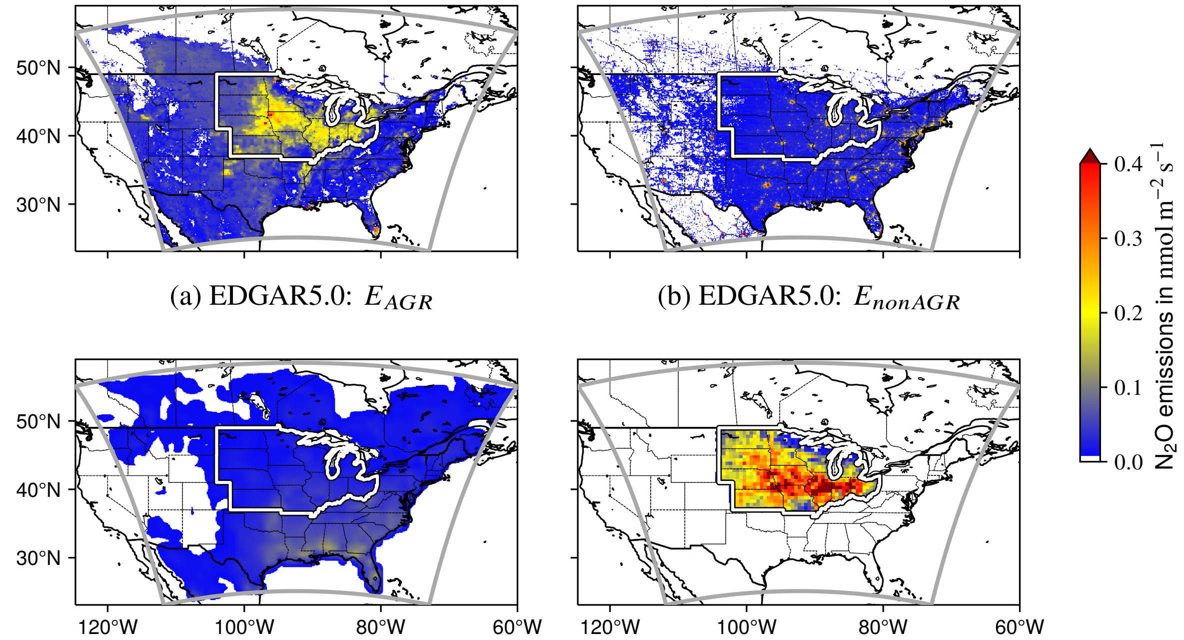

(a) EDGAR5.0: E_{AGR}

(b) EDGAR5.0: E_{nonAGR}

(c) EDGAR2: E_N

(d) DayCent

Figure 5.4: Gridded Midwest N_2O emissions in EDGAR and estimated with DayCent. (a) EDGAR5.0 agricultural (E_{AGR}) and (b) non-agricultural (E_{nonAGR}) N_2O emissions within the model domain (gray box) in July 2015. The U.S. Midwest is encircled in white. (c) EDGAR2 natural N_2O emissions (E_N) in 1990. (d) Direct soil N_2O emissions in the U.S. Midwest in July 2015 estimated with DayCent. (Panel (d) adapted from Eckl et al., 2021)

amount peaks, followed by a plateau during summer at 0.09 nmol m^{-2} s^{-1}. The harvest season in fall features a local peak at 0.11 nmol m^{-2} s^{-1}. A future update of EDGAR5.0 will contain a seasonal cycle for some crop related emissions (Crippa et al., 2020). E_{nonAGR} shows no significant change over the year and is on average 0.04 nmol m^{-2} s^{-1} in both versions. Natural emissions account for 0.02 nmol m^{-2} s^{-1} per month.

From 2011 to 2015 DayCent emissions in the Midwest range between 0.23–0.35 nmol m^{-2} s^{-1}, 0.12–0.21 nmol m^{-2} s^{-1}, and 0.06–0.08 nmol m^{-2} s^{-1} in June, July, and October, respectively (see Figure 5.5 and Table 5.4). June and July emissions are significantly larger than in EDGAR, despite excluding manure management, indirect soil, and agricultural waste burning emissions. DayCent's October emissions are within the magnitude of agricultural EDGAR emissions.

We estimate total agricultural Midwest emissions from 2011 to 2015 by combining DayCent direct soil emissions and the EPA GHG inventory (see Section 3.4.2), resulting in 0.32–0.48 nmol m^{-2} s^{-1}, 0.16–0.30 nmol m^{-2} s^{-1}, and 0.08–0.11 nmol m^{-2} s^{-1} in June, July, and October, respectively (see Table 5.4). Direct DayCent emissions account for 70–75 % of total agricultural Midwest emissions. Roughly 10 % originate from direct emissions from minor crops such as vegetables that are not covered by DayCent. Indirect emissions and fluxes from manure management are responsible for around 13 % and 5 %, respectively. The contribution of agricultural waste burning is negligible.

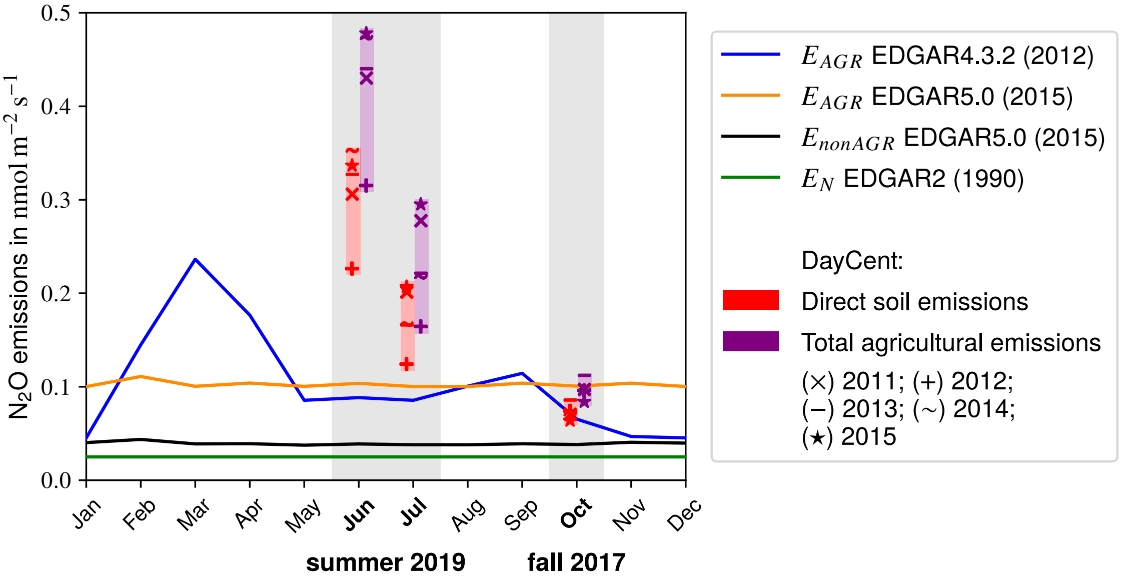

Figure 5.5: Monthly Midwest N$_2$O emissions in EDGAR and estimated with DayCent. EDGAR emissions are split into agricultural E_{AGR}, non-agricultural E_{nonAGR}, and natural fluxes E_N (see Section 3.4.1). E_{nonAGR} in EDGAR4.3.2 is almost identical to EDGAR5.0 and, hence, not drawn here. Total agricultural DayCent emissions are estimated utilizing the EPA GHG inventory (see Section 3.4.2). (Figure adapted from Eckl et al., 2021)

Overall, in June/July total agricultural Midwest emissions are on average over four/two times larger than EDGAR's E_{AGR}. The 2012 emissions are significantly lower than in the other years causing the large range across years in the summer months. During this year, the most extensive drought since the 1930s occurred across a large swath of the U.S., including most of the Midwest, which lead to widespread harvest failure (NOAA/NCEI, 2020). This event might explain the low values and indicates that during an average climatological year DayCent emissions are at the upper end of the range. Furthermore, in contrast to EDGAR4.3.2 which states constant emissions in June and July, DayCent emissions are much higher in June than in July. Sweeney et al. (2015) derived annual N$_2$O climatologies at Midwest sites from NOAA/ESRL Aircraft Network measurements and found highest N$_2$O mole fractions in June, which is consistent with our DayCent estimates.

5.5 Quantifying Agricultural Emissions

In the following, an example of the model optimization process for Oct 10, 2017 is presented in Section 5.5.1. Optimization results for the remaining days are provided in the appendix (see Figure A.1 and A.2). The results of optimizing EDGAR for the ten investigated research flights is presented in Section 5.5.2 and are finally discussed in Section 5.5.3.

Emission sectors:	**June:**	**July:**	**October:**
Direct DayCent emissions:	0.23–0.35	0.12–0.21	0.06–0.08
Direct *Tier 1* emissions:	0.04–0.05	0.02–0.03	~0.01
Indirect emissions:	0.04–0.06	0.02–0.04	~0.01
Manure Management:	~0.02	~0.01	0.0–0.1
Agricultural waste burning:	~0.0	~0.0	~0.0
Total:	*0.32–0.48*	*0.16–0.30*	*0.08–0.11*

N_2O emissions averaged over the U.S. Midwest region in nmol m^{-2} s^{-1} in 2011–2015

Table 5.4: Total agricultural N_2O emissions in the U.S. Midwest in 2011–2015 based on DayCent estimates and the EPA GHG inventory (EPA, 2020). Direct *Tier 1* emissions are N_2O fluxes from minor crops such as vegetables that are not covered by the DayCent estimates of direct emissions. The calculation of the different fluxes is described in Section 3.4.2. Ranges are the minimum and maximum of the monthly estimates in 2011–2015.

5.5.1 Case Study: 10 October 2017

On Oct 10, 2017 a PBL transect was flown in the eastern part of the Midwest, south of lake Erie (see Figure 5.2 and 5.6b). The observed N_2O enhancement time series during the PBL transect is depicted in Figure 5.6a. Around 12:00 local standard time (LST) the C-130 descended from roughly 7 km AGL to approximately 300 m AGL and stayed there for over 45 min. When the C-130 dived from the free troposphere into the PBL at around 12:15 LST, N_2O enhancements of ~3 ppb were observed. During the transect, peak enhancements up to 7 ppb were measured. To the end of the transect, the signal flattened out. The below background values at the beginning of the time series occurred prior to the PBL transect in the free troposphere. Free tropospheric air might have a different history and hence different background which can lead to negative values if we subtract the PBL background. During the transect, two flask samples were collected. Their summed 10-day HYSPLIT footprints are shown in Figure 5.6b constraining the region which is quantified in the course of the optimization. Emissions originate mostly from Ohio and partly from Michigan and Indiana. There, EDGAR as well as DayCent estimates large fluxes from soils (see Figure 5.4) indicating that the observed plume is dominated by agricultural emissions. Simulating N_2O enhancements along the transect with EDGAR5.0 (plus natural EDGAR2 emissions) and NARR meteorological initial and boundary conditions confirms that agricultural emissions dominate (see Figure 5.6a). However, there is a large discrepancy between model and observations. Only enhancements up to 1 ppb are simulated. By applying a scaling factor F_{AGR} of 8.3 the model is able to reproduce our measurements. The calculation of the uncertainties is presented below. Maps of simulated total N_2O enhancements (emitted from $E_{AGR} + E_{nonAGR} + E_N$) at approximately the transect altitude (i.e., 300 m AGL) are provided in Figure 5.6c and 5.6d for prior and optimized agricultural emissions, respectively. Additionally, the PBL transect is shown, color-coded with the observed enhancements. For the non-optimized

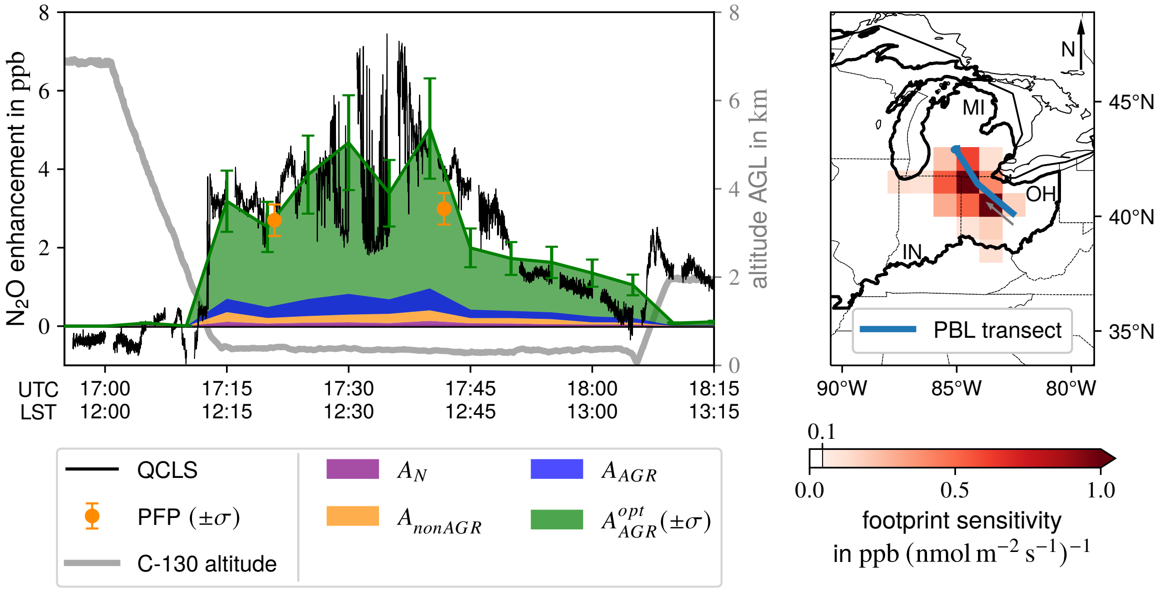

(a) N_2O enhancements along PBL transect (b) HYSPLIT footprints of PFPs

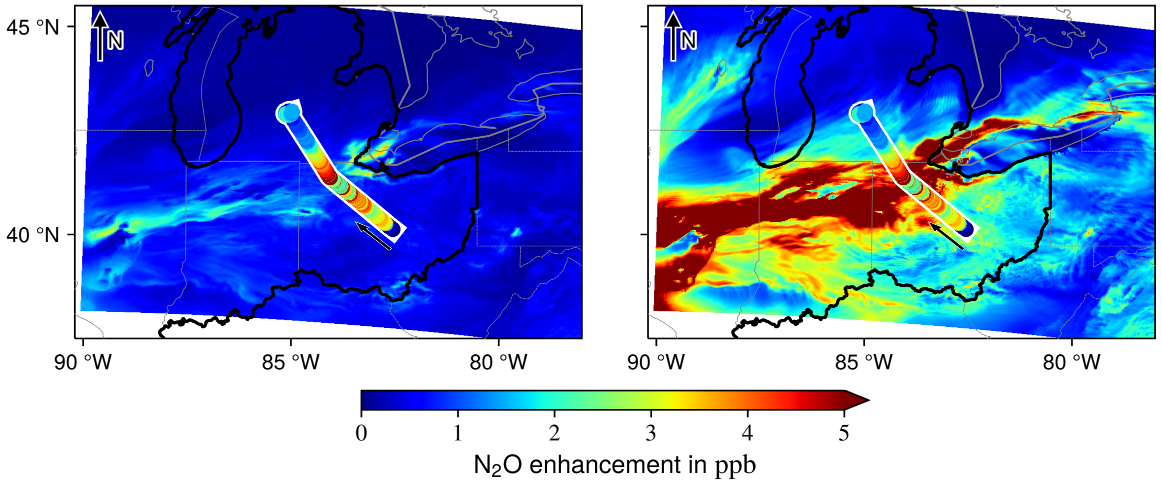

(c) $F_{AGR} = 1.0$ (prior) (d) $F_{AGR} = 8.3$ (optimized)

Figure 5.6: Example model optimization for 10 Oct 2017 with EDGAR5.0 (plus EDGAR2 E_N) and NARR meteorological initial and boundary conditions. (a) Prior ($F_{AGR} = 1.0$) and optimized ($F_{AGR} = 8.3$) simulated N_2O enhancements along the flight track together with observed enhancements. Modeled enhancements consist of an agricultural A_{AGR} (or optimized agricultural A^{opt}_{AGR}), non-agricultural A_{nonAGR}, and natural portion A_N. The PFP uncertainty is $\sigma = \pm 0.4$ ppb. The time is given in UTC and LST. (b) Summed 10-day HYSPLIT footprint of the two PFPs collected during the PBL transect. The thick black line encircles the U.S. Midwest. The states Ohio (OH), Michigan (MI), and Indiana (IN) are labeled. (c) Map of total, non-optimized simulated N_2O enhancements (emitted from $E_{AGR} + E_{nonAGR} + E_N$) at 300 m AGL and at 12:30 LST. The PBL transect is color-coded with the observed N_2O enhancements. (d) As (c) but with optimized E_{AGR}. (Panels (a) and (d) adapted from Eckl et al., 2021)

case, the significant underestimation of the observations by the simulations is again prominent. After the optimization, there is a good agreement between measurements and model. This good agreement supports the assumption that errors in EDGAR's spatial distribution are small and suggests that the atmospheric transport is well simulated.

Repeating the optimization 10 000 times with randomly perturbed error sources (see Section 5.3.2) delivers a distribution of agricultural scaling factors F_{AGR} for this particular transect. The outcome of this Monte Carlo simulation is shown in Figure 5.7. The average F_{AGR} is $\mu = 6.8$ with a standard deviation of $\sigma = 2.3$ and, hence, smaller than considering only the above simulation, but still significant. It must be noted that the produced distribution is not normal, but consists of two normal distributions with scaling factor averages of approximately four and eight. The model transport error is responsible for this. It is considered by picking randomly one of three simulations with different meteorological initial and boundary conditions. However, especially in complex meteorological situations three samples are not enough to account for this error. Thus, non-normal distributions may occur if the transport differs strongly among the three simulations. On 10 Oct 2017, NARR and GDAS-FNL simulations produce the normal distribution on the right hand side (green) and ERA5 simulations are responsible for the normal distribution on the left hand side (blue). A comparison between wind measurements onboard the C-130 and the three model runs indicates that the wind speed in the ERA5 simulations exhibits much larger errors (50 %) than in the NARR or GDAS-FNL simulations which

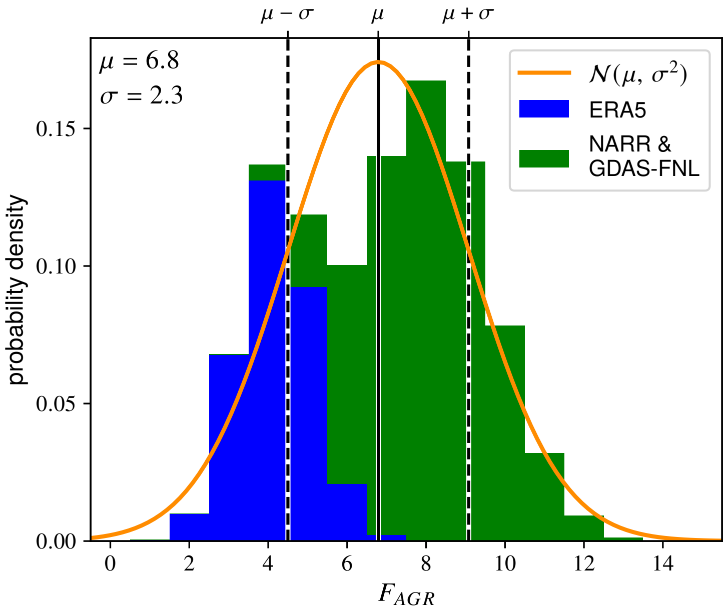

Figure 5.7: Histogram of the Monte Carlo simulation for EDGAR5.0 for 10 Oct 2017. Following Section 5.3.2, 10 000 model optimizations are performed where potential error sources are randomly perturbed. The arithmetic mean (μ) of the resulting distribution is the overall agricultural scaling factor F_{AGR} for this transect and the standard deviation (σ) is the uncertainty. The corresponding normal distribution ($\mathcal{N}(\mu, \sigma^2)$) is displayed in orange. It is distinguished between optimizations based on ERA5 and NARR/GDAS-FNL simulations.

are close to the observations (errors in the order of 10 %) (see Table 5.3). This might explain the final non-normal distribution, which is only found for this particular flight. Monte Carlo simulations for the nine remaining transects are characterized by normal distributed F_{AGR}.

5.5.2 Results

The optimization presented in the previous Section 5.5.1 is executed for all ten research flights and for both EDGAR versions. Figure 5.8 shows the resulting averages and standard deviations for the agricultural scaling factors F_{AGR} of the Monte Carlo simulations. As both inventories have a comparable spatial distribution, factors vary due to differences in total emissions. EDGAR4.3.2 scaling factors are considerably higher for October 2017 and slightly higher for June/July 2019 than EDGAR5.0. In 2017, the average F_{AGR} is 6.3 ± 4.6 for EDGAR4.3.2 and 3.5 ± 2.7 for EDGAR5.0. Scaling factors for 2019 are significantly higher than for 2017 reaching values of over 20 and are on average 11.4 ± 6.6 (EDGAR4.3.2) and 9.9 ± 5.7 (EDGAR5.0). Figure 5.8 also shows scaling factors which are bias corrected for differences between simulated and observed wind speeds and PBL heights (see Equation 5.5). According to Table 5.3, the

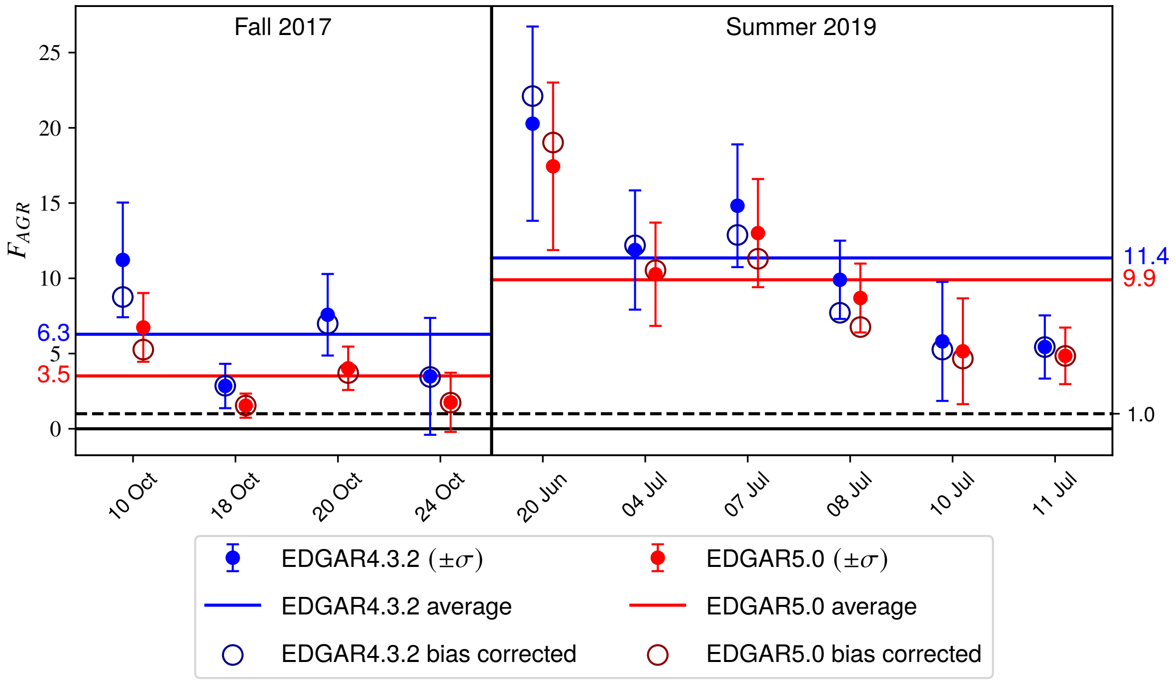

Figure 5.8: Mean and standard deviation (σ) of agricultural scaling factors F_{AGR} for the investigated research flights resulting from Monte Carlo simulations. The bias corrected values are corrected for differences between simulated and observed wind speed and PBL height following Equation 5.5. For reasons of clarity their uncertainties are not displayed. They are similar to the non-bias-corrected uncertainties. Averages are only given for the four flights in fall 2017 and six flights in summer 2019 for the non-bias-corrected values. (Figure adapted from Eckl et al., 2021)

simulated values are mostly higher than the observed values. Thus, the bias correction mostly causes an increase of the simulated N_2O enhancements and hence a decrease of F_{AGR}. In total, however, the impact of the bias correction on F_{AGR} is insignificant and hence not further considered in the following. Table A.3 in the appendix provides a detailed listing of all derived agricultural scaling factors.

Applying the agricultural scaling factors to the EDGAR inventories and averaging them over the Midwest area delivers Midwest N_2O emissions for the ten investigated research flights. Figure 5.9 displays EDGAR5.0 emissions of this region with non-optimized and optimized agricultural emissions. EDGAR4.3.2 fluxes are not displayed since optimizing them results in (nearly) the same, because both versions differ (nearly) only in their strength of E_{AGR} which is adjusted in the course of the optimization. In EDGAR5.0, non-optimized Midwest N_2O fluxes are 0.16 nmol m^{-2} s^{-1}, consisting of 62 % agricultural, 25 % non-agricultural, and 13 % natural emissions. In contrast, EDGAR4.3.2 estimates 0.11–0.12 nmol m^{-2} s^{-1} for October and 0.15 nmol m^{-2} s^{-1} for June/July due to the seasonal cycle of E_{AGR} (see Section 5.4). Optimizing October 2017 results in average total emissions of 0.42 ± 0.57 nmol m^{-2} s^{-1}. During our June/July 2019 flights N_2O emissions are larger with an average of 1.06 ± 0.57 nmol m^{-2} s^{-1}. Table A.4 and A.5 in the appendix provide a more explicit listing of optimized Midwest N_2O emissions.

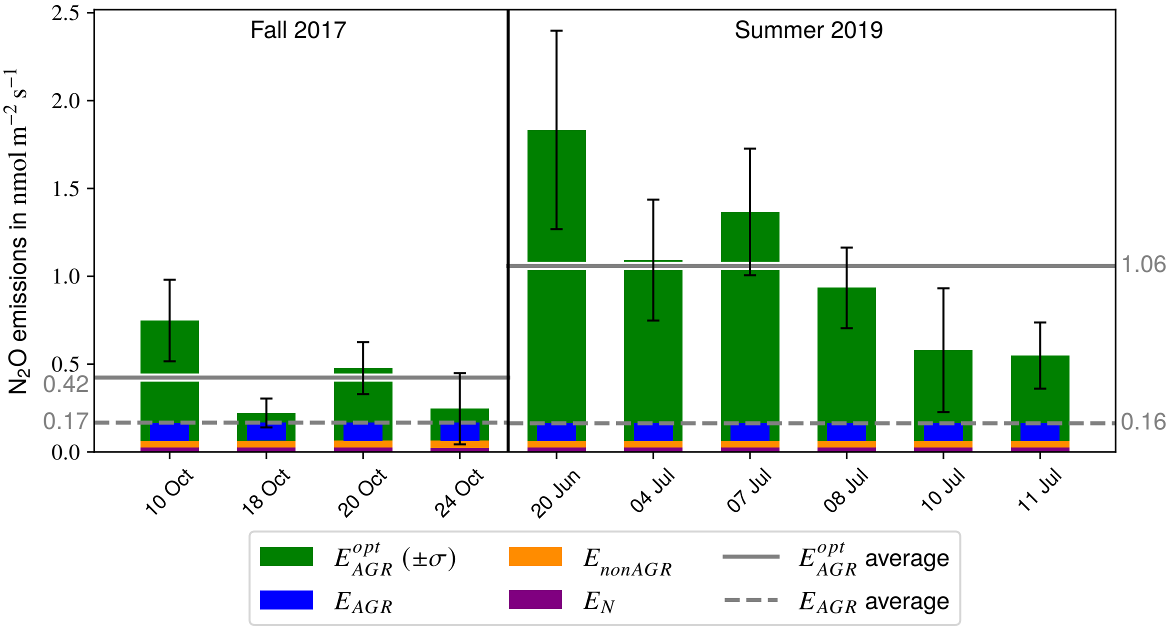

Figure 5.9: EDGAR5.0 Midwest N_2O emissions with prior (E_{AGR}) and optimized agricultural emissions (E_{AGR}^{opt}). Beside the agricultural emissions, non-agricultural (E_{nonAGR}) and natural emissions (E_N; from EDGAR2) are shown. Horizontal lines are 2017 and 2019 averages of total emissions ($E_{AGR}^{(opt)} + E_{nonAGR} + E_N$). (Figure adapted from Eckl et al., 2021)

5.5.3 Discussion

Altogether, both EDGAR versions exhibit a significant underestimation of agricultural emissions. Seasonal differences are likely one cause for the difference in scaling factors and Midwest emissions between 2017 and 2019. Additionally, during the 2019 aircraft campaign an extreme flooding event occurred that likely influenced our results (discussed below). Although EDGAR4.3.2 exhibits a seasonal cycle, its agricultural scaling factor also varies considerably between 2017 and 2019. Hence, the Midwest seasonality is not captured in the EDGAR inventory, which appears to be caused by the flooding.

Optimized emissions for June/July 2019 are two to three times higher compared to DayCent emissions (2011–2015). Despite this, DayCent emissions are closer to our optimized emissions compared to EDGAR during the same period. In contrast, DayCent and EDGAR emissions are both too low by a similar magnitude in October compared to our optimized results. It is important to note here that no DayCent simulations for the campaign years were available. Regional characteristics like soil type, climate, and agricultural practice are most likely comparable between the DayCent simulation years and the campaign years. Hence, as DayCent considers these regional characteristics, it performs much better on the regional scale in the summer than the emission factor approach that is used in EDGAR. However, regional conditions like soil conditions, weather, and N-fertilizer application rates and timing probably differ between the simulation and campaign years, preventing a more quantitative evaluation of DayCent. For that flux calculations for 2017 and 2019 incorporating the corresponding regional conditions would be necessary. DayCent has not been applied to estimate emissions specific to 2017 and 2019 so it is not clear if the model would underestimate the values for these years although this may be the case given the historical data from 2011–2015.

Fu et al. (2017), who also used an Eulerian approach to solve for N_2O, reported emissions of 3.00–4.38 $\mathrm{nmol\,m^{-2}\,s^{-1}}$ during June 1–20, 2010 for the Corn Belt, which is significantly higher than our estimates for June/July 2019. Griffis et al. (2013) estimated the Corn Belt emissions to be around 2 $\mathrm{nmol\,m^{-2}\,s^{-1}}$ and 1 $\mathrm{nmol\,m^{-2}\,s^{-1}}$ in June/July 2010 and 2011, respectively, which is consistent with our findings. Kort et al. (2008) and Miller et al. (2012) derived scaling factors for the central U.S. To be able to compare their results to ours, we estimated the corresponding flux densities for the Midwest region using their scaling factors for the respective EDGAR versions. Kort et al. (2008) derived 0.54 $\mathrm{nmol\,m^{-2}\,s^{-1}}$ for May/June 2003 and Miller et al. (2012) 0.57/0.25 $\mathrm{nmol\,m^{-2}\,s^{-1}}$ and 0.94/0.53 $\mathrm{nmol\,m^{-2}\,s^{-1}}$ for June/July 2004 and 2008, respectively. Both studies show lower values than our estimate. Miller et al. (2012) stated that maximum emissions occurred in June. Our DayCent calculations are also highest in June. This could partly explain our lower estimates compared to Fu et al. (2017) as we report for the end of June/beginning of July after the expected emission peak. Moreover, Fu et al. (2017) only scaled Corn Belt emissions and kept other regions unmodified which could lead to higher estimates, if they sampled other regions with lower emission rates than the Corn Belt. Overall, our estimates are in the range of previous top-down studies. However, the spread among the studies is large.

The nature of soil N_2O fluxes leads to significant temporal variability in the emissions that is not represented in EDGAR. DayCent is capable of representing those variations to a certain extent. For instance, precipitation events may enhance soil N_2O emissions (see Section 2.2.2). DayCent has the potential to simulate such events since it considers meteorology. Within 24 h previous to some of the here investigated research flights, precipitation occurred close to the PBL transect (see Figure A.3), which might have influenced our derived agricultural scaling factors for these flights. As we cannot see a clear correlation between the strength of the scaling factor for a flight and the presence of rain in the proximity of the transect, our results are probably not dominated by precipitation induced emission pulses. Within seven days before each flight (nearly) the whole Midwest experienced precipitation (see Figure 2.2.2), which probably influenced our optimization result because soils were regularly moisturized. Overall, in the Corn Belt the October 2017 and June/July 2019 precipitation amount was approximately 100 % and more than 10 % larger than the 1901–2000 mean, respectively (NOAA, 2020a). Hence, Midwest soil N_2O emissions are likely enhanced in these two periods due to above-average precipitation amounts. Chapter 7 analyzes the influence of precipitation and soil moisture on the results presented herein in greater detail.

Top-down studies based on ground-based measurements (Turner et al., 2015) and tall tower measurements (Griffis et al., 2013; Griffis et al., 2017) show the important role of indirect soil N_2O emissions from nitrogen leaching and volatilization processes in the Midwest. Characterized by a high temporal and spatial variability, these emissions could account for about half of the total emissions on a yearly basis (Griffis et al., 2017). In this study, the spatial and temporal heterogeneity of indirect emissions could lead to higher/lower optimization results if we measure during times or in areas with above/below-average N_2O indirect emissions. However, we are not able to distinguish between direct and indirect N_2O emissions in this study and hence cannot quantify this. Considering the different agricultural sectors in EDGAR (direct soil emissions, indirect emissions, manure management, and agricultural waste burning) separately in our model runs resulted in simulated N_2O enhancements along the transects consisting of N_2O from mainly direct and indirect emissions. Since the spatial distributions of direct and indirect emissions in EDGAR are similar in the Midwest, the corresponding simulated plumes exhibited similar shapes. Hence, we could not tell whether we should scale direct or indirect emissions. For that reason, we decided to consider agricultural emissions in total rather than its individual components in this study. By averaging over the optimization results of several transects during which we measured in different areas and at different times, we try to minimize the effect of the heterogeneity of N_2O emissions.

Especially in 2019, weather conditions in the study domain were unusually extreme. During the campaign, the U.S. was experiencing its wettest period in 125 years, with severe flooding in the Midwest (NOAA, 2020b) forcing the farmers to significantly delay planting in the affected regions (USDA, 2020) and postponing the peak emission period. Depending on whether the zenith is shifted closer to or further away from our investigated period this event may have either amplified or lowered our emission estimates. Additionally, the above-average humidity might have enhanced soil N_2O emissions leading to higher estimates (see Section 2.2.2). As indirect N_2O emissions play an important role in the Midwest, flooding-induced emissions pulses of indirect emissions from streams and rivers probably also boosted soil N_2O fluxes. The influence of this flooding event cannot be quantified within this study, as this would require more data over longer periods spanning the whole event. However, in a follow-up study we plan to use DayCent simulations driven with those flooding conditions to gain insights on how soil N_2O emissions were affected.

5.6 Summary

Unique continuous in situ airborne N_2O measurements of ten research flights were used to quantify N_2O emissions in the U.S. Midwest using a top-down approach. In October 2017 average emissions are 0.42 nmol m^{-2} s^{-1}. The agricultural portion is on average 6.3 times higher than in EDGAR4.3.2 and 3.5 times higher than in EDGAR5.0. June/July 2019 emissions are on average 1.06 nmol m^{-2} s^{-1}. For that, agricultural EDGAR4.3.2 fluxes have to be scaled by an average factor of 11.4. EDGAR5.0 performs better again, but still requires an agricultural scaling factor of 9.9. Uncertainties of scaling factors and Midwest N_2O emission estimates are on the order of 50 %. Our 2019 estimates are most likely influenced by an extreme flooding event, which is difficult to capture in EDGAR as the inventory uses a climatological average emissions dataset. Agricultural soil emissions estimated with DayCent in 2011–2015 are 0.32–0.48, 0.16–0.30, and 0.08–0.11 nmol m^{-2} s^{-1} in June, July, and October, respectively. These historical emission estimates are higher than non-optimized EDGAR emissions, but still significantly lower than our optimized fluxes. Our findings are in the range of previous top-down estimates for the Corn Belt and central U.S. However, a quantitative comparison of those studies shows that the range of derived N_2O surface fluxes is large, likely due to the temporal complexity of soil N_2O emissions.

6 Studying the Seasonality of U.S. Midwest N_2O Emissions

Soil N_2O emissions exhibit a pronounced seasonality (see Section 2.2.2, Chapter 5, and Butterbach-Bahl et al., 2013). In this chapter, seasonal variations of observed N_2O emissions in the U.S. Midwest are analyzed (**RQ1**) and evaluated against state-of-the-art bottom-up estimates (**RQ2**). To this end, PFP measurements of N_2O available from five ACT-America campaigns covering all four seasons (see Section 3.2) are used. During each research flight, up to twelve air mass samples have been collected evenly distributed along constant altitude transects without the intention of catching or missing GHG enhancements. These measurements are combined with dedicated HYSPLIT simulations, which relate observed N_2O enhancements to emissions from surface sources (see Section 3.3.2). Similar to the approach presented in the previous Chapter 5 (hereafter referred to as “Method 1”), discrepancies between measured and simulated N_2O enhancements are minimized by scaling agricultural EDGAR4.3.2 and EDGAR5.0 bottom-up fluxes, thus allowing to quantify N_2O emissions of the U.S. Midwest. However, there are two fundamental differences between Method 1 and the approach used for the analysis in the present chapter (hereafter referred to as “Method 2”). First, the available PFP measurements are discrete samples and do not provide continuous measurements like the QCLS dataset. Second, Method 1 is based on dedicated WRF-Chem forward simulations requiring a high amount of computational resources. In contrast, Method 2 makes use of HYSPLIT backward simulations already available within the framework of the ACT-America project (B. C. Baier, University of Colorado-Boulder and NOAA/GML). Therefore, a comparison of the results of both approaches is given in this chapter. The derived emission rates for all seasons are finally used to evaluate EDGAR and DayCent estimates of direct soil emissions.

In the following, the relevant observational data is presented in Section 6.1, followed by a description of the methodology in Section 6.2. Section 6.3 gives an overview of all PFP measurements. Results are presented and discussed in Section 6.4. Finally, Section 6.5 summarizes and concludes this chapter.

6.1 Observational Data

In the course of all five ACT-America campaigns, PFP samples have been collected onboard of both deployed aircraft, NASA’s C-130 and B-200, and have been analyzed for N_2O dry air mole fractions (see Section 3.2). The covered seasons and years are visualized in Figure 6.1. While the winter 2017 campaign sampled the second half of winter and early spring (mid-January until mid-March), fall 2017 and spring 2018 field deployments roughly took place in mid-fall (early October until mid-November) and mid-spring (mid-April until mid-May), respectively. Measurements in 2016 cover the second half of summer (mid-July until end of August), while in 2019 early/mid-summer (mid-June until end of July) is sampled, with an overlap in July. All four seasons were studied enabling to investigate seasonal differences of soil N_2O emissions.

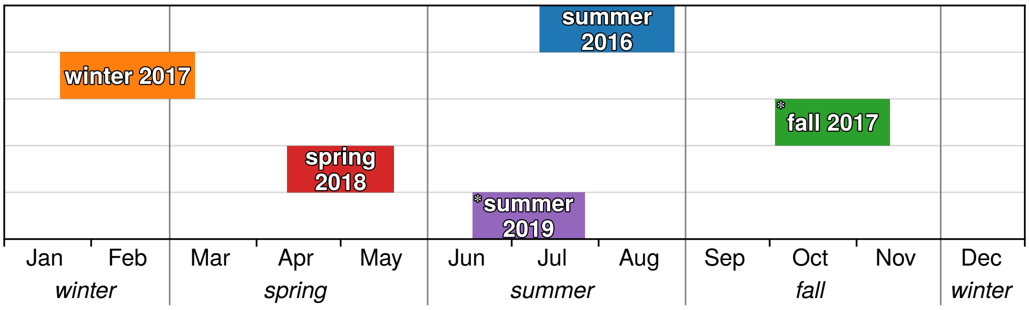

Figure 6.1: Seasons and years covered during the five ACT-America campaigns. Campaigns including the DLR QCLS deployment are marked with a star. Indicated time periods of each field deployment span from the first to the last conducted research flight. The meteorological seasons are given as well.

During each ACT-America field deployment approximately 250–300 PFPs were collected (see Table 6.1), which in total sums up to nearly 1400 air samples taken above the Midwest, East Coast, and Gulf Coast of the U.S.

This thesis focuses on regional N_2O emissions; therefore, only PFPs collected within the PBL are considered for the following analysis. In the PBL, N_2O enhancements predominantly originate from the surrounding area, while enhancements in the free troposphere might also originate from remote N_2O emissions (see Section 2.1.2). According to the tagging included in the ACT-America data merge (Davis et al., 2018), approximately 50 % of all PFPs have been collected within the PBL. Around 140–170 data points remain per campaign, summing up to nearly 800 PFP samples.

Furthermore, since this analysis focuses on N_2O emissions from soils, only PFPs dominated by soil N_2O emissions have been selected. To this end, simulated N_2O enhancements based on the EDGAR inventory are used (see Section 6.2.1). PFPs which, according to the simulated enhancements, were impacted by at least two-thirds by agricultural emissions and emissions originating from soils under natural vegetation, are chosen for further analysis. Selected PFPs are listed in Table 6.1. Please note that depending on the choice of the two different EDGAR inventory versions used as a filter, a different amount of samples remains for the subsequent analysis. This is the result of the difference in monthly amounts of agricultural emissions in both inventories; agricultural emissions in EDGAR4.3.2 exhibit a seasonality while in EDGAR5.0 they are constant throughout the year (see Section 5.4).

The HYSPLIT footprint summarized over all selected PFPs (collected within PBL and dominated by soil N_2O emissions according to EDGAR5.0) for all five ACT-America campaigns is depicted in Figure 6.2. Mainly N_2O emissions originating from the central U.S. Midwest and the Gulf Coast contribute to the observed N_2O enhancements, constraining the region which is characterized in the following.

Campaign:	total	# of PFPs: in PBL	in PBL & soil filter EDGAR4.3.2	 EDGAR5.0
Summer 2016	274	163	79	72
Winter 2017	295	150	129	55
Fall 2017	272	158	32	64
Spring 2018	294	173	112	95
Summer 2019	241	136	72	68
Total:	*1376*	*780*	*424*	*354*

Table 6.1: Number of PFPs collected during the five ACT-America field deployments onboard NASA's C-130 and B-200. Tags in the in situ data merge of the campaigns (Davis et al., 2018) enable to distinguish between PFPs collected inside and outside of the PBL. The soil filter (see Section 6.1) allows only PFPs whose footprint enhancements consist of minimum two-thirds agricultural enhancements and enhancements from soils under natural vegetation.

6.2 The HYSPLIT Footprint Approach (Method 2)

The goal is to quantify N_2O emissions in the U.S. Midwest (and the southerly region, see Figure 6.2) using PFP measurements and specific HYSPLIT backward simulations. By combining the backward simulations with EDGAR emissions, N_2O enhancements at the time and location of the PFP samples are simulated (see Section 6.2.1). Discrepancies between observed and modeled enhancements are then minimized by scaling agricultural EDGAR emissions to quantify Midwest N_2O emissions (see Section 6.2.2). This approach (Method 2) is based on a similar concept but includes some important differences to the approach used in the previous Chapter 5 (Method 1), outlined in Section 6.2.3.

6.2.1 Simulated Footprint Enhancement

To simulate N_2O enhancements, ten-day HYSPLIT footprints, available for each single PFP sample, are used (see Section 3.3.2). Footprints are a quantitative description of the sensitivity of a receptor to a source region. Here, the receptor is the N_2O enhancement at the time and location of a PFP sample and the source is the emission of N_2O. Thus, the footprint of a PFP sample describes from where and to what extent N_2O emissions influence the measurement. In other words, N_2O fluxes (e.g., in $\mathrm{nmol\,m^{-2}\,s^{-1}}$) are translated into mole fraction enhancements expected at the time and location of the corresponding PFP (e.g., in ppb). The unit of a footprint is $\mathrm{ppb/(nmol\,m^{-2}\,s^{-1})}$. HYSPLIT footprints are provided as hourly data on a regular latitude-longitude grid. To allow for a combination with other gridded datasets like monthly EDGAR emissions (having e.g. a different temporal resolution), they are re-projected so that grids coincide. This enables a grid cell-wise comparison with footprint sensitivities. Let n_t,

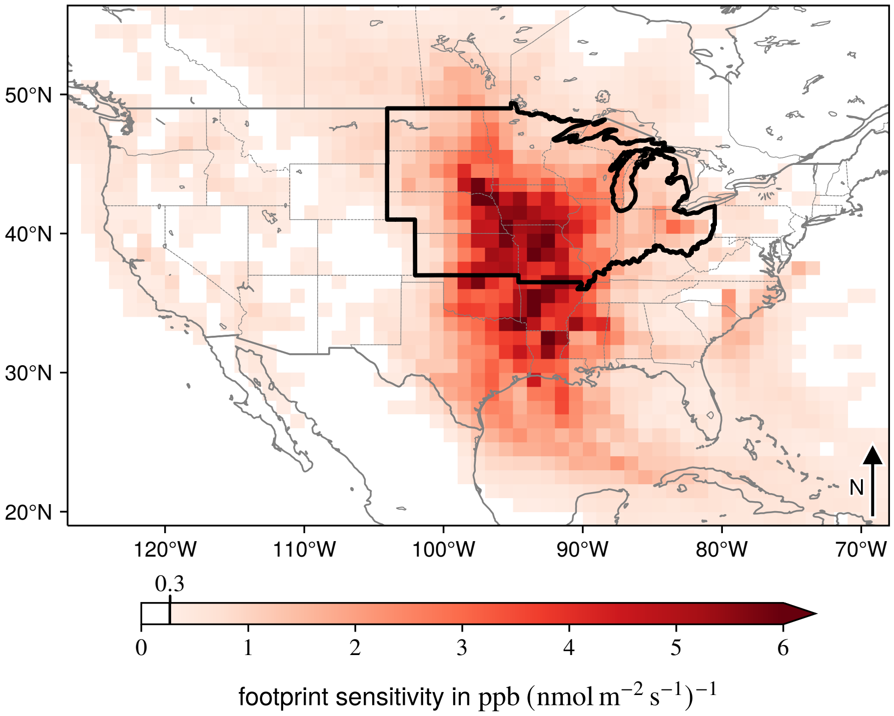

Figure 6.2: Total sum of HYSPLIT PFP footprints for all five ACT-America campaigns. Only PFPs are considered if collected within the PBL and dominated by soil N_2O emissions following EDGAR5.0 footprint enhancements (see Section 6.1). The U.S. Midwest is encircled in black.

n_{lat}, and n_{lon} be the length of the time, latitude, and longitude dimension of the shared grid, respectively. For simplicity, in the following footprints (and other three-dimensional data) are considered as one-dimensional arrays $\mathbf{H}$ of length $n_f = n_t \cdot n_{lat} \cdot n_{lon}$, where h_i is the i^{th} component.

Simulated N_2O enhancements for all PFPs are calculated by adding up the product of HYSPLIT footprints and EDGAR4.3.2 as well as EDGAR5.0 emission estimates. Both inventory versions provide gridded agricultural E_{AGR}, non-agricultural E_{nonAGR}, and natural E_N (from EDGAR2) N_2O emissions (see Section 3.4.1). Let $\mathbf{E}^f$ be the N_2O fluxes of one of the three emission sectors on the same grid as the footprint $\mathbf{H}$, where e_i^f is the i^{th} of n_f components. Then, the N_2O enhancement at the receptor c_f^{enh} (hereafter referred to as "footprint enhancement") due to emissions from $\mathbf{E}^f$ is calculated via the dot product of $\mathbf{H}$ and $\mathbf{E}^f$:

$$c_f^{enh} = \mathbf{H} \cdot \mathbf{E}^f = \sum_{i=1}^{n_f} h_i \cdot e_i^f \tag{6.1}$$

This approach is comparable to Method 1, whereby N_2O enhancements emitted from EDGAR are propagated forward in time through the atmosphere. In contrast, here the air mass sampled by the PFP is followed backward in time through the atmosphere to estimate the contribution of EDGAR fluxes on the measurement.

6.2.2 Footprint Scaling Factor

N_2O emissions are quantified by minimizing the difference between simulated/footprint (c_f^{enh}) and observed enhancements (c_{obs}^{enh}). Following Equation 5.1 in the previous chapter, c_{obs}^{enh} is estimated by subtracting a background mole fraction from the PFP mole fraction. Here, for each campaign the 5th percentile of all PFPs collected within the PBL is used as the background (see Figure 6.3). Background values range from 329.1 ppb to 331.8 ppb during the five ACT-America field deployments. The fall 2017 and summer 2019 values are within the uncertainty of the backgrounds estimated using the high-resolution QCLS dataset, i.e. 329.9 ± 0.8 ppb and 331.3 ± 0.8 ppb, respectively (see Section 5.3.1). The increase of derived background values from summer 2016 to summer 2019 reflects the growth rate of the global atmospheric N_2O abundance of around 1 ppb yr^{-1} (NOAA/ESRL, 2021b).

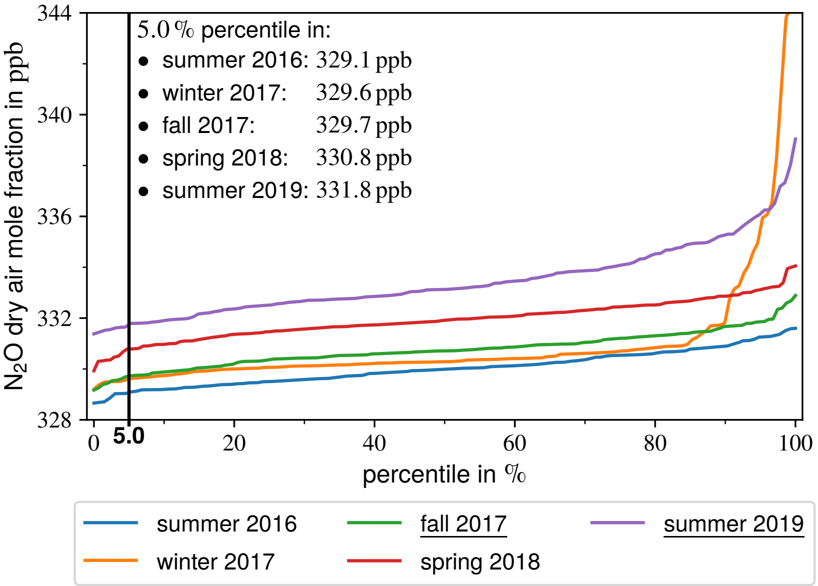

Figure 6.3: Percentiles of PFP N_2O dry air mole fractions calculated for all five ACT-America field deployments. Only PFPs collected within the PBL are considered. The 5th percentile defines the observed N_2O background mole fraction. Campaigns including the DLR QCLS deployment are underlined.

In Method 1, discrepancies between modeled and observed N_2O enhancements are minimized by scaling agricultural emissions by a certain factor F_{AGR}. Adapting this methodology, which is described in Section 5.3.1, allows to derive an agricultural scaling factor for each single PFP sample F_{AGR}^f. Analogue to Equation 5.4, F_{AGR}^f is defined as:

$$F_{AGR}^{f} = \frac{c_{obs}^{enh} - c_{f,nonAGR}^{enh} - c_{f,N}^{enh}}{c_{f,AGR}^{enh}} \tag{6.2}$$

Where $c_{f,AGR}^{enh}$, $c_{f,nonAGR}^{enh}$, and $c_{f,N}^{enh}$ is the footprint enhancement due to agricultural, non-agricultural, and natural EDGAR emissions. Here it is important to recapitulate that this approach assumes that E_{AGR}, E_{nonAGR}, and E_N cover all relevant N_2O emissions and that discrepancies between observation and simulation are only due to underestimated agricultural emissions.

6.2.3 Comparison of Method 1 and Method 2

Method 1 as well as Method 2 are used to quantify N_2O emissions by minimizing discrepancies between observed and simulated N_2O enhancements via scaling of agricultural EDGAR emissions with corresponding scaling factors. Due to the similarity of both approaches, the sources of uncertainties affecting the agricultural scaling factors and their contributions are of similar nature. A detailed description of the uncertainty assessment is provided in Section 5.3.2. According to Chapter 5, footprint scaling factors exhibit an uncertainty of approximately 50 %. However, there are two essential differences between both approaches:

1. For Method 2, the model transport of N_2O enhancements through the atmosphere is realized via HYSPLIT backward simulations rather than WRF forward simulations as for Method 1. HYSPLIT uses meteorological input generated with the WRF model. Hence, the uncertainty of F^f_{AGR} due to the model transport of N_2O through the atmosphere is composed of uncertainties in both, the WRF transport and the HYSPLIT dispersion calculation. The WRF related transport error is assumed to be similar to Method 1, because in both cases WRF is driven by ERA5 initial and boundary conditions and analysis nudging is applied (see Section 5.2). Compared to the WRF related transport error, the HYSPLIT uncertainty is assumed to be insignificant. This assumption is based on Hegarty et al. (2013), who evaluated HYSPLIT and two other state-of-the-art dispersion models with measurements from controlled tracer releases. They found differences among the underlying meteorological models to be larger than differences among the dispersion models, indicating that uncertainties most likely arise from the meteorological models. Thus, the backward approach results in insignificantly larger uncertainties than the forward approach.

2. For Method 2, discrete PFP measurements of N_2O are used rather than continuous QCLS measurements as for Method 1. This only allows for a point-wise determination of footprint scaling factors for each single PFP (six to twelve in total for each flight) while continuous measurements enable a scaling of the integrated measurement along a whole PBL transect. Footprint scaling factors derived from discrete samples therefore might be strongly biased in either direction if modeled and observed enhancements are spatially misaligned, e.g. due to uncertainties in the model transport or due to misplacement of N_2O emissions in the EDGAR inventory. Furthermore, non-continuous measurements have the inherent risk to miss smaller-scale enhancements, depending on sampling strategy and frequency. To allow for a statistically large enough sample size, the following discussion focuses on the analysis of the distribution of footprint scaling factors on a campaign basis. This does not allow for an exact quantification of Midwest N_2O emissions but still for discussing seasonal effects of emissions for the ACT-America field campaign periods and sites.

6.3 Overview of Four Seasons of N_2O Measurements

To understand seasonal features of N_2O abundances above the eastern half of the U.S., this section compares nearly 1400 PFP samples collected in the course of ACT-America (see

Table 6.1) on a campaign basis. Figure 6.4 provides an overview of this dataset. Roughly three years lie between the first and the last measurement. Hence, trends in the global atmospheric N_2O abundance have to be considered to enable a fair comparison of measurements taken during the different campaigns. NOAA/ESRL (2021a) provides precise measurements of monthly northern hemispheric N_2O mole fractions based on long-term measurements at several ground sites around the world. At the beginning of the first ACT-America campaign in summer 2016, concentrations were 329.5 ± 0.3 ppb and increased steadily until the end of the summer 2019 campaign by 2.7 ± 0.4 ppb to 332.2 ± 0.2 ppb. In the plots in Figure 6.4, this increase since summer 2016 is subtracted.

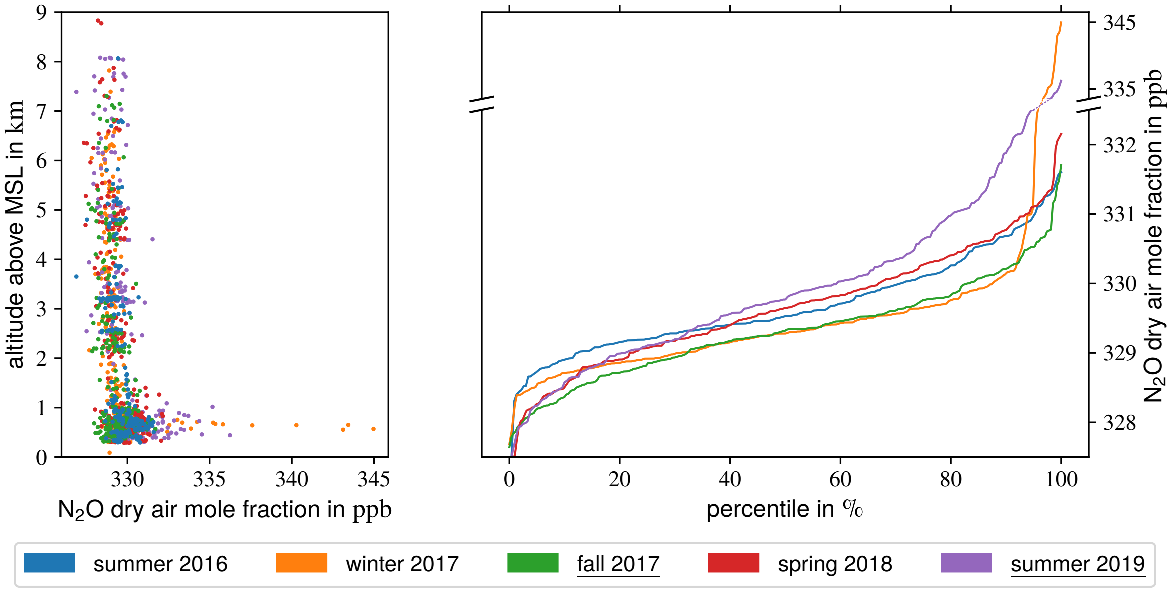

(a) PFP vs. altitude (b) Percentiles

Figure 6.4: Overview of all PFP N_2O measurements collected during all five ACT-America field deployments. Trends in the N_2O abundance in the Northern Hemisphere between summer 2016 and summer 2019 (NOAA/ESRL, 2021a) have been subtracted. Campaigns including the DLR QCLS deployment are underlined. (a) PFP measurements vs. altitude above MSL. (b) Percentiles of PFP measurements.

Figure 6.4a shows the vertical distribution of all de-trended PFP N_2O measurements. Mole fractions above 4 km reflect the average northern hemispheric N_2O abundance following NOAA/ESRL (i.e., 329.5 ± 0.3 ppb). Below 4 km, mole fractions slightly increase towards lower altitudes. Within the PBL, highest N_2O mole fractions up to 345 ppb are observed. This vertical distribution is expected, since most N_2O sources are located at the surface (see Section 2.2.1). Overall, the vertical structure of the profiles of the different campaigns is comparable. However, two features are prominent: First, in summer 2019 enhanced N_2O mole fractions over 335 ppb are observed and, second, measurements during winter 2017 show even more extreme values up to 345 ppb. Please note that in reality these dry air mole fractions are up to 2.7 ppb larger since they have been corrected for trends in the northern hemispheric N_2O abundance. As discussed in the previous chapter, the large values in summer 2019 might be caused by the extreme Midwest flooding occurring before and during the campaign period. The extreme winter 2017 values might be affected by the typically lower PBL height compared to other seasons (see Section 2.1.2). N_2O emissions released at the surface are distributed within a smaller vertical layer (i.e., PBL), resulting in larger N_2O dry air mole fractions. Another reason for the large winter 2017 mole fractions might be freezing/thawing processes in soils which are capable of inducing strong N_2O emission pulses (see Section 2.2.2). Both prominent features are further investigated below.

The percentiles of all PFP N_2O measurements are displayed in Figure 6.4b. Similar to Figure 6.4a, winter 2017 and summer 2019 are prominent since during both campaigns significantly larger N_2O mole fractions have been sampled compared to observations from the other campaigns. Moreover, 20 % of the measurements in 2019 show values larger than 331 ppb, while during the other campaigns this is only the case for 1–6 % of the samples. The shape of the percentile curves indicates the character of the underlying emission drivers. The few very high mole fractions in winter 2017 probably are caused by spatially and temporarily constrained emission pulses due to freezing/thawing. However, summer 2019 measurements suggest a driving parameter that enhances N_2O emissions over a large area and over a long period, as e.g. the flooding event. Furthermore, there is an obvious difference between results from the summer 2016 and summer 2019 measurements, which is another indicator for the impact of the 2019 flooding on N_2O emissions. It is worth noting that the 2019 measurements (June/July) were closer to the main growing season in spring than the summer 2016 measurements (July/August), probably leading to larger N_2O emissions released during the 2019 campaign. However, even the spring 2018 curve is significantly exceeded by the summer 2019 curve, indicating the large impact of the flooding. Beside these two features, discussed in more detail in the following sections, differences in the percentiles among the campaigns are mostly less than 0.4 ppb. These differences are regarded as insignificant, mainly because the monthly N_2O dry air mole fraction from the NOAA/ESRL dataset, used to correct for trends in the N_2O abundance, itself exhibits uncertainties from ±0.2 ppb to ±0.4 ppb. Hence, variations of the N_2O dry air mole fraction in the free troposphere above the Midwest appears to reflect variations of the northern hemispheric atmospheric N_2O abundance.

6.4 Results and Discussion

In this section, N_2O emission fluxes in the U.S. Midwest and the corresponding seasonality is analyzed. As most anthropogenic N_2O emissions originate from agriculture and as only N_2O emissions from soils are expected to exhibit a strong seasonality, this section focuses on the seasonality of agricultural N_2O emissions. Therefore, footprint agricultural scaling factors F^{f}_{AGR} are derived for all selected PFPs (see Section 6.1). Like in Method 1, these scaling factors are multiplied with agricultural EDGAR emissions (E_{AGR}). Total Midwest N_2O emissions are then estimated by averaging the sum of scaled E_{AGR}, non-agricultural (E_{nonAGR}), and natural (E_N) EDGAR emissions over the Midwest region. There is no need to distinguish between EDGAR4.3.2 and EDGAR5.0 because the scaled fluxes are equivalent. Both inventories have the same spatial distribution of emissions and only differ in the magnitude of the monthly N_2O emissions, which is adjusted when scaling emissions (see Section 6.2.1).

A comparison of the scaled Midwest N_2O emissions for all ACT-America campaigns allows to discuss the seasonality of emissions. Figure 6.5 displays the mean, median, and interquartile range (IQR; distance between lower and upper quartile, which spans the box) of the scaled emissions as derived for all selected PFPs from all five campaigns. In winter 2017, Midwest emissions are largest. Lowest fluxes are estimated for summer 2016, followed by fall 2017 and spring 2018. Summer 2019 emissions exceed the estimates from all other campaigns except the winter campaign. Table A.8 in the appendix gives the detailed values for the scaled Midwest fluxes for all campaigns.

In the following, Section 6.4.1 analyzes N_2O emissions during the course of the growing season – from spring to fall. The prominent winter 2017 emissions are investigated in Section 6.4.2. Summer 2019 results are separately discussed in Section 6.4.3, since the extreme flooding event most likely influenced N_2O emissions. Finally, in Section 6.4.4, the scaled Midwest emissions are compared to the results of Method 1, discussed in the previous Chapter 5, and other top-down studies.

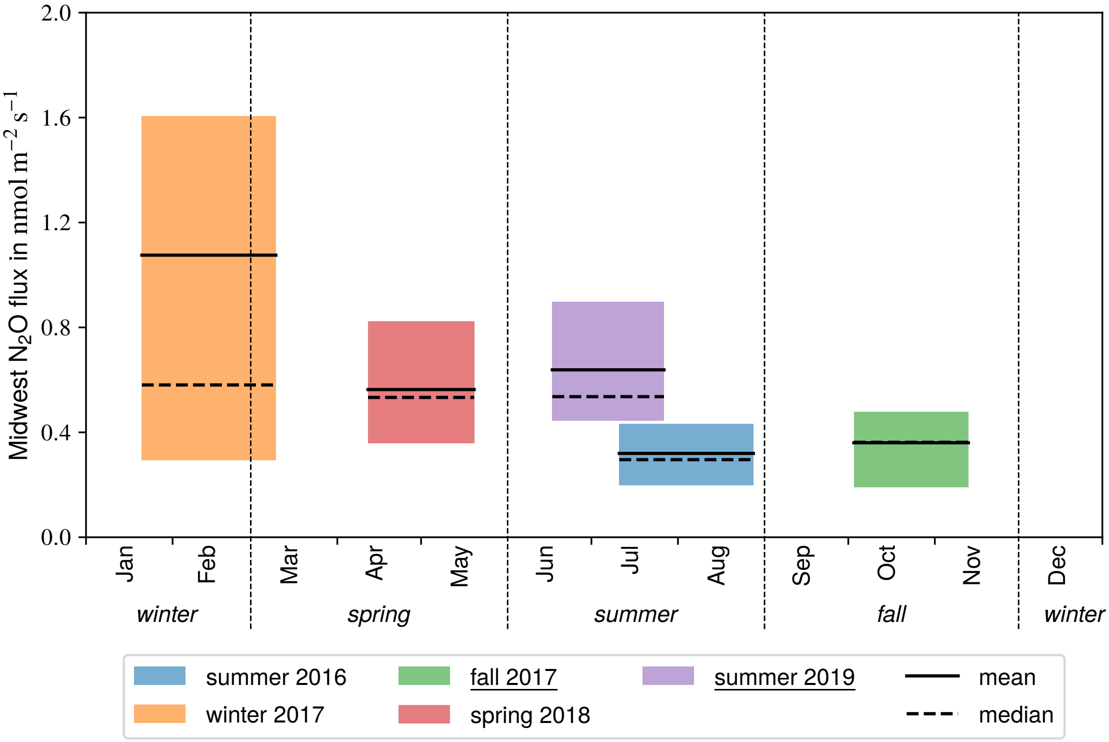

Figure 6.5: Scaled Midwest N_2O emissions calculated for all ACT-America campaigns. For each campaign, N_2O fluxes using the mean and median scaling factor are given. The extension in y-direction defines the lower and upper quartile. The width of each bar is constrained by the first and last research flight of the respective campaign. Meteorological seasons are indicated. Campaigns including the DLR QCLS deployment are underlined.

6.4.1 N_2O Emissions During the Growing Season: Spring to Fall

Variations of Midwest N_2O emissions in the course of the growing season – from spring to fall – are investigated by comparing the results of the spring 2018, summer 2016, and fall 2017 field deployments. Overall, the averages of the scaled emissions in spring and fall are roughly 75 % and 13 % larger than in summer, respectively (see Figure 6.5). Mean and median of the three campaigns are close to each other indicating that emissions are not dominated by extreme emission events. Agricultural emissions and the fertilization practice plays an important role for variations of N_2O emissions in the growing season. In the following, agricultural emissions are considered in greater detail and are compared to EDGAR. Additionally, the role of fertilization is discussed.

Agricultural Emissions – EDGAR Bottom-Up vs. Observational Top-Down:

Footprint scaling factors (F^f_{AGR}) for the spring 2018, the summer 2016, and the fall 2017 field campaign describe the variations of agricultural N_2O emissions in the study region over the course of the growing season. Figure 6.6 (lower panels) displays the distributions of F^f_{AGR} of all ACT-America campaigns as boxplots using anthropogenic N_2O emissions from EDGAR4.3.2 (Figure 6.6a) and EDGAR5.0 (Figure 6.6b) (Table A.6 and A.7 in the appendix lists explicit values, respectively). The upper panels show monthly unmodified agricultural emissions (E_{AGR}) averaged over the Midwest and for the two EDGAR versions. As discussed in Section 5.4, the spatial distribution as well as the yearly emission total of E_{AGR} are equal in both inventories. However, EDGAR4.3.2 agricultural emissions exhibit a seasonality while in EDGAR5.0 emissions are evenly distributed over the course of the year. According to EDGAR4.3.2, N_2O fluxes are lowest in winter (Nov–Jan), highest in March and relatively constant in summer, followed by a smaller increase in September. A more detailed description of unmodified EDGAR N_2O fluxes is provided in Section 5.4.

Overall, both EDGAR versions seem to underestimate agricultural N_2O emission fluxes significantly. For spring 2018, summer 2016, and fall 2017 observations, scaling factors between approximately two and five are derived. A comparison between EDGAR4.3.2 and EDGAR5.0 shows that EDGAR4.3.2 performs better in spring (~50 % lower scaling factor) while EDGAR5.0 performs better in fall (~65 % lower scaling factor). For summer, scaling factors are similar for both inventory versions. The differences in spring and fall are caused by the inherent seasonality in EDGAR4.3.2. However, EDGAR4.3.2 does not perfectly capture the entire seasonal variability in the study region, because there is a difference between the resulting scaling factors for the three campaigns.

Since EDGAR5.0 exhibits no seasonal cycle, variations of EDGAR5.0 scaling factors for the spring 2018, summer 2016, and fall 2017 campaign indicate the seasonality of agricultural N_2O emissions in the study region: Emissions (or scaling factors) are 90 % larger in spring and 10 % larger in fall than in summer. In contrast, according to the EDGAR4.3.2 seasonality, agricultural emissions during the spring campaign exceed emissions during the summer campaign by 40 % while emissions during the fall campaign are 40 % lower. However, if not the campaign months are considered but largest EDGAR4.3.2 fluxes in spring (March) and fall (September) are compared to summer (July), emissions are 170 % and 30 % larger, respectively. These seasonal differences qualitatively coincide with the seasonal differences of the EDGAR5.0 scaling factors, which are significantly larger in spring and slightly larger in fall than in summer as well. Quantitatively, differences in the EDGAR5.0 scaling factors are two to three times lower than in the EDGAR4.3.2 seasonality. If the EDGAR4.3.2 seasonality was delayed by roughly one month, the observed seasonal cycle in EDGAR5.0 scaling factors would be captured.

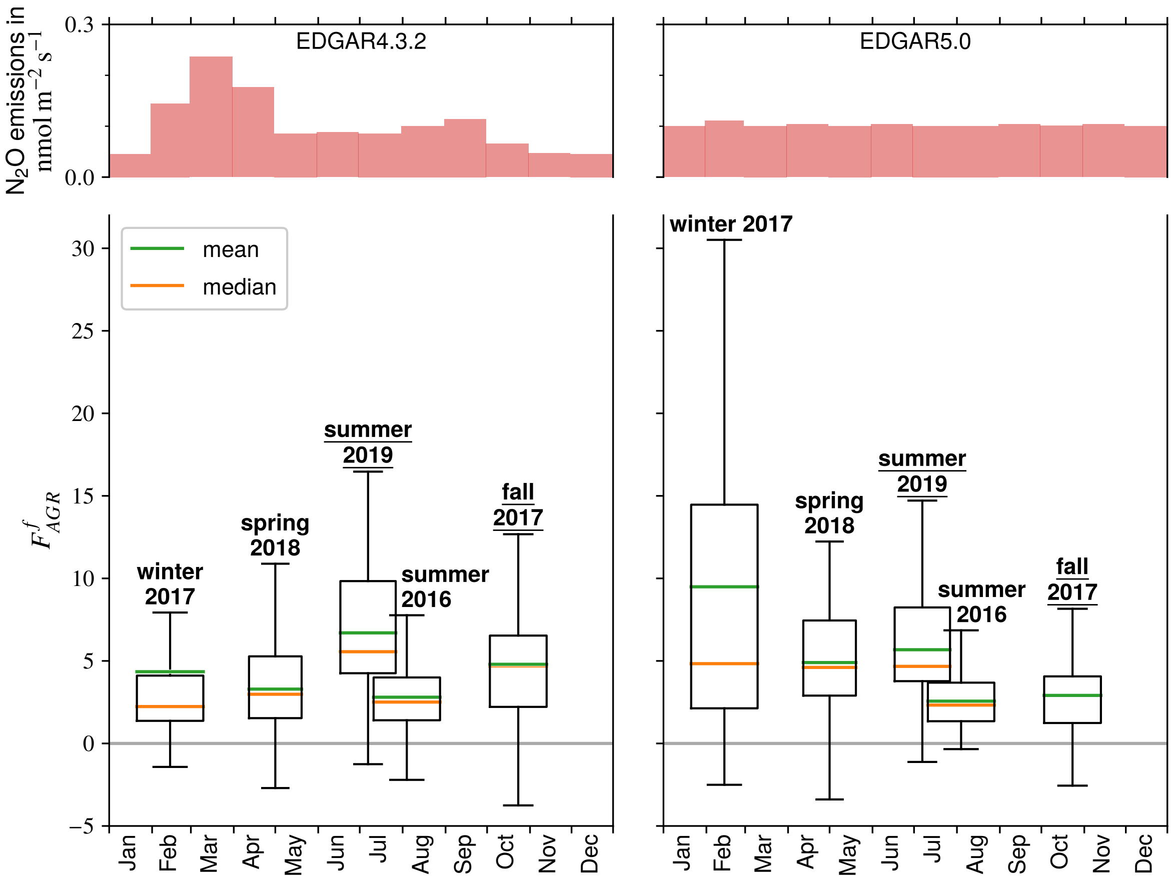

(a) EDGAR4.3.2 (b) EDGAR5.0

Figure 6.6: PFP agricultural scaling factors (F^f_{AGR}) derived for all five ACT-America campaigns for the EDGAR4.3.2 (a) and EDGAR5.0 (b) N_2O emission inventories (lower panels). The width of each boxplot is constrained by the first and last research flight of the respective campaign. The lower and upper quartiles span the height of each box. The whiskers are defined as 1.5 times the IQR. Outliers are not displayed. Campaigns including the DLR QCLS deployment are underlined. The upper panels show the unmodified agricultural emissions in EDGAR (E_{AGR}) averaged over the Midwest.

Role of Fertilization Activity:

The application of N-fertilizer affects the seasonality of agricultural N_2O emissions. Figure 6.7 summarizes the fertilization practice for corn and soybeans in the U.S. This can be used as a proxy for the total fertilization practice in the Midwest because both crops together account for roughly 75 % of the harvested area there (NASS, 2021). Over 96 % of corn fields are fertilized, while for soybeans it is less than 28 % since they are N-fixing crops capable of absorbing nitrogen from atmospheric N_2 (see Section 2.2.2). Although the exact timing of the fertilizer application is vague, the data enables to roughly estimate the seasonality of the fertilization practice. Corn is mainly treated with N in spring before planting (>60 %). Only roughly 25 % is fertilized in fall. For soybeans it is vice versa, 35 % of the fertilized area is treated in spring and 45 % in fall. As both crops are planted in spring (USDA, 2020), the fertilization “at planting” occurs in spring, while the fertilization “after planting” occurs in either late spring or summer. In winter, no fertilizer at all is applied (omitted in Figure 6.7). Overall, both crops are mainly fertilized in spring and fall, while in summer application rates are low. Since much more corn than soybean fields are fertilized (see above), application rates in spring are higher than in fall.

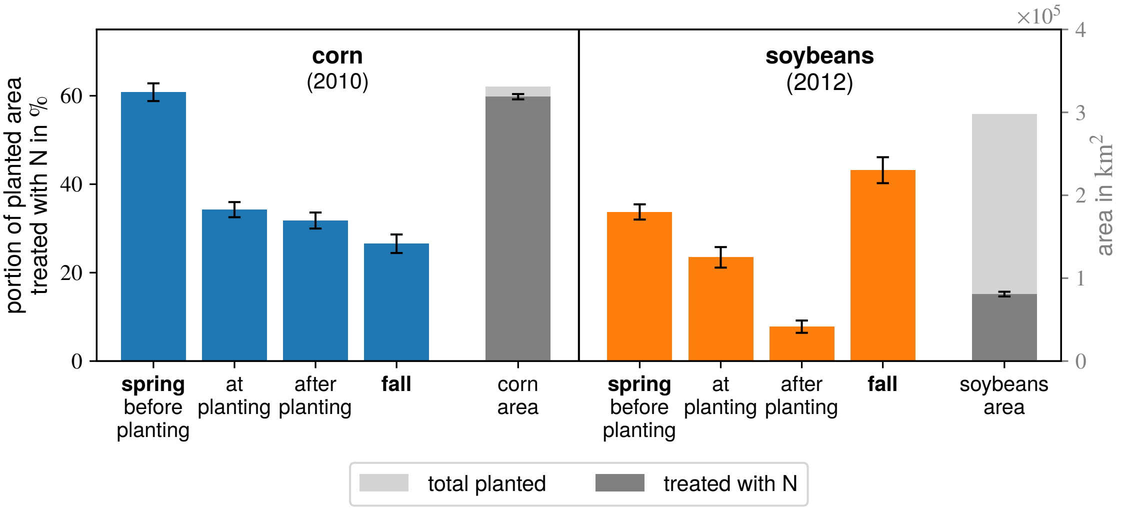

Figure 6.7: U.S. N-fertilizer application practice for corn and soybeans in 2010 and 2012, respectively. Due to multiple fertilization in a year the sum of the shares exceeds 100 %. Data are obtained from USDA’s Agricultural Resource Management Survey (ARMS, 2015). The survey is based on information from farms in the contiguous U.S. See https://www.ers.usda.gov/data-products/arms-farm-financial-and-crop-production-practices/documentation/ for more details. The planted areas cover all farms participating in the survey. Given uncertainties are the standard errors.

This fertilization practice is in line with the EDGAR5.0 scaling factors for the spring, summer, and fall field deployments, i.e. factors are largest in spring, followed by fall and are lowest in summer (EDGAR4.3.2 scaling factors are not considered here since they are influenced by the seasonality of the inventory). Thus, fertilization appears to induce the seasonality and variability of agricultural N_2O emissions in the study region. This statement is also supported by the IQR of EDGAR4.3.2 and EDGAR5.0 scaling factors, which is larger in spring and fall than in summer, because the agricultural N_2O emissions are more variable in spring and fall caused by the temporally and spatially highly variable application rates of fertilizers. However, beside the fertilizer application, soil conditions and precipitation, which strongly drive soil N_2O emissions, also vary from season to season influencing the seasonality of emissions. This is further investigated in the next Chapter 7.

6.4.2 N_2O Emissions During Winter 2017: Freezing/Thawing Events

Scaled Midwest N_2O emissions for the winter 2017 field deployment show the largest variability and highest values compared to all other ACT-America campaigns (see Figure 6.5). Average emission estimates exceed the summer 2016 estimates by approximately 230 %. The mean emission flux is significantly larger than the median emission flux, meaning that a few extreme emission events dominate the winter N_2O fluxes. These events cause the unusual N_2O dry air mole fractions of larger than 340 ppb observed during the winter deployment. According to Section 6.3, a shallow PBL, typically observed in winter, might also result in unusual large N_2O mole fractions leading to positively biased top-down emission estimates. However, N_2O fluxes presented herein are most likely not affected by this effect since results are based on model simulations which account for the PBL height. The next Chapter 7 shows that freezing/thawing is most likely responsible for the extreme emission events. Globally, this process accounts for up to 28 % of yearly cropland N_2O emissions (Wagner-Riddle et al., 2017). The prominence of scaled winter emissions suggests that freezing/thawing significantly contributes to the Midwest N_2O budget as well.

EDGAR's agricultural N_2O emissions do not capture the high winter emissions in the study region. Scaling factors for EDGAR5.0 reach values of over 30 demonstrating the large magnitude of freezing/thawing induced emission pulses (see Figure 6.6). EDGAR4.3.2 scaling factors are less prominent due to the incorporated seasonality of agricultural emissions, which states largest emissions in March. The seasonality is solely based on agricultural activity and not soil processes (Janssens-Maenhout et al., 2019). Theoretically, assuming that EDGAR4.3.2 emissions are accurate, the derived scaling factors could be used to quantify the contribution of freezing/thawing induced emissions to the Midwest N_2O budget. However, uncertainties are high and as concluded in the previous Section 6.4.1, the EDGAR4.3.2 seasonality may be delayed by one month (compared to the observations in this study). This would lead to a significant increase of EDGAR4.3.2 scaling factors for winter 2017, highlighting the need to implement freezing/thawing induced N_2O emissions in the inventory.

6.4.3 N_2O Emissions During Summer 2019: The Extreme Flooding Event

Top-down emission estimates derived for summer 2019 are larger than for all other campaigns except the winter campaign (see Figure 6.5). Compared to summer 2016, average emissions are twice as high, while spring 2018 emissions are exceeded by roughly 14 %. Like in winter, the median is considerably lower than the mean indicating that a few, large N_2O emission events significantly contribute to average emissions of the investigated period and region. In contrast, mean and median of all other campaigns (except winter) are close to each other indicating that emissions are dominated by more average conditions. Two reasons for the prominent 2019 emission estimates are identified: First, the summer 2019 campaign took place roughly one month earlier than the 2016 campaign and, hence, closer to the main fertilization activity in spring. Second, the extreme flooding event, resulting in a delay of the growing season (USDA, 2020), strongly impacted soil N_2O emissions in the Midwest (see also next Chapter 7). Since both reasons mainly affect agricultural N_2O emissions, their influence is discussed using agricultural scaling factors.

Agricultural scaling factors for summer 2019 are on average 120–140 % larger than for summer 2016 (see Figure 6.6). As described above, 2019 measurements (conducted in June/July) occurred roughly one month earlier than in 2016 (July/August). According to DayCent estimates of agricultural N_2O emissions in the Midwest calculated for the years 2011–2015 (see Section 5.4), emissions in June are on average 70 % larger than in July. Hence, a large part of the discrepancy between the scaling factors derived for the two summer campaigns can probably be traced back to the different sampling months. The remaining uncertainty might be attributed to the extreme flooding event. However, this relies on two assumptions: First, small interannual variability (and hence representativity of both measurement periods) and, second, no general trend in emissions between the campaign years 2016 to 2019.

1. The interannual variability of summer N_2O emissions is evaluated using DayCent 2011–2015 simulations of agricultural N_2O emissions in the Midwest. The relative standard deviation of emissions in these five years is 14 % and 17 % in June and July, respectively. Although five years are not sufficient to accurately determine the interannual variability, the relative standard deviations strongly indicate that the interannual variability of summer N_2O emissions in the Midwest is lower than the potential impact of the flooding but not negligible.

2. The general trend in average Midwest emissions from 2016 to 2019 is evaluated using a study of Tian et al. (2018) who estimate global fluxes of soil N_2O emissions since the preindustrial era with an ensemble of terrestrial biosphere models. The authors report that emissions in the entire U.S. stayed constant at $0.8 \pm 0.3\,\mathrm{Tg\,N_2O\text{-}N\,yr^{-1}}$ from the 1990s to 2007–2016. Hence, it is plausible that average agricultural emissions in the study region might have stayed constant between 2016 and 2019 as well. In contrast, it has to be noted that the crop diversity in the Midwest has declined while the fertilizer consumption increased over the course of the last decades (see Appendix A.11). Both factors would favor N_2O emissions, indicating that average agricultural emissions in the study region might be larger in 2019 than in 2016.

As a conclusion, the flooding event might have enhanced agricultural emissions in June/July 2019 by roughly 70 %, resulting in an approximate Midwest N_2O flux of $0.18\,\mathrm{nmol\,m^{-2}\,s^{-1}}$. However, a detailed and accurate quantification of this event is not possible with the available data. To allow for a thorough analysis, a process-based model is required, which should be driven by the specific 2019 flooding conditions. This is planned for a follow-up study using the DayCent model. Alternatively, a well characterized seasonality of agricultural N_2O emissions including year-to-year variability in the study region would enable a quantification using the ACT-America N_2O dataset.

6.4.4 Comparison With Other Studies

Top-down studies quantifying N_2O emissions in the U.S. Midwest are rare. Figure 6.8 presents the results of this thesis in the context of other top-down studies focusing on N_2O emissions in the Midwest and surrounding regions. The results of this chapter (Method 2) are first compared to the results of Method 1, followed by a comparison to the DayCent estimated fluxes of agricultural Midwest emissions for the years 2011–2015 (see Section 3.4.2) and, finally, to other top-down results reported in the literature.

Comparison of Results of Method 1 and Method 2:

Section 6.2.3 gives a detailed description of the differences between both methods. A comparison of the results of Method 1 and Method 2 shows that, in principle, both approaches deliver consistent results. Fluxes derived with Method 2 are within the uncertainty of Method 1 but tend to be at the lower end. This can be traced back to two reasons:

1. Method 2 is based on PFP samples taken over the course of five campaigns in total and, hence, the spatial coverage is larger than of Method 1. While Method 1 uses measurements focused on the central Midwest (see Figure 5.1b), Method 2 includes observations related to sample locations in adjacent regions (see Figure 6.2). In the latter case, N_2O emissions are expected to be lower than in the densely farmed Midwest, leading to lower emission values on average.

2. The temporal resolution of Method 1 (based on continuous measurement) is larger than of Method 2 (based on discrete samples). In Method 1, derived N_2O fluxes are based on continuous N_2O measurements along a transect. Hence, also small-scale features are completely accounted for. In contrast, during each research flight maximum twelve PFP samples were collected evenly distributed along the transect. These might miss plume enhancements, resulting in a low bias in N_2O fluxes derived with Method 2 (see Section 6.2.1). EDGAR5.0 scaling factors for the C-130 flight on the 04 Jul 2019 demonstrate this: Average scaling factors ($\pm\sigma$) are significantly lower when using Method 2 (6.7 ± 3.4; five PFPs) rather than Method 1 (10.3 ± 3.4). Thus, for a single research flight Method 1 delivers a more robust result than Method 2. Analyzing the PFPs on a campaign basis reduces the consequences of undersampling but the sample size is likely still not sufficient to completely eliminate the bias.

Overall, lower estimates for PFP deduced emissions are mainly caused by a larger footprint and likely a low bias due to undersampling.

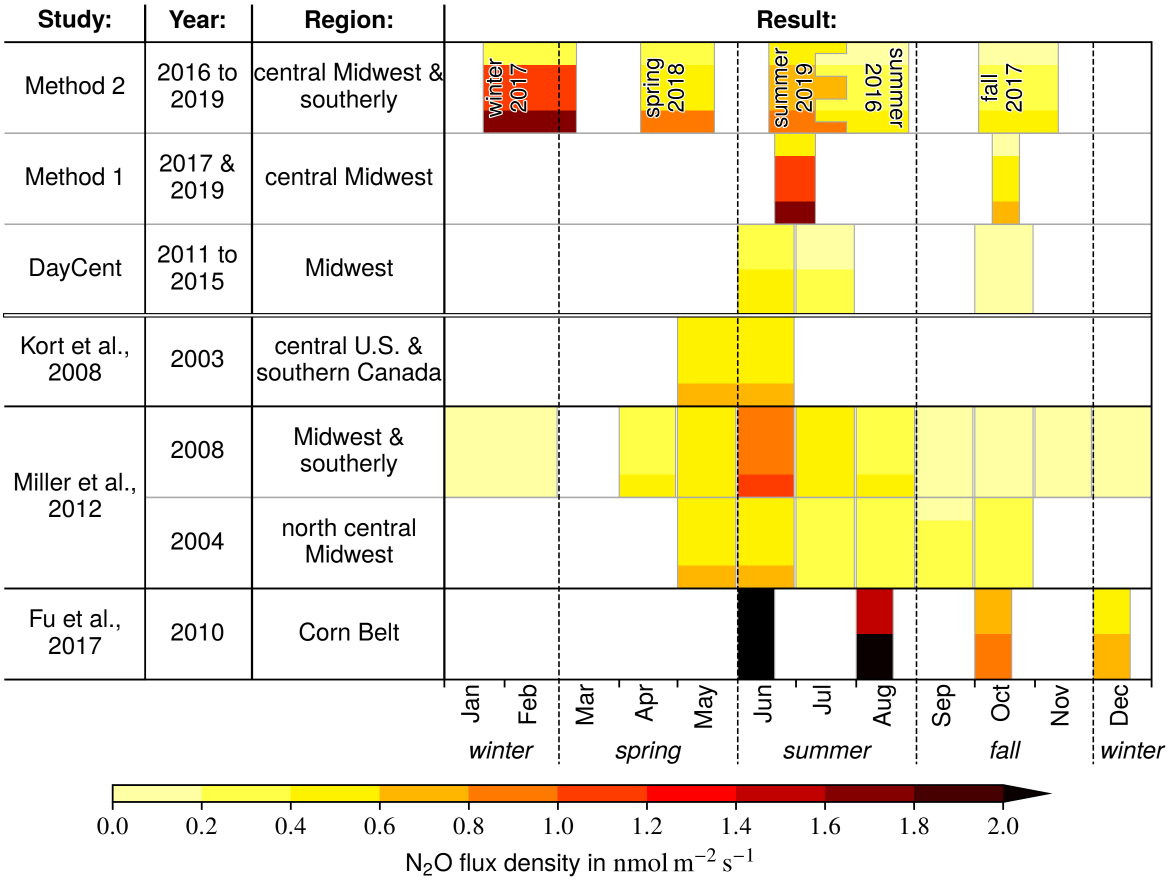

Figure 6.8: Comparison of N_2O emission estimates for the U.S. Midwest. For each study, the central color describes emission averages and the colors above and below indicate the uncertainty range. The range of results for Method 2 is spanned by the lower and upper quartile of estimates. Minimum and maximum DayCent estimates for the years 2011 to 2015 are given. Fu et al. (2017) only provides minimum and maximum estimates as well. Please see text for more details.

Comparison to Results From the DayCent Model:

The process-based model DayCent, introduced in Section 3.4.2, provides more sophisticated bottom-up estimates of soil N_2O emissions than EDGAR. Figure 6.8 displays minimum and maximum DayCent estimates of total agricultural N_2O emissions in the Midwest for June, July, and October from 2011 to 2015. As discussed in the previous Chapter 5, even though the DayCent estimates do not reflect the campaign years itself, they agree better with the scaled emissions, with a very good agreement for summer 2016. A larger discrepancy is found for the comparison with the scaled fluxes for fall 2017, maybe due to unusually much rain in this period (twice as much as on average; see Section 5.5.3). The largest discrepancy is found for the summer 2019 campaign, which can be attributed to the flooding event. Upcoming dedicated DayCent simulations for the campaign periods will be used for further analysis of these assumptions.

Comparison to Other Top-Down Studies:

Finally, the results of this study are compared to available top-down studies quantifying N_2O emissions in the U.S. Midwest and adjacent regions, i.e. Fu et al. (2017), Miller et al. (2012), and Kort et al. (2008). These studies are described in detail in Chapter 5. In short, Kort et al. (2008) and Miller et al. (2012) quantify N_2O emissions by combining airborne flask measurements and tall tower measurements, respectively, with EDGAR emissions using a Bayesian approach. Miller et al. (2012) estimates for the year 2004 are based on continuous measurements while estimates for the year 2008 are based on flask samples taken on a daily basis. Similar to this study, both studies report scaling factors for the EDGAR inventory. The fluxes shown in Figure 6.8 are derived by scaling the respective EDGAR versions (32FT2000 and 4.0) and represent average values for the U.S. Midwest. In contrast, Fu et al. (2017) focuses on estimating N_2O emissions of the Corn Belt using tall tower measurements (continuous as well as daily flask samples) and a forward model approach.

Winter N_2O emission estimates derived herein are significantly larger compared to the results of Miller et al. (2012). For January to February 2008, Miller et al. (2012) estimated N_2O flux densities of less than $0.2\,\mathrm{nmol\,m^{-2}\,s^{-1}}$, while Method 2 emission estimates for winter 2017 are higher (0.3–$1.6\,\mathrm{nmol\,m^{-2}\,s^{-1}}$). This can most probably be attributed to the occurrence of freezing/thawing processes: In Jan–Feb 2017 average temperatures in the central U.S. were significantly higher (271.4 K) than in Jan–Feb 2008 (267.2 K) (NOAA, 2020a). Hence, during the period of the winter 2017 measurements, N_2O emission pulses due to thawing were much more likely than during the measurements in winter 2008. Another reason for the large discrepancy between both studies might be due to the nature of N_2O emission events during freezing/thawing, which are short but intense (a few hours to days; Teepe et al., 2001; Müller et al., 2003). There is an inherent risk that these are missed using the Miller et al. (2012) approach. The low spatial (four tall tower sites) and temporal resolution (daily flask samples) of the measurements therefore might cause a low bias. In contrast, airborne measurements exhibit a higher spatial and temporal resolution and, hence, are better suited to catch such events. In turn, freezing/thawing events may be under- or overrepresented due to a lower temporal coverage compared to tall tower measurements leading to a low or high bias. Overall, a combination of both measurement approaches would be ideal to quantify N_2O emissions which are dominated by freezing/thawing induced N_2O emission pulses.

In spring, summer, and fall, a comparison of all top-down studies generally delivers more consistent results. Average Midwest N_2O emission estimates for the ACT-America field deployments are in line with Kort et al. (2008) and Miller et al. (2012). In spring and early summer average flux densities are largest while in the second half of summer and in fall average estimates are approximately half as large. However, following Miller et al. (2012) fall emissions tend to be lower than summer emissions which is opposite to the results presented here. The flooding influenced summer 2019 emissions are on average 0.2–$0.4\,\mathrm{nmol\,m^{-2}\,s^{-1}}$ larger than Kort et al. (2008) or Miller et al. (2012) 2004 estimates, which is in line with the above estimated effect of the flooding (i.e., $0.18\,\mathrm{nmol\,m^{-2}\,s^{-1}}$). However, June 2008 estimates by Miller et al. (2012) are prominent. With average fluxes within 0.8–$1.0\,\mathrm{nmol\,m^{-2}\,s^{-1}}$ they significantly exceed all other studies (except Fu et al., 2017). They do not provide any explanation for the large June emissions. Estimates provided by Fu et al. (2017) significantly exceed all other studies with maximum fluxes of over 4 nmol m^{-2} s^{-1} in June. This is most likely because Fu et al. (2017) quantifies only the most densely farmed part of the Midwest, the Corn Belt, where N_2O fluxes are largest. The other studies sample, similar to the present study, most of the Midwest plus adjacent regions and fluxes are then averaged over the whole Midwest. Thus, areas with less agriculture and, hence, less N_2O emissions contribute to average emissions leading to lower total estimates.

6.5 Concluding Remarks

A unique and extensive airborne flask measurement dataset sampled above the eastern half of the U.S. and spanning four seasons was used to investigate the seasonality of N_2O emissions in the U.S. Midwest. Using a top-down approach, average emissions in spring 2018 and fall 2017 are found to be approximately 75 % and 13 % larger than in summer 2016, respectively. This is plausible since it follows the seasonality of the fertilization practice. Interestingly, largest emissions are observed during winter measurements in 2017 (roughly 230 % larger than in summer 2016), which can be attributed to freezing/thawing induced N_2O emission pulses, contributing significantly to the Midwest N_2O budget. Agricultural N_2O emissions are also found to be enhanced (by roughly 70 %) during the summer 2019 measurements (compared to summer 2016), most probably due to an unusual strong flooding event in 2019. A comparison between EDGAR bottom-up and top-down estimates shows that, overall, agricultural EDGAR emissions from spring to fall have to be scaled by factors between two and five while winter emissions have to be scaled by factors up to 30, since EDGAR4.3.2 obviously misses the large freezing/thawing induced winter emissions. While EDGAR5.0 N_2O emissions exhibit no seasonality at all, this study further shows that agricultural emissions in EDGAR4.3.2 would reproduce the top-down derived seasonality from spring to fall if shifted by one month. Historical DayCent estimates of total agricultural N_2O emissions in the U.S. Midwest are closer to the scaled emissions than EDGAR but still tend to underestimates emissions. Other top-down studies which quantify Midwest N_2O emissions are rare. Results presented here are consistent with the few previous top-down estimates but uncertainties are large highlighting the need of further studies to fully characterize the seasonality of Midwest N_2O emissions.

The Method 2 approach employed here is a straightforward adaption of Method 1 to exploit results from discrete airborne measurements. A comparison shows that both approaches deliver consistent results for fall 2017 and summer 2019. However, due to the low temporal resolution of PFP measurements, Method 2 is more sensitive to even small errors in the model transport or in the spatial distribution of EDGAR N_2O emissions (see Section 6.2.3). Thus, the derived flux densities inhibit larger uncertainties, nevertheless providing a unique dataset to characterize Midwest N_2O emissions. To allow for a more thorough evaluation of Method 2 and a more accurate quantification of Midwest N_2O emissions, a follow-up study is planned. The envisaged approach will quantify emissions by combining PFP measurements, HYSPLIT footprints, and EDGAR emissions via a more elaborate but well-established Bayesian approach (e.g., Kort et al., 2008; Miller et al., 2012; Thompson & Stohl, 2014; Ganesan et al., 2015; Petrescu et al., 2021).

7 Sensitivity Analysis of the Drivers of U.S. Midwest N_2O Emissions

The results discussed in Chapter 5 and 6 reveal that there is a strong day-to-day and seasonal variability in the N_2O emission strength. This is somewhat expected since the process of soil N_2O emissions is highly complex and depends on a large number of interacting driving parameters (hereafter referred to as "drivers"), which include soil characteristics, weather conditions, and agricultural practices like fertilization (see Section 2.2.2). The two dominant meteorological drivers are soil moisture and soil temperature (Butterbach-Bahl et al., 2013). Motivated by the extraordinary strong emissions observed in winter 2017 (cold temperatures) and summer 2019 (flooding event), this chapter investigates whether a clear correlation can be found between one of the important drivers and the U.S. Midwest soil N_2O emission amounts. Additionally, the importance of precipitation-induced N_2O emission events for the Midwest budget is investigated (**RQ3**).

Similar to the approach presented in the previous Chapter 6, HYSPLIT footprint simulations are used, which are available for all PFP samples collected in the course of the five ACT-America field campaigns. In this case, footprints are combined with ERA5 reanalyses (ERA5, 2017; Hersbach et al., 2020) to analyze the soil conditions and precipitation that may have influenced the results of the PFP measurements. The correlation of footprint soil conditions and precipitation with Midwest N_2O emission estimates based on the results of Chapter 5 (Method 1) and 6 (Method 2) is used to investigate the possible influence of the soil emission drivers. While results of the fall 2017 and summer 2019 campaign (see Method 1 in Chapter 5) are used to discuss the influence on the day-to-day variability of emissions, results based on the PFP dataset (see Method 2 in Chapter 6) are the basis to examine the impact of meteorological drivers in different seasons.

In the following, the approach is presented in Section 7.1. The sensitivity of soil N_2O emissions on the emission drivers is analyzed in Section 7.2 (day-to-day basis) and 7.3 (seasonal basis). Finally, Section 7.4 summarizes and concludes this chapter.

7.1 Footprint Parameter Approach

The goal is to analyze the sensitivity of U.S. Midwest N_2O emissions to soil moisture, soil temperature, and precipitation. To this end, correlations between the Midwest N_2O emissions derived with Method 1 and Method 2 and the drivers at the source region of the emissions (hereafter referred to as “footprint parameters”) are examined. Footprint parameters are constrained by combining HYSPLIT simulations and ERA5 reanalyses. Both datasets are shortly presented in the following Section 7.1.1. The calculation of footprint parameters from these data is described in Section 7.1.2.

7.1.1 Data Basis

HYSPLIT footprints quantitatively describe the sensitivity of a receptor (i.e., PFP sample) to a source region (see Figure 7.1a for an example) and, thus, enable to relate ERA5 fields of soil moisture, soil temperature, and precipitation to the PFP measurements. Since correlations to the results of Chapter 5 and 6 are investigated, the footprints are filtered in the same manner as the PFPs in Method 2: Only footprints remain whose corresponding PFP samples have been collected within the PBL and were dominated by N_2O emissions from soils, ensuring that predominantly soil emissions from the U.S. Midwest and adjacent regions are analyzed (see Section 6.1 for more detailed explanations). As a result, for each ACT-America campaign roughly 50–100 footprints are available, constraining the study region of this analysis, i.e. mostly the central U.S. Midwest and the Gulf Coast (see Figure 6.2 in previous chapter). Analogue to Method 2, the temporally and spatially resolved footprints are in the following considered as one-dimensional arrays $\mathbf{H}$ of length $n_f = n_t \cdot n_{lat} \cdot n_{lon}$, where h_i is the i^{th} component and n_t, n_{lat}, and n_{lon} is the length of the time, latitude, and longitude dimension, respectively (see Section 6.2.1 for more detailed explanations).

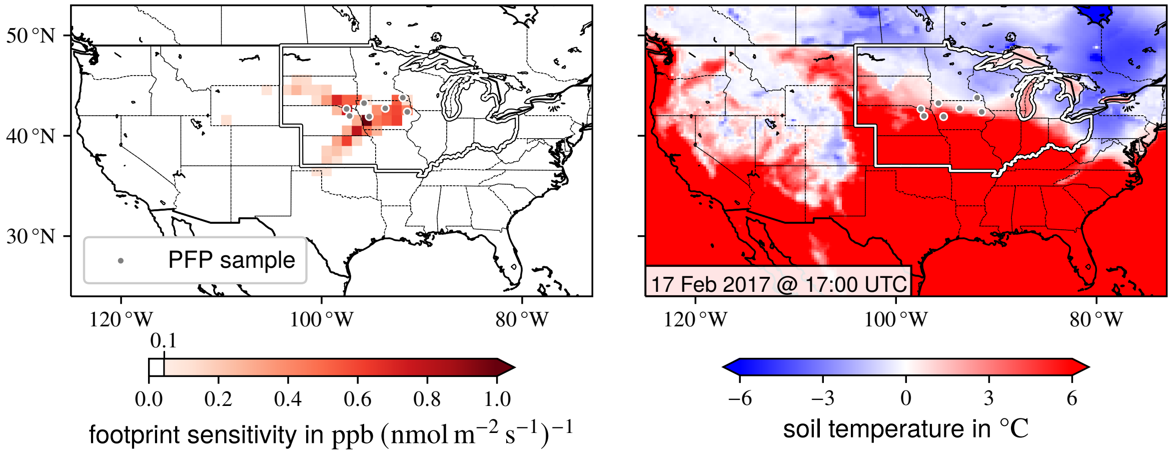

(a) Summed HYSPLIT footprint

(b) ERA5 soil temperature

Figure 7.1: (a) Summed HYSPLIT footprint of all PFPs which have been collected within the PBL between 17:00 and 23:00 UTC on the 17 Feb 2017. (b) ERA5 soil temperature in the uppermost soil layer (from the surface down to 7 cm) at 17:00 UTC on the 17 Feb 2017. The U.S. Midwest in encircled in white.

ERA5 provides hourly gridded fields of soil moisture, soil temperature, and accumulated precipitation with a horizontal resolution of 30 km × 30 km. The soil quantities are available for four different soil layers down to a depth of 289 cm. Several experimental studies exist which

investigate the response of N_2O emissions on varying soil conditions (e.g., Schmidt et al., 2000; Parkin & Kaspar, 2006; Castellano et al., 2010; Kroon et al., 2010; Keane et al., 2018). In these studies, typically soil moisture and temperature in depths down to 30 cm are measured. Thus, here only ERA5 soil parameters in the two uppermost layers are considered, ranging from the surface down to 7 cm and from 7 cm down to 28 cm. Figure 7.1b displays an example ERA5 soil temperature field.
The ERA5 soil moisture is reported as volumetric soil water content Θ. Usually the water-filled pore space (WFPS) is considered to discuss the sensitivity of N_2O emissions to soil moisture and, hence, Θ is converted to WFPS. If Θ_{sat} is the water content at which all pores are filled (i.e., the soil is saturated), then WFPS is defined as:

$$\mathrm{WFPS} = \frac{\Theta}{\Theta_{sat}} \tag{7.1}$$

Θ_{sat} depends on the soil type. In the soil parameterization of ERA5 (ECMWF, 2016) it is distinguished between seven different soil textures with specific Θ_{sat} following van Genuchten (1980) and Clapp and Hornberger (1978). These are used for the conversion.

7.1.2 Methodology

ERA5 reanalysis data of soil temperature, soil moisture, and hourly accumulated precipitation are combined with the HYSPLIT footprints to estimate their influence on the observed N_2O dry air mole fraction. Let $\mathbf{M}^{soil}$, $\mathbf{T}^{soil}$, and $\mathbf{P}$ be the ERA5 fields of soil moisture, soil temperature, and hourly accumulated precipitation on the same grid as the footprint $\mathbf{H}$, where μ_i^{soil}, ϑ_i^{soil}, and p_i is the i^{th} of n_f components, respectively. Averaging $\mathbf{M}^{soil}$ weighted with $\mathbf{H}$, delivers a scalar value M_f^{soil} that constrains the soil moisture at the footprint of a PFP sample (hereafter referred to as "footprint moisture"):

$$M_f^{soil} = \frac{\sum_{i=1}^{n_f} h_i \; \mu_i^{soil}}{\sum_{i=1}^{n_f} h_i} \tag{7.2}$$

$\mathbf{T}^{soil}$ and $\mathbf{P}$ are analogously averaged to estimate the footprint temperature T_f^{soil} and footprint precipitation P_f. These quantities together with M_f^{soil} constrain the average soil conditions or precipitation at the source region of a PFP measurement. Using the uppermost ERA5 soil layer (0–7 cm depth) and the next deeper one (7–28 cm depth) to calculate M_f^{soil} and T_f^{soil} delivers similar results. Thus, in the following only footprint soil conditions based on the uppermost ERA5 soil layer are considered. It has to be noted that since footprints for each single PFP typically span large areas and cover ten days, the weighted averages are characterized by different soil conditions and weather situations. Hence, this approach allows for a qualitative analysis of the sensitivity to different parameters, rather than for a specific, quantitative analysis.

The uncertainty of M_f^{soil}, T_f^{soil}, and P_f is affected by errors in the HYSPLIT footprint as well as by errors in the ERA5 fields. For the footprint soil moisture, uncertainties are additionally introduced by the conversion of volumetric water content to WFPS (see Equation 7.1). These error sources are difficult to quantify. However, it is assumed that due to averaging over a large area and long time period (ten days), errors statistically average out to a certain extent (if they are not systematic). Hence, the final uncertainties of the footprint quantities are assumed to be small enough for a general evaluation of the driving effect of soil conditions and precipitation on N_2O emissions. This assumption is supported by Li et al. (2020), who evaluated the soil moisture and soil temperature in ERA5 and four other widely used reanalysis datasets against observations. Good agreement between model and observations was found with the ERA5 model exhibiting the highest skill.

7.2 Drivers of Daily Emission Variations

To investigate the influence of soil moisture, soil temperature, and precipitation on daily variations of soil N_2O emissions in the U.S. Midwest, the results of Method 1 (see Chapter 5) are compared to the corresponding footprint parameters. Using Method 1, Midwest N_2O emissions were quantified for four flights in fall 2017 and six flights in summer 2019 by scaling agricultural EDGAR emissions. Resulting average Midwest N_2O emissions are within 0.16–1.77 $\mathrm{nmol\,m^{-2}\,s^{-1}}$. Correlations among these top-down derived emissions and the footprint parameters are expected to indicate whether or to what extent the different drivers affect the amount of N_2O emissions and, hence, to study their day-to-day variations. Figure 7.2 displays the top-down derived Midwest N_2O fluxes against the footprint soil moisture M_f^{soil} (left panel), the footprint soil temperature T_f^{soil} (central panel), and the footprint precipitation P_f (right panel) of the ten PBL transects. For each of the transects, the average PFP footprint quantity is displayed with the error bars indicating minimum and maximum values.

According to the correlation, the influence of the soil moisture on the N_2O emissions is small. The average M_f^{soil} (see left panel of Figure 7.2) during all transects ranges between 50 % and 70 % WFPS. Theoretically, the N_2O soil emissivity is maximal for a WFPS of 70–80 % (see Section 2.2.2) and, thus, in the observed WFPS range a positive correlation between M_f^{soil} and the Midwest N_2O emissions is expected. However, there is no obvious or a negative correlation, also if 2017 and 2019 results are treated separately, indicating that the soil moisture does not have a strong impact on the emissions of the ten investigated days.
In contrast, the soil temperature shows a somewhat clearer positive correlation with N_2O emissions ($R = 0.59$), which is expected since increasing soil temperatures favor soil N_2O emissions (see Section 2.2.2). For soil temperatures between 285 K and 295 K, Midwest fluxes increase moderately with temperature and for temperatures around 295 K emissions increase strongly. The only exception in the correlation are the results of the flight on Jun 20, 2019. Highest Midwest N_2O fluxes are calculated, while corresponding soil temperatures are moderate (292 K). In this particular case, other drivers or a combination with other drivers, like the comparatively high soil moisture (left panel), might have a stronger impact. Another important factor is the application of N-fertilizer, which is known to boost emissions. However, detailed data about time and location of fertilizing activities are not available. The negative correlation between soil moisture and temperature is prominent. The heat capacity of soils increases with the soil moisture (Ochsner, 2019), which explains why wet/dry soils tend to be cooler/warmer. This is further considered in the following Sections 7.3.1 and 7.3.3.

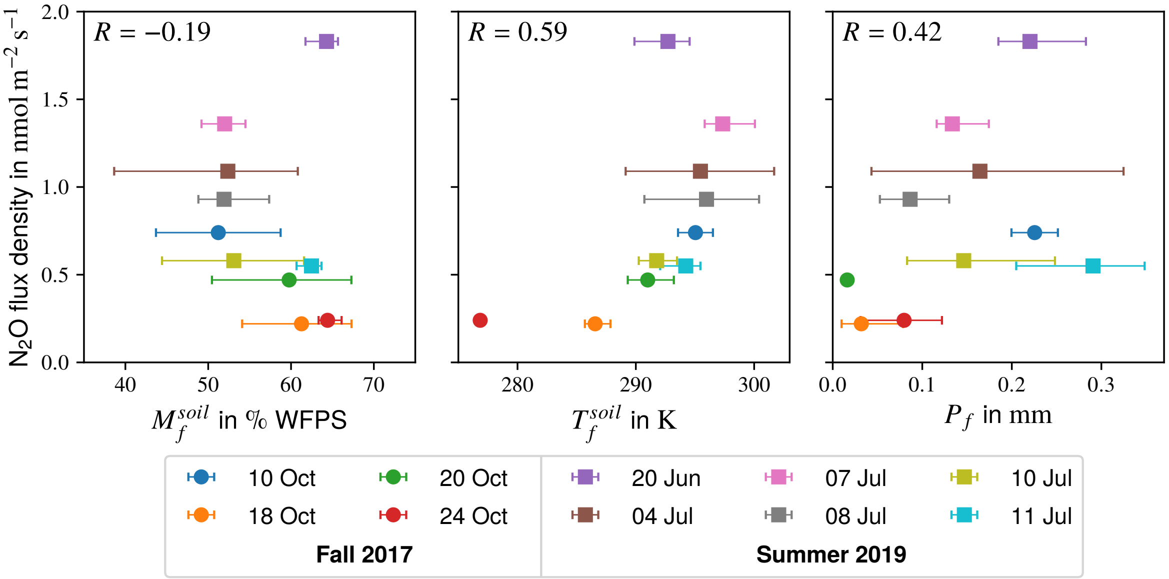

Figure 7.2: Footprint soil conditions vs. U.S. Midwest N_2O emissions derived with Method 1 (see Chapter 5). Displayed are the footprint WFPS M_f^{soil} (left panel), soil temperature T_f^{soil} (center panel), and hourly accumulated precipitation P_f (right panel), averaged over all PFPs which were collected during the ten analyzed PBL transects. The ranges indicate the minimum and maximum PFP footprint quantity of the respective transect. M_f^{soil} and T_f^{soil} are based on ERA5 data in the uppermost soil layer (0–7 cm depth).

Another parameter well known to induce soil N_2O emissions is the moistening of soils by precipitation (see Section 2.2.2). This effect also influences the results of the top-down study as indicated by the positive correlation between footprint precipitation and Midwest N_2O fluxes ($R = 0.42$; see right panel in Figure 7.2). However, the exact relationship between P_f and N_2O fluxes is not clear. Overall, more precipitation appears to favor soil N_2O emissions but other drivers probably play a more dominant role regarding the variations among top-down derived Midwest fluxes of the ten transects. Following the discussion above, soil temperature is the most dominant of the three investigated drivers.

In summary, the day-to-day variations in the top-down derived Midwest N_2O fluxes seem to be driven by soil temperature, while soil moisture probably plays only a minor role since otherwise a positive correlation between emission estimates and M_f^{soil} would be observed (see previous paragraph). Additionally, precipitation events may enhance daily emission estimates like expected from other studies (e.g., Nakayama et al., 2020). The observed non-linear relationship between N_2O emissions and soil temperature is in line with other experimental studies (see Section 2.2.2; Schindlbacher et al., 2004; Schaufler et al., 2010). However, a detailed comparison is difficult, since the relationship strongly depends on various parameters like soil type and vegetation.
Overall, it has to be pointed out that this sensitivity analysis is a strongly simplified consideration. Although soil moisture and temperature are generally assumed to be the most important drivers

of soil N_2O fluxes, it cannot be ruled out that other drivers like the planted crop type or soil pH-value also contribute to the observed day-to-day variations of Midwest N_2O fluxes. Furthermore, the driving effect of soil moisture, soil temperature, and precipitation also depends on the soil type, preceding soil conditions, reactive N availability, crop type, and much more (see Section 2.2.2). Additionally, synergies and asynergies among the drivers exist and, thus, they are spatially and temporally highly heterogeneous. The employed footprints which are used to relate N_2O emissions to soil conditions cover large areas and, hence, a wide variety of soil conditions and properties. Averaging them enables to detect the dominant drivers on a regional scale, while locally the situation might be completely different. However, with the available data neither can the individual contributions of the drivers be quantified nor can their heterogeneity be investigated. Therefore, a process-based model like DayCent is required enabling the simulation of the full complexity of soil N_2O emissions and thus the contributions of different drivers.

7.3 Dominance of Drivers in Different Seasons

To study the dominant drivers of soil N_2O emissions during different seasons, a similar analysis as in the previous Section 7.2 is utilized, based on all ACT-America field data. Footprint soil conditions (M_f^{soil} and T_f^{soil}) and precipitation (P_f) are compared to the corresponding Midwest N_2O emissions derived with Method 2 for each collected PFP sample. While in the previous Chapter 6 the average of the top-down derived emissions on a campaign basis is discussed, in this section the variability is considered reflecting the heterogeneity of N_2O emissions which is caused by the influence of the drivers. Hence, studying the relationship between M_f^{soil}, T_f^{soil}, and P_f and the top-down derived Midwest emissions of individual PFPs allows to investigate their possible influence.

Correlations between footprint driver quantities and N_2O emissions are used to detect the dominant drivers during all campaigns. Figure 7.3 displays the footprint soil moisture (left column), footprint soil temperature (center column), and footprint precipitation (right column) of all PFPs (collected within PBL and dominated by soil N_2O emissions; see Section 7.1.1) against their top-down derived N_2O emissions. The five ACT-America campaigns are considered separately (rows). Lowest Midwest N_2O emissions are derived for summer 2016, followed by fall 2017, and spring 2018. Summer 2019 emissions are larger, probably due to the extreme flooding event in this year. Winter 2017 fluxes are dominated by a few extreme emission events which significantly exceed the estimates for the other campaigns. M_f^{soil} and P_f are comparable among the five campaigns while T_f^{soil}, like expected, tends to be higher in summer, followed by spring and fall, and is lowest in winter.
Overall, correlations between N_2O emissions and soil moisture, soil temperature, and precipitation are weak. Each campaign spans six weeks and covers large areas and, hence, significantly different soil properties and conditions were sampled. As a result, the contributions of different emission drivers to each PFP sample can be highly variable weakening the correlations, unless a single driver dominates significantly. However, the present analysis enables to study whether the most important driver for each season can be identified and to investigate the dominant

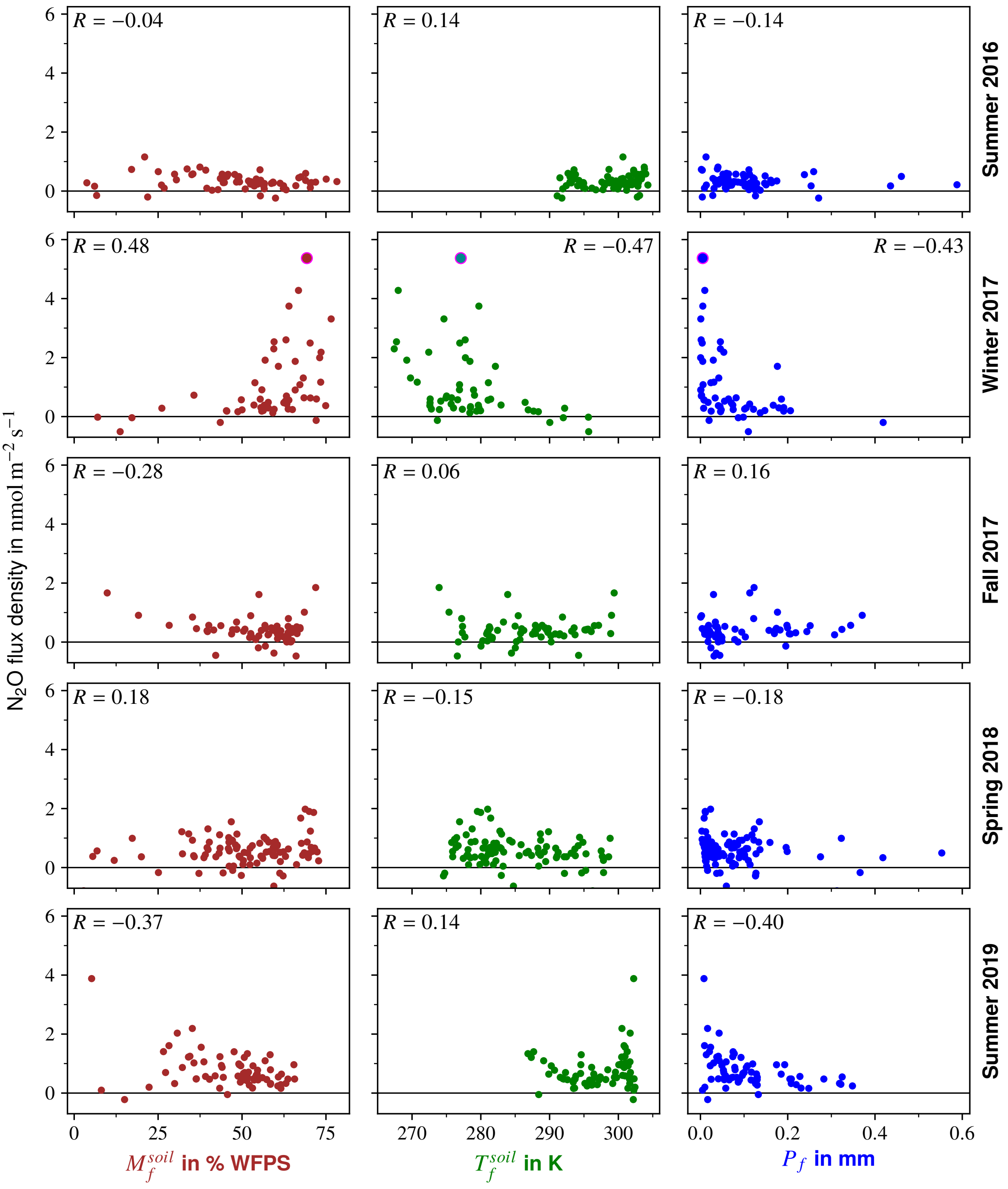

Figure 7.3: Footprint soil moisture M_f^{soil} (left column), soil temperature T_f^{soil} (center column), and precipitation P_f (right column) vs. U.S. Midwest N_2O emissions derived with Method 2 (see Chapter 6) for all five ACT-America campaigns (rows). Respective correlation coefficients R are indicated. Only footprint quantities of PFPs collected within the PBL and dominated by soil emissions are shown (see Section 6.1). M_f^{soil} and T_f^{soil} are based on ERA5 data in the uppermost soil layer (0–7 cm depth). In winter 2017 (second row), one PFP sample is highlighted (magenta border). This measurement is further considered in Section 7.3.2.

drivers for exceptional emissions events.
The large heterogeneity of N_2O emissions as well as of the emission drivers and the resulting low correlation between emission estimates and M_f^{soil}, T_f^{soil}, and P_f also explains the difference in correlations presented here compared to correlations discussed in the previous Section 7.2. In the previous section, ten days are analyzed and, hence, soil conditions and properties are most likely more comparable during the measurement periods than if measurements spanning several weeks and a larger area are considered. As a result, correlations observed in the previous section are not/less visible in Figure 7.3.

7.3.1 Summer 2016 and 2019: Influence of the Extreme Flooding Event

Compared to other seasons, maximum soil N_2O fluxes are small in summer 2016. This can certainly be traced back to the limited availability of reactive N-compounds in soils, which is low in summer compared to spring and fall because less fertilizer is applied (see Section 6.4.1). As shown in the first row of Figure 7.3, the effect of soil moisture, soil temperature, and precipitation on soil N_2O emissions in the study region is ambiguous. Only the footprint soil temperature is weakly positive correlated to the emissions, indicating that this is the most dominant of the three drivers considered.
For a more differentiated analysis, Figure 7.4 shows a zoomed excerpt of the soil temperature against the N_2O emissions derived for summer 2016 (left panel) and summer 2019 (right panel), color-coded with the soil moisture. Overall, colder soils tend to be wetter while warmer soils tend to be dryer. Hence, the driving effect of soil temperature appears to be counteracted by the soil moisture and vice versa which might cause the generally weak correlations between footprint soil conditions and emissions. However, for temperatures higher than 295 K the driving effect of soil temperature is visible, probably because of the nonlinear response of soil N_2O fluxes to increasing soil temperatures (see Section 2.2.2 and Schaufler et al., 2010). In contrast, for temperatures below 295 K, the driving effect of soil moisture seems to be more important, since relatively wet soils (M_f^{soil} around 70 % WFPS) appear to induce the variability in the derived flux densities. However, T_f^{soil} is mostly higher than 295 K and, hence, in general soil temperature probably plays a more important role in summer 2016 than soil moisture.

The results for the summer 2019 campaign (last row in Figure 7.3) indicate that also the soil temperature is the dominant of the three N_2O emission drivers considered, since only T_f^{soil} is weakly positive correlated to the emissions. For temperatures above 295 K, the correlation between T_f^{soil} and the emissions is positive (see Figure 7.4 right panel). Soil temperatures of 300 K seem to explain the large emissions for a low soil moisture around 30 % WFPS. However, although in general warming of soils favors N_2O fluxes, below 295 K emissions decrease for increasing soil temperatures. The soil moisture is most likely not responsible for that since M_f^{soil} is relatively constant. Overall, no reason for this negative correlation between soil temperature and emissions could be found.

Differences between both summer campaigns can partly be attributed to the different timing of observations. Measurements in 2019 occurred approximately one month earlier than in 2016 (see Section 6.1). Thus, average soil temperatures are slightly lower in 2019 ($\overline{T}_f^{soil} = 297\,\mathrm{K}$)

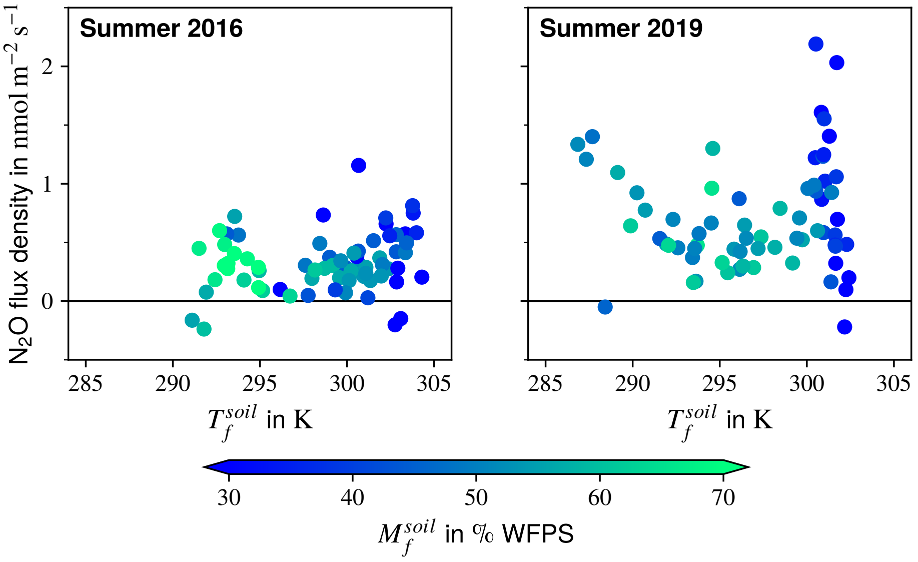

Figure 7.4: Zoom in footprint soil temperature T_f^{soil} vs. U.S. Midwest N_2O emissions derived with Method 2 for the summer 2016 (left panel) and summer 2019 (right panel) campaign, color-coded with the footprint soil moisture M_f^{soil}.

than in 2016 ($\overline{T}_f^{soil}$ = 299 K) and, hence, the driving effect of soil temperature is probably less pronounced. Additionally, in 2019 more reactive nitrogen might be available because the campaign is closer to the main fertilization activities in spring (see Section 6.4.1) leading to larger emission events.

Another obvious explanation for the differences between the two summer campaigns is the exceptional flooding in 2019. Due to this event, conditions in the Midwest were extreme and as outlined in Chapter 5, the planting season was significantly delayed. Hence, in June/July 2019 probably more fertilizer is applied than usual in this time of the year, probably leading to unusually large direct N_2O emissions. Indirect emissions are most likely enhanced as well, because flooding presumably boosts runoff (see Section 5.5.3). Interestingly, unlike expected due to the flooding, the soil moisture in general does not significantly differ in the study region between 2016 ($\overline{M}_f^{soil}$ = 48 % WFPS) and 2019 ($\overline{M}_f^{soil}$ = 46 % WFPS). However, at specific times and in specific regions of the Midwest, the flooding enhanced the soil moisture. Figure 7.5 shows the ERA5 soil moisture in May and June averaged over the U.S. Midwest region. In June 2019, soils were not unusually wet compared to the 2000–2020 average while in May 2019, soils were wetter than usual in this time of the year. On the one hand, this might lead to enhanced soil emissions in May but, on the other hand, might dampened N_2O fluxes if soils were water saturated (see Section 2.2.2). However, emissions presented here appear to be not influenced by flooding induced wetter than average conditions. As a conclusion, the delayed growing season and fertilization activity seems to be the main reason for the large N_2O emissions during the 2019 field deployment.

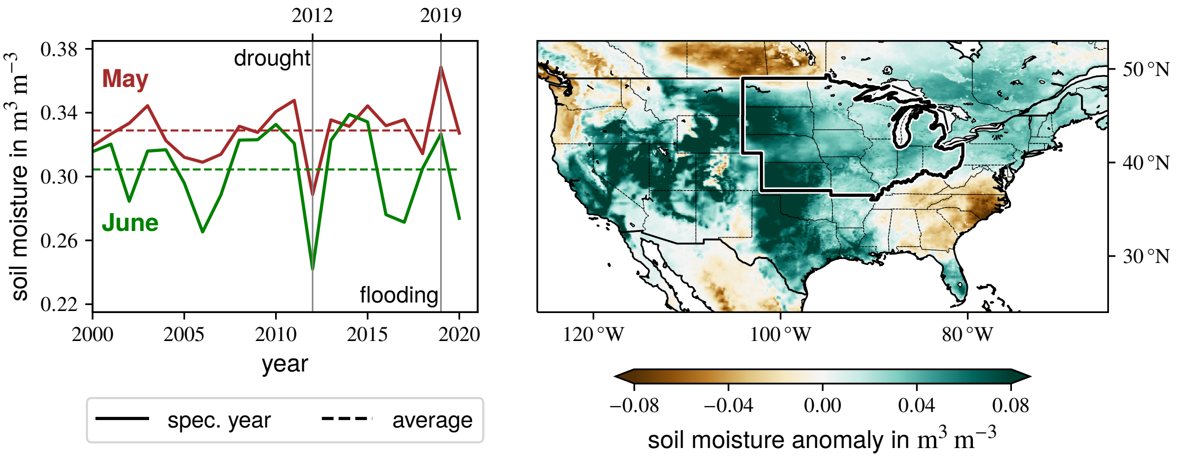

(a) Soil moisture in May and June

(b) Soil moisture anomaly in May 2019

Figure 7.5: ERA5 soil moisture (Muñoz Sabater, 2019) in May and June in the uppermost soil layer (0–7 cm depth) averaged over the U.S. Midwest region. (a) Time series of the soil moisture in May and June. The 2012 drought (see Section 5.4) and the 2019 flooding is indicated. (b) Map of the deviation of the soil moisture in May 2019 from the 2000–2020 average for May. The U.S. Midwest is encircled in black.

7.3.2 Winter 2017: Influence of Freezing/Thawing Events

Winter 2017 (second row in Figure 7.3) is characterized by exceptional large N$_2$O emissions in the study region (up to nearly 6 nmol m^{-2} s^{-1}). A strong impact of precipitation induced emission pulses of N$_2$O can be excluded, since largest emissions are found for lowest values of P_f in combination with a negative correlation towards higher P_f. Furthermore, the observed range of P_f is similar (or even less pronounced) compared to the other ACT-America deployments, indicating that precipitation does not explain the large deviation. The large emissions come along with a footprint soil moisture of around 70 % WFPS which is mostly favorable for the release of soil N$_2$O emissions. However, during the other ACT-America deployments, similar M_f^{soil} values are observed together with much lower emissions (<3 nmol m^{-2} s^{-1}), indicating that the soil moisture is not predominantly responsible for the large winter emissions.

However, the observed soil temperatures are, as expected from a winter deployment, generally lower compared to the other campaign periods. Figure 7.6a displays the probability density of T_f^{soil} during the winter deployment. Footprint soil temperatures are mainly around the freezing point (265–280 K), indicating that freezing/thawing processes (see Section 2.2.2 and Butterbach-Bahl et al., 2013) are predominantly responsible for the extreme emissions in winter 2017. A footprint is typically distributed over a large area and, thus, an average footprint soil temperature of 265 K to 280 K may also cover regions where the soil freezes and thaws. Figure 7.6b, which shows the distribution of soil temperatures yielding T_f^{soil} of a single PFP measurement, demonstrates this. While T_f^{soil} is 277 K for this PFP sample, a significant part of the footprint area exhibits soil temperatures around the freezing point which potentially induces N$_2$O emission bursts. Teepe et al. (2004) investigated the influence of freezing duration and soil moisture on thawing induced N_2O emissions for different soil types in a laboratory experiment. They found that an increased freezing duration significantly increases emissions on thawing. The influence of soil moisture is important as well, with largest emissions occurring for a WFPS of 64 %. Thus, the encountered footprint soil moisture (60–75 % WFPS) is an important prerequisite for the freezing/thawing induced large N_2O emissions. Since winter 2017 measurements predominantly occurred at the end of winter, it is also likely that long freezing periods preceded the thawing events contributing to the large emissions.

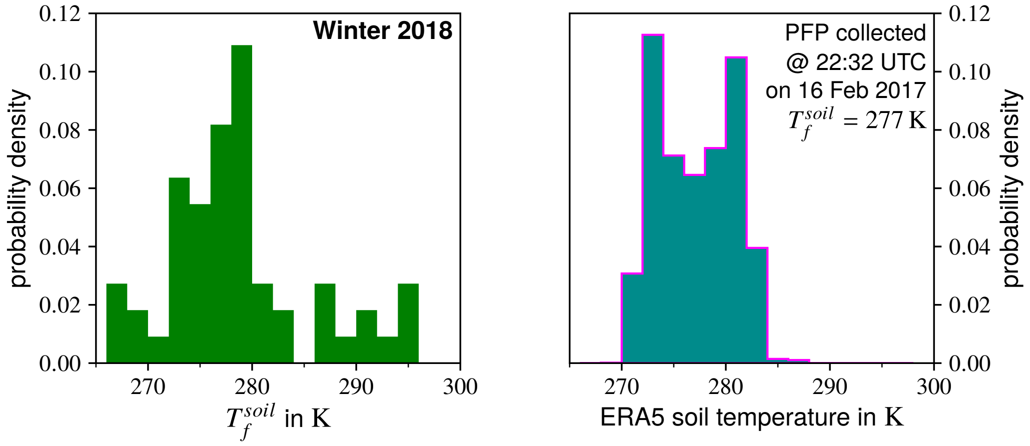

(a) Campaign

(b) Single PFP sample

Figure 7.6: (a) Probability density of footprint soil temperature T_f^{soil} during the ACT-America deployment in winter 2017. (b) Probability density of ERA5 soil temperature yielding T_f^{soil} of a single PFP measurement. The corresponding PFP sample is highlighted in Figure 7.3.

In summary, the results of this sensitivity study suggest that N_2O emissions in the study region in winter 2017 are governed by freezing/thawing processes. However, to study the effect of freezing/thawing induced N_2O emissions, a more detailed analysis is needed including dedicated measurements and simulations of the underlying processes with a process-based model.

7.3.3 Spring 2018 and Fall 2017

Distributions of footprint soil moisture, soil temperature, and precipitation are similar in fall 2017 and spring 2018 (third and fourth row in Figure 7.3, respectively). However, typically more reactive N-compounds are available in spring due to the application of a higher amount of fertilizer (see Section 6.4.1) leading to generally higher emissions compared to fall. In both seasons precipitation induced N_2O emission events are not the dominant reason for the observed N_2O enhancements as indicated by the weak correlations between P_f and Midwest emissions. Neglecting very dry soils with a WFPS of less than 25 %, the correlations of the soil moisture are slightly positive while correlations of the soil temperature are near zero or negative. Thus, in spring 2018 as well as in fall 2017 the driving effect of soil moisture seems to slightly dominate with largest N_2O fluxes around 70 % WFPS. However, results are ambiguous because soil moisture and temperature are correlated. Figure 7.7 shows M_f^{soil} against T_f^{soil} for the fall 2017 (left panel) and spring 2018 (right panel) field campaigns. The correlations between soil moisture and temperature are negative. Hence, like in summer 2016 (see Section 7.3.1), the driving effect of soil moisture appears to counteract the driving effect of soil temperature, resulting in weak correlations with the N_2O emissions.

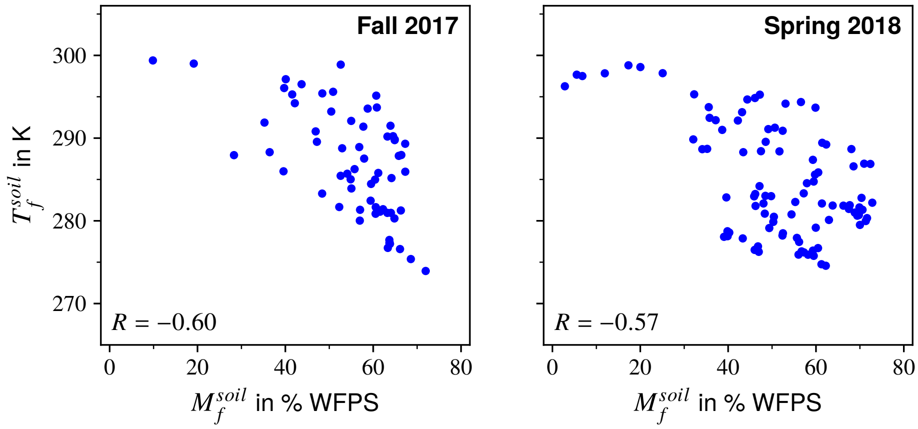

Figure 7.7: Footprint soil moisture M_f^{soil} vs. footprint soil temperature T_f^{soil} for the ACT-America field deployments in fall 2017 (left panel) and spring 2018 (right panel). Only footprint quantities of PFPs collected within the PBL and dominated by soil emissions are shown (see Section 6.1).

Freezing/thawing processes might also influence spring and fall N_2O emissions in the study region. Figure 7.8 displays the climatological first and last 0 °C freeze in the U.S. In the northern half of the Midwest, freezing starts in September and in the southern half in October (see Figure 7.8a). Farther south the first freeze occurs in November and at the Gulf Coast in December. The last day with temperatures below 0 °C is in May/April in the Midwest and in March farther south (see Figure 7.8b). Thus, during the fall 2017 (October/November) as well as during the spring 2018 campaign (April/May), frost and hence also freezing/thawing induced N_2O fluxes are likely. However, the magnitude of such emissions is expected to be much lower than in winter 2017 due to two reasons. First, the soil temperature in spring and fall is generally higher than in winter. Although parts of the footprints may experience soil frost, the share is most likely smaller than during winter 2017 and, hence, also the sampled N_2O enhancements emitted on thawing. Second, N_2O fluxes on thawing increase with the preceding freezing duration (see Section 7.3.2). In spring and fall short freezing periods of, e.g. only one night are common, leading to much less thawing induced N_2O emissions compared to winter, where typically long-term freezing periods prevail.

7.4 Concluding Remarks

HYSPLIT footprints, available for all PFP samples collected in the course of five ACT-America campaigns in four seasons, were used to investigate correlations between U.S. Midwest soil

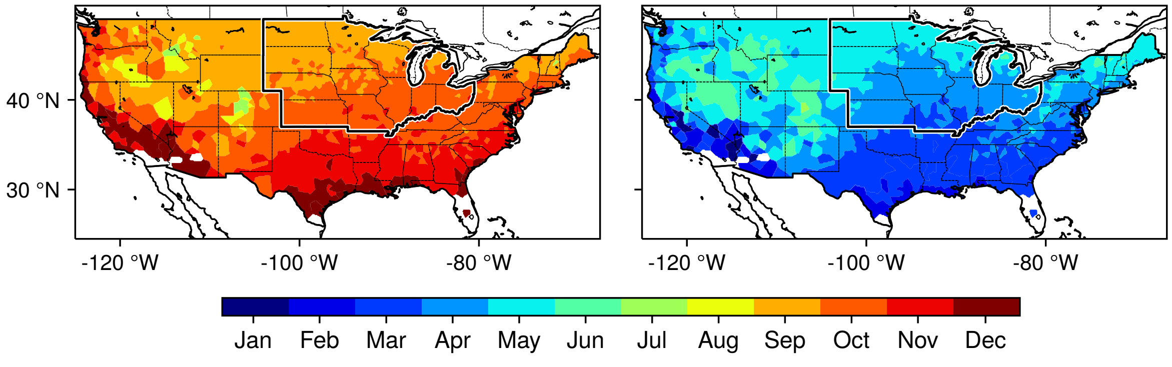

(a) Median first 0 °C freeze

(b) Median last 0 °C freeze

Figure 7.8: Climatology of first (a) and last (b) 0 °C freeze in the U.S. In total, 1350 stations across the country recorded freezing days from 1980 to 2009. Here, for each station the median of the period of record is shown gridded via nearest neighbor interpolation. The U.S. Midwest is encircled by a thick black line. Data obtained from the Vegetation Impact Program by the Midwestern Regional Climate Center (VIP-MRCC, 2021).

N_2O emissions and their dominant meteorological drivers, i.e. soil moisture, soil temperature, and precipitation. By combining the footprints with ERA5 reanalyses, the soil conditions and precipitation that may influence the measurements were estimated. Correlations between these footprint parameters and Midwest N_2O emissions derived with Method 1 and Method 2 were then used to analyze the most dominant drivers of soil emissions.

The comparison of footprint parameters and the results of Method 1 shows that soil temperature appears to significantly drive day-to-day variations in the top-down derived Midwest N_2O emissions while soil moisture seems to only play a minor role. Furthermore, precipitation likely enhances daily emission.
The comparison of footprint parameters and the results of Method 2 shows that, overall, in soils which are warmer than 295 K, the soil temperature seems to be the dominant driver of U.S. Midwest N_2O emissions while in cooler soils, the soil moisture seems to be more dominant. Hence, summer emissions tend to be temperature-driven while spring and fall emissions tend to be moisture-driven. Additionally, in spring and fall freezing/thawing induced emissions pulses are possible. In winter 2017, extreme emission events are observed which are induced by freezing/thawing processes. The flooding event in 2019 and the resulting delay of the planting season most likely enhances N_2O emissions in June, probably because (shortly preceding) fertilizer application rates are larger than usual in this time of the year. Despite the flooding, soil conditions and precipitation are found to not differ significantly between the two summer campaigns, indicating that these drivers are not responsible for the large summer 2019 emissions. For a comparison with the results presented herein, no other studies which investigate drivers of N_2O emissions on a seasonal and regional scale were found.

With the available data and methods, the most important drivers of soil N_2O emissions can be constrained and the drivers for exceptional emission events can be investigated. However, for a more explicit and quantitative analysis of soil N_2O emission drivers in the U.S. Midwest, more dedicated measurements are needed to capture the large heterogeneity of soil emissions. Airborne measurements are well-suited therefore as they provide a large spatial coverage. Additional simulations with a process-based model could provide further valuable insights into soil N_2O emissions and might enable a quantification of the contributions of the underlying emission drivers.

8 Summary and Conclusion

N_2O is an important anthropogenically emitted long-lived GHG and the dominant ozone depleting substance in the stratosphere. Despite its crucial role in the atmosphere, N_2O is (nearly) not considered in national emission reduction plans which have been submitted to the Paris Agreement. Since more vigorous efforts are necessary to meet the target of the Paris Agreement, the need to reduce anthropogenic N_2O emissions becomes undeniable. The urgency of this matter is underlined by an unexpected strong increase of N_2O emissions in recent years. To develop efficient mitigation strategies, detailed knowledge about sources and sinks of N_2O is essential. However, due to the absence of direct atmospheric N_2O measurements and the complexity of processes that drive N_2O emissions, emission estimates are rare and the few existing estimates exhibit large uncertainties, especially on a regional scale. A hotspot of N_2O emissions is the U.S. Midwest. The agriculture in this region is one of the most productive in the world but also causes large N_2O emissions which are of global relevance. Although being an important N_2O source region, emissions in the Midwest are only insufficiently characterized.

This thesis aims at demonstrating the ability of the chosen top-down approach to evaluate bottom-up estimates of regional N_2O emissions and, thus, to pave the way for the development of emission reduction strategies. It is hypothesized (see Chapter 1) that airborne in situ measurements are well-suited to characterize N_2O emissions in an intensively cultivated agricultural region and to evaluate bottom-up inventories. To test this hypothesis, N_2O emissions in the U.S. Midwest have been characterized using high-resolution airborne in situ measurements and model simulations. To this end, a QCLS has been optimized for N_2O measurements and was successfully deployed during two of five ACT-America campaigns gathering a unique continuous in situ N_2O dataset above the Midwest. Together with nearly 1400 PFP measurements, which were collected during all five ACT-America campaigns, an exceptional N_2O dataset covering four seasons was available to characterize Midwest N_2O emissions. Resulting top-down emission estimates were compared to two state-of-the-art bottom-up inventories, namely EDGAR and DayCent. The following three research questions were answered to test the hypothesis:

RQ1: Can N_2O emissions in the U.S. Midwest be quantified by using regional-scale airborne in situ measurements in combination with atmospheric transport model simulations?

Regional-scale airborne in situ measurements of N_2O together with atmospheric transport model simulations are well-suited to quantify N_2O emissions from an intensively cultivated agricultural region. Two different top-down approaches were used to constrain N_2O emissions in the U.S. Midwest:

Method 1: Continuous N_2O measurements of ten research flights above the U.S. Midwest were used to quantify emissions in October 2017 and June/July 2019. With regional WRF-Chem forward simulations, N_2O enhancements emitted from the EDGAR inventory were propagated through the atmosphere and compared to the observations. Discrepancies were minimized by scaling agricultural emissions in EDGAR, thus quantifying emissions. While this approach is already established to constrain CH_4 emissions, it is novel for N_2O. Resulting Midwest N_2O emissions for October 2017 and June/July 2019 are $0.42\,\mathrm{nmol\,m^{-2}\,s^{-1}}$ and $1.06\,\mathrm{nmol\,m^{-2}\,s^{-1}}$, respectively (see Figure 5.9). The uncertainty, evaluated by a Monte Carlo approach, is on the order of 50 % due to errors in the model simulations and uncertainties in the observed N_2O background mole fraction. Daily variations are observed to be large, as expected from the high spatio-temporal variability of soil N_2O emissions. It is shown that an extreme flooding event in 2019 most likely enhanced emissions.

Method 2: PFP N_2O measurements of all five ACT-America field campaigns were used to analyze the seasonality of Midwest N_2O emissions. Up to twelve air mass samples have been collected during each research flight, summing up to 50–100 datapoints per campaign which were used to analyze soil N_2O emissions from the Midwest. Such discrete measurements have the inherent risk of undersampling by missing smaller-scale structures. Hence, results were summarized for each, individual campaign dataset and discussed on a campaign-basis to allow for a statistically large enough sample size. With dedicated HYSPLIT footprints already available within the ACT-America framework, N_2O enhancements emitted from the EDGAR inventory were simulated. As in the previous top-down approach, agricultural EDGAR emissions were scaled to minimize the discrepancy between observation and simulation. Resulting Midwest N_2O emissions are largest in winter 2017 (0.29–$1.60\,\mathrm{nmol\,m^{-2}\,s^{-1}}$), followed by spring 2018 (0.36–$0.82\,\mathrm{nmol\,m^{-2}\,s^{-1}}$), fall 2017 ($0.20$–$0.48\,\mathrm{nmol\,m^{-2}\,s^{-1}}$), and summer 2016 ($0.20$–$0.43\,\mathrm{nmol\,m^{-2}\,s^{-1}}$) (see Figure 6.5). Mainly due to fertilization activity, emissions in spring and fall are about 75 % and 13 % larger than in summer, respectively. Average winter estimates exceed the summer estimates by roughly 230 % due to extreme soil N_2O emission events induced by freezing/thawing processes (see answer to **RQ3**). The exceptional flooding event in 2019 caused a delay of the growing season in the Midwest, leading to roughly 70 % larger agricultural emissions than usual in this time of the year.

Challenging for regional top-down studies is the large spatio-temporal heterogeneity of soil N_2O emissions which is especially relevant in intensively cultivated agricultural regions. Airborne measurements with their great spatial coverage on several days are well-suited to capture this heterogeneity. Using continuous (Method 1) instead of point measurements (Method 2) enables to analyze N_2O emissions of individual transects or flights rather than on a campaign basis and, thus, enables a more specific quantification of a region. A prerequisite for both top-down approaches is that the spatial distribution of N_2O emissions is well known. While Method 1 is relatively insensitive to errors in the spatial distribution, Method 2 is sensitive because simulations and observations are compared point-wise. Interpreting the PFP measurements and HYSPLIT footprints with a Bayesian approach is expected to deliver more robust results and is planned in the near future (see Chapter 9). However, a comparison between both top-down approaches shows that results agree within their uncertainties. Results are also in the range of previous, ground-based top-down studies, which focus on specific locations of the Midwest, giving confidence in the emission estimates presented herein.

RQ2: How do state-of-the-art bottom-up estimates of N_2O emissions in the U.S. Midwest compare to the airborne top-down emission estimates derived herein?

Monthly *Tier 1–2* estimates of the two most recent EDGAR versions (4.3.2 and 5.0) were considered as well as historical DayCent *Tier 3* estimates of soil N_2O emissions for June, July, and October 2011–2015. *The emission factor-based EDGAR inventory significantly underestimates N_2O emissions in the U.S. Midwest, while emissions estimated with the biogeochemical model DayCent are closer to the herein derived top-down estimates.*

Agricultural EDGAR emissions have to be scaled by average factors between five and ten to meet the top-down emission estimates for October 2017 and June/July 2019, respectively (Method 1). On a daily basis, scaling factors up to even 20 (20 Jun 2019) are derived. For summer 2016, spring 2018, and winter 2017, EDGAR emissions have to be scaled by factors between two and ten to obtain the best agreement between bottom-up and top-down estimates (Method 2). Scaling factors differ between the two EDGAR versions evaluated herein, because only version 4.3.2 includes a seasonal cycle. This seasonality is consistent with the top-down derived seasonal variations in the Midwest from spring to fall, but EDGAR's growing season starts roughly one month earlier. Furthermore, the EDGAR seasonality lacks the large winter emissions in the Midwest (see answer to **RQ1**). Overall, EDGAR significantly underestimates Midwest N_2O emissions because the emission factors do not capture the regional characteristics of the Midwest (e.g., agricultural practice, soil characteristics, meteorology), which strongly influence N_2O emissions. Especially when conditions are unusual, differences between EDGAR and the top-down estimates are large. A prominent example of this is demonstrated by the case studies analyzed during the flooding in 2019 – scaling factors of up to 20 are derived.

DayCent estimates of direct soil N_2O emissions were available for the Midwest on a monthly basis from 2011 to 2015. Although these estimates do not cover the ACT-America measurement years (2016–2019), the comparison with N_2O fluxes derived herein allows to evaluate the potential of such *Tier 3* emission estimates. DayCent estimates for summer are two to three times lower than the top-down estimates for June/July 2019 and, hence, perform significantly better than EDGAR (factor around ten). Contrary, DayCent October estimates are similar to EDGAR, i.e. by a factor of approximately five lower than the top-down estimates for October 2017. DayCent simulations which are driven by the specific conditions during the measurements are expected to be closer to the top-down estimates. Overall, it is shown that, as expected, DayCent is better suited to quantify regional N_2O emissions than EDGAR, since DayCent considers regional characteristics such as soil conditions and weather. However, due to the complexity of the processes parameterized in the model and large inaccuracies in the input data (e.g., fertilization application rates) top-down studies as the one presented here are absolutely necessary to evaluate the model.

RQ3: Can dominant drivers of N_2O emissions in the U.S. Midwest be identified using regional-scale airborne in situ measurements and atmospheric transport model simulations?

Airborne flask measurements and atmospheric transport model simulations are a useful tool to constrain the dominant drivers of N_2O emissions in the U.S. Midwest but they have limitations regarding quantifying their influence. Earlier studies have shown that Midwest N_2O emissions are dominated by soil emissions which are predominantly driven by soil moisture, soil temperature, and precipitation. Hence, averages of these three drivers at the source region of each PFP measurement were estimated via HYSPLIT footprints. Correlations between average footprint soil conditions/precipitation and Midwest N_2O emissions were used to investigate the dominant drivers.

Results of this study indicate that if soils are warmer than 295 K – which is mostly the case in summer – the soil temperature predominantly drives Midwest N_2O emissions. In cooler soils – which is mostly the case in spring and fall – the soil moisture is found to be more important. Precipitation events are able to boost daily N_2O emissions but, based on the current dataset, this driving effect is less prominent on a seasonal scale. Freezing/thawing induced N_2O emissions are most likely responsible for the high top-down emission estimates in winter 2017 and, thus, it is concluded that this effect contributes considerably to the Midwest N_2O budget. Interestingly, N_2O emission estimates in the flooding year 2019 are most likely not enhanced because of unusual soil conditions but because of the delay of the growing season and enhanced indirect N_2O emission due to an increased runoff. However, it has to be noted that the influence of emission drivers cannot be quantified with the employed approach alone, because the available dataset is not sufficient to describe the full complexity of soil N_2O emissions. To quantify the influence of emission drivers, a process-based model, which simulates the full complexity of soil processes, and more extensive, dedicated measurements are required.

To conclude, the hypothesis of this thesis that **regional-scale airborne in situ measurements are well-suited to characterize N_2O emissions from area sources such as intensively cultivated agricultural regions and to evaluate related bottom-up emission estimates** is *confirmed with certain limitations*.

Airborne in situ measurements are well-suited to quantify N_2O emissions in the U.S. Midwest and thus likely in other intensively cultivated agricultural regions as well. The most dominant driving parameters of soil N_2O emissions can also be identified, while for a precise quantification more dedicated studies are needed. However, for both, the emission quantification as well as for the driver identification, measurement instruments with a high accuracy and precision are mandatory, because atmospheric N_2O enhancements are typically less than 1 % of the N_2O background. Furthermore, the spatial and temporal coverage of the observations and hence the flight strategy is crucial. Due to the large spatio-temporal heterogeneity of soil N_2O emissions, the whole target region has to be sampled (e.g., via PBL transects across the region) on several days over a longer period. The actual required number of flights probably depends on the region and season, while less research flights are needed if continuous and not discrete measurements are available. In addition to the demanding measurement requirements, the spatial distribution

of N_2O emissions has to be well known to allow for a proper source attribution.
The complexity of soil N_2O emissions, like the dependence on soil conditions or fertilization, challenges bottom-up estimates. An emission factor-based approach is not able to capture the large heterogeneity of N_2O emissions in intensively cultivated agricultural regions. In the case of the U.S. Midwest, this results in a large underestimation of emissions. I would like to note that in other agricultural regions, the magnitude of the underestimation might be different or EDGAR might even overestimate emissions. However, overall the emission factor approach is only suitable to a limited extent to quantify regional N_2O emissions. Defining region-specific emission factors based on measurements might improve bottom-up estimates significantly. In regions with little agriculture, emission factor-based bottom-up estimates might perform better as the complexity of soil N_2O emissions is less relevant. Contrary, a process-based model is well-suited to quantify regional N_2O emissions in an intensively cultivated agricultural region. Furthermore, such models enable to quantify the influence of soil emission drivers and the consequences of unusual conditions like due to flooding. The downside is, that process-based models are complex and require a large variety of input data which are, for example in the case of fertilizer application rates, often difficult to compile and highly uncertain. Thus, measurements become important to constrain the model and to adjust input parameters for a certain region.

This work is an important contribution to the endeavor to meet the target of the Paris Agreement. The analyses presented herein quantify a globally relevant N_2O source region and provide a guideline for the characterization of N_2O emissions in other regions around the world, aiding the effort to establish a national N_2O inventory system, like the proposed German initiative ITMS. Such inventory systems are the basis for the development of efficient N_2O emission reduction strategies and, hence, to mitigate global warming.

9 Outlook

The present thesis demonstrates the great potential of and the urgent need for regional-scale airborne in situ measurements within the PBL to better understand and quantify N_2O emissions in intensively cultivated agricultural regions. However, the heterogeneity of soil N_2O emissions poses a major challenge for both, bottom-up as well as top-down estimates, which hampered a full characterization of N_2O emissions in the U.S. Midwest. To further enhance the understanding of N_2O emissions, the following follow-up studies are planned using the unique N_2O dataset gathered within the ACT-America project:

1. The seasonality of N_2O emissions in the U.S. Midwest during the ACT-America project will be quantified via a Bayesian approach using PFP measurements and HYSPLIT simulations. This study is complementary to Chapter 6, where a more straightforward but less established emission factor approach is used (Method 2). The goal is to evaluate Method 2 and to allow for a better understanding of the seasonality and dependencies of Midwest N_2O emission drivers.

2. In collaboration with Stephen M. Ogle (Natural Resource Ecology Laboratory, Colorado State University, Fort Collins, CO, USA) DayCent simulations driven by the specific ACT-America conditions are planned, enabling the investigation of the following research questions:

   - How do dedicated DayCent *Tier 3* N_2O emission estimates for the U.S. Midwest compare to the top-down estimates derived herein?

   - Can the general seasonality of N_2O emissions in the U.S. Midwest be quantified using DayCent simulations and top-down estimates derived herein?

   - Does the DayCent model adequately reflect the influence of soil N_2O emission drivers – including freezing/thawing processes – in the U.S. Midwest?

   - How and to what extent altered the 2019 flooding event soil N_2O emissions in the U.S. Midwest?

Although the present thesis is, to my best knowledge, the most extensive analysis of N_2O emissions in the U.S. Midwest, more top-down studies are necessary for a comprehensive analysis of the drivers of Midwest N_2O emissions and to evaluate state-of-the-art methods to estimate emission patterns. To cover the high temporal variability on various scales, long term projects with regular airborne measurements spanning wide areas of the Midwest are necessary. Combining a process-based model like DayCent capable of simulating the temporal and spatial variability of N_2O emissions, with extensive airborne and tall tower top-down studies at selected spots and times, could be a cost effective approach that would limit the number of flights needed to produce accurate estimates for the region and improve national reporting of emissions (Ogle et al., 2020).

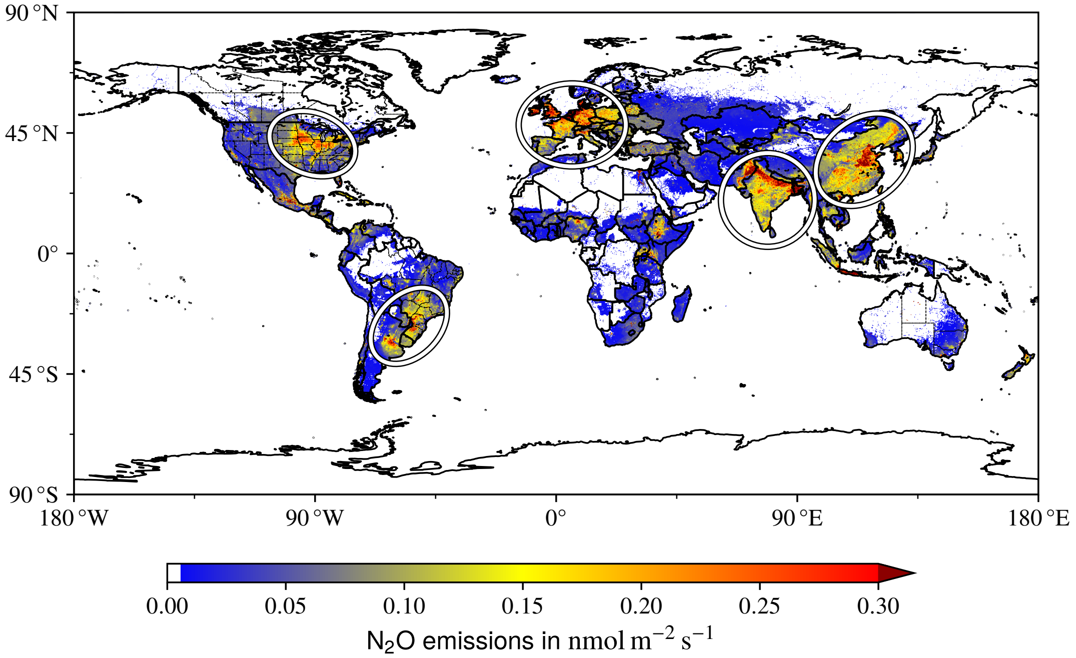

Figure 9.1: Anthropogenic N_2O emissions worldwide in 2015 following EDGAR5.0. Some N_2O emission hotspot regions are encircled in white.

The U.S. Midwest is only one among several N_2O emission hotspot worldwide (see Figure 9.1), which are all insufficiently characterized. Example regions are the pampas in South America, India, China, and parts of Europe – especially Benelux. Since N_2O emission reduction is an important building block on the way to meet the target of the Paris Agreement, emission monitoring systems for these hotspot regions but also minor N_2O source regions are essential, because they constitute the science basis for policy makers to develop effective emission reduction strategies. This work provides valuable guidance for the characterization of source regions which is a crucial prerequisite for the development of a national N_2O monitoring system, such as the German initiative ITMS. Overall, based on the results presented herein, the following two main aspects have to be addressed for the development of national inventory systems:

1. More airborne as well as ground-based N_2O measurements with large spatial and temporal coverage are needed to quantify source regions. As shown in this study, airborne in situ measurements along regional-scale PBL transects are well-suited for that. Complementary measurements with remote sensing instruments which measure at the surface, aboard aircraft, or from satellites would enable more extensive top-down studies. Satellite measurements are especially desirable because of their large spatial and temporal coverage. However, a lot of effort has to be put into the development and optimization of N_2O instruments to fulfill the high requirements of N_2O measurements, especially regarding accuracy and precision.

2. The development and evaluation of *Tier 3* N_2O emission estimates has to be encouraged. For that, top-down studies are the prerequisite to evaluate and set up the underlying process-based model for a certain region. Additionally, the monitoring of anthropogenic activities, which influence N_2O emissions and, hence, are needed for process-based model simulations, has to be improved. For example, as shown in this study, temporally resolved maps of fertilizer application rates are rare causing errors in *Tier 3* emission estimates because assumptions about fertilization activity have to be made.

A Appendix

A.1 Publications

Eckl, M., Roiger, A., Kostinek, J., Fiehn, A., Huntrieser, H., Knote, C., Barkley, Z. R., Ogle, S. M., Baier, B. C., Sweeney, C., & Davis, K. J. (2021). Quantifying Nitrous Oxide Emissions in the U.S. Midwest: A Top-Down Study Using High Resolution Airborne In-Situ Observations. *Geophysical Research Letters*, *48*(5), e2020GL091266. https://doi.org/10.1029/2020gl091266

As co-author, sorted by the name of the lead author:

Barkley, Z. R., Davis, K. J., Feng, S., Cui, Y. Y., Fried, A., Weibring, P., Richter, D., Walega, J. G., Miller, S. M., **Eckl, M.**, Roiger, A., Fiehn, A., & Kostinek, J. (2021). Analysis of Oil and Gas Ethane and Methane Emissions in the Southcentral and Eastern United States Using Four Seasons of Continuous Aircraft Ethane Measurements. *Journal of Geophysical Research: Atmospheres*, *126*(10), e2020JD034194. https://doi.org/10.1029/2020JD034194

Fiehn, A., Kostinek, J., **Eckl, M.**, Klausner, T., Gałkowski, M., Chen, J., Gerbig, C., Röckmann, T., Maazallahi, H., Schmidt, M., Korbeń, P., Neçki, J., Jagoda, P., Wildmann, N., Mallaun, C., Bun, R., Nickl, A.-L., Jöckel, P., Fix, A., & Roiger, A. (2020). Estimating CH_4, CO_2 and CO emissions from coal mining and industrial activities in the Upper Silesian Coal Basin using an aircraft-based mass balance approach. *Atmospheric Chemistry and Physics*, *20*(21), 12675–12695. https://doi.org/10.5194/acp-20-12675-2020

Kostinek, J., Roiger, A., **Eckl, M.**, Fiehn, A., Luther, A., Wildmann, N., Klausner, T., Fix, A., Knote, C., Stohl, A., & Butz, A. (2021). Estimating Upper Silesian coal mine methane emissions from airborne in situ observations and dispersion modeling. *Atmospheric Chemistry and Physics*, *21*(11), 8791–8807. https://doi.org/10.5194/acp-21-8791-2021

Kostinek, J., Roiger, A., Davis, K. J., Sweeney, C., DiGangi, J. P., Choi, Y., Baier, B., Hase, F., Groß, J., **Eckl, M.**, Klausner, T., & Butz, A. (2019). Adaptation and performance assessment of a quantum and interband cascade laser spectrometer for simultaneous airborne in situ observation of CH_4, C_2H_6, CO_2, CO, and N_2O. *Atmospheric Measurement Techniques*, *12*(3), 1767–1783. https://doi.org/10.5194/amt-12-1767-2019

Nickl, A.-L., Mertens, M., Roiger, A., Fix, A., Amediek, A., Fiehn, A., Gerbig, C., Galkowski, M., Kerkweg, A., Klausner, T., **Eckl, M.**, & Jöckel, P. (2020). Hindcasting and forecasting of regional methane from coal mine emissions in the Upper Silesian Coal Basin using the online nested global regional chemistry–climate model MECO(n) (MESSy v2.53). *Geoscientific Model Development*, *13*(4), 1925–1943. https://doi.org/10.5194/gmd-13-1925-2020

Wei, Y., Shrestha, R., Pal, S., Gerken, T., Feng, S., McNelis, J., Singh, D., Thornton, M. M., Boyer, A. G., Shook, M. A., Chen, G., Baier, B. C., Barkley, Z. R., Barrick, J. D., Bennett, J. R., Browell, E. V., Campbell, J. F., Campbell, L. J., Choi, Y., Collins, J., Dobler, J., **Eckl, M.**, Fiehn, A., Fried, A., DiGangi, J. P., Barton-Grimley, R., Halliday, H., Klausner, T., Kooi, S., Kostinek, J., Lauvaux, T., Lin, B., McGill, M. J., Meadows, B., Miles, N. L., Nehrir, A. R., Nowak, J. B., Obland, M., O'Dell, C., Fao, R. M. P., Richardson, S. J., Richter, D., Roiger, A., Sweeney, C., Walega, J., Weibring, P., Williams, C. A., Yang, M. M., Zhou, Y., & Davis, K. J. (2021). Atmospheric Carbon and Transport – America (ACT-America) Datasets: Description, Management, and Delivery. *Earth and Space Science*, *8*(7), e2020EA001634. https://doi.org/10.1029/2020EA001634

A.2 Meteorological Quantities

The following definitions of the potential temperature θ (1) and virtual potential temperature θ_v (2) are taken from the Glossary of Meteorology of the American Meteorological Society (AMS; https://glossary.ametsoc.org/wiki/Welcome):

1. The potential temperature θ is "the [theoretical] temperature that an unsaturated parcel of dry air would have if brought adiabatically and reversibly from its initial state to a standard pressure, p_0, typically 100 kPa" (AMS, 2021a):

   $$\theta = T \left(\frac{p_0}{p} \right)^{\frac{R_a}{c_p}} \tag{A.1}$$

   Where T is the absolute temperature of the air parcel in K, p is the pressure of the air parcel in Pa, R_a is the the gas constant of air in $\mathrm{J\,K^{-1}\,kg^{-1}}$, and c_p is the specific heat capacity at a constant pressure in $\mathrm{J\,K^{-1}\,kg^{-1}}$. The unit of θ is K.

2. The virtual potential temperature θ_v is "the theoretical potential temperature of dry air that would have the same density as moist air" (AMS, 2021b):

   $$\theta_v = \theta \; (1 + 0.61\, r - r_L) \tag{A.2}$$

   Where θ is the potential temperature in K, r is the mixing ratio of water vapor in $\mathrm{kg\,kg^{-1}}$, and r_L is the mixing ratio of liquid water in $\mathrm{kg\,kg^{-1}}$. The unit of θ_v is K.

A.3 Global N_2O Sources in 2007–2016

Source:		**Emissions in Tg N yr^{-1}**
Natural		
Natural soils		5.6 (4.9–6.5)
Oceans		3.4 (2.5–4.3)
Inland waters, estuaries, coastal zones		0.3 (0.3–0.4)
Lightning and atmospheric production		0.4 (0.2–1.2)
Natural total		*9.7 (8.0–12.0)*
Anthropogenic		
Agriculture (direct emissions from N additions)	Direct soil emissions	2.3 (1.4–3.8)
	Manure left on pasture	1.2 (0.9–1.3)
	Manure management	0.3 (0.2–0.5)
	Aquaculture	0.1 (0.0–0.2)
	Subtotal	*3.8 (2.5–5.8)*
Other direct sources	Fossil fuels and industry	1.0 (0.8–1.1)
	Waste and waste water	0.3 (0.2–0.5)
	Biomass burning	0.6 (0.5–0.8)
	Subtotal	*1.9 (1.6–2.3)*
Indirect emissions from anthropogenic N additions	Inland waters, estuaries, coastal zones	0.5 (0.2–0.7)
	Atmospheric N deposition	0.9 (0.5–1.6)
	Subtotal	*1.3 (0.7–2.2)*
Perturbed fluxes from climate/CO_2/land cover change		0.2 (−0.6–1.1)
Anthropogenic total		*7.3 (4.2–11.4)*
Total		**17.0 (12.2–23.5)**

Table A.1: Global N_2O sources of 2007–2016 following Tian et al. (2020). Due to rounding given totals/subtotals can be different to the sum of individual contributions. Sources are given in Tg N yr^{-1}. The ranges are minimum-maximum estimates.

A.4 Configuration of WRF Simulations

This section presents the configuration of the WRF simulations used for the study in Chapter 5 to analyze ten research flights (Method 1). The center of the outer domain (D01) is located at 41.827 °N and 92.364 °W (see Figure 5.1). The inner domains (D02) are different in the simulations for the ten research flights. Table A.2 presents the different setups of the inner domains. For more information about WRF parameter names, the reader is referred to the WRF user guide (https://www2.mmm.ucar.edu/wrf/users/docs/user_guide_v4/contents.html).

Day:	`i_parent_start`	`j_parent_start`	`s_we`	`e_we`	`s_sn`	`e_sn`
Fall 2017						
10 Oct	153	100	1	446	1	281
18 Oct	89	93	1	441	1	341
20 Oct	89	100	1	441	1	306
24 Oct	85	102	1	386	1	296
Summer 2019						
20 Jun	116	23	1	321	1	476
04 Jul	70	107	1	396	1	476
07 Jul	92	77	1	466	1	311
08 Jul	71	106	1	411	1	261
10 Jul	71	95	1	411	1	326
11 Jul	94	90	1	431	1	316

Table A.2: Inner domain setups of the WRF simulations used to analyze ten research flights with Method 1 (see Chapter 5).

The remaining configuration is independent of the simulated day. An example WRF configuration file (“`namelist.input`”) for the flight on the 10 Oct 2017 is presented below:

```
&time_control
run_days                     =       2,
run_hours                    =       0,
run_minutes                  =       0,
run_seconds                  =       0,
start_year                   =    2017,    2017,
start_month                  =      10,      10,
start_day                    =      09,      09,
start_hour                   =      00,      00,
start_minute                 =      00,      00,
start_second                 =      00,      00,
end_year                     =    2017,    2017,
end_month                    =      10,      10,
end_day                      =      11,      11,
end_hour                     =      00,      00,
end_minute                   =      00,      00,
```

```
end_second                  =       00,       00,
interval_seconds            =     3600,
input_from_file             =   .true.,   .true.,
fine_input_stream           =        0,        0,
history_interval            =       60,        5,
frames_per_outfile          =       12,       12,
restart                     = .false.,
restart_interval            =      360,
io_form_history             =        2,
io_form_restart             =        2,
io_form_input               =        2,
io_form_boundary            =        2,
debug_level                 =        0,
auxinput4_inname            = "wrflowinp_d<domain>",
auxinput4_interval          =       60,       60,
io_form_auxinput4           =        2,
history_outname             = "wrfout_d<domain>_<date>",
rst_outname                 = "wrfrst_d<domain>_<date>",
auxinput1_inname            = "metoa_em.d<domain>.<date>"
auxinput11_end_h            =       48,       48,
auxinput11_interval         =        1,        1,
io_form_auxinput5           =        2,
auxinput5_interval_m        =       60,
auxinput5_inname            = "wrfchemi_d<domain>_<date>"
frames_per_auxinput5        =        1,
force_use_old_data          =        T,
iofields_filename           = "iofields.txt","iofields.txt",
ignore_iofields_warning     = .true.,
/

&domains
time_step                   =       60,
time_step_fract_num         =        0,
time_step_fract_den         =        1,
max_dom                     =        2,
use_adaptive_time_step      = .false.,
s_we                        =        1,        1,
e_we                        =      278,      446,
s_sn                        =        1,        1,
e_sn                        =      253,      281,
s_vert                      =        1,        1,
e_vert                      =       51,       51,
dx                          =    15000,     3000,
dy                          =    15000,     3000,
grid_id                     =        1,        2,
parent_id                   =        0,        1,
i_parent_start              =        1,      153,
j_parent_start              =        1,      100,
parent_grid_ratio           =        1,        5,
parent_time_step_ratio      =        1,        5,
p_top_requested             =    10000,
feedback                    =        1,
smooth_option               =        1,
num_metgrid_soil_levels     =        4,
```

```
 num_metgrid_levels          =      38,
 interp_type                 =       2,
 lagrange_order              =       1,
 zap_close_levels            =     500,
 use_surface                 =  .true.,
 lowest_lev_from_sfc         = .false.,
 force_sfc_in_vinterp        =       1,
 max_ts_locs                 =       0,
 eta_levels                  = 1.0000,0.9975,0.9937,0.9884,0.9821,
          0.9758,0.9695,0.9632,0.9568,0.9505,0.9442,0.9368,0.9295,
          0.9221,0.9147,0.9074,0.9000,0.8926,0.8853,0.8779,0.8705,
          0.8632,0.8558,0.8474,0.8389,0.8263,0.8084,0.7895,0.7684,
          0.7474,0.7211,0.6947,0.6579,0.6211,0.5842,0.5474,0.5105,
          0.4737,0.4337,0.3895,0.3463,0.3053,0.2674,0.2326,0.2000,
          0.1684,0.1389,0.1105,0.0758,0.0368,0.0000
/

 &physics
 mp_physics                  =     8,     8,
 ra_lw_physics               =     4,     4,
 ra_sw_physics               =     4,     4,
 radt                        =     5,     5,
 swint_opt                   =     1,
 slope_rad                   =     0,     0,
 topo_shading                =     0,     0,
 sf_sfclay_physics           =     5,     5,
 sf_surface_physics          =     2,     2,
 sf_urban_physics            =     0,     0,
 bl_pbl_physics              =     5,     5,
 bldt                        =     0,     0,
 cu_physics                  =     1,     0,
 shcu_physics                =     0,     0,
 cudt                        =     0,     0,
 ishallow                    =     0,
 isfflx                      =     1,
 ifsnow                      =     0,
 icloud                      =     1,
 surface_input_source        =     1,
 num_soil_layers             =     4,
 num_land_cat                =    21,
 mp_zero_out                 =     2,
 mp_zero_out_thresh          = 1.e-8,
 maxiens                     =     1,
 maxens                      =     3,
 maxens2                     =     3,
 maxens3                     =    16,
 ensdim                      =   144,
 sst_update                  =     1,
 seaice_threshold            =   271,
 /

 &fdda
 grid_fdda                   =       1,         0,
 grid_sfdda                  =       1,         0,
```

```
gfdda_inname                =  "wrffdda_d<domain>",
sgfdda_inname               =  "wrfsfdda_d<domain>",
gfdda_end_h                 =      48,         0,
sgfdda_end_h                =      48,         0,
gfdda_interval_m            =      60,         0,
sgfdda_interval_m           =      60,         0,
fgdt                        =       0,         0,
if_no_pbl_nudging_uv        =       0,         0,
if_no_pbl_nudging_t         =       1,         1,
if_no_pbl_nudging_q         =       1,         1,
if_zfac_uv                  =       0,         0,
k_zfac_uv                   =      10,        10,
if_zfac_t                   =       0,         0,
k_zfac_t                    =      10,        10,
if_zfac_q                   =       0,         0,
k_zfac_q                    =      10,        10,
guv                         =  0.0003,    0.0001,
guv_sfc                     =  0.0003,    0.0001,
gt                          =  0.0003,    0.0001,
gt_sfc                      =     0.0,       0.0,
gq                          =  0.0003,    0.0001,
gq_sfc                      =     0.0,       0.0,
if_ramping                  =       1,
dtramp_min                  =    60.0,
rinblw                      =   250.0,
io_form_gfdda               =       2,
io_form_sgfdda              =       2,
obs_nudge_opt               =       1,         1,
max_obs                     =  150000,
fdda_start                  =     0.0,       0.0,
fdda_end                    =    2880,      2880,
obs_nudge_wind              =       1,         1,
obs_coef_wind               =  4.0E-4,    4.0E-4,
obs_nudge_temp              =       1,         1,
obs_coef_temp               =  4.0E-4,    4.0E-4,
obs_nudge_mois              =       1,         1,
obs_coef_mois               =  4.0E-4,    4.0E-4,
obs_nudge_pstr              =       0,         0,
obs_coef_pstr               =  4.0E-4,    4.0E-4,
obs_rinxy                   =     100,       100,
obs_no_pbl_nudge_uv         =       0,         0,
obs_no_pbl_nudge_t          =       1,         1,
obs_no_pbl_nudge_q          =       1,         1,
obs_sfc_scheme_horiz        =       1,
obs_sfc_scheme_vert         =       0,
obs_dpsmx                   =     7.5,
obs_nudgezfullr1_uv         =      50,
obs_nudgezrampr1_uv         =      50,
obs_nudgezfullr2_uv         =      50,
obs_nudgezrampr2_uv         =      50,
obs_nudgezfullr4_uv         =   -5000,
obs_nudgezrampr4_uv         =      50,
obs_nudgezfullr1_t          =      50,
obs_nudgezrampr1_t          =      50,
```

```
obs_nudgezfullr2_t           =      50,
obs_nudgezrampr2_t           =      50,
obs_nudgezfullr4_t           =   -5000,
obs_nudgezrampr4_q           =      50,
obs_nudgezfullr1_q           =      50,
obs_nudgezrampr1_q           =      50,
obs_nudgezfullr2_q           =      50,
obs_nudgezrampr2_q           =      50,
obs_nudgezfullr4_q           =   -5000,
obs_nudgezrampr4_q           =      50,
obs_nudgezfullmin            =      50,
obs_nudgezrampmin            =      50,
obs_nudgezmax                =    3000,
obs_max_sndng_gap            =      20,
obs_sfcfact                  =     0.5,
obs_sfcfacr                  =    0.67,
obs_rinsig                   =     0.1,
obs_twindo                   =     2.0,       2.0,
obs_npfi                     =     200,
obs_ionf                     =       2,         2,
obs_idynin                   =       1,
obs_dtramp                   =    60.0,
obs_prt_freq                 =      10,        10,
obs_prt_max                  =      10,
obs_ipf_errob                =  .true.,
obs_ipf_nudob                =  .true.,
obs_ipf_in4dob               =  .true.,
obs_ipf_init                 =  .true.,
obs_scl_neg_qv_innov         =       1,
/

&dynamics
w_damping                    =       1,
diff_opt                     =       1,       1,
diff_6th_opt                 =       0,       0,
diff_6th_factor              =    0.12,    0.12,
km_opt                       =       4,       4,
damp_opt                     =       3,
dampcoef                     =     0.2,     0.2,
time_step_sound              =       8,       8,
epssm                        =     0.1,     0.1,
mix_full_fields              = .false., .false.,
zdamp                        =   5000.,   5000.,
base_temp                    =    290.,
khdif                        =      0.,      0.,
kvdif                        =      0.,      0.,
non_hydrostatic              =  .true.,  .true.,
chem_adv_opt                 =       2,       2,
moist_adv_opt                =       2,       2,
scalar_adv_opt               =       2,       2,
tke_adv_opt                  =       2,       2,
do_avgflx_em                 =       1,       1,
do_avgflx_cugd               =       0,       0,
/
```

```
 &bdy_control
 spec_bdy_width              =       7,
 spec_zone                   =       1,
 relax_zone                  =       6,
 spec_exp                    =     0.0,
 specified                   =  .true., .false.,
 nested                      = .false.,  .true.,
 /

 &namelist_quilt
 nio_tasks_per_group        = 0,
 nio_groups                 = 1,
 /

&chem
 chem_opt                   =      15,      15,
 kemit                      =      10,
 emi_inname                 = "wrfchemi_d<domain>_<date>",
 input_chem_inname          = "wrfchemi_d<domain>_<date>",
 chemdt                     =   0.033,   0.033,
 emiss_inpt_opt             =       1,       1,
 emiss_opt                  =      22,      22,
 io_style_emissions         =       2,
 chem_conv_tr               =       0,       0,
 chem_in_opt                =       0,       0,
 bio_emiss_opt              =       0,       0,
 gaschem_onoff              =       0,       0,
 biomass_burn_opt           =       0,       0,
 have_bcs_chem              =  .true., .false.,
 /
```

A.5 Agricultural Scaling Factors Derived With Method 1

Day:	EDGAR4.3.2		EDGAR5.0	
	unmodified	bias corrected	unmodified	bias corrected
Fall 2017				
10 Oct	11.2 ± 3.8	8.8 ± 4.1	6.7 ± 2.3	5.3 ± 2.4
18 Oct	2.8 ± 1.5	2.9 ± 1.5	1.5 ± 0.8	1.6 ± 0.8
20 Oct	7.6 ± 2.7	7.0 ± 2.5	4.0 ± 1.4	3.7 ± 1.3
24 Oct	3.5 ± 3.9	3.4 ± 3.8	1.8 ± 2.0	1.7 ± 1.9
Average:	*6.3 ± 4.6*	*5.5 ± 4.0*	*3.5 ± 2.7*	*3.1 ± 2.3*
Summer 2019				
20 Jun	20.3 ± 6.5	22.1 ± 7.3	17.4 ± 5.6	19.0 ± 6.3
04 Jul	11.9 ± 4.0	12.2 ± 4.7	10.3 ± 3.4	10.5 ± 4.0
07 Jul	14.8 ± 4.1	12.9 ± 3.3	13.0 ± 3.6	11.3 ± 2.9
08 Jul	9.9 ± 2.6	7.7 ± 2.1	8.7 ± 2.3	6.8 ± 1.8
10 Jul	5.8 ± 4.0	5.3 ± 3.6	5.2 ± 3.5	4.7 ± 3.2
11 Jul	5.4 ± 2.1	5.4 ± 1.9	4.9 ± 1.9	4.8 ± 1.7
Average:	*11.4 ± 6.6*	*10.9 ± 7.2*	*9.9 ± 5.7*	*9.5 ± 6.2*

Table A.3: Mean and standard deviation of agricultural scaling factors F_{AGR} for the ten investigated research flights from Monte Carlo simulations. The bias corrected values are corrected for differences between simulated and observed wind speed and PBL height following Equation 5.5.

A.6 U.S. Midwest N_2O Emissions Derived With Method 1

N_2O emissions in the U.S. Midwest consist of agricultural E_{AGR}, non-agricultural E_{nonAGR}, and natural emissions E_N. For the model optimization in Chapter 5, anthropogenic emissions are obtained from EDGAR4.3.2 and EDGAR5.0, and natural emissions are obtained from EDGAR2. Averaged over the U.S. Midwest, non-agricultural emissions are 0.04 nmol m^{-2} s^{-1} and natural emissions are 0.02 nmol m^{-2} s^{-1}. The agricultural emissions are optimized using Method 1 delivering E^{opt}_{AGR}. Prior as well as optimized agricultural emissions for EDGAR4.3.2 and EDGAR5.0 are listed in Table A.4 and Table A.5, respectively.

Day:	Prior		Optimized		Optimized & bias corrected	
	AGR	total	AGR	total	AGR	total
Fall 2017						
10 Oct	0.06	0.12	0.67 ± 0.23	0.74 ± 0.23	0.53 ± 0.24	0.59 ± 0.24
18 Oct	0.06	0.12	0.16 ± 0.08	0.22 ± 0.08	0.16 ± 0.08	0.22 ± 0.08
20 Oct	0.05	0.12	0.41 ± 0.15	0.47 ± 0.15	0.38 ± 0.13	0.44 ± 0.13
24 Oct	0.05	0.12	0.18 ± 0.20	0.24 ± 0.20	0.18 ± 0.19	0.24 ± 0.19
Average:	*0.06*	*0.12*	*0.35 ± 0.27*	*0.42 ± 0.27*	*0.31 ± 0.23*	*0.37 ± 0.23*
Summer 2019						
20 Jun	0.09	0.15	1.75 ± 0.56	1.82 ± 0.56	1.91 ± 0.63	1.97 ± 0.63
04 Jul	0.09	0.15	1.03 ± 0.34	1.09 ± 0.34	1.06 ± 0.41	1.12 ± 0.41
07 Jul	0.09	0.15	1.31 ± 0.36	1.37 ± 0.36	1.14 ± 0.29	1.20 ± 0.29
08 Jul	0.09	0.15	0.88 ± 0.23	0.94 ± 0.23	0.69 ± 0.18	0.75 ± 0.18
10 Jul	0.09	0.15	0.52 ± 0.36	0.58 ± 0.36	0.47 ± 0.32	0.53 ± 0.32
11 Jul	0.09	0.15	0.49 ± 0.19	0.55 ± 0.19	0.49 ± 0.17	0.55 ± 0.17
Average:	*0.09*	*0.15*	*1.00 ± 0.57*	*1.06 ± 0.57*	*0.96 ± 0.62*	*1.02 ± 0.62*

All values are N_2O emission flux densities in nmol m^{-2} s^{-1}.

Table A.4: EDGAR4.3.2 prior and optimized agricultural (AGR) N_2O emissions averaged over the U.S. Midwest. Total emissions consist of prior/optimized agricultural (E_{AGR}/E^{opt}_{AGR}), non-agricultural (E_{nonAGR}), and natural emissions (E_N). The bias corrected values are corrected for differences between simulated and observed wind speed and PBL height following Equation 5.5. Due to rounding, the sum of agricultural, non-agricultural, and natural emissions might differ from the given totals.

Day:	Prior		Optimized		Optimized & bias corrected	
	AGR	total	AGR	total	AGR	total
Fall 2017						
10 Oct	0.10	0.17	0.68 ± 0.23	0.75 ± 0.23	0.53 ± 0.25	0.60 ± 0.25
18 Oct	0.10	0.17	0.16 ± 0.08	0.22 ± 0.08	0.16 ± 0.08	0.22 ± 0.08
20 Oct	0.10	0.17	0.41 ± 0.15	0.48 ± 0.15	0.38 ± 0.14	0.44 ± 0.14
24 Oct	0.10	0.17	0.18 ± 0.20	0.25 ± 0.20	0.18 ± 0.20	0.24 ± 0.20
Average:	*0.10*	*0.17*	*0.36 ± 0.28*	*0.42 ± 0.28*	*0.31 ± 0.23*	*0.38 ± 0.23*
Summer 2019						
20 Jun	0.10	0.16	1.77 ± 0.56	1.83 ± 0.56	1.93 ± 0.64	1.99 ± 0.64
04 Jul	0.10	0.16	1.03 ± 0.34	1.09 ± 0.34	1.06 ± 0.41	1.12 ± 0.41
07 Jul	0.10	0.16	1.30 ± 0.36	1.37 ± 0.36	1.13 ± 0.29	1.20 ± 0.29
08 Jul	0.10	0.16	0.87 ± 0.23	0.93 ± 0.23	0.68 ± 0.18	0.74 ± 0.18
10 Jul	0.10	0.16	0.52 ± 0.35	0.58 ± 0.35	0.47 ± 0.32	0.53 ± 0.32
11 Jul	0.10	0.16	0.49 ± 0.19	0.55 ± 0.19	0.49 ± 0.17	0.55 ± 0.17
Average:	*0.10*	*0.16*	*1.00 ± 0.57*	*1.06 ± 0.57*	*0.96 ± 0.63*	*1.02 ± 0.63*

All values are N_2O emission flux densities in nmol m^{-2} s^{-1}.

Table A.5: As Table A.4 but for EDGAR5.0 N_2O emissions. Optimized emissions are (nearly) equal to optimized EDGAR4.3.2 emissions. Section 5.5 provides an explanation for that.

A.7 U.S. Midwest N_2O Emissions on a Daily Basis Derived With Method 1

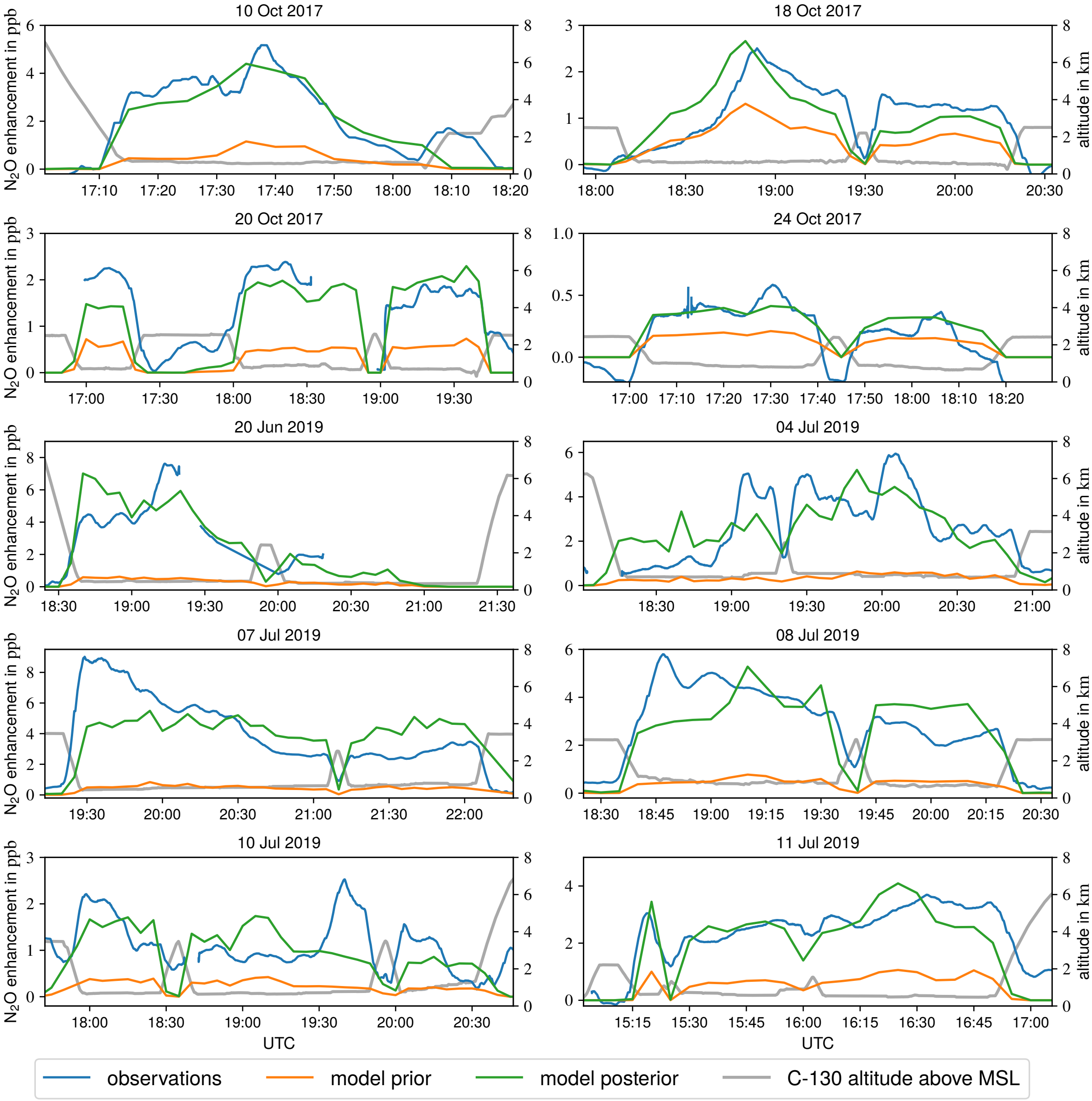

Figure A.1: Observed vs. simulated N_2O enhancements (emitted from EDGAR4.3.2/EDGAR2 $E_{AGR} + E_{nonAGR} + E_N$) for each of the ten research flights analyzed with Method 1. For an easier visual comparison the 5 min-moving average of the observation is shown. The simulated enhancements are the average of the three model runs with different initial and boundary meteorological conditions (ERA5, GDAS-FNL, and NARR) on the closest grid points in space and time to each observation. (Figure adopted from Eckl et al., 2021)

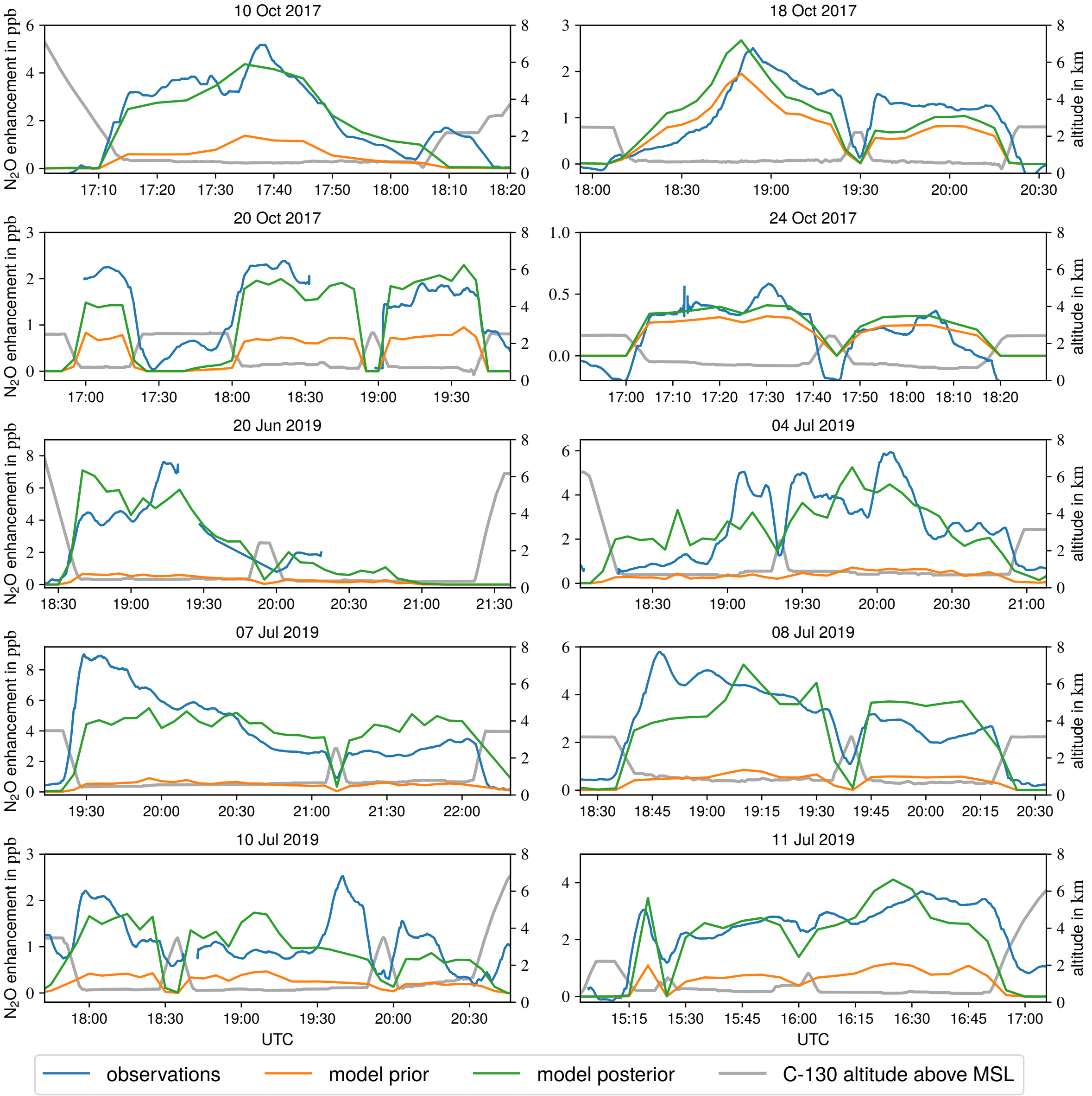

Figure A.2: As Figure A.1 but simulated N_2O enhancement emitted from EDGAR5.0/EDGAR2 $E_{AGR} + E_{nonAGR} + E_N$. (Figure adopted from Eckl et al., 2021)

A.8 Precipitation During the Flight Transects Analyzed With Method 1

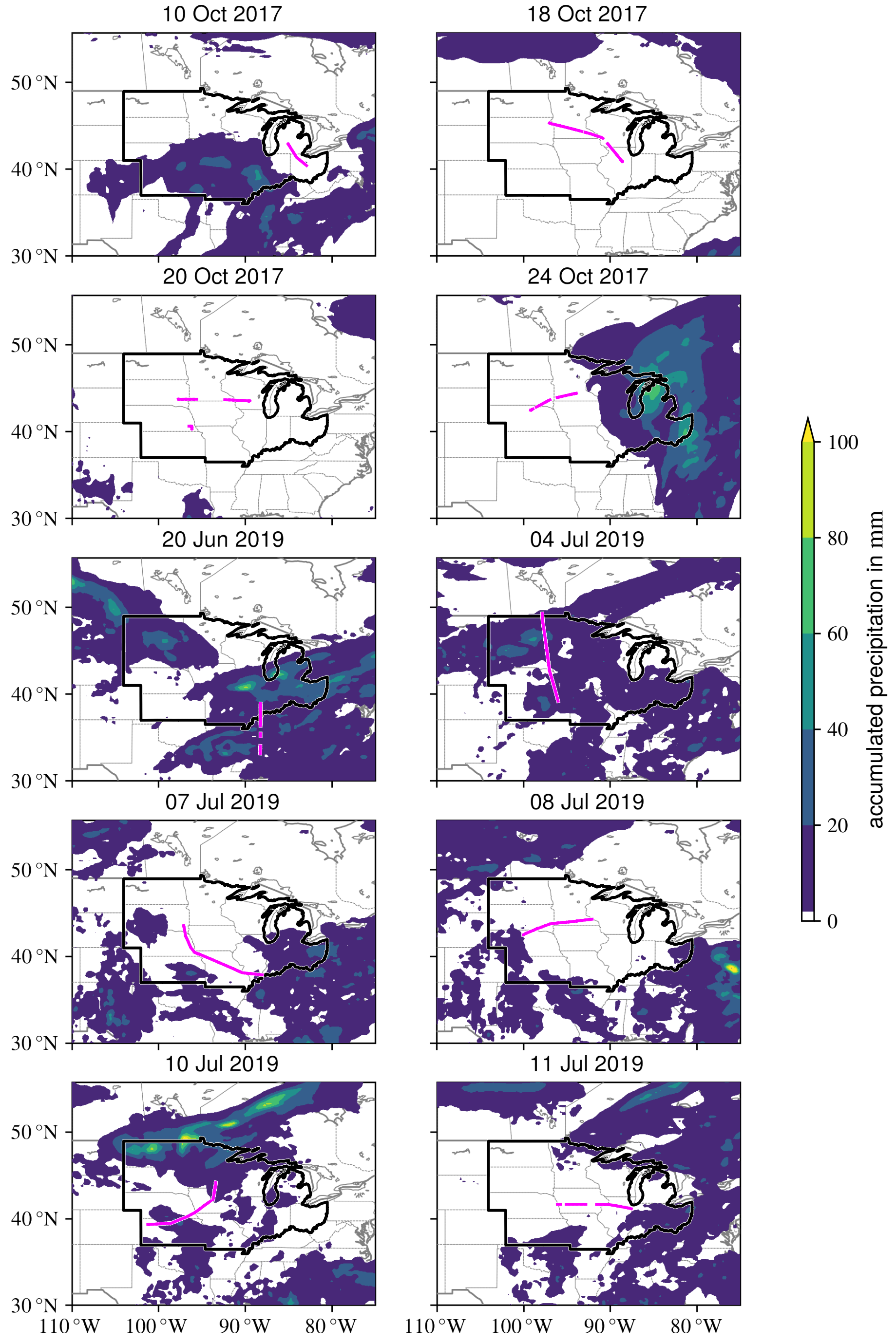

Figure A.3: Accumulated precipitation from ERA5 reanalysis data for the ten research flights analyzed with Method 1. The accumulation period encompasses 24 h before takeoff plus the whole flight. The U.S. Midwest is encircled in black. The PBL transects of the research flights are indicated in pink. (Figure adapted from Eckl et al., 2021)

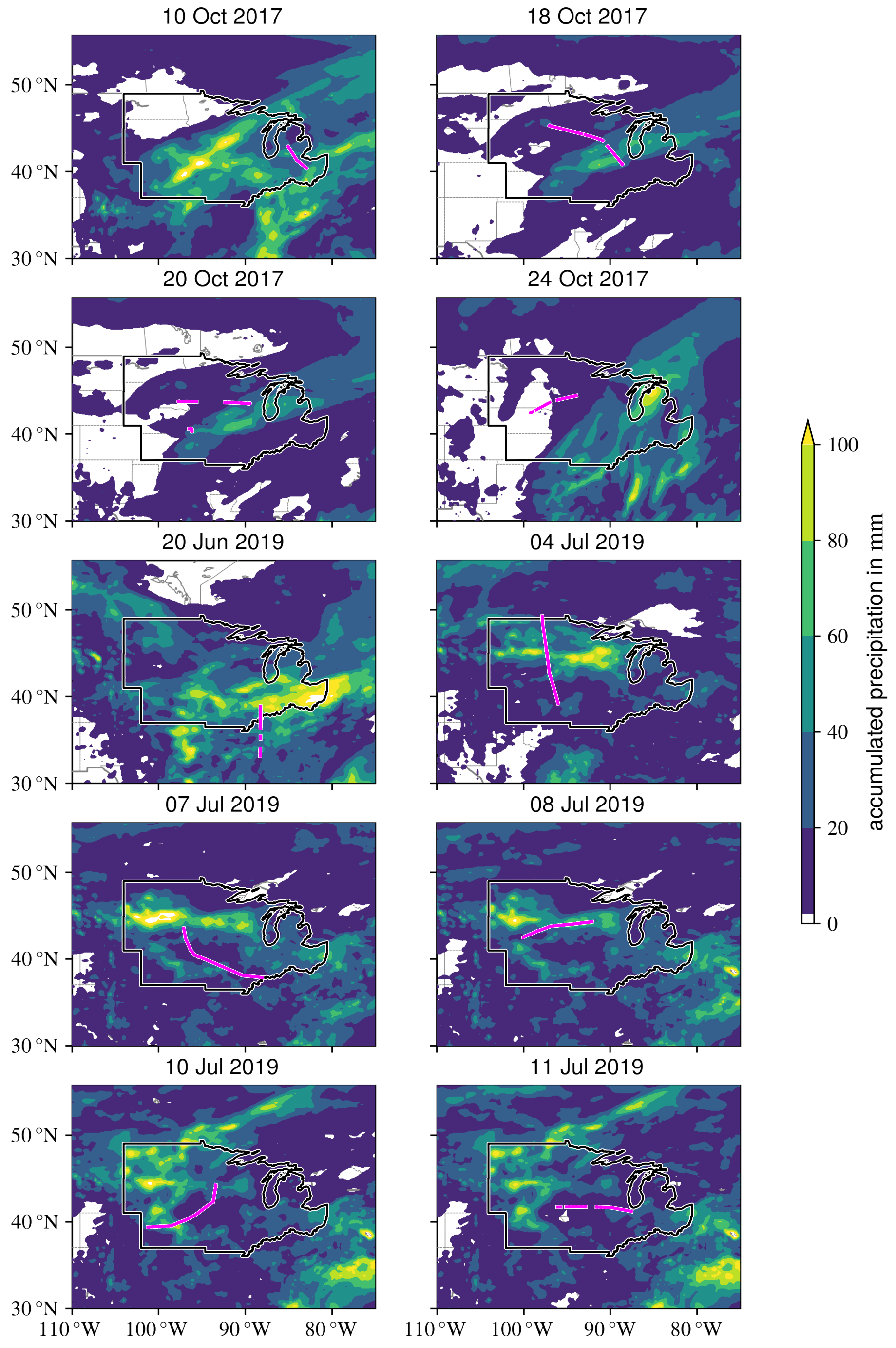

Figure A.4: As Figure A.3 but with an accumulation period spanning from 7 days before takeoff to touchdown. (Figure adapted from Eckl et al., 2021)

A.9 Agricultural Scaling Factors Derived With Method 2

Campaign:	Mean:	Median:	Lower quartile:	Upper quartile:
Summer 2016	2.8	2.5	1.4	4.0
Winter 2017	4.4	2.2	1.4	4.1
Fall 2017	4.8	4.7	2.2	6.5
Spring 2018	3.3	3.0	1.5	5.3
Summer 2019	6.7	5.6	4.3	9.8

Table A.6: EDGAR4.3.2 agricultural scaling factors derived with Method 2 for the five ACT-America campaigns. The mean, median, lower quartile, and upper quartile of the distribution of the scaling factors derived for each PFP sample (F^f_{AGR}) is displayed.

Campaign:	Mean:	Median:	Lower quartile:	Upper quartile:
Summer 2016	2.6	2.3	1.4	3.7
Winter 2017	9.5	4.8	2.1	14.5
Fall 2017	2.9	2.9	1.2	4.1
Spring 2018	4.9	4.6	2.9	7.5
Summer 2019	5.7	4.7	3.8	8.2

Table A.7: As Table A.6 but for EDGAR5.0 agricultural scaling factors derived with Method 2.

A.10 U.S. Midwest N_2O Emissions Derived With Method 2

Campaign:	Mean:	Median:	Lower quartile:	Upper quartile:
Summer 2016	0.32	0.30	0.20	0.43
Winter 2017	1.08	0.58	0.29	1.60
Fall 2017	0.36	0.36	0.19	0.48
Spring 2018	0.56	0.53	0.36	0.82
Summer 2019	0.64	0.54	0.45	0.90

All values are N_2O emission flux densities in nmol m^{-2} s^{-1}.

Table A.8: U.S. Midwest N_2O emissions derived with Method 2 for the five ACT-America campaigns. The mean, median, lower quartile, and upper quartile of the distribution of the Midwest emissions derived for each PFP sample is displayed, consisting of scaled agricultural (E_{AGR}^{opt}), non-agricultural (E_{nonAGR}), and natural N_2O emissions (E_N).

A.11 Agricultural Practice and Trends of N_2O Emissions in the U.S. Midwest

The possible amount of soil N_2O emissions depends on the availability of reactive N-compounds in soils (see Section 2.2.2). In regions with intensive agriculture, like the U.S. Midwest, the addition of such N-compounds occurs mainly due to field crops and fertilization. In the following, long-term trends of agricultural N_2O emission amounts and seasonality in the Midwest are investigated and evaluated considering these two aspects (crop diversity and fertilization). Here it is important to highlight, that the following analysis focuses only on emissions from agriculture in the Midwest. Trends from this area show a different result (as described below) compared to the constant trend of total N_2O emissions in the whole U.S. since the 1990s (Tian et al., 2018).

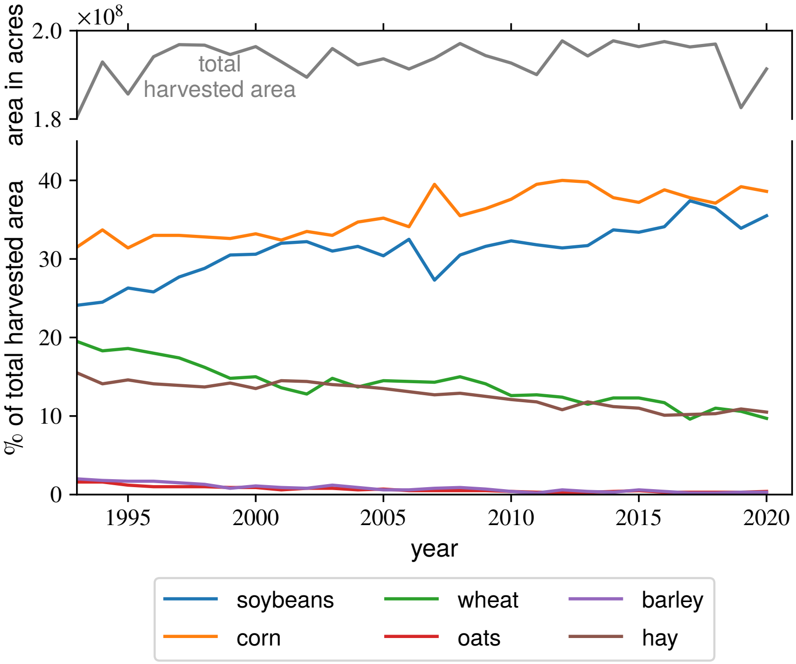

Figure A.5: Yearly total harvested area in the U.S. Midwest (upper panel) and the share of major crops (lower panel). These crops together account for 94–96 % of the total harvested area. Data obtained from NASS (2021).

A reduced crop diversity as well as the presence of legumes like soybeans favors soil N_2O emissions (see Section 2.2.2). Figure A.5 displays the yearly harvested area in the U.S. Midwest (upper panel) and the share of major crops (lower panel) from 1993 to 2020. On average, roughly 40 % of the whole Midwest region are harvested. Interannual variations are relatively small in this timeframe with a relative standard deviation of 2.2 %. Crop failure in 2019 due to the flooding lead to a significant drop by 7.3 % compared to the previous year. Corn and soybeans are the dominant crops in the Midwest. Their fractions have increased steadily from around 32 % and 24 % in 1993 to 39 % and 36 % in 2020, respectively. In contrast, the share of wheat and hay has decreased constantly to roughly 10 % each. Oats and barley only play a minor role in the Midwest. Overall, about 95 % of the total harvested area is planted with corn, soybeans, wheat, and hay. The decline of crop diversity and increase of legumes/soybean planted area from 1993–2020 most likely enhanced Midwest N_2O emissions. Extrapolating both trends suggests that emissions will enhance further in the near future. Moreover, if the share of soybeans increases at the expense of corn, the seasonality of soil N_2O emissions will change. Corn is mainly fertilized in spring and soybeans mainly in fall (see Section 6.4.1) and, thus, spring emissions might decline while fall emissions increase. However, soybeans are fertilized less intensely than corn leading to overall less fertilization and, hence, lower emissions. In contrast legumes like soybeans themselves favor N_2O fluxes resulting in larger emissions if the soybean cultivation increases. Overall, quantifying the impact of a changing crop diversity on soil N_2O emissions is challenging because underlying processes are complex and the relevant factors interact. Therefore, a process-based model is required with detailed knowledge about crop distribution and condition.

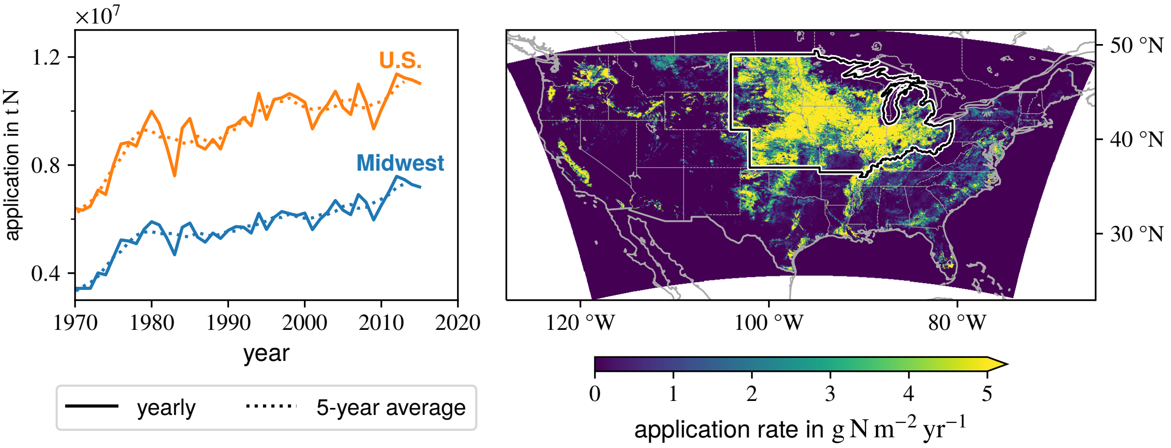

(a) Application in 1970–2015

(b) Gridded application in 2015

Figure A.6: N-fertilizer application in the contiguous U.S. in 1970–2015. (a) Time series of yearly application. (b) Gridded application rates in 2015. The Midwest is encircled by a thick black line. Data obtained from Cao et al. (2017).

The application of N-based synthetic fertilizer directly influences N_2O emissions from soils (see Section 2.2.2). Figure A.6a displays a times series of fertilizer application in the contiguous U.S. in 1970–2015. A detailed description of the underlying data of Figure A.6 is provided by Cao et al. (2018). From 1970 to 1980 the fertilizer application increased in the U.S. as well as in the Midwest by roughly 50 %. From 1980 to 2015, there is a slight increase in both domains of around 20–25 %. Overall, approximately half of the country's N-fertilizer is applied in the Midwest indicating the importance of this region regarding the N_2O budget of the U.S. Considering the map of fertilizer application rates in 2015 (see Figure A.6b), the Midwest is prominent. Large application rates of over $5\,\mathrm{g\,N\,m^{-2}\,yr^{-1}}$ in nearly the whole region highlights it as a hotspot of agricultural N_2O emissions. The increasing trend of N fertilizer application from 1970 to 2015 leads to an increase of agricultural N_2O emission in the U.S. and particularly in the Midwest. Extrapolating this trend suggests that U.S. and Midwest soil N_2O emissions will increase further. Assuming that the timing of the fertilizer application (mostly in spring followed by fall) does not change, variations of soil fluxes among spring, summer, and fall will become larger. However, data are too sparse to quantify this. Investigating the impact of fertilizer application trends with a process-based model is challenging as well. For regional studies, highly resolved spatial-temporal data of fertilizer application rates are needed but those are rare. Furthermore, none of the datasets provide a higher temporal resolution than one year, which hampers the quantification of seasonal or daily variations of soil N_2O emissions because assumptions must be made about the timing of fertilization. Overall, more effort must be put in a detailed monitoring of the fertilization practice as this is a basic prerequisite for the simulation of agricultural N_2O emissions.

B List of Symbols and Abbreviations

B.1 Symbols

Symbol:	**Unit:**	**Description:**
$\mathcal{N}(\mu, \sigma^2)$	–	normal distribution with mean μ and variance σ^2
η	m^{-3}	number density of sample air
Θ	$\mathrm{m}^3\,\mathrm{m}^{-3}$	volumetric soil water content
Θ_{sat}	$\mathrm{m}^3\,\mathrm{m}^{-3}$	Θ at which the soil is saturated
θ	K	potential temperature (see Appendix A.2)
θ_v	K	virtual potential temperature (see Appendix A.2)
λ	m	wavelength of electromagnetic radiation
μ	–	arithmetic mean
ρ	$\mathrm{kg\,m}^{-3}$	density of air
σ	–	standard deviation
τ_r	s	instrument response time
τ_λ	–	spectral optical depth (in wavelength λ)
A_{obs}	$(\mathrm{mol\,mol}^{-1})$ s	integral of c^{enh}_{obs} along a transect
A_{mod}	$(\mathrm{mol\,mol}^{-1})$ s	integral of c^{enh}_{mod} along a transect
A_{AGR}	$(\mathrm{mol\,mol}^{-1})$ s	agricultural portion of A_{mod}
A^{opt}_{AGR}	$(\mathrm{mol\,mol}^{-1})$ s	agricultural portion of A_{mod} based on E^{opt}_{AGR}
A_{nonAGR}	$(\mathrm{mol\,mol}^{-1})$ s	non-agricultural, anthropogenic portion of A_{mod}
A_N	$(\mathrm{mol\,mol}^{-1})$ s	natural portion of A_{mod}
b	$\mathrm{mol\,mol}^{-1}$	y-intercept of calibration curve
c_p	$\mathrm{J\,K}^{-1}\,\mathrm{kg}^{-1}$	specific heat capacity at constant pressure

Continued on next page . . .

Symbol:	**Unit:**	**Description:**
c	mol mol^{-1}	N_2O dry air mole fraction
c^*	mol mol^{-1}	dilution corrected c (see Section 4.4)
$c(p_{cell})$	mol mol^{-1}	c retrieved at p_{cell}
$c(p_{set})$	mol mol^{-1}	c retrieved at p_{set}
c_x	mol mol^{-1}	dry air mole fraction of species x
c_x^m	mol mol^{-1}	mole fraction of species x in moist air
$c_{\mathrm{H_2O}}$	mol mol^{-1}	mole fraction of H_2O
c_{obs}	mol mol^{-1}	observed N_2O dry air mole fraction
c_{obs}^{bg}	mol mol^{-1}	observed N_2O background mole fraction
c_{obs}^{enh}	mol mol^{-1}	observed N_2O enhancement
c_{mod}^{enh}	mol mol^{-1}	simulated N_2O enhancement along transect
c_{mod}^*	mol mol^{-1}	bias corrected c_{mod}^{enh} (see Section 5.3.2)
c_f^{enh}	mol mol^{-1}	simulated footprint N_2O enhancement
$c_{f,AGR}^{enh}$	mol mol^{-1}	agricultural portion of c_f^{enh}
$c_{f,nonAGR}^{enh}$	mol mol^{-1}	non-agricultural, anthropogenic portion of c_f^{enh}
$c_{f,N}^{enh}$	mol mol^{-1}	natural portion of c_f^{enh}
c^i	mol mol^{-1}	QCLS N_2O measurement corresponding to c_{PFP}^i
c_{PFP}^i	mol mol^{-1}	i^{th} of N PFP N_2O measurements
d	m	length of the sample cell
E_{AGR}	mol m^{-2} s^{-1}	agricultural EDGAR N_2O emissions
E_{AGR}^{opt}	mol m^{-2} s^{-1}	scaled agricultural EDGAR N_2O emissions
E_{nonAGR}	mol m^{-2} s^{-1}	non-agricultural EDGAR N_2O emissions
E_N	mol m^{-2} s^{-1}	natural EDGAR N_2O emissions
$\mathbf{E}^f$	mol m^{-2} s^{-1}	EDGAR N_2O emissions on the **H**-grid
e_i^f	mol m^{-2} s^{-1}	i^{th} of n_f components of $\mathbf{E}^f$
F_{AGR}	–	agricultural scaling factor
F_{AGR}^E	–	multiplication factor for E_{AGR} (see Section 5.3.1)
F_{AGR}^f	–	footprint agricultural scaling factor

Continued on next page . . .

Symbol:	**Unit:**	**Description:**
GWP_{100}	–	GWP on a 100 year horizon
g	$\mathrm{m\,s^{-2}}$	gravitational acceleration ($g \approx 9.81\,\mathrm{m\,s^{-2}}$)
$\mathbf{H}$	$(\mathrm{mol\,m^{-2}\,s^{-1}})^{-1}$	one-dimensional HYSPLIT footprint of length n_f
h_i	$(\mathrm{mol\,m^{-2}\,s^{-1}})^{-1}$	i^{th} of n_f components of $\mathbf{H}$
H_m	$\mathrm{mol\,mol^{-1}}$	x_m of high calibration standard
H_t	$\mathrm{mol\,mol^{-1}}$	x_t of high calibration standard
h	m	altitude
h_p	m	altitude above MSL up to which p_{cell} is regulated
I_0	$\mathrm{W\,m^{-2}}$	intensity of incoming radiation
$I_{0,\lambda}$	$\mathrm{W\,m^{-2}}$	intensity of incoming radiation of wavelength λ
I	$\mathrm{W\,m^{-2}}$	intensity of outgoing radiation
I_λ	$\mathrm{W\,m^{-2}}$	intensity of outgoing radiation of wavelength λ
$J(F_{AGR})$	–	cost function
k_{cell}	$\mathrm{m^2}$	absorption cross section of air in the sample cell
k_λ	$\mathrm{m^2}$	spectral absorption cross section (in wavelength λ)
L_m	$\mathrm{mol\,mol^{-1}}$	x_m of low calibration standard
L_t	$\mathrm{mol\,mol^{-1}}$	x_t of low calibration standard
$\mathbf{M}^{soil}$	% WFPS	ERA5 soil moisture field on the $\mathbf{H}$-grid
μ_i^{soil}	% WFPS	i^{th} of n_f components of $\mathbf{M}^{soil}$
M_f^{soil}	% WFPS	footprint soil moisture
$\overline{M}_f^{soil}$	% WFPS	campaign-average of M_f^{soil}
m	$\mathrm{mol\,mol^{-1}}$	slope of calibration curve
N	–	total number of collected PFP samples
n	mol	amount of substance
n_t	–	length of time dimension of HYSPLIT footprint

Continued on next page . . .

Symbol:	**Unit:**	**Description:**
n_{lon}	–	length of longitude (x) dimension of **H**
n_{lat}	–	length of latitude (y) dimension of **H**
n_f	–	product of n_t, n_{lon}, and n_{lat} (length of **H**)
$P(p_{cell},\ p_{set})$	–	relative deviation of $c(p_{cell})$ to $c(p_{set})$
$\overline{P}(p_{cell},\ p_{set})$	–	average over all $P(p_{cell},\ p_{set})$ (see Section 4.3)
$\mathbf{P}$	m	ERA5 hourly precipitation field on the **H**-grid
p_i	m	i^{th} of n_f components of **P**
P_f	m	footprint precipitation (hourly accumulated)
p	Pa	pressure
p_0	Pa	standard pressure (p_0 = 1000 hPa = 1 bar)
p_g	Pa	pressure of a gas cylinder
p_{cell}	Pa	pressure in the QCLS sample cell
p_{set}	Pa	set pressure in the QCLS sample cell
Q	$\mathrm{m^3\,s^{-1}}$	volumetric flow rate
q	$\mathrm{kg\,kg^{-1}}$	specific humidity
R	–	correlation coefficient
R_a	$\mathrm{J\,K^{-1}\,kg^{-1}}$	gas constant of air ($R_a \approx 287\,\mathrm{J\,K^{-1}\,kg^{-1}}$ for dry air)
R_u	$\mathrm{J\,K^{-1}\,mol^{-1}}$	universal gas constant ($R_u \approx 8.314\,\mathrm{J\,K^{-1}\,mol^{-1}}$)
r	$\mathrm{kg\,kg^{-1}}$	mass mixing ratio of water vapor
r_L	$\mathrm{kg\,kg^{-1}}$	mass mixing ratio of liquid water
T	K	absolute temperature
T_0	K	standard temperature (T_0 = 273.15 K)
T_{cell}	K	temperature in the QCLS sample cell
$\mathbf{T}^{soil}$	K	ERA5 soil temperature field on the **H**-grid
ϑ_i^{soil}	K	i^{th} of n_f components of $\mathbf{T}^{soil}$
T_f^{soil}	K	footprint soil temperature
$\overline{T}_f^{soil}$	K	campaign-average of T_f^{soil}
t_0	UTC	start time of PBL transect

Continued on next page . . .

Symbol:	Unit:	Description:
t_{end}	UTC	end time of PBL transect
U	$\mathrm{m\,s^{-1}}$	horizontal wind speed
U_{obs}	$\mathrm{m\,s^{-1}}$	observed wind speed averaged along transect
U_{mod}	$\mathrm{m\,s^{-1}}$	modeled wind speed averaged along transect
V	$\mathrm{m^3}$	volume
V_0	$\mathrm{m^3}$	volume of air at T_0 and p_0
V_{cell}	$\mathrm{m^3}$	volume of the QCLS sample cell
V_g	$\mathrm{m^3}$	volume of a gas cylinder
$W(c_{\mathrm{H_2O}})$	–	QCLS dilution correction of c (see Section 4.4)
x_c	$\mathrm{mol\,mol^{-1}}$	calibrated dry air mole fraction of any species
x_m	$\mathrm{mol\,mol^{-1}}$	measured dry air mole fraction of any species
x_t	$\mathrm{mol\,mol^{-1}}$	true dry air mole fraction of any species
Z_{obs}	m	observed PBL height averaged along transect
Z_{mod}	m	modeled PBL height averaged along transect
z_{PBL}	m	height of the PBL (AGL)

B.2 Abbreviations

Chemical formulas:

CO	carbon monoxide
CO_2	carbon dioxide *(German: Kohlenstoffdioxid)*
CH_4	methane *(German: Methan)*
C_2H_6	ethane
H_2O	water vapor
N	nitrogen
NO	nitric oxide
$NO_3{}^-$	nitrate

NO_x	generic term for nitrogen oxides
NH_3	ammonia
NH_4^+	ammonium
N_2	molecular nitrogen
N_2O	nitrous oxide *(German: Distickstoffmonoxid)*
$O(^1D)$	excited oxygen
O_2	molecular oxygen
O_3	ozone

Acronyms:

ACT-America	Atmospheric Carbon and Transport-America
AGL	above ground level
AMS	American Meteorological Society
ARMS	USDA's Agricultural Resource Management Survey
ARW	Advanced Research WRF
DayCent	daily time-step version of the CENTURY model
DLR	Deutsches Zentrum für Luft- und Raumfahrt
ECMWF	European Centre for Medium-Range Weather Forecasts
EDGAR	Emissions Database for Global Atmospheric Research
EDGAR2	EDGAR version 2.0
EDGAR4.3.2	EDGAR version 4.3.2
EDGAR5.0	EDGAR version 5.0
EPA	Environmental Protection Agency
ERA5	5th generation atmospheric reanalysis data
ESRL	Earth System Research Laboratories
EZ	entrainment zone
FA	free atmosphere
FDDA	WRF Four-Dimensional Data Assimilation
GDAS-FNL	Global Data Assimilation System Final analysis
GHG	Greenhouse Gas
GML	Global Monitoring Laboratory
GMST	Global Mean Surface Temperature
GWP	global warming potential
HITRAN	high-resolution transmission molecular absorption database

HYSPLIT	Hybrid Single Particle Lagrangian Integrated Trajectory model
ICL	interband cascade laser
IN	Indiana
IPCC	Intergovernmental Panel on Climate Change
IQR	interquartile range (distance between lower and upper quartile)
IR	terrestrial infrared radiation ($\lambda \gtrsim 4\,\mu\mathrm{m}$)
ITMS	Integrated Greenhouse Gas Monitoring System for Germany
LST	local standard time
MFC	mass flow controller
MFM	mass flow meter
MI	Michigan
ML	well-mixed layer
MSL	mean sea level
MW	der mittlere Westen der USA *(in German abstract)*
NARR	North American Regional Reanalysis
NASA	National Aeronautics and Space Administration
NCAR	National Center for Atmospheric Research
NCEP	National Centers for Environmental Prediction
NIR	near-infrared radiation ($780\,\mathrm{nm} \lesssim \lambda \lesssim 4\,\mu\mathrm{m}$)
NOAA	National Oceanic and Atmospheric Administration
NWP	Numerical Weather Prediction
OH	Ohio
PBL	Planetary Boundary Layer
PFP	Programmable Flask Package
PTFE	Polytetrafluoroethylene
QCL	quantum cascade laser
QCLS	Quantum Cascade Laser Spectrometer
RMSE	root-mean-square error
RRTMG	rapid radiative transfer method for general circulation models
SL	surface layer
UN	United Nations
UNFCCC	United Nations Framework Convention on Climate Change
USDA	U.S. Department of Agriculture
UTC	Universal Time Coordinated
UV	ultraviolet radiation ($10\,\mathrm{nm} \lesssim \lambda \lesssim 380\,\mathrm{nm}$)

VIS	visible radiation (380 nm $\lesssim \lambda \lesssim$ 780 nm)
WFPS	water-filled pore space
WMO	World Meteorological Organization
WRF	Weather Research and Forecasting model
WRF-Chem	WRF model coupled to Chemistry

C Bibliography

Abalos, D., De Deyn, G. B., Kuyper, T. W., & van Groenigen, J. W. (2013). Plant species identity surpasses species richness as a key driver of N_2O emissions from grassland. *Global Change Biology*, *20*(1), 265–275. https://doi.org/10.1111/gcb.12350

AMS. (2021a). “potential temperature”. Glossary of Meteorology [last accessed: 10 May 2021]. https://glossary.ametsoc.org/wiki/Potential_temperature

AMS. (2021b). “virtual potential temperature”. Glossary of Meteorology [last accessed: 10 May 2021]. https://glossary.ametsoc.org/wiki/Virtual_potential_temperature

Archer, D., Eby, M., Brovkin, V., Ridgwell, A., Cao, L., Mikolajewicz, U., Caldeira, K., Matsumoto, K., Munhoven, G., Montenegro, A., & Tokos, K. (2009). Atmospheric Lifetime of Fossil Fuel Carbon Dioxide. *Annual Review of Earth and Planetary Sciences*, *37*, 117–134. https://doi.org/10.1146/annurev.earth.031208.100206

ARMS. (2015). USDA’s Agricultural Resource Management Survey - Farm Financial and Crop Production Practices - Tailored Reports: Crop Production Practices (2013 survey) [last updated: April 23, 2015; last accessed: March, 22, 2021]. https://data.ers.usda.gov/reports.aspx?ID=17883

Baier, B. C., Sweeney, C., Choi, Y., Davis, K. J., DiGangi, J. P., Feng, S., Fried, A., Halliday, H., Higgs, J., Lauvaux, T., Miller, B. R., Montzka, S. A., Newberger, T., Nowak, J. B., Patra, P., Richter, D., Walega, J., & Weibring, P. (2020). Multispecies Assessment of Factors Influencing Regional CO_2 and CH_4 Enhancements During the Winter 2017 ACT-America Campaign. *Journal of Geophysical Research: Atmospheres*, *125*(2), e2019JD031339. https://doi.org/10.1029/2019JD031339

Barkley, Z. R., Davis, K. J., Feng, S., Balashov, N., Fried, A., DiGangi, J., Choi, Y., & Halliday, H. S. (2019a). Forward Modeling and Optimization of Methane Emissions in the South Central United States Using Aircraft Transects Across Frontal Boundaries. *Geophysical Research Letters*, *46*(22), 13564–13573. https://doi.org/10.1029/2019gl084495

Barkley, Z. R., Lauvaux, T., Davis, K. J., Deng, A., Fried, A., Weibring, P., Richter, D., Walega, J. G., DiGangi, J., Ehrman, S. H., Ren, X., & Dickerson, R. R. (2019b). Estimating Methane Emissions From Underground Coal and Natural Gas Production in Southwestern Pennsylvania. *Geophysical Research Letters*, *46*(8), 4531–4540. https://doi.org/10.1029/2019GL082131

Barkley, Z. R., Lauvaux, T., Davis, K. J., Deng, A., Miles, N. L., Richardson, S. J., Cao, Y., Sweeney, C., Karion, A., Smith, M., Kort, E. A., Schwietzke, S., Murphy, T., Cervone, G., Martins, D., & Maasakkers, J. D. (2017). Quantifying methane emissions from natural gas production in north-eastern Pennsylvania. *Atmospheric Chemistry and Physics*, *17*(22), 13941–13966. https://doi.org/10.5194/acp-17-13941-2017

Battye, W., Aneja, V. P., & Schlesinger, W. H. (2017). Is nitrogen the next carbon? *Earth's Future*, *5*(9), 894–904. https://doi.org/10.1002/2017ef000592

Beck, M., Hofstetter, D., Aellen, T., Faist, J., Oesterle, U., Ilegemes, M., Gini, E., & Melchior, H. (2002). Continuous Wave Operation of a Mid-Infrared Semiconductor Laser at Room Temperature. *Science*, *295*(5553), 301–305. https://doi.org/10.1126/science.1066408

Bouwman, A. F. (1998). Nitrogen oxides and tropical agriculture. *Nature*, *392*(6679), 866–867. https://doi.org/10.1038/31809

Butterbach-Bahl, K., Baggs, E. M., Dannenmann, M., Kiese, R., & Zechmeister-Boltenstern, S. (2013). Nitrous oxide emissions from soils: How well do we understand the processes and their controls? *Philosophical Transactions of the Royal Society B: Biological Sciences*, *368*(1621), 20130122. https://doi.org/10.1098/rstb.2013.0122

Cao, P., Lu, C., & Yu, Z. (2017). Agricultural nitrogen fertilizer uses in the continental U.S. during 1850-2015: a set of gridded time-series data. *PANGAEA*. *Supplement to:* Cao, Lu, and Yu (2018). https://doi.org/10.1594/PANGAEA.883585

Cao, P., Lu, C., & Yu, Z. (2018). Historical nitrogen fertilizer use in agricultural ecosystems of the contiguous United States during 1850–2015: application rate, timing, and fertilizer types. *Earth System Science Data*, *10*(2), 969–984. https://doi.org/10.5194/essd-10-969-2018

Capasso, F. (2010). High-performance midinfrared quantum cascade lasers. *Optical Engineering*, *49*(11), 111102. https://doi.org/10.1117/1.3505844

Castellano, M. J., Schmidt, J. P., Kaye, J. P., Walker, C., Graham, C. B., Lin, H., & Dell, C. J. (2010). Hydrological and biogeochemical controls on the timing and magnitude of nitrous oxide flux across an agricultural landscape. *Global Change Biology*, *16*(10), 2711–2720. https://doi.org/10.1111/j.1365-2486.2009.02116.x

Catoire, V., Robert, C., Chartier, M., Jacquet, P., Guimbaud, C., & Krysztofiak, G. (2017). The SPIRIT airborne instrument: a three-channel infrared absorption spectrometer with quantum cascade lasers for in situ atmospheric trace-gas measurements. *Applied Physics B*, *123*(244). https://doi.org/10.1007/s00340-017-6820-x

Chen, F., & Dudhia, J. (2001). Coupling an Advanced Land Surface–Hydrology Model with the Penn State–NCAR MM5 Modeling System. Part I: Model Implementation and Sensitivity. *Monthly Weather Review*, *129*(4), 569–585. https://doi.org/10.1175/1520-0493(2001)129<0569:caalsh>2.0.co;2

Chen, Z., Griffis, T. J., Millet, D. B., Wood, J. D., Lee, X., Baker, J. M., Xiao, K., Turner, P. A., Chen, M., Zobitz, J., & Wells, K. C. (2016). Partitioning N_2O emissions within the U.S. Corn Belt using an inverse modeling approach. *Global Biogeochemical Cycles*, *30*(8), 1192–1205. https://doi.org/10.1002/2015gb005313

Ciais, P., Sabine, C., Bala, G., Bopp, L., Brovkin, V., Canadell, J., Chhabra, A., DeFries, R., Galloway, J., Heimann, M., Jones, C., Quéré, C. L., Myneni, R. B., Piao, S., & Thornton, P. (2013). Carbon and Other Biogeochemical Cycles. In T. F. Stocker, D. Qin, G.-K. Plattner, M. Tignor, S. K. Allen, J. Boschung, A. Nauels, Y. Xia, V. Bex, & P. M. Midgley (Eds.), *Climate Change 2013: The Physical Science Basis. Contribution of Working Group I to the Fifth Assessment Report of the Intergovernmental Panel on Climate Change* (pp. 465–570). Cambridge University Press.

Clapp, R. B., & Hornberger, G. M. (1978). Empirical equations for some soil hydraulic properties. *Water Resources Research*, *14*(4), 601–604. https://doi.org/10.1029/WR014i004p00601

Corazza, M., Bergamaschi, P., Vermeulen, A. T., Aalto, T., Haszpra, L., Meinhardt, F., O'Doherty, S., Thompson, R., Moncrieff, J., Popa, E., Steinbacher, M., Jordan, A., Dlugokencky, E., Brühl, C., Krol, M., & Dentener, F. (2011). Inverse modelling of European N_2O emissions: assimilating observations from different networks. *Atmospheric Chemistry and Physics*, *11*(5), 2381–2398. https://doi.org/10.5194/acp-11-2381-2011

Crippa, M., Oreggioni, G., Guizzardi, D., Muntean, M., Schaaf, E., Lo Vullo, E., Solazzo, E., Monforti-Ferrario, F., Olivier, J. G. J., & Vignati, E. (2019). *Fossil CO_2 and GHG emissions of all world countries - 2019 Report, EUR 29849 EN, JRC117610*. Publications Office of the European Union, Luxembourg. https://doi.org/10.2760/687800

Crippa, M., Solazzo, E., Huang, G., Guizzardi, D., Koffi, E., Muntean, M., Schieberle, C., Friedrich, R., & Janssens-Maenhout, G. (2020). High resolution temporal profiles in the Emissions Database for Global Atmospheric Research. *Scientific Data*, *7*(121). https://doi.org/10.1038/s41597-020-0462-2

Dai, C., Wang, Q., Kalogiros, J. A., Lenschow, D. H., Gao, Z., & Zhou, M. (2014). Determining Boundary-Layer Height from Aircraft Measurements. *Boundary-Layer Meteorology*, *152*(3), 277–302.

Dameris, M. (2010). Klimawandel und die Chemie der Atmosphäre - wie wird sich die stratosphärische Ozonschicht entwickeln? *Angewandte Chemie*, *122*(44), 8268–8279. https://doi.org/10.1002/ange.201001643

Davidson, E. A. (1991). Fluxes of nitric oxide and nitrous oxide from terrestrial ecosystems. In J. E. Rogers & W. B. Whitman (Eds.), *Microbial Production and Consumption of Greenhouse Gases : Methane, Nitrogen Oxides, and Halomethanes* (pp. 219–235). American Society for Microbiology, Washington D.C.

Davidson, E. A., Keller, M., Erickson, H. E., Verchot, L. V., & Veldkamp, E. (2000). Testing a Conceptual Model of Soil Emissions of Nitrous and Nitric Oxides. *BioScience*, *50*(8), 667–680. https://doi.org/10.1641/0006-3568(2000)050[0667:tacmos]2.0.co;2

Davis, K. J., Obland, M. D., Lin, B., Lauvaux, T., O'Dell, C., Meadows, B., Browell, E. V., DiGangi, J. P., Sweeney, C., McGill, M. J., Barrick, J. D., Nehrir, A. R., Yang, M. M., Bennett, J. R., Baier, B. C., Roiger, A., Pal, S., Gerken, T., Fried, A., Feng, S., Shrestha, R., Shook, M. A., Chen, G., Campbell, L. J., Barkley, Z. R., & Pauly, R. M. (2018).

ACT-America: L3 Merged In Situ Atmospheric Trace Gases and Flask Data, Eastern USA. ORNL DAAC, Oak Ridge, Tennessee, USA [version: 1.2; last accessed: 30 March 2021]. https://doi.org/10.3334/ORNLDAAC/1593

Davis, K. J., Browell, E. V., Feng, S., Lauvaux, T., Obland, M. D., Pal, S., Baier, B. C., Baker, D. F., Baker, I. T., Barkley, Z. R., Bowman, K. W., Cui, Y. Y., Denning, A. S., DiGangi, J. P., Dobler, J. T., Fried, A., Gerken, T., Keller, K., Lin, B., Nehrir, A. R., Normile, C. P., O'Dell, C. W., Ott, L. E., Roiger, A., Schuh, A. E., Sweeney, C., Wei, Y., Weir, B., Xue, M., & Williams, C. A. (2021). The Atmospheric Carbon and Transport (ACT) – America Mission [in press]. *Bulletin of the American Meteorological Society*, 1–54. https://doi.org/10.1175/BAMS-D-20-0300.1

Del Grosso, S. J., & Parton, W. J. (2012). Climate change increases soil nitrous oxide emissions. *New Phytologist*, *196*(2), 327–328. https://doi.org/10.1111/j.1469-8137.2012.04334.x

Del Grosso, S. J., Parton, W. J., Keough, C. A., & Reyes-Fox, M. (2011). Special features of the DayCent modeling package and additional procedures for parameterization, calibration, validation, and applications. In L. R. Ahuja & L. Ma (Eds.), *Methods of Introducing System Models into Agricultural Research* (pp. 155–176). American Society of Agronomy, Crop Science Society of America, Soil Science Society of America. https://doi.org/10.2134/advagricsystmodel2.c5

Del Grosso, S. J., Parton, W. J., Mosier, A. R., Hartman, M. D., Brenner, J., Ojima, D. S., & Schimel, D. S. (2001). Simulated Interaction of Carbon Dynamics and Nitrogen Trace Gas Fluxes Using the DAYCENT Model. In M. Schaffer, L. Ma, & S. Hansen (Eds.), *Modeling Carbon and Nitrogen Dynamics for Soil Management* (pp. 303–332). CRC Press.

Deng, A., Stauffer, D., Gaudet, B., Dudhia, J., Hacker, J., Bruyere, C., Wu, W., Vandenberghe, F., Liu, Y., & Bourgeois, A. (2009). Update on WRF-ARW end-to-end multi-scale FDDA system. *10th WRF Users' Workshop*.

Díaz-Isaac, L. I., Lauvaux, T., & Davis, K. J. (2018). Impact of physical parameterizations and initial conditions on simulated atmospheric transport and CO_2 mole fractions in the US Midwest. *Atmospheric Chemistry and Physics*, *18*(20), 14813–14835. https://doi.org/10.5194/acp-18-14813-2018

Dlugokencky, E. (2021a). NOAA - Global Monitoring Laboratory (GML) - Carbon Cycle Greenhouse Gases - Trends in Atmospheric Methane [last accessed: 14 Jun 2021]. https://gml.noaa.gov/ccgg/trends_ch4/

Dlugokencky, E. (2021b). NOAA - Global Monitoring Laboratory (GML) - Carbon Cycle Greenhouse Gases - Trends in Atmospheric Nitrous Oxide [last accessed: 14 Jun 2021]. https://gml.noaa.gov/ccgg/trends_n2o/

Dlugokencky, E., & Tans, P. (2021). NOAA - Global Monitoring Laboratory (GML) - Carbon Cycle Greenhouse Gases - Trends in Atmospheric Carbon Dioxide [last accessed: 14 Jun 2021]. https://gml.noaa.gov/ccgg/trends/global.html

Draxler, R. R., & Hess, G. D. (1997). *Description of the HYSPLIT_4 Modeling System* (tech. rep.). NOAA Technical Memorandum ERL ARL-224. Air Resources Laboratory, Silver Springs, Maryland.

Dyroff, C., Fütterer, D., & Zahn, A. (2010). Compact diode-laser spectrometer ISOWAT for highly sensitive airborne measurements of water-isotope ratios. *Applied Physics B*, *98*(2), 537–548. https://doi.org/10.1007/s00340-009-3775-6

Eckl, M., Roiger, A., Kostinek, J., Fiehn, A., Huntrieser, H., Knote, C., Barkley, Z. R., Ogle, S. M., Baier, B. C., Sweeney, C., & Davis, K. J. (2021). Quantifying Nitrous Oxide Emissions in the U.S. Midwest: A Top-Down Study Using High Resolution Airborne In-Situ Observations. *Geophysical Research Letters*, *48*(5), e2020GL091266. https://doi.org/10.1029/2020gl091266

ECMWF. (2016). Part IV: Physical Processes. *IFS Documentation CY41R2*. ECMWF. https://doi.org/10.21957/TR5RV27XU

EDGAR. (2020). Emission Database for Global Atmospheric Research [last accessed: 20 Jul 2020]. https://edgar.jrc.ec.europa.eu/

EDGAR4.3.2. (2017). Emissions Database for Global Atmospheric Research, version 4.3.2. https://edgar.jrc.ec.europa.eu/dataset_ghg432

EDGAR5.0. (2019). Emissions Database for Global Atmospheric Research, version 5.0. https://edgar.jrc.ec.europa.eu/dataset_ghg50

Emmert, J. T., Drob, D. P., Picone, J. M., Siskind, D. E., Jones, M., Mlynczak, M. G., Bernath, P. F., Chu, X., Doornbos, E., Funke, B., Goncharenko, L. P., Hervig, M. E., Schwartz, M. J., Sheese, P. E., Vargas, F., Williams, B. P., & Yuan, T. (2021). NRLMSIS 2.0: A Whole-Atmosphere Empirical Model of Temperature and Neutral Species Densities. *Earth and Space Science*, *8*(3), e2020EA001321. https://doi.org/10.1029/2020EA001321

EPA. (2020). Inventory of U.S. Greenhouse Gas Emissions and Sinks: 1990–2018 [last accessed: 12 Mar 2021]. https://www.epa.gov/ghgemissions/inventory-us-greenhouse-gas-emissions-and-sinks

EPA. (2021). Inventory of U.S. Greenhouse Gas Emissions and Sinks: 1990–2019: 2021 Annex 3 – Part B: Metholdological Descriptions for Additional Source or Sink Categories. 430-R-21-005. [last accessed: 15 Jun 2021]. https://www.epa.gov/sites/production/files/2021-04/documents/us-ghg-inventory-2021-annex-3-additional-source-or-sink-categories-part-b.pdf

ERA5. (2017). Copernicus Climate Change Service (C3S) (2017): ERA5: Fifth generation of ECMWF atmospheric reanalyses of the global climate. [last accessed: 02 Mar 2020]. https://cds.climate.copernicus.eu/cdsapp#!/home

FAO. (2020). Food and Agriculture Organization of the United Nations - FAOSTAT [last accessed: 20 Jul 2020]. http://www.fao.org/faostat/en/#compare

Fiehn, A., Kostinek, J., Eckl, M., Klausner, T., Gałkowski, M., Chen, J., Gerbig, C., Röckmann, T., Maazallahi, H., Schmidt, M., Korbeń, P., Neçki, J., Jagoda, P., Wildmann, N., Mallaun, C., Bun, R., Nickl, A.-L., Jöckel, P., Fix, A., & Roiger, A. (2020). Estimating CH_4, CO_2 and CO emissions from coal mining and industrial activities in the Upper Silesian Coal Basin using an aircraft-based mass balance approach. *Atmospheric Chemistry and Physics*, *20*(21), 12675–12695. https://doi.org/10.5194/acp-20-12675-2020

Firestone, M. K., & Davidson, E. A. (1989). Microbiological basis of NO and N_2O production and consumption in soil. In M. O. Andreae & D. S. Schimel (Eds.), *Exchange of Trace Gases between Terrestrial Ecosystems and the Atmosphere* (pp. 7–21). John Wiley & Sons Ltd.

Fried, A., Diskin, G., Weibring, P., Richter, D., Walega, J. G., Sachse, G., Slate, T., Rana, M., & Podolske, J. (2008). Tunable infrared laser instruments for airborne atmospheric studies. *Applied Physics B*, *92*(3), 409–417. https://doi.org/10.1007/s00340-008-3136-x

Friedlingstein, P., O'Sullivan, M., Jones, M. W., Andrew, R. M., Hauck, J., Olsen, A., Peters, G. P., Peters, W., Pongratz, J., Sitch, S., Le Quéré, C., Canadell, J. G., Ciais, P., Jackson, R. B., Alin, S., Aragão, L. E. O. C., Arneth, A., Arora, V., Bates, N. R., Becker, M., Benoit-Cattin, A., Bittig, H. C., Bopp, L., Bultan, S., Chandra, N., Chevallier, F., Chini, L. P., Evans, W., Florentie, L., Forster, P. M., Gasser, T., Gehlen, M., Gilfillan, D., Gkritzalis, T., Gregor, L., Gruber, N., Harris, I., Hartung, K., Haverd, V., Houghton, R. A., Ilyina, T., Jain, A. K., Joetzjer, E., Kadono, K., Kato, E., Kitidis, V., Korsbakken, J. I., Landschützer, P., Lefèvre, N., Lenton, A., Lienert, S., Liu, Z., Lombardozzi, D., Marland, G., Metzl, N., Munro, D. R., Nabel, J. E. M. S., Nakaoka, S., Niwa, Y., O'Brien, K., Ono, T., Palmer, P. I., Pierrot, D., Poulter, B., Resplandy, L., Robertson, E., Rödenbeck, C., Schwinger, J., Séférian, R., Skjelvan, I., Smith, A. J. P., Sutton, A. J., Tanhua, T., Tans, P. P., Tian, H., Tilbrook, B., van der Werf, G., Vuichard, N., Walker, A. P., Wanninkhof, R., Watson, A. J., Willis, D., Wiltshire, A. J., Yuan, W., Yue, X., & Zaehle, S. (2020). Global Carbon Budget 2020. *Earth System Science Data*, *12*(4), 3269–3340. https://doi.org/10.5194/essd-12-3269-2020

Fu, C., Lee, X., Griffis, T. J., Dlugokencky, E. J., & Andrews, A. E. (2017). Investigation of the N_2O emission strength in the U. S. Corn Belt. *Atmospheric Research*, *194*, 66–77. https://doi.org/10.1016/j.atmosres.2017.04.027

Fu, W. Q. (2006). Radiative Transfer (Chapter 4) [Figure 4.7a,c on p. 118 – Reprinted from Publication, ©2006, with permission from Elsevier]. *In Wallace and Hobbs (2006a): Atmospheric Science - An Introductory Survey* (pp. 113–152). Elsevier. https://doi.org/10.1016/B978-0-12-732951-2.50009-0

Ganesan, A. L., Manning, A. J., Grant, A., Young, D., Oram, D. E., Sturges, W. T., Moncrieff, J. B., & O'Doherty, S. (2015). Quantifying methane and nitrous oxide emissions from the UK and Ireland using a national-scale monitoring network. *Atmospheric Chemistry and Physics*, *15*(11), 6393–6406. https://doi.org/10.5194/acp-15-6393-2015

GDAS-FNL. (2015). National Centers for Environmental Prediction, National Weather Service, NOAA, U.S. Department of Commerce: NCEP GDAS/FNL 0.25 Degree Global Tropospheric Analyses and Forecast Grids, updated daily [last accessed: 28 May 2020]. https://doi.org/10.5065/D65Q4T4Z

Gidden, M. J., Riahi, K., Smith, S. J., Fujimori, S., Luderer, G., Kriegler, E., van Vuuren, D. P., van den Berg, M., Feng, L., Klein, D., Calvin, K., Doelman, J. C., Frank, S., Fricko, O., Harmsen, M., Hasegawa, T., Havlik, P., Hilaire, J., Hoesly, R., Horing, J., Popp, A., Stehfest, E., & Takahashi, K. (2019). Global emissions pathways under different socioeconomic scenarios for use in CMIP6: A dataset of harmonized emissions trajectories through the end of the century. *Geoscientific Model Development*, *12*(4), 1443–1475. https://doi.org/10.5194/gmd-12-1443-2019

Grell, G. A., Peckham, S. E., Schmitz, R., McKeen, S. A., Frost, G., Skamarock, W. C., & Eder, B. (2005). Fully coupled “online” chemistry within the WRF model. *Atmospheric Environment*, *39*(37), 6957–6975. https://doi.org/10.1016/j.atmosenv.2005.04.027

Griffis, T. J., Lee, X., Baker, J. M., Russelle, M. P., Zhang, X., Venterea, R., & Millet, D. B. (2013). Reconciling the differences between top-down and bottom-up estimates of nitrous oxide emissions for the U.S. Corn Belt. *Global Biogeochemical Cycles*, *27*(3), 746–754. https://doi.org/10.1002/gbc.20066

Griffis, T. J., Chen, Z., Baker, J. M., Wood, J. D., Millet, D. B., Lee, X., Venterea, R. T., & Turner, P. A. (2017). Nitrous oxide emissions are enhanced in a warmer and wetter world. *Proceedings of the National Academy of Sciences*, *114*(45), 12081–12085. https://doi.org/10.1073/pnas.1704552114

Gvakharia, A., Kort, E. A., Smith, M. L., & Conley, S. (2020). Evaluating Cropland N_2O Emissions and Fertilizer Plant Greenhouse Gas Emissions With Airborne Observations. *Journal of Geophysical Research: Atmospheres*, *125*(16), e2020JD032815. https://doi.org/10.1029/2020jd032815

Gvakharia, A., Kort, E. A., Smith, M. L., & Conley, S. (2018). Testing and evaluation of a new airborne system for continuous N_2O, CO_2, CO, and H_2O measurements: the Frequent Calibration High-performance Airborne Observation System (FCHAOS). *Atmospheric Measurement Techniques*, *11*(11), 6059–6074. https://doi.org/10.5194/amt-11-6059-2018

Hall, B. D., Dutton, G. S., & Elkins, J. W. (2007). The NOAA nitrous oxide standard scale for atmospheric observations. *Journal of Geophysical Research: Atmospheres*, *112*(D9), D09305. https://doi.org/10.1029/2006JD007954

Harazono, Y., Iwata, H., Sakabe, A., Ueyama, M., Takahashi, K., Nagano, H., Nakai, T., & Kosugi, Y. (2015). Effects of water vapor dilution on trace gas flux, and practical correction methods. *Journal of Agricultural Meteorology*, *71*(2), 65–76. https://doi.org/10.2480/agrmet.d-14-00003

Hegarty, J., Draxler, R. R., Stein, A. F., Brioude, J., Mountain, M., Eluszkiewicz, J., Nehrkorn, T., Ngan, F., & Andrews, A. (2013). Evaluation of Lagrangian Particle Dispersion Models with Measurements from Controlled Tracer Releases. *Journal of Applied Meteorology and Climatology*, *52*(12), 2623–2637. https://doi.org/10.1175/JAMC-D-13-0125.1

Hersbach, H., Bell, B., Berrisford, P., Hirahara, S., Horányi, A., Muñoz-Sabater, J., Nicolas, J., Peubey, C., Radu, R., Schepers, D., Simmons, A., Soci, C., Abdalla, S., Abellan, X., Balsamo, G., Bechtold, P., Biavati, G., Bidlot, J., Bonavita, M., De Chiara, G., Dahlgren, P., Dee, D., Diamantakis, M., Dragani, R., Flemming, J., Forbes, R., Fuentes, M., Geer, A., Haimberger, L., Healy, S., Hogan, R. J., Hólm, E., Janisková, M., Keeley, S., Laloyaux, P., Lopez, P., Lupu, C., Radnoti, G., de Rosnay, P., Rozum, I., Vamborg, F., Villaume, S., & Thépaut, J.-N. (2020). The ERA5 global reanalysis. *Quarterly Journal of the Royal Meteorological Society*, *146*(730), 1999–2049. https://doi.org/10.1002/qj.3803

Hirsch, A. I., Michalak, A. M., Bruhwiler, L. M., Peters, W., Dlugokencky, E. J., & Tans, P. P. (2006). Inverse modeling estimates of the global nitrous oxide surface flux from 1998-2001. *Global Biogeochemical Cycles*, *20*(1), GB1008. https://doi.org/10.1029/2004gb002443

Iacono, M. J., Delamere, J. S., Mlawer, E. J., Shephard, M. W., Clough, S. A., & Collins, W. D. (2008). Radiative forcing by long-lived greenhouse gases: Calculations with the AER radiative transfer models. *Journal of Geophysical Research: Atmospheres*, *113*(D13), D13103. https://doi.org/10.1029/2008jd009944

IPCC. (2006). *2006 IPCC Guidelines for National Greenhouse Gas Inventories* (H. S. Eggleston, L. Buendia, K. Miwa, T. Ngara, & K. Tanabe, Eds.). Institute for Global Environmental Strategies (IGES).

IPCC. (2013). *Climate Change 2013: The Physical Science Basis. Contribution of Working Group I to the Fifth Assessment Report of the Intergovernmental Panel on Climate Change* (T. F. Stocker, D. Qin, G.-K. Plattner, M. Tignor, S. K. Allen, J. Boschung, A. Nauels, Y. Xia, V. Bex, & P. M. Midgley, Eds.). Cambridge University Press, Cambridge, United Kingdom; New York, NY, USA.

IPCC. (2018). *Global Warming of 1.5 °C. An IPCC Special Report on the impacts of global warming of 1.5 °C above pre-industrial levels and related global greenhouse gas emission pathways, in the context of strengthening the global response to the threat of climate change, sustainable development, and efforts to eradicate poverty* (V. Masson-Delmotte, P. Zhai, H.-O. Pörtner, D. Roberts, J. Skea, P. R. Shukla, A. Pirani, W. Moufouma-Okia, C. Péan, R. Pidcock, S. Connors, J. B. R. Matthews, Y. Chen, X. Zhou, M. I. Gomis, E. Lonnoy, T. Maycock, M. Tignor, & T. Waterfield, Eds.). https://www.ipcc.ch/sr15/

Jacob, D. J., Turner, A. J., Maasakkers, J. D., Sheng, J., Sun, K., Liu, X., Chance, K., Aben, I., McKeever, J., & Frankenberg, C. (2016). Satellite observations of atmospheric methane and their value for quantifying methane emissions. *Atmospheric Chemistry and Physics*, *16*(22), 14371–14396. https://doi.org/10.5194/acp-16-14371-2016

Janssens-Maenhout, G., Crippa, M., Guizzardi, D., Muntean, M., Schaaf, E., Dentener, F., Bergamaschi, P., Pagliari, V., Olivier, J. G. J., Peters, J. A. H. W., van Aardenne, J. A., Monni, S., Doering, U., Petrescu, A. M. R., Solazzo, E., & Oreggioni, G. D. (2019). EDGAR v4.3.2 Global Atlas of the three major greenhouse gas emissions for the period

1970–2012. *Earth System Science Data*, *11*(3), 959–1002. https://doi.org/10.5194/essd-11-959-2019

Janssens-Maenhout, G., Pagliari, V., Guizzardi, D., & Muntean, M. (2013). *Global emission inventories in the Emission Database for Global Atmospheric Research (EDGAR) - Manual (I): Gridding: EDGAR emissions distribution on global gridmaps*. Institute for Environmental; Sustainability (Joint Research Centre), Publications Office of the European Union, LB-NA-25785-EN-N. https://doi.org/10.2788/81454

Kain, J. S. (2004). The Kain-Fritsch Convective Parameterization: An Update. *Journal of Applied Meteorology and Climatology*, *43*(1), 170–181. https://doi.org/10.1175/1520-0450(2004)043<0170:tkcpau>2.0.co;2

Kanter, D. R., Ogle, S. M., & Winiwarter, W. (2020). Building on Paris: integrating nitrous oxide mitigation into future climate policy. *Current Opinion in Environmental Sustainability*, *47*, 1–6. https://doi.org/10.1016/j.cosust.2020.04.005

Karion, A., Sweeney, C., Pétron, G., Frost, G., Hardesty, R. M., Kofler, J., Miller, B. R., Newberger, T., Wolter, S., Banta, R., Brewer, A., Dlugokencky, E., Lang, P., Montzka, S. A., Schnell, R., Tans, P., Trainer, M., Zamora, R., & Conley, S. (2013). Methane emissions estimate from airborne measurements over a western United States natural gas field. *Geophysical Research Letters*, *40*(16), 4393–4397. https://doi.org/10.1002/grl.50811

Keane, B. J., Ineson, P., Vallack, H. W., Blei, E., Bentley, M., Howarth, S., McNamara, N. P., Rowe, R. L., Williams, M., & Toet, S. (2018). Greenhouse gas emissions from the energy crop oilseed rape (*Brassica napus*); the role of photosynthetically active radiation in diurnal N_2O flux variation. *GCB Bioenergy*, *10*(5), 306–319. https://doi.org/10.1111/gcbb.12491

Kim, M., Bewley, W. W., Canedy, C. L., Kim, C. S., Merritt, C. D., Abell, J., Vurgaftman, I., & Meyer, J. R. (2015). High-power continuous-wave interband cascade lasers with 10 active stages. *Optics Express*, *23*(8), 9664–9672. https://doi.org/10.1364/oe.23.009664

Kitzler, B., Zechmeister-Boltenstern, S., Holtermann, C., Skiba, U., & Butterbach-Bahl, K. (2006). Nitrogen oxides emission from two beech forests subjected to different nitrogen loads. *Biogeosciences*, *3*(3), 293–310. https://doi.org/10.5194/bg-3-293-2006

Klausner, T., Mertens, M., Huntrieser, H., Galkowski, M., Kuhlmann, G., Baumann, R., Fiehn, A., Jöckel, P., Pühl, M., Roiger, A., Helmig, D., & Bruhwiler, L. (2020). Urban greenhouse gas emissions from the Berlin area: A case study using airborne CO_2 and CH_4 in situ observations in summer 2018. *Elementa: Science of the Anthropocen*, *8*(1), 15/1–24. https://doi.org/10.1525/elementa.411

Kooijmans, L. M. J., Uitslag, N. A. M., Zahniser, M. S., Nelson, D. D., Montzka, S. A., & Chen, H. (2016). Continuous and high-precision atmospheric concentration measurements of COS, CO_2, CO and H_2O using a quantum cascade laser spectrometer (QCLS). *Atmospheric Measurement Techniques*, *9*(11), 5293–5314. https://doi.org/10.5194/amt-9-5293-2016

Kort, E. A., Eluszkiewicz, J., Stephens, B. B., Miller, J. B., Gerbig, C., Nehrkorn, T., Daube, B. C., Kaplan, J. O., Houweling, S., & Wofsy, S. C. (2008). Emissions of CH_4 and N_2O over the United States and Canada based on a receptor-oriented modeling framework and COBRA-NA atmospheric observations. *Geophysical Research Letters*, *35*(18), L18808. https://doi.org/10.1029/2008GL034031

Kostinek, J., Roiger, A., Davis, K. J., Sweeney, C., DiGangi, J. P., Choi, Y., Baier, B., Hase, F., Groß, J., Eckl, M., Klausner, T., & Butz, A. (2019). Adaptation and performance assessment of a quantum and interband cascade laser spectrometer for simultaneous airborne in situ observation of CH_4, C_2H_6, CO_2, CO, and N_2O. *Atmospheric Measurement Techniques*, *12*(3), 1767–1783. https://doi.org/10.5194/amt-12-1767-2019

Kostinek, J. A. D. (2019). *Quantification of greenhouse gas fluxes by a new airborne laser absorption spectrometer* (Doctoral dissertation). Ludwig-Maximilians-Universität München, Faculty of Physics. Munich, Germany. https://doi.org/10.5282/edoc.25402

Kroeze, C., Mosier, A., & Bouwman, L. (1999). Closing the global N_2O budget: A retrospective analysis 1500–1994. *Global Biogeochemical Cycles*, *13*(1), 1–8. https://doi.org/10.1029/1998GB900020

Kroon, P. S., Schrier-Uijl, A. P., Hensen, A., Veenendaal, E. M., & Jonker, H. J. J. (2010). Annual balances of CH_4 and N_2O from a managed fen meadow using eddy covariance flux measurements. *European Journal of Soil Science*, *61*(5), 773–784. https://doi.org/10.1111/j.1365-2389.2010.01273.x

Larsen, K. S., Andresen, L. C., Beier, C., Jonasson, S., Albert, K. R., Ambus, P., Arndal, M. F., Carter, M. S., Christensen, S., Holmstrup, M., Ibrom, A., Kongstad, J., van der Linden, L., Maraldo, K., Michelsen, A., Mikkelsen, T. N., Pilegaard, K., Priemé, A., Ro-Poulsen, H., Schmidt, I. K., Selsted, M. B., & Stevnbak, K. (2010). Reduced N cycling in response to elevated CO_2, warming, and drought in a Danish heathland: Synthesizing results of the CLIMAITE project after two years of treatments. *Global Change Biology*, *17*(5), 1884–1899. https://doi.org/10.1111/j.1365-2486.2010.02351.x

Leuzinger, S., Luo, Y., Beier, C., Dieleman, W., Vicca, S., & Körner, C. (2011). Do global change experiments overestimate impacts on terrestrial ecosystems? *Trends in Ecology & Evolution*, *26*(5), 236–241. https://doi.org/10.1016/j.tree.2011.02.011

Li, M., Wu, P., & Ma, Z. (2020). A comprehensive evaluation of soil moisture and soil temperature from third-generation atmospheric and land reanalysis data sets. *International Journal of Climatology*, *40*(13), 5744–5766. https://doi.org/10.1002/joc.6549

Lin, J. C., Gerbig, C., Wofsy, S. C., Andrews, A. E., Daube, B. C., Davis, K. J., & Grainger, C. A. (2003). A near-field tool for simulating the upstream influence of atmospheric observations: The Stochastic Time-Inverted Lagrangian Transport (STILT) model. *Journal of Geophysical Research*, *108*(D16), 4493. https://doi.org/10.1029/2002jd003161

Luther, A., Kleinschek, R., Scheidweiler, L., Defratyka, S., Stanisavljevic, M., Forstmaier, A., Dandocsi, A., Wolff, S., Dubravica, D., Wildmann, N., Kostinek, J., Jöckel, P., Nickl, A.-L., Klausner, T., Hase, F., Frey, M., Chen, J., Dietrich, F., Neçki, J., Swolkień, J., Fix, A., Roiger, A., & Butz, A. (2019). Quantifying CH_4 emissions from hard coal mines using mobile sun-viewing Fourier transform spectrometry. *Atmospheric Measurement Techniques*, *12*(10), 5217–5230. https://doi.org/10.5194/amt-12-5217-2019

MacFarling Meure, C. (2004). *The natural and anthropogenic variations of carbon dioxide, methane and nitrous oxide during the Holocene from ice core analysis* (Doctoral dissertation). University of Melbourne.

MacFarling Meure, C., Etheridge, D., Trudinger, C., Steele, P., Langenfelds, R., van Ommen, T., Smith, A., & Elkins, J. (2006). Law Dome CO_2, CH_4 and N_2O ice core records extended to 2000 years BP. *Geophysical Research Letters*, *33*(14), L14810. https://doi.org/10.1029/2006GL026152

McManus, J. B., Nelson, D. D., & Zahniser, M. S. (2015). Design and performance of a dual-laser instrument for multiple isotopologues of carbon dioxide and water. *Optics Express*, *23*(5), 6569–6586. https://doi.org/10.1364/oe.23.006569

McManus, J. B., Zahniser, M. S., & Nelson, D. D. (2011). Dual quantum cascade laser trace gas instrument with astigmatic Herriott cell at high pass number. *Applied Optics*, *50*(4), A74–A85. https://doi.org/10.1364/ao.50.000a74

Miller, S. M., Kort, E. A., Hirsch, A. I., Dlugokencky, E. J., Andrews, A. E., Xu, X., Tian, H., Nehrkorn, T., Eluszkiewicz, J., Michalak, A. M., & Wofsy, S. C. (2012). Regional sources of nitrous oxide over the United States: Seasonal variation and spatial distribution. *Journal of Geophysical Research: Atmospheres*, *117*(D6), D06310. https://doi.org/10.1029/2011JD016951

Müller, C., Kammann, C., Ottow, J. C. G., & Jäger, H.-J. (2003). Nitrous oxide emission from frozen grassland soil and during thawing periods. *Journal of Plant Nutrition and Soil Science*, *166*(1), 46–53. https://doi.org/10.1002/jpln.200390011

Muñoz Sabater, J. (2019). ERA5-Land monthly averaged data from 1981 to present. Copernicus Climate Change Service (C3S) Climate Data Store (CDS) [last accessed: 14 June 2021]. https://doi.org/10.24381/cds.68d2bb30

Myhre, G., Shindell, D., Bréon, F.-M., Collins, W., Fuglestvedt, J., Huang, J., Koch, D., Lamarque, J.-F., Lee, D., Mendoza, B., Nakajima, T., Robock, A., Stephens, G., Takemura, T., & Zhang, H. (2013). Anthropogenic and Natural Radiative Forcing. In T. F. Stocker, D. Qin, G.-K. Plattner, M. Tignor, S. K. Allen, J. Boschung, A. Nauels, Y. Xia, V. Bex, & P. M. Midgley (Eds.), *Climate Change 2013: The Physical Science Basis. Contribution of Working Group I to the Fifth Assessment Report of the Intergovernmental Panel on Climate Change* (pp. 659–740). Cambridge University Press.

Nakanishi, M., & Niino, H. (2006). An Improved Mellor–Yamada Level-3 Model: Its Numerical Stability and Application to a Regional Prediction of Advection Fog. *Boundary-Layer Meteorology*, *119*(2), 397–407. https://doi.org/10.1007/s10546-005-9030-8

Nakayama, N., Toma, Y., Iwai, Y., Furutani, H., Hondo, T., Hatano, R., & Toyoda, M. (2020). Mass spectrometric multiple soil-gas flux measurement system with a portable high-resolution mass spectrometer (MULTUM) coupled to an automatic chamber for continuous field observations. *Atmospheric Measurement Techniques*, *13*(12), 6657–6673. https://doi.org/10.5194/amt-13-6657-2020

NARR. (2005). National Centers for Environmental Prediction, National Weather Service, NOAA, U.S. Department of Commerce: NCEP North American Regional Reanalysis, updated monthly [last accessed: 27 May 2020]. https://rda.ucar.edu/datasets/ds608.0

NASS. (2021). USDA's National Agricultural Statistics Service - Quick Stats [last accessed: 16 April 2021]. https://quickstats.nass.usda.gov/

NCEP. (2004a). National Centers for Environmental Prediction, National Weather Service, NOAA, U.S. Department of Commerce: NCEP ADP Global Surface Observational Weather Data, October 1999 - continuing. Obtained from: Research Data Archive at the National Center for Atmospheric Research, Computational and Information Systems Laboratory, Boulder, CO, USA [last accessed: 28 Oct 2020]. https://doi.org/10.5065/4f4p-e398

NCEP. (2004b). Satellite Services Division, Office of Satellite Data Processing and Distribution, NESDIS, NOAA, U.S. Department of Commerce and National Centers for Environmental Prediction, National Weather Service, NOAA, U.S. Department of Commerce: NCEP ADP Global Upper Air Observational Weather Data, October 1999 - continuing. Obtained from: Research Data Archive at the National Center for Atmospheric Research, Computational and Information Systems Laboratory, Boulder, CO, USA [last accessed: 28 Oct 2020]. https://doi.org/10.5065/39c5-z211

Niklaus, P. A., Roux, X. L., Poly, F., Buchmann, N., Scherer-Lorenzen, M., Weigelt, A., & Barnard, R. L. (2016). Plant species diversity affects soil–atmosphere fluxes of methane and nitrous oxide. *Oecologia*, *181*, 919–930. https://doi.org/10.1007/s00442-016-3611-8

Niklaus, P. A., Wardle, D. A., & Tate, K. R. (2006). Effects of Plant Species Diversity and Composition on Nitrogen Cycling and the Trace Gas Balance of Soils. *Plant and Soil*, *282*, 83–98. https://doi.org/10.1007/s11104-005-5230-8

Nisbet, E., & Weiss, R. (2010). Top-Down Versus Bottom-Up. *Science*, *328*(5983), 1241–1243. https://doi.org/10.1126/science.1189936

NOAA. (2020a). National Centers for Environmental Information, Climate at a Glance: Regional Mapping [published Oct 2020, retrieved on Nov 11, 2020]. https://www.ncdc.noaa.gov/cag/regional/mapping

NOAA. (2020b). National Centers for Environmental Information, Climate at a Glance: Regional Rankings [published Jun 2020, retrieved on Jul 20, 2020]. https://www.ncdc.noaa.gov/cag/regional/rankings

NOAA. (2021). National Centers for Environmental Information (NCEI) - U.S. Billion-Dollar Weather and Climate Disasters [last accessed: 29 April 2021]. https://doi.org/10.25921/STKW-7W73

NOAA/ESRL. (2021a). Combined Nitrous Oxide data from the NOAA/ESRL Global Monitoring Division [last accessed: 30 Apr 2021]. https://gml.noaa.gov/aftp/data/hats/n2o/combined/GML_global_N2O.txt

NOAA/ESRL. (2021b). Halocarbons & other Atmospheric Trace Species (HATS) - Nitrous Oxide (N_2O) – Combined Data Set [last accessed: 09 Jun 2021]. https://gml.noaa.gov/hats/combined/N2O.html

NOAA/NCEI. (2020). U.S. Billion-Dollar Weather and Climate Disasters [last accessed: 20 Dec 2020]. https://doi.org/10.25921/stkw-7w73

Ochsner, T. (2019). *Rain or Shine: An Introduction to Soil Physical Properties and Processes*. Oklahoma State University Libraries. https://doi.org/10.22488/okstate.21.000000

Ogle, S. M., Butterbach-Bahl, K., Cardenas, L., Skiba, U., & Scheer, C. (2020). From research to policy: optimizing the design of a national monitoring system to mitigate soil nitrous oxide emissions. *Current Opinion in Environmental Sustainability*, *47*, 28–36. https://doi.org/10.1016/j.cosust.2020.06.003

Olivier, J. G. J., Bouwman, A. F., Berdowski, J. J. M., Veldt, C., Bloos, J. P. J., Visschedijk, A. J. H., van der Maas, C. W. M., & Zandveld, P. Y. J. (1999). Sectoral emission inventories of greenhouse gases for 1990 on a per country basis as well as on 1°×1°. *Environmental Science & Policy*, *2*(3), 241–263. https://doi.org/10.1016/s1462-9011(99)00027-1

Olivier, J. G. J., Bouwman, A. F., van der Maas, C. W. M., Berdowski, J. J. M., Veldt, C., Bloos, J. P. J., Visschedijk, A. J. H., Zandveld, P. Y. J., & Haverlag, J. L. (1996). Description of EDGAR Version 2.0: A set of global emission inventories of greenhouse gases and ozone-depleting substances for all anthropogenic and most natural sources on a per country basis and on 1°×1° grid. *National Institute of Public Health and the Environment (RIVM) report no. 771060 002 / TNO-MEP report no. R96/119*. http://hdl.handle.net/10029/10497

Park, S., Croteau, P., Boering, K. A., Etheridge, D. M., Ferretti, D., Fraser, P. J., Kim, K.-R., Krummel, P. B., Langenfelds, R. L., van Ommen, T. D., Steele, L. P., & Trudinger, C. M. (2012). Trends and seasonal cycles in the isotopic composition of nitrous oxide since 1940. *Nature Geoscience*, *5*(4), 261–265. https://doi.org/10.1038/ngeo1421

Parkin, T. B., & Kaspar, T. C. (2006). Nitrous Oxide Emissions from Corn-Soybean Systems in the Midwest. *Journal of Environmental Quality*, *35*(4), 1496–1506. https://doi.org/10.2134/jeq2005.0183

Parton, W. J., Hartman, M., Ojima, D., & Schimel, D. (1998). DAYCENT and its land surface submodel: description and testing. *Global and Planetary Change*, *19*(1), 35–48. https://doi.org/10.1016/S0921-8181(98)00040-X

Petrescu, A. M. R., Qiu, C., Ciais, P., Thompson, R. L., Peylin, P., McGrath, M. J., Solazzo, E., Janssens-Maenhout, G., Tubiello, F. N., Bergamaschi, P., Brunner, D., Peters, G. P., Höglund-Isaksson, L., Regnier, P., Lauerwald, R., Bastviken, D., Tsuruta, A., Winiwarter, W., Patra, P. K., Kuhnert, M., Oreggioni, G. D., Crippa, M., Saunois, M., Perugini, L., Markkanen, T., Aalto, T., Zwaaftink, C. D. G., Tian, H., Yao, Y., Wilson, C., Conchedda, G., Günther, D., Leip, A., Smith, P., Haussaire, J.-M., Leppänen, A., Manning, A. J., McNorton, J., Brockmann, P., & Dolman, A. J. (2021). The consolidated European synthesis of CH_4 and N_2O emissions for the European Union and United Kingdom: 1990–2017. *Earth System Science Data*, *13*(5), 2307–2362. https://doi.org/10.5194/essd-13-2307-2021

Pitt, J. R., Le Breton, M., Allen, G., Percival, C. J., Gallagher, M. W., Bauguitte, S. J.-B., O'Shea, S. J., Muller, J. B. A., Zahniser, M. S., Pyle, J., & Palmer, P. I. (2016). The development and evaluation of airborne in situ N_2O and CH_4 sampling using a quantum cascade laser absorption spectrometer (QCLAS). *Atmospheric Measurement Techniques*, *9*(1), 63–77. https://doi.org/10.5194/amt-9-63-2016

Powers, J. G., Klemp, J. B., Skamarock, W. C., Davis, C. A., Dudhia, J., Gill, D. O., Coen, J. L., Gochis, D. J., Ahmadov, R., Peckham, S. E., Grell, G. A., Michalakes, J., Trahan, S., Benjamin, S. G., Alexander, C. R., Dimego, G. J., Wang, W., Schwartz, C. S., Romine, G. S., Liu, Z., Snyder, C., Chen, F., Barlage, M. J., Yu, W., & Duda, M. G. (2017). The Weather Research and Forecasting Model: Overview, System Efforts, and Future Directions. *Bulletin of the American Meteorological Society*, *98*(8), 1717–1737. https://doi.org/10.1175/bams-d-15-00308.1

Prather, M. J., Holmes, C. D., & Hsu, J. (2012). Reactive greenhouse gas scenarios: Systematic exploration of uncertainties and the role of atmospheric chemistry. *Geophysical Research Letters*, *39*(9), L09803. https://doi.org/10.1029/2012GL051440

Prather, M. J., Hsu, J., DeLuca, N. M., Jackman, C. H., Oman, L. D., Douglass, A. R., Fleming, E. L., Strahan, S. E., Steenrod, S. D., Søvde, O. A., Isaksen, I. S. A., Froidevaux, L., & Funke, B. (2015). Measuring and modeling the lifetime of nitrous oxide including its variability. *Journal of Geophysical Research: Atmospheres*, *120*(11), 5693–5705. https://doi.org/10.1002/2015jd023267

Ravishankara, A. R., Daniel, J. S., & Portmann, R. W. (2009). Nitrous Oxide (N_2O): The Dominant Ozone-Depleting Substance Emitted in the 21st Century. *Science*, *326*(5949), 123–125. https://doi.org/10.1126/science.1176985

Reay, D. S., Davidson, E. A., Smith, K. A., Smith, P., Melillo, J. M., Dentener, F., & Crutzen, P. J. (2012). Global agriculture and nitrous oxide emissions. *Nature Climate Change*, *2*(6), 410–416. https://doi.org/10.1038/nclimate1458

Rogers, R. E., Deng, A., Stauffer, D. R., Gaudet, B. J., Jia, Y., Soong, S.-T., & Tanrikulu, S. (2013). Application of the Weather Research and Forecasting Model for Air Quality Modeling in the San Francisco Bay Area. *Journal of Applied Meteorology and Climatology*, *52*(9), 1953–1973. https://doi.org/10.1175/jamc-d-12-0280.1

Santoni, G. W., Daube, B. C., Kort, E. A., Jiménez, R., Park, S., Pittman, J. V., Gottlieb, E., Xiang, B., Zahniser, M. S., Nelson, D. D., McManus, J. B., Peischl, J., Ryerson, T. B., Holloway, J. S., Andrews, A. E., Sweeney, C., Hall, B., Hintsa, E. J., Moore, F. L., Elkins, J. W., Hurst, D. F., Stephens, B. B., Bent, J., & Wofsy, S. C. (2014). Evaluation of the airborne quantum cascade laser spectrometer (QCLS) measurements of the carbon and greenhouse gas suite – CO_2, CH_4, N_2O, and CO – during the CalNex and HIPPO campaigns. *Atmospheric Measurement Techniques*, *7*(6), 1509–1526. https://doi.org/10.5194/amt-7-1509-2014

Saunois, M., Stavert, A. R., Poulter, B., Bousquet, P., Canadell, J. G., Jackson, R. B., Raymond, P. A., Dlugokencky, E. J., Houweling, S., Patra, P. K., Ciais, P., Arora, V. K., Bastviken, D., Bergamaschi, P., Blake, D. R., Brailsford, G., Bruhwiler, L., Carlson, K. M., Carrol, M., Castaldi, S., Chandra, N., Crevoisier, C., Crill, P. M., Covey, K., Curry, C. L., Etiope, G., Frankenberg, C., Gedney, N., Hegglin, M. I., Höglund-Isaksson, L., Hugelius, G., Ishizawa, M., Ito, A., Janssens-Maenhout, G., Jensen, K. M., Joos, F., Kleinen, T., Krummel, P. B., Langenfelds, R. L., Laruelle, G. G., Liu, L., Machida, T., Maksyutov, S., McDonald, K. C., McNorton, J., Miller, P. A., Melton, J. R., Morino, I., Müller, J., Murguia-Flores, F., Naik, V., Niwa, Y., Noce, S., O'Doherty, S., Parker, R. J., Peng, C., Peng, S., Peters, G. P., Prigent, C., Prinn, R., Ramonet, M., Regnier, P., Riley, W. J., Rosentreter, J. A., Segers, A., Simpson, I. J., Shi, H., Smith, S. J., Steele, L. P., Thornton, B. F., Tian, H., Tohjima, Y., Tubiello, F. N., Tsuruta, A., Viovy, N., Voulgarakis, A., Weber, T. S., van Weele, M., van der Werf, G. R., Weiss, R. F., Worthy, D., Wunch, D., Yin, Y., Yoshida, Y., Zhang, W., Zhang, Z., Zhao, Y., Zheng, B., Zhu, Q., Zhu, Q., & Zhuang, Q. (2020). The Global Methane Budget 2000–2017. *Earth System Science Data*, *12*(3), 1561–1623. https://doi.org/10.5194/essd-12-1561-2020

Schaufler, G., Kitzler, B., Schindlbacher, A., Skiba, U., Sutton, M. A., & Zechmeister-Boltenstern, S. (2010). Greenhouse gas emissions from European soils under different land use: Effects of soil moisture and temperature. *European Journal of Soil Science*, *61*(5), 683–696. https://doi.org/10.1111/j.1365-2389.2010.01277.x

Schindlbacher, A., Zechmeister-Boltenstern, S., & Butterbach-Bahl, K. (2004). Effects of soil moisture and temperature on NO, NO_2, and N_2O emissions from European forest soils. *Journal of Geophysical Research*, *109*(D17), D17302. https://doi.org/10.1029/2004jd004590

Schmidt, U., Thöni, H., & Kaupenjohann, M. (2000). Using a boundary line approach to analyze N_2O flux data from agricultural soils. *Nutrient Cycling in Agroecosystems*, *57*(2), 119–129. https://doi.org/10.1023/A:1009854220769

Seinfeld, J. H., & Pandis, S. N. (2016). *Atmospheric chemistry and physics : From air pollution to climate change* (3^{rd} Ed.). John Wiley & Sons, Inc.

Skamarock, W. C., Klemp, J. B., Dudhia, J., Gill, D. O., Liu, Z., Berner, J., Wang, W., Powers, J. G., Duda, M. G., Barker, D. M., & Huang, X.-Y. (2019). *A Description of the Advanced Research WRF Model Version 4 (NCAR/TN-556+STR)* (tech. rep.). National Center for Atmospheric Resarch (NCAR/UCAR), Mesoscale and Microscale Meteorology Laboratory (MMM). Boulder, CO, USA, UCAR/NCAR. https://doi.org/10.5065/1dfh-6p97

Solazzo, E., Crippa, M., Guizzardi, D., Muntean, M., Choulga, M., & Janssens-Maenhout, G. (2021). Uncertainties in the Emissions Database for Global Atmospheric Research (EDGAR) emission inventory of greenhouse gases. *Atmospheric Chemistry and Physics*, *21*(7), 5655–5683. https://doi.org/10.5194/acp-21-5655-2021

Stehfest, E., & Bouwman, L. (2006). N_2O and NO emission from agricultural fields and soils under natural vegetation: summarizing available measurement data and modeling of global annual emissions. *Nutrient Cycling in Agroecosystems*, *74*(3), 207–228. https://doi.org/10.1007/s10705-006-9000-7

Stein, A. F., Draxler, R. R., Rolph, G. D., Stunder, B. J. B., Cohen, M. D., & Ngan, F. (2015). NOAA's HYSPLIT Atmospheric Transport and Dispersion Modeling System. *Bulletin of the American Meteorological Society*, *96*(12), 2059–2077. https://doi.org/10.1175/bams-d-14-00110.1

Stull, R. (2006). The Atmospheric Boundary Layer (Chapter 9) [Figure 9.16a on p. 392 – Reprinted from Publication, ©2006, with permission from Elsevier]. *In Wallace and Hobbs (2006a): Atmospheric Science - An Introductory Survey* (pp. 375–417). Elsevier. https://doi.org/10.1016/B978-0-12-732951-2.50014-4

Sweeney, C., Baier, B. C., Miller, J. B., Lang, P., Miller, B. R., Lehman, S., Michel, S. E., & Yang, M. M. (2018). ACT-America: L2 In Situ Atmospheric Gas Concentrations from Flasks, Eastern USA. https://doi.org/10.3334/ORNLDAAC/1575

Sweeney, C., Karion, A., Wolter, S., Newberger, T., Guenther, D., Higgs, J. A., Andrews, A. E., Lang, P. M., Neff, D., Dlugokencky, E., Miller, J. B., Montzka, S. A., Miller, B. R., Masarie, K. A., Biraud, S. C., Novelli, P. C., Crotwell, M., Crotwell, A. M., Thoning, K., & Tans, P. P. (2015). Seasonal climatology of CO_2 across North America from aircraft measurements in the NOAA/ESRL Global Greenhouse Gas Reference Network. *Journal of Geophysical Research: Atmospheres*, *120*(10), 5155–5190. https://doi.org/10.1002/2014jd022591

Teepe, R., Brumme, R., & Beese, F. (2001). Nitrous oxide emissions from soil during freezing and thawing periods. *Soil Biology and Biochemistry*, *33*(9), 1269–1275. https://doi.org/10.1016/S0038-0717(01)00084-0

Teepe, R., Vor, A., Beese, F., & Ludwig, B. (2004). Emissions of N_2O from soils during cycles of freezing and thawing and the effects of soil water, texture and duration of freezing. *European Journal of Soil Science*, *55*(2), 357–365. https://doi.org/10.1111/j.1365-2389.2004.00602.x

Thompson, G., Field, P. R., Rasmussen, R. M., & Hall, W. D. (2008). Explicit Forecasts of Winter Precipitation Using an Improved Bulk Microphysics Scheme. Part II: Implementation of a New Snow Parameterization. *Monthly Weather Review*, *136*(12), 5095–5115. https://doi.org/10.1175/2008mwr2387.1

Thompson, R. L., Lassaletta, L., Patra, P. K., Wilson, C., Wells, K. C., Gressent, A., Koffi, E. N., Chipperfield, M. P., Winiwarter, W., Davidson, E. A., Tian, H., & Canadell, J. G. (2019). Acceleration of global N_2O emissions seen from two decades of atmospheric inversion. *Nature Climate Change*, *9*(12), 993–998. https://doi.org/10.1038/s41558-019-0613-7

Thompson, R. L., & Stohl, A. (2014). FLEXINVERT: An atmospheric Bayesian inversion framework for determining surface fluxes of trace species using an optimized grid.

Geoscientific Model Development, *7*(5), 2223–2242. https://doi.org/10.5194/gmd-7-2223-2014

Tian, H., Xu, R., Canadell, J. G., Thompson, R. L., Winiwarter, W., Suntharalingam, P., Davidson, E. A., Ciais, P., Jackson, R. B., Janssens-Maenhout, G., Prather, M. J., Regnier, P., Pan, N., Pan, S., Peters, G. P., Shi, H., Tubiello, F. N., Zaehle, S., Zhou, F., Arneth, A., Battaglia, G., Berthet, S., Bopp, L., Bouwman, A. F., Buitenhuis, E. T., Chang, J., Chipperfield, M. P., Dangal, S. R. S., Dlugokencky, E., Elkins, J. W., Eyre, B. D., Fu, B., Hall, B., Ito, A., Joos, F., Krummel, P. B., Landolfi, A., Laruelle, G. G., Lauerwald, R., Li, W., Lienert, S., Maavara, T., MacLeod, M., Millet, D. B., Olin, S., Patra, P. K., Prinn, R. G., Raymond, P. A., Ruiz, D. J., van der Werf, G. R., Vuichard, N., Wang, J., Weiss, R. F., Wells, K. C., Wilson, C., Yang, J., & Yao, Y. (2020). A comprehensive quantification of global nitrous oxide sources and sinks. *Nature*, *586*(7828), 248–256. https://doi.org/10.1038/s41586-020-2780-0

Tian, H., Yang, J., Xu, R., Lu, C., Canadell, J. G., Davidson, E. A., Jackson, R. B., Arneth, A., Chang, J., Ciais, P., Gerber, S., Ito, A., Joos, F., Lienert, S., Messina, P., Olin, S., Pan, S., Peng, C., Saikawa, E., Thompson, R. L., Vuichard, N., Winiwarter, W., Zaehle, S., & Zhang, B. (2018). Global soil nitrous oxide emissions since the preindustrial era estimated by an ensemble of terrestrial biosphere models: Magnitude, attribution, and uncertainty. *Global Change Biology*, *25*(2), 640–659. https://doi.org/10.1111/gcb.14514

Tittel, F. K., Bakhirkin, Y., Kosterev, A. A., & Wysocki, G. (2006). Recent Advances in Trace Gas Detection Using Quantum and Interband Cascade Lasers. *The Review of Laser Engineering*, *34*(4), 275–282. https://doi.org/10.2184/lsj.34.275

Turner, P. A., Griffis, T. J., Lee, X., Baker, J. M., Venterea, R. T., & Wood, J. D. (2015). Indirect nitrous oxide emissions from streams within the US Corn Belt scale with stream order. *Proceedings of the National Academy of Sciences*, *112*(32), 9839–9843. https://doi.org/10.1073/pnas.1503598112

UNFCCC. (2015). Paris Agreement [last accessed: 30 April 2021]. https://treaties.un.org/doc/Treaties/2016/02/20160215%2006-03%20PM/Ch_XXVII-7-d.pdf

USDA. (2020). Economics, Statistics and Market Information System - Crop Progress [last accessed: 20 Jul 2020]. https://usda.library.cornell.edu/concern/publications/8336h188j?locale=en#release-items

USDA-NASS. (2020). United States Department of Agriculture - National Agricultural Statistics Service - Statistics by State [last accessed: 23 Jul 2020]. https://www.nass.usda.gov/Statistics_by_State/index.php

Ussiri, D. A. N., & Lal, R. (2013). *Soil Emission of Nitrous Oxide and its Mitigation*. Springer Netherlands. https://doi.org/10.1007/978-94-007-5364-8

van Genuchten, M. T. (1980). A Closed-form Equation for Predicting the Hydraulic Conductivity of Unsaturated Soils. *Soil Science Society of America Journal*, *44*(5), 892–898. https://doi.org/10.2136/sssaj1980.03615995004400050002x

VIP-MRCC. (2021). GIS: Freeze Map Interface. Vegetation Impact Program (VIP), Midwestern Regional Climate Center (MRCC). Illinois State Water Survey, Prairie Research Institute, University of Illinois at Urbana-Champaign [last accessed: 24 March 2021]. https://mrcc.illinois.edu/gismaps/freeze_guidance.htm

Vurgaftman, I., Bewley, W. W., Canedy, C. L., Kim, C. S., Kim, M., Lindle, J. R., Merritt, C. D., Abell, J., & Meyer, J. R. (2011). Mid-IR Type-II Interband Cascade Lasers. *IEEE Journal of Selected Topics in Quantum Electronics*, *17*(5), 1435–1444. https://doi.org/10.1109/jstqe.2011.2114331

Wagner-Riddle, C., Congreves, K. A., Abalos, D., Berg, A. A., Brown, S. E., Ambadan, J. T., Gao, X., & Tenuta, M. (2017). Globally important nitrous oxide emissions from croplands induced by freeze–thaw cycles. *Nature Geoscience*, *10*(4), 279–283. https://doi.org/10.1038/ngeo2907

Wagner-Riddle, C., Furon, A., McLaughlin, N. L., Lee, I., Barbeau, J., Jayasundara, S., Parkin, G., von Bertoldi, P., & Warland, J. (2007). Intensive measurement of nitrous oxide emissions from a corn-soybean-wheat rotation under two contrasting management systems over 5 years. *Global Change Biology*, *13*(8), 1722–1736. https://doi.org/10.1111/j.1365-2486.2007.01388.x

Wallace, J. M., & Hobbs, P. V. (2006, May 1). *Atmospheric Science - An Introductory Survey* (2^{nd} Ed., Vol. 92). Elsevier. https://doi.org/10.1016/C2009-0-00034-8

Wei, Y., Shrestha, R., Pal, S., Gerken, T., Feng, S., McNelis, J., Singh, D., Thornton, M. M., Boyer, A. G., Shook, M. A., Chen, G., Baier, B. C., Barkley, Z. R., Barrick, J. D., Bennett, J. R., Browell, E. V., Campbell, J. F., Campbell, L. J., Choi, Y., Collins, J., Dobler, J., Eckl, M., Fiehn, A., Fried, A., DiGangi, J. P., Barton-Grimley, R., Halliday, H., Klausner, T., Kooi, S., Kostinek, J., Lauvaux, T., Lin, B., McGill, M. J., Meadows, B., Miles, N. L., Nehrir, A. R., Nowak, J. B., Obland, M., O'Dell, C., Fao, R. M. P., Richardson, S. J., Richter, D., Roiger, A., Sweeney, C., Walega, J., Weibring, P., Williams, C. A., Yang, M. M., Zhou, Y., & Davis, K. J. (2021). Atmospheric Carbon and Transport – America (ACT-America) Datasets: Description, Management, and Delivery. *Earth and Space Science*, *8*(7), e2020EA001634. https://doi.org/10.1029/2020EA001634

WMO. (2021). State of the Climate 2020 (WMO-No. 1264). World Meteorological Organization. https://library.wmo.int/doc_num.php?explnum_id=10618

Xiang, B., Miller, S. M., Kort, E. A., Santoni, G. W., Daube, B. C., Commane, R., Angevine, W. M., Ryerson, T. B., Trainer, M. K., Andrews, A. E., Nehrkorn, T., Tian, H., & Wofsy, S. C. (2013). Nitrous oxide (N_2O) emissions from California based on 2010 CalNex airborne measurements. *Journal of Geophysical Research: Atmospheres*, *118*(7), 2809–2820. https://doi.org/10.1002/jgrd.50189

Xu, R., Tian, H., Pan, S., Prior, S. A., Feng, Y., & Dangal, S. R. S. (2020). Global N_2O Emissions From Cropland Driven by Nitrogen Addition and Environmental Factors: Comparison and Uncertainty Analysis. *Global Biogeochemical Cycles*, *34*(12), e2020GB006698. https://doi.org/10.1029/2020GB006698

Danksagung

An dieser Stelle bedanke ich mich herzlich bei allen Kolleg*innen, Freunden und meiner Familie für die Unterstützung während meiner Promotion am DLR. Ohne sie wäre diese Arbeit nicht zu Stande gekommen.

Ein sehr großer Dank geht an Prof. Dr. Markus Rapp für die Möglichkeit am DLR zu promovieren. Sein Interesse und die konstruktiven Diskussionen über Ergebnisse und weitere Schritte haben mich stets motiviert und bilden die Grundlage meiner Arbeit. Insbesondere danke ich Dr. Anke Roiger für die hervorragende Betreuung in allen Phasen meiner Promotion. Dank ihr war es mir möglich an spannenden Messkampagnen und interessanten Konferenzen im In- und Ausland teilzunehmen. Ihre fortlaufende Unterstützung und persönliche Motivation habe diese Arbeit zu dem gemacht, was sie heute ist.

Vielen Dank an Dr. Julian Kostinek für die Einarbeitung in das Messinstrument und die Hilfe bei jeglichen technischen und experimentellen Fragen. Weiterhin danke ich Dr. Alina Fiehn und Dr. Heidi Huntrieser für regelmäßige wissenschaftliche Diskussionen und die gemeinsame Lösung kleinerer und größerer Probleme bei der Auswertung. Zudem gebührt diesen Dreien zusammen mit Dr. Theresa Klausner, Dr. Klaus-Dirk Gottschaldt und Magdalena Pühl (falls ich jemanden vergessen habe, Entschuldigung) großer Dank für das ausführliche Korrekturlesen und hilfreiche Tipps beim zusammenschreiben. Vielen Dank auch an die restliche Nachwuchsgruppe „Treibhausgase“ für die angenehme und motivierende Arbeitsatmosphäre. Nicht zu vergessen ist mein Bürokollege Christopher Heckl, der mit anregenden Fahrraddiskussionen für angenehme Ablenkungen von der Arbeit gesorgt hat.

Weiterhin danke ich dem Team von ACT-America für die wundervolle Kampagnenzeit in den USA. Besonderer Dank gilt Kenneth J. Davis für die Möglichkeit an der Kampagne teilzunehmen und für seine Hilfe in allen Belangen vor, während und nach der Kampagne. Zudem will ich speziell Zachary R. Barkley für die geduldige Unterstützung bei der Ausarbeitung meiner wissenschaftlicher Publikation danken. Außerdem danke ich herzlich Bianca C. Baier für die HYSPLIT Simulationen, welche den zweiten Teil dieser Arbeit ermöglicht haben. Großer Dank gebührt auch Stephen M. Ogle für die Bereitstellung der DayCent Simulationen und für seine Hilfe bei deren Interpretation.

Zu guter Letzt will ich mich bei meinen Eltern Josef und Theresia und meinen beiden Geschwistern Maria und Benedikt bedanken, die mich stets unterstützt und motiviert haben. Und am wichtigsten, Isi: Danke für drei Jahre offenes Ohr, Geduld, Motivieren, Aushalten von Berg- und Talfahrten . . .